Effects of Thermal and Mechanical Treatments on the Fatigue Performance of Friction Welded Joints

Doctoral Thesis
(Dissertation)

To be awarded the degree
Doctor of Engineering (Dr.-Ing)

submitted by

Mahmoud Basha Mohamed Moustafa

from Cairo, Egypt

approved by the
Faculty of Natural and Material Sciences,
Clausthal University of Technology

Date of oral examination
22.05.2018

Dean
Prof. Dr.-Ing. Karl-Heinz Spitzer

Chairperson of the Board of Examiners
Prof. Dr.-Ing. habil. Joachim Deubener

Supervising tutor
Prof. Dr.-Ing. habil. Lothar Wagner

Reviewer
Prof. Dr.-Ing. Volker Wesling

Printed and published with the support of the German Academic Exchange Service

Acknowledgments

This doctoral study was carried out in the Institute of Materials Science and Engineering– Clausthal University of Technology.

All praises to Allah the Almighty for giving me the blessing, chance, strength and endurance to complete this study.

My sincere gratitude is dedicated to my supervisor Prof. Lothar Wagner for giving me the opportunity to pursue my Ph.D. degree at TU-Clausthal and for his continuous generous guidance and considerate support, from the early stage of this research, as well as providing me with extraordinary experiences throughout the work. Besides, I would also like to express my appreciation to the co-referent Prof. Dr.-Ing Volker Wesling for taking his precious time to review my thesis manuscript.

I am grateful to the German Academic Exchange Service (DAAD) and the Egyptian Ministry of Higher Education (MoHE) for the financial support in the framework of the German Egyptian Research Long-term Scholarship program (GERLS). Furthermore, I would like to express my sincere gratitude and appreciation to Prof. Dr. Nahid Abd-El-salam and Prof. Dr. A. Elsabbagh for helping me to get this scholarship.

Kind acknowledgments I owe to Dr. rer. nat. M. Wollmann and Dr.-Ing. M. Mhaede for their continuous support during this study. Special thanks are directed to my friend M. Sc. Othman for his considerable contributions and discussions throughout this work. Furthermore, I owe my deepest gratitude to Dr.-Ing. M. Harhash and Dr. Ing M. Soliman for their valuable review and comments on this work.

Many thanks go to all the members in our research group, M. Sc. S. Levin und M. Sc. E. Weber, for their friendly and scientific assist. Moreover, I would like to thank the technical staffs at IWW, especially Mr. J. Schumann, Mr. G. Neuse, Mr. P. König and Mr. U. Körner for their technical support. Furthermore, I owe thanks to Dr. -Ing. J. Fuhr who supported me performing some experimental tasks at Curtiss-Wright Surface Technologies (CWST) in the USA.

This work is dedicated to the memory of my father who taught me the meaning of life, to my beloved mother the origin of my success.

I would like to express my deep thanks and appreciation to my uncle Khalil. Additionally, great thanks to my sisters, Doaa, Samya and Hadir, and brothers, Mohamed and Ahmed, for their continuous prayers, love and support.

But most of all, I would like to thank my dearest ones; my wife, Mai, and my sons, Abdelrahman, Ziad and Muhammad for making life wonderful.

This page intentionally left blank

Abstract

Friction welding (FRW) is presented as one of the most economical, simple and productive welding methods. FRW is a solid state joining process providing a unique approach for joining alloys that are usually unsuitable to weld using fusion welding techniques. Residual stresses (RS) in FRW may be considerably less than those induced in fusion welds since FRW occurs at lower temperature. However, the rigid clamping system used in FRW can still produce high tensile RS in the welding joints. These RS can remarkably affect the service performance of the welded materials by reducing their fatigue life and promoting the fatigue crack growth process. This has instigated the demand for techniques and methods that can relieve the tensile RS in welded parts. Therefore, the main objective of this study is to improve the surface layer properties and impact toughness as well as to enhance the fatigue performance of rotary and orbital friction-welded metallic joints. In this study, the continuous drive rotary friction welding (RFW) has been used to weld similar joints from commercially pure titanium (CP-Ti) and dissimilar joints of stainless steel AISI 316L to carbon steel AISI 1012. The process parameters were varied in a wide extent to determine the optimum operating parameters using the design of experiment (DoE) technique. In addition, the orbital friction welding (OFW) was used to weld joints from the high temperature titanium alloy Ti-6Al-2Sn-4Zr-2Mo-0.1Si (Ti-6242). Combination of mechanical surface treatments such as shot peening (SP) and roller burnishing (RB) and thermal ones namely post-weld heat treatment (PWHT) have been applied on the weld joints to introduce compressive RS that compensate the tensile ones at the weld, which results in significant improvements of the fatigue life of these joints up to 87%. The process parameters of the SP and RB have been varied until reaching the optimum parameters that led to improved surface layer properties and enhanced fatigue performance. The residual stress depth profiles and surface residual stress distribution across the weld line were measured using the incremental hole-drilling method (IHD) and laboratory X-Ray diffraction (LXRD), respectively. The phase transformations during welding processes were investigated using X-ray diffraction technique. This investigation demonstrated that both SP and RB markedly increased in the fatigue performance and hardness levels of the joints welded by rotary and orbital friction welding. A significant enhancement in the ductility of the joints has been reported after PWHT process. Moreover, applying SP and RB after PWHT led to a remarkable improvement of the fatigue life of the welded joints. According to these results, it is recommended to apply a combination of surface treatments and PWHT after FRW to improve the integrity of the weld. Furthermore, it could be concluded that the mechanical surface treatment (SP and RB) can control the fracture location either in the weld zone or the lower strength base metal of the welded joints by distinguishing the reinforcement zone.

Kurzfassung

Reibschweißen (FRW) wird als eines der wirtschaftlichsten, einfachsten und produktivsten Schweißverfahren vorgestellt. FRW ist ein Festkörperfügeverfahren, das einen einzigartigen Ansatz zum Verbinden von Legierungen bietet, die normalerweise nicht zum Schweißen unter Verwendung von Schmelzschweißtechniken geeignet sind. Eigenspannungen (RS) in FRW können beträchtlich geringer sein als diejenigen, die in Schmelzschweißstellen induziert werden, da FRW bei niedrigeren Temperaturen auftritt. Das in FRW verwendete starre Spannsystem kann jedoch immer noch hohe Zugeigenspannungen in den Schweißverbindungen erzeugen. Diese RS können die Betriebsleistung der geschweißten Materialien erheblich beeinflussen, indem sie ihre Ermüdungslebensdauer verringern und den Ermüdungsrisswachstumsprozess fördern. Dies hat zu einer Nachfrage nach Techniken und Verfahren geführt, die die Zugeigenspannungen in geschweißten Teilen verringern können. Daher ist das Hauptziel dieser Studie die Verbesserung der Oberflächeneigenschaften und Schlagzähigkeit sowie die Verbesserung der Ermüdungsfestigkeit von rotations- und orbital-reibgeschweißten metallischen Verbindungen. In dieser Studie wurde das Rotationsreibschweißen mit kontinuierlichem Antrieb (RFW) zum Schweißen ähnlicher Verbindungen von kommerziell reinem Titan (CP-Ti) und verschiedenen Verbindungen von rostfreiem Stahl AISI 316L zu Kohlenstoffstahl AISI 1012 verwendet. Die Prozessparameter wurden in einem weiten Ausmaß zur Bestimmung der optimalen Betriebsparameter unter Verwendung der Design of Experiment (DoE) –Technik variiert. Zusätzlich wurde das Orbitalreibschweißen (OFW) zum Schweißen von Verbindungen aus der Hochtemperatur-Titanlegierung Ti-6Al-2Sn-4Zr-2Mo-0,1Si (Ti-6242) verwendet. Eine Kombination von mechanischen Oberflächenbehandlungen wie Kugelstrahlen (SP) und Festwalzen (RB) und thermischer Behandlung, nämlich Wärmebehandlung nach dem Schweißen (PWHT) wurden auf die Schweißverbindungen angewendet, um Druckeigenspannungen einzubringen, die die Zugeigenspannungen in der Schweißnaht kompensieren, was zu einer signifikanten Verbesserung der Ermüdungslebensdauer dieser

Verbindungen von bis zu 87% führt. Die Prozessparameter von SP und RB wurden variiert, bis die optimalen Parameter, die zu verbesserten Oberflächeneigenschaften und verbesserten Ermüdungseigenschaften führten, erreicht wurden. Die Eigenspannungs-Tiefenprofile und die Oberflächen-Eigenspannungsverteilung über die Schweißnaht wurden mit Hilfe der inkrementellen Lochbohrmethode (IHD) bzw. der Labor- Röntgendiffration (LXRD) gemessen. Die Phasenumwandlungen während der Schweißprozesse wurden mittels Röntgendiffration untersucht. Diese Untersuchung zeigte, dass sowohl SP als auch RB die Ermüdungseigenschaften und die Härte der durch rotation- und orbitalreibgeschweißten Verbindungen deutlich erhöhten. Nach dem PWHT-Verfahren wurde eine signifikante Verbesserung der Duktilität der Verbindung festgestellt. Darüber hinaus führte die Anwendung von SP und RB nach PWHT zu einer bemerkenswerten Verbesserung der Ermüdungslebensdauer der Schweißverbindungen. Gemäß diesen Ergebnissen wird empfohlen, eine Kombination von Oberflächenbehandlungen und PWHT nach FRW anzuwenden, um das Widerstandsvermögen der Schweißnaht zu verbessern. Darüber hinaus konnte gefolgert werden, dass durch die mechanische Oberflächenbehandlung (SP und RB) der Bruch entweder in der Schweißzone oder dem unteren Basismetall der Schweißverbindungen durch Unterscheiden der behandelten Zone eingestellt werden kann

Table of Contents

This page intentionally left blank

Nomenclature

Greek symbols

Symbol	Term	Unit
γ_2	Secondary austenite	[-]
δ	δ-ferrite phase	[-]
γ	Austenite phase	[-]
α	Alpha phase of Ti-alloys with hcp crystal structure	[-]
β	Beta phase of Ti-alloys with bcc crystal structure	[-]
2θ	Scattering angle	[°]
σa	Stress amplitude	[MPa]
Ø	Diameter	[mm]
σ	True stress	[MPa]
ψ	Tilting angle of sample	[°]
λ	Wavelength	[Å]

Latin symbols

Symbol	Term	Unit
BI	Beraha I	[-]
BII	Beraha II	[-]
D	Predetermined displacement	[mm]
d (hkl)	Interplanar spacing	[Å]
El	Elongation	[%]
F	applied force	[kN]
f	Frequency	[Hz]
L	Central weld length (approx.)	[mm]
LA	Unclamping length of the welding sample	[mm]
LBI	Lichtenegger and Bloech I	[-]
$M_{23}C_6$	Chromium-rich carbide	[-]
M_f	Martensite finish	[-]
M_s	Martensite start	[-]
N_F	Total fatigue life or Number of cycles to failure	[cycles]

N_I	Number of cycles to fatigue crack nucleation	[cycles]
N_P	Number of cycles for propagating fatigue cracks	[cycles]
P1	Friction pressure	[bar]
P2	Forging pressure	[bar]
P_N	Axial friction pressure	[bar]
R	Stress ratio	[-]
RA	Reduction of area	[%]
R_a	Average surface roughness	[µm]
R_z	Maximum height of the roughness profile	[µm]
t	Time	[s]
T	Temperature	[°C]
t1	Friction time	[s]
t2	forging time	[s]
T_m	Melting temperature	[°C]
UTS or R_m	Ultimate tensile strength	[MPa]
V2A	Vogel's special reagent	[-]
W	Flash width	[mm]
w	Angular speed	[°/s]
YS or R_p	Yield strength	[MPa]

Abbreviations

Acronym	Term
AC	Air cooling
AISI	American iron and steel institute
AISI 1012	Low carbon steel 1012
AISI 316L	Austenitic stainless steel 316L
ANOVA	Analysis of variance
APUs	auxiliary power units
AW	As-welded state
AW EP	As-welded electropolished
AW MP	As-welded mechanically polished
AW RB	As-welded + Roller burnishing
AW RB (WZ)	As-welded + Roller burnishing in weld zone only
AW SP	As-welded + Shot peening
AW SP (WZ)	As-welded + Shot peening in weld zone only
AW SP 45°	As-welded + Shot peening at peening angle of 45°
AWS	American Welding Society
BLISK	BLaded dISK
BWJ	Black white joints
CDFW	Continuous-drive friction welding
CP-Ti	Commercially pure titanium
CWZ	Central weld zone
DMW	Dissimilar metals welding
DoE	Design of experiment
EDX	Energy dispersive X-ray spectroscopy
EP	Electropolished specimens
FCC	Face-centered cubic structure
FRW	Friction welding
HAZ	Heat affected zone
HCF	High cycle fatigue
HP	High pressure
HV	Hardness vicker
IFW	Inertia friction welding
IGP	Intergranular precipitation of chromium carbide (sensitization)
IHD	Incremental hole-drilling method

LCF	Low cycle fatigue
LFW	Linear friction welding
LXRD	Laboratory X-ray diffraction
MCVN	Miniaturized Charpy V-notch specimens
MOFW	Multi-orbital friction welding
MP	Mechanically-polished specimens
NME	No metallurgical effect
OFW	Orbital friction welding
OM	Optical microscopy
OPS	Finer silicon oxide polishing suspension
PDZ	Partially deformed zone
PM or BM	Parent metal/Parent material or Base metal/Base material
PWHT	Post-weld heat treatment state
PWHT RB	Post-weld heat treated + Roller burnishing
PWHT SP	Post-weld heat treated + Shot peening
RB	Roller burnishing
RS	Residual stresses
SA	Solution annealed
SAD	Selected area diffraction
SCC	Stress corrosion cracking
SCCW 14	Spherically conditioned (rounded) cut wire shots
SEM	Scanning electron microscopy
SHT	Solution heat treatment
SIP	Strain-induced precipitation of carbides
S–N	Stress – number of cycle curve
SOFW	Single-orbital friction welding (also used as OFW)
SP	Shot peening
SPDZ	Severe plastic deformed zone
SSCS	Saturation Curve Solver by Shock form Aeronautique Inc.
SSW	Solid-state welding
Ti-6242	High temperature titanium alloy Ti-6Al-2Sn-4Zr-2Mo-0.1Si
TMAZ	Thermo-mechanically affected zone
WQ	Water quenching
WZ	Weld zone (here a distance of 5 mm right and left the weld line)
XRD	X-ray diffraction

1. Motivation and Objectives

By developing the technology of today, joining of similar and dissimilar materials has always been a necessity in engineering applications. The most suitable approach in joining two different materials is to weld. The fact that the microstructural and mechanical properties of welding zone are naturally different from the properties of the original material at post-welding process has came up, and these differences initiate some significant problems. Among the modern welding techniques used in engineering today, the solid-state welding (SSW) processes are widely used. Bonding is achieved by the introduction of mechanical, electrical or thermal energy and/or diffusion. These processes differ in times, pressures and temperatures used as well as methods of applying heat [1].

Friction welding (FRW) is a solid state joining process which can produce high-quality welds between two components with either similar or dissimilar material. When proper welding parameters are chosen, friction welding can join two dissimilar materials in a full-strength weld, without sacrificing weld integrity or strength. The friction welding process creates a weld interface that consists of an entirely new material composed of the two original materials. FRW has many advantages over conventional welding processes. The major advantage of friction welding relies on the direct conversion of mechanical energy into thermal energy at the joint interface. The very high-temperature gradient in the joint area accounts for a very small HAZ. Due to the narrow HAZ, the welding distortion is minimal. The process is very energy-efficient resulting in short joining times. Additionally, during the burn-off and forging stages, the hot plasticized material is expelled out from the weld interface, which implies that surface oxides and contaminations are removed, and a high-integrity weld is accomplished. FRW can be fully automated, and no welder certification is required. In contrast to fusion welding, filler materials, flux or shielding gases are not needed for friction welding. Joint preparation in friction welding is minimal; a saw cut surface is most commonly used. Due to the short cycles times, the automation possibilities and the reduced labor cost is one of the most significant benefits of the process. The process is environmentally friendly, producing little smoke, fumes or slag [16]. In this thesis, two subcategories of FRW were studied on similar and dissimilar joints by applying orbital friction welding (OFW) and rotary friction welding (RFW).

OFW has been primarily employed as an alternative method to linear friction welding (LFW) of BLISK (BLaded dISK) manufacturing in previous study [54]. A blisk is a single aero-engine part consisting of a rotor disk and blades. in OFW, the two components to be joined are rotated around their longitudinal axes in the same sense with identical angular speed. The two longitudinal axes are parallel except for a small distance offset (amplitude). When the motion of the components ceases, the parts need to be correctly aligned to form a weld. The material used in OFW was Ti-6Al-2Sn-4Zr-2Mo-0.1Si (Ti-6242) as a high temperature titanium alloy with adequate creep strength. The main application of Ti-6242 with bi-modal microstructure are blades and disks in the compressor section of aero-engines. This alloy is applied in the high pressure (HP) compressor stages for which the temperature exceeds 350 °C where Ti-6Al-4V cannot be used because of creep considerations. A good example for the application of Ti-6242 material with bi-modal microstructure is the impeller shown in **Figure 1.1-a)**. Impellers are used as last compressor stage in small, low flow aero-engines and in auxiliary power units (APUs) [90].

RFW was applied in this study on similar and dissimilar material couples. In RFW, one part is held stationary while forced to rub counter to another rotating part under axial force [10]. It is used broadly for joining rotationally symmetrical materials. Similar joints of commercially pure titanium (CP-Ti), which are used in sea water piping systems, have been welded. CP-Ti pipes are used as an efficient substitution for copper-nickel alloys as they can increase the life by five times which consequently reduce the cost over the entire service life [93-96]. Dissimilar joints of austenitic stainless steel (AISI 316L) and carbon steel (AISI 1012) were joined together by RFW. This combination of materials has a wide application in chemical and petrochemical industries. An example of application for these dissimilar joints is the pump shafts (**Figure 1.1-b)**). Most commonly the carbon steel part of the shaft may be the shaft on the electric motor and the corrosion resistant alloy part of the shaft is used in a corrosive environment. Welding stainless steel to low carbon steel is most commonly used over more expensive corrosion resistant material. Therefore, friction welding of black white joints (BWJ) allows pump manufacturers the ability to use composite rather than one-piece shafts promoting a significant cost saving and satisfactory service performance [82].

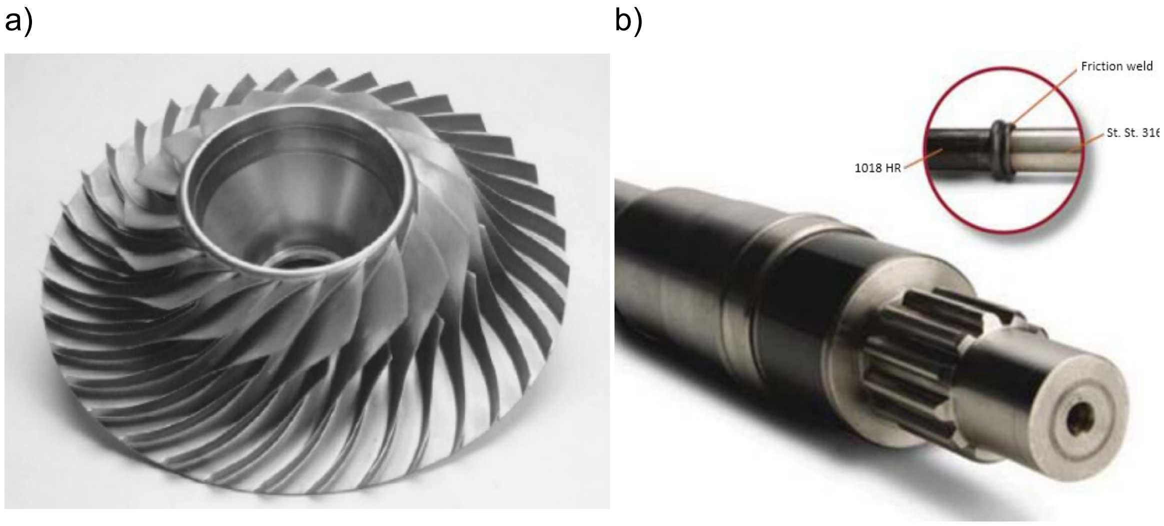

Figure 1.1 a) Impeller used in a small engine for regional jets, Ti-6242, bi-modal microstructure [90] and b) bi-metal pump shaft blank, rotary friction-welded AISI 316L to AISI 1018 [82].

1.1. Objectives of the study

Due to an ever-increasing demand for enhancing the service life of the welded components, and since fatigue is a major cause of weld failures, improvement of the welded joints fatigue strength becomes more essential. One of the effective ways to significantly improve the fatigue life is to convert the induced welding tensile residual stresses (RS), which are disadvantageous to fatigue performance, to compressive RS [26]. The improvement residual stress techniques can be divided into two main groups, mechanical methods such as shot peening (SP), roller burnishing (RB) etc. and thermal ones such as thermal stress relief, spot heating etc. [122].

Therefore, based on the available state of the art, several studies, such as [53,108,112,115,153] were concerned with applying a single residual stress improvement technique attempting to improve the fatigue performance of friction welded joints.

The current thesis gives a contribution to the earlier studies by means of combining thermal and /or mechanical treatment techniques such as SP together with PWHT to enhance the fatigue performance of rotary and orbital friction welded joints. The applied combined treatments can lead additionally to the enhancement of the surface layer properties and maintain or even improve the impact toughness of the friction welded joints.

On one hand, it is known that post-weld heat treated (PWHT) reduces or eliminate the tensile RS, however it does not introduce compressive ones [25,26]. On the other hand, SP and RB can eliminate the tensile RS and replace them with local compressive ones at the weld joints [27]. The compressive RS resulting from SP and RB can approach the yield strength of the base metal. Any applied cyclic stresses will be superimposed on the local compressive RS. Provided the cyclic stress range does not exceed the yield strength, the stress cycles in the vicinity of the weld remain in the compressive range. This effectively impedes crack propagation thereby increasing the fatigue strength or life of the welded joint substantially [124].

Figure 1.2 shows an overview of the study approaches and experimental methodologies in order to reach that general goal. The main aims of this study are to deliver treatment guidelines for enhancement the fatigue life of orbital and rotary friction welded joints.

Motivation & research demands

- Improving the weld joint fatigue performance of orbital and rotary friction-welded joints.
- Clarifying the role of the thermal and/or mechanical treatments of the transformation possibilities of the induced tensile residual stresses after welding to compressive ones.
- Identifying the influence of the afore-mentioned treatments on the impact toughness.

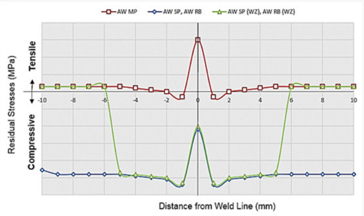

Investigation approaches

- Optimization of the friction welding parameters for:
    - ➢ RFW of AISI 1012 to AISI 316L
    - ➢ RFW of CP-Ti
    - ➢ OFW of Ti-6242 [54]
- Mechanical and metallurgical characterization of the welded joints

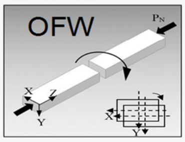

Bimodal Ti-6242

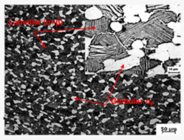

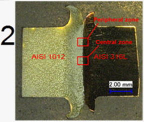

AISI 1012 to AISI 316L

- Adapting the PWHT process as a thermal treatment to improve the weld residual stresses.
- Optimization of shot peening (SP) and roller burnishing (RB) parameters.

For all combined treatments of the welded joints:

- Determining the surface layer properties (microhardness, roughness and residual stresses).
- Estimating the fatigue behavior.
- Evaluating the impact toughness behavior.

Experimental methodology

- Applying DoE technique using Minitab by using the full-factorial design method.
- Evaluating the weld mechanical characteristics using tensile, hardness and toughness testing
- Investigating the weld microstructure constituents and their composition using optical, SEM-EDX and XRD.

Tensile specimens

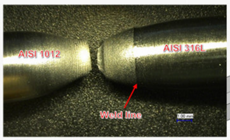

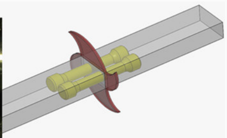

Fracture location

- Conducting different PWHT temperatures on the welded joints to relieve most of the internal residual stresses.
- Optimizing SP process at a wide range of Almen intensities and impingement angles using SCCW14 at full coverage.
- Optimizing RB process at a wide range of burnishing pressures using feed rate of 0.17 mm/rev and rotational speed of 150 rpm.

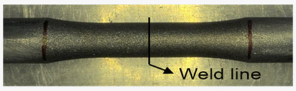

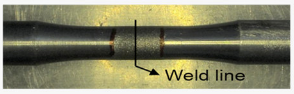

- Evaluating the microhardness-depth profiles and surface roughness.
- Evaluating Surface residual stress distribution and depth profile residual stresses.
- Performing the rotating bending fatigue tests in air at R = -1.
- Conducting a series of Charpy V-notch tests.
- Investigating the fracture surface Topography.

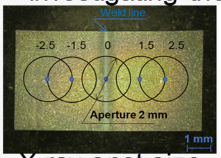

X-ray spot size and locations

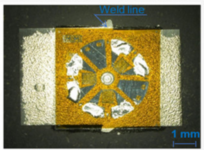

Strain gauge rosette

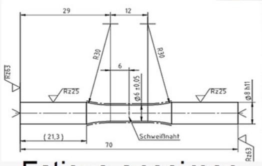

Fatigue specimen

Charpy specimens

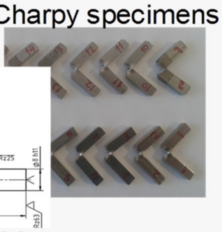

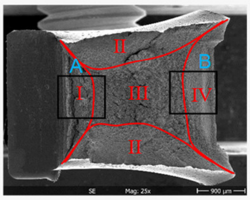

Goals

providing treatment guidelines for enhancement the fatigue life of orbital and rotary friction-welded joints.

Figure 1.2 An overview of the study approaches and experimental methodologies.

For achieving these general goals, the following six treatment combinations were applied:

1. As-welded: AW
2. Post-weld Heat Treated: PWHT
3. As-welded + Shot Peening; AW SP
4. As-welded + Roller Burnishing: AW RB
5. Post-weld Heat Treated + Shot Peening: PWHT SP
6. Post-weld Heat Treated + Roller Burnishing: PWHT RB

A plan of experiments based on the design of experiment method using Minitab 17 was designed. The aims of the optimization of RFW of AISI 1012 to AISI 316L are maximizing the tensile strength and minimizing the burn off length (metal loss), while for RFW of CP-Ti are maximizing the central weld length and minimizing the flash width to reduce the third part region in the friction welded joint. By statistical analysis, an optimal level of combination of processing parameters is achieved. To validate the optimization, an experiment was conducted at optimum parameters. The results were analyzed and interpreted in terms of estimated effects, analysis of variance (ANOVA), normal probability plots, and main effects plots. Based on these analyses, the significant factors were determined, and predictive models were formulated.

Afterwards, the mechanical and metallurgical characterization of the welded joints under as-welded AW state and post-weld heat treated PWHT state were studied and compared in detail to analyze the effect of AW and PWHT process on microstructures, element diffusion and mechanical properties of the friction welded joint, and the effect factors on fracture mechanism and mechanical properties of the AW and PWHT joints were also evaluated. The microstructures and element diffusion were analyzed by optical microscopy (OM), scanning electron microscopy (SEM) with an energy dispersive X-ray spectroscopy (EDX) to identify the phases formed at the weld interface. The welded joints were then mechanically surface treated by either shot peeing (SP) or roller burnishing (RB). An attempt was made to optimize the SP, and RB parameters to enhance the surface layer properties, fatigue performance, as well as the impact toughness at both AW and PWHT conditions. Fatigue crack nucleation sites and fracture surface Topography after impact tests were investigated by scanning electron microscopy (SEM). The depth profile RS and surface residual stress distribution across the weld line has been measured using the incremental hole-drilling method (IHD) and Laboratory X-Ray Diffraction (LXRD), respectively.

1.2. Thesis outline

This thesis consists of six chapters including this one. **Chapter 2** presents the actual state of the art and the subject-related theoretical background focusing on friction welding processes, mechanical surface treatments and RS in welded joints. **Chapter 3** is concerned with a detailed description of the experimental procedure used in this investigation presenting the mechanical and metallurgical techniques utilized to characterize the resultant welded joints and base metal. The results and discussion of dissimilar welded joints characterizations of AISI 316L to AISI 1012 by RFW is presented in **Chapter 4**, while the results of similar welded joints characterizations of CP-Ti and Ti-6242 are discussed in **Chapter 5**. The main results of this thesis are summarized in **Chapter 6.**

2. Literature Survey

2.1. Solid State Welding Processes

Solid state welding (SSW) refers to a group of welding processes that produce coalescence welds at temperatures primarily below the melting point of the parent materials being joined, without utilizing of brazing or solder filler metal. Pressure may or may not be applied [2]. SSW theory emphasizes that the driving force for two parts of metal to form a metallic bond to each other exists if the barriers to welding such as oxides, contaminants and surface roughness can be eliminated. All SSW processes are based on this concept and use some combination of heat, pressure, and time to overcome the barriers. In other words, SSW requires particularly that the atoms of one part be brought adequately close to the atoms of another part to allow interatomic forces to bridge interface as shown in **Figure 2.1-a)** [3].

However, there are major difficulties in occurring that: first, metal surfaces are rough on an atomic scale; even a finely ground surface, presents peaks and valleys that are thousands of atoms deep. Under light pressure, only a few opposing hills of the metal surfaces precisely touch. Second, the number of contacting surfaces can be extended by applying more pressure; but a layer of oxides and occluded gas which is present on all metal surfaces under normal atmospheric conditions **Figure 2.1-b)** is encountered, and for welding to occur, these layers must be removed [4]. Since there is no melting, except in so far as it may be accidentally included [5, 6], there is no hazard for the formation of faults that are only associated with fusion welding processes such as porosity, slag inclusions, and solidification cracking. SSW processes can be quite effective at welding dissimilar materials that cannot be welded with fusion welding due to metallurgical incompatibilities such as thermal expansion and conductivity. The equipment is typically very expensive, and some processes involve significant preparation time of the parts to be welded. Most of these processes are limited to certain joint designs, and some of them are not conducive to a production environment. Nondestructive testing methods do not always work well with solid- state welding processes because of the difficulties associated with distinguishing a true metallurgical bond when there is no solidification.

Temperature, pressure and time to produce SSW are adapted to suit the materials involved, the workpieces characteristics as well as the technique and the facilities being utilized. In general, an effective temperature for SSW is at least 0.7 of the melting temperature (T_m) of the metal to be joined. The pressure applied will depend on the workpieces nature, the surface conditions and the overall deformation that can be tolerated. The welding time varies over a wide range depending on which process is going to be applied, but it is kept in a predetermined range to secure the required closeness at the faying surfaces, development of interatomic bonding and disappearance of interfacial oxide particle and voids. SSW approaches include cold, diffusion, explosion, forge, ultrasonic, hot pressure, roll, and friction welding [4].

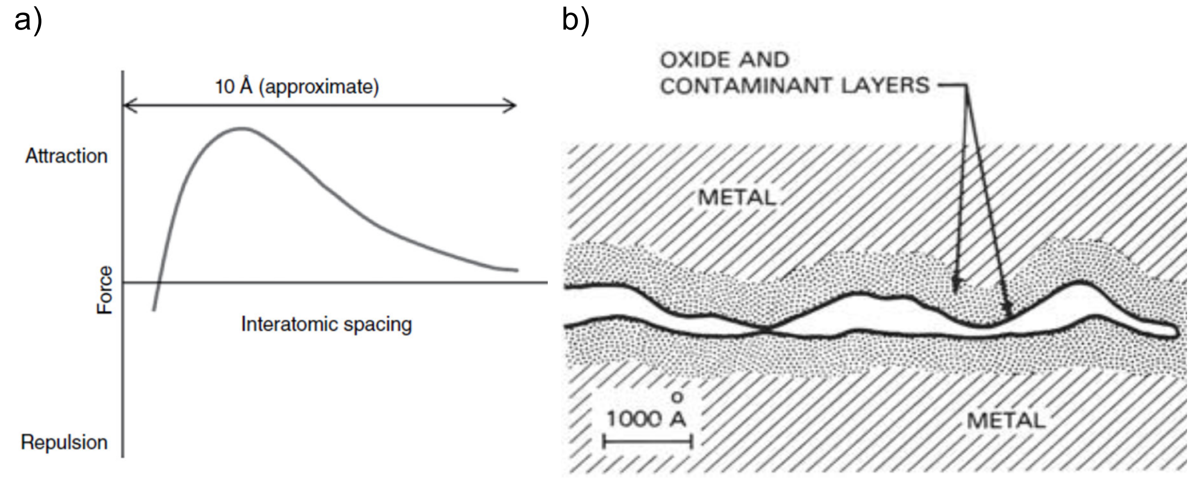

Figure 2.1 a) To achieve spontaneous bonding between two metals, the interatomic spacing must be very close [3] and b) Metal surface under normal atmospheric conditions [4].

2.1.1. Friction Welding Processes

Friction welding is one of solid state welding processes the two elements in friction welding are forced to rub against each other, thereby generating heat at the interface. This heat softens the material on either side of the rubbing interface, and the softened material then begins to flow together to initiate a weld. Once enough heat has been generated, the rubbing action is terminated, and the pressure is maintained or increased for a period to promote the solid phase weld. Therefore, the friction welding process employs a machine which is designed to convert mechanical energy into heat at the joint to be welded using relative movement between workpieces [7].

The definition of friction welding process in the American Welding Society (AWS) C6.1-89 Standard is as follows: “Friction welding is a solid-state joining process that produces coalescence of materials under compressive force contact of workpieces rotating or moving relative to one another to produce heat and plastically displace material from the faying surfaces. Under normal conditions, the faying surfaces do not melt. Filler metal, flux, and shielding gas are not required with this process” [8].

Basically, there are three variants of friction welding: rotary, linear and orbital (**Figure 2.2**). Rotary friction welding is the oldest and most popular method where one component is rotated about its axis while the other remains stationary. Then the two components are brought together under friction pressure. Depending on how rotational energy is converted into frictional heat, rotary friction welding can be divided into two major process variations: direct drive (continuous drive) and inertia drive (stored energy). The direct drive has been used commercially since the 1940s. It requires constant energy from a source for any desired duration. The inertia drive, which was developed in the early 1960s, uses the kinetic energy stored in a rotating flywheel [8]. In linear friction welding (LFW), the parts move under friction pressure relative to each other in a reciprocating fashion through a small linear displacement (amplitude) in the plane of the joint to be made. This method has been used since the 1980s. Another method is orbital friction welding (OFW), which is a combination of linear and rotational friction welding. With this friction welding process, the center of one component relative to the other component is moved around a 2D curve, e.g. a circle, to provide the rubbing action. In other words, in OFW, the two parts to be joined are rotated around their longitudinal axes in the same sense with the same constant angular speed. The two longitudinal axes are parallel except for a small distance offset (amplitude). When the motion of the components ceases, the parts need to be correctly aligned to form a weld. This method was introduced in the early 1970s [9].

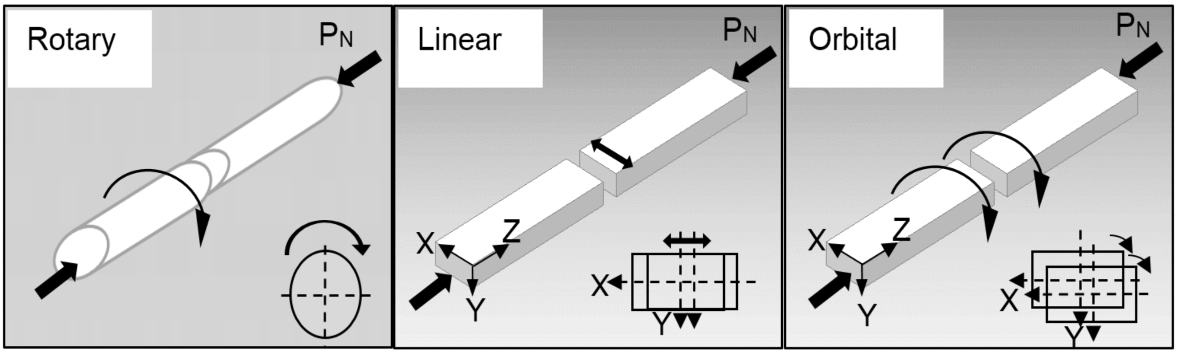

Figure 2.2 Three variants of friction welding.

2.1.1.1. Rotary Friction Welding

Since the introduction of Rotary friction welding (RFW) during Second World War, it is by far the most popular of all friction welding processes which has been used extensively for joining of structural materials which are rotationally symmetrical. There are two process variants: continuous-drive friction welding (CDFW) and inertia friction welding (IFW). The main difference between these two approaches is the means of giving energy to the welding interface. The basic principle of rotary friction welding is represented in **Figure 2.3** where one part is held stationary while forced to rub against another rotating part under axial force [10].

In CDFW, the rotating part is attached to a motor driven unit, while the other is restrained from rotation remaining stationary. The motor driven element is rotated at a predetermined speed during the heating period; the parts to be welded are moved together, and suddenly a friction welding force is applied. Heat is generated as the friction surfaces rub together. Such process continues for a predetermined time, or until a preset amount of axial shortening takes place. The driving force is dropped, and the rotating workpiece is made to stop (either by the application of a braking force or by its resistance to rotation). The friction welding force can be either increased or not; if increased, it is denominated forging force and kept for a predetermined time after rotation ceases to increase the upset of the heated metal at the joint. The friction weld is then completed [8, 11-15]. **Figure 2.4-a)** shows the relationship of the CDFW parameters characteristics [7].

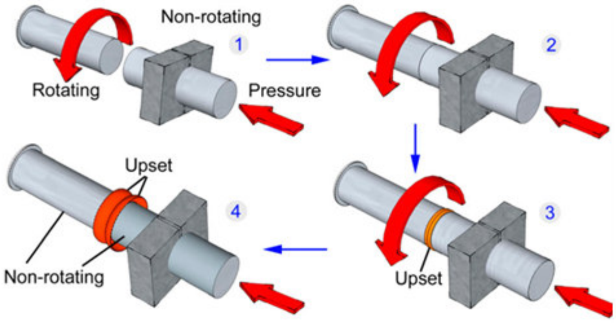

Figure 2.3 Schematic of the RFW process [10].

The main variables in the CDFW process are rotational speed, axial force and welding time. These variables determine the amount of energy input to the weld and the rate of heat generation at the interface. It is to be noted that the rate of heat generation is not constant across the interface and that it also varies during the different phases of the welding cycle. During welding, axial shortening (also called upset, burn-off or axial displacement) and resisting torque of friction undergo changes.

According to the shape of the friction torque curve in **Figure 2.4-a)**, the process can be divided into three phases [16]. In the initial phase, the torque rises rapidly to a peak value after the start of the process. It then decreases gradually to the equilibrium value. The rapid rise and gradual fall of torque is associated with the interlocking and breaking of asperities and subsequent softening of the material at the faying surfaces by frictional heating. Friction torque remains somewhat constant in the second phase, indicating that the process reaches a balance between strain rate hardening and temperature softening. Forging takes place in the third phase, which starts at the time of braking. Spindle rotation is immediately retarded, and the deceleration depends on the braking time. Axial force in this phase is usually increased to effect forging. The friction torque again rises after the onset of this phase, reaching another peak before sharply falling off to zero. This peak varies with deceleration and applied axial force. Under some circumstances, this final peak can be omitted by delaying the onset of the forging force. In CDFW, more often two stage friction force is applied; however, one stage friction force is sometimes used.

In the case of IFW, one of the welded components is held stationary while the other is attached to a flywheel. The wheel is accelerated to rotational speed, in this way, a predetermined amount of energy is stored which is going to be converted into heat. The drive motor to the flywheel assembly is then disengaged, and the workpieces are brought together by an axial friction force, which causes the faying surfaces to rub against each other under pressure. The energy stored in the rotating flywheel is utilized to generate heat through friction at the rubbing interface. The friction force is maintained for a predetermined time after the rotation ceases or increased (forging force) increasing the amount of upset and flash, which usually improves the weld quality and the mechanical properties [14]. If the frictional heating has brought the interfacial area to a welding temperature, the rising torque causes the flywheel rotation to stop suddenly, and the friction weld is formed. In this process, the speed of rotation is continuously changing during the welding cycle. The energy made available for this welding operation will depend on the flywheel size, shape, weight and rotating speed [8, 11-15]. **Figure 2.4-b)** shows the relationship of the inertia friction welding parameters [7]. In this process, the speed of rotation is continuously changing during the welding cycle.

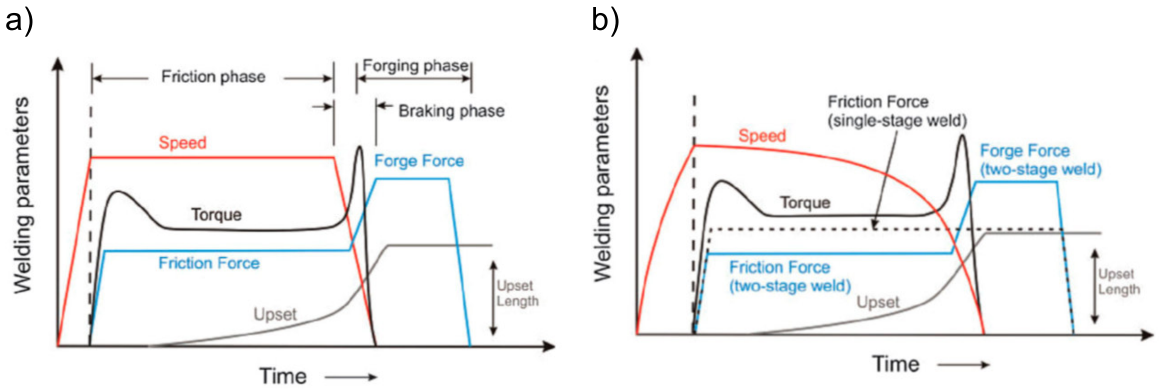

Figure 2.4 Schematic variation of welding parameters with time for a) CDFW process and b) IFW process [7].

The classification of single-stage and two-stage process in **Figure 2.4-b)** is vague and limited to RFW. While friction force can remain constant throughout the process, it can also be applied in two or more steps. Besides, both single-stage friction and two-stage friction processes are followed by forging stage at the end of welding, without altering the characteristics of the phases processes of RFW.

There are three controllable variables in IFW [16]: flywheel mass (expressed by moment of inertia), rotational speed and axial force. The inertia of the rotating component-flywheel combination can be altered by varying the size of the flywheel. The speed of rotation varies continuously throughout the fraction phase. The rate at which the speed decreases depends on the inertia of the rotating component-flywheel combination, and on the axial pressure. The events described for CDFW (**Figure 2.4-a)**) also occur in inertia friction welding. Apart from rotational speed, the variations of friction welding parameters with time are like those shown for CDFW (**Figure 2.4-b)**). Unlike the direct drive process, duration of rotation and forging time in the third phase is not predetermined but controlled by the three parameters [16]. If the axial force differs in phase 2 and 3, the process is called two stage welding; otherwise it is one stage welding.

Both processes (inertia and direct drive friction welding) produce excellent solid-state bonds. There are subtle differences or advantages of one process over the other. However, these advantages are not universal but depend upon the application (size, material combination, geometry consideration) [8]. For instance, lower rotational speed and axial force are generally used in direct drive machine. CDFW also offers greater latitude in process variable, since heating time (duration of rotation), or upset distance is preset, and the forging phase can be controlled by braking time, axial force and forging time. As the delivered energy to the interface in inertia welding is much quicker than in the direct drive type, temperature gradients are sharper producing a narrower HAZ.

Compared to other types of friction welding, RFW has been investigated much more broadly. The reason can be attributed to the relative's simplicity of the process machinery of rotary friction welding. There is a wealth of information on the process, but mostly gathered empirically (trial and error methods). Other factors which can affect the friction welding process are surface conditions, specimen geometry, material properties, axial shortening rate and the coefficient of friction. For different materials, each of these optimized parameters is different [7].

2.1.1.2. Linear Friction Welding

Linear friction welding is a rather new process aimed at extending the current applications for rotary friction welding to non-axisymmetric components [17]. However, the two processes differ greatly in terms of heat input and stress field imposed on the interface. For instance, the interfacial energy generation in LFW is more uniform than that in rotary friction welding.

Linear friction welding is a process where frictional heat is produced as one component is moved in a direct reciprocating mode relative to another under normal pressure (**Figure 2.5-a)**). This process is divided into four distinct phases [18-20], which includes the initial phase, the transition phase, the equilibrium phase and the deceleration (or forging) phase (**Figure 2.5-b)**). The detailed changes of process variables during LFW are illustrated in **Figure 2.5-c)**. Following the first two very short phases, there is phase III when axial shortening of the workpieces starts as a result of plasticity and material is being ejected from the weld interface. When the desired upset has reached a preset limit the two objects are brought to rest very rapidly (less than 0.1 s) and forging pressure may remain to preserve the bond. The last phase is considered important in the FRW industry to consolidate the weld and may affect RS developed in the joints [18-19].

Currently, the LFW process is an established technology for the manufacture of titanium alloy integrated bladed disks (blisks) for aero-engines [21]. However, due to the significant cost saving that can be achieved when fabricating components [22], LFW is finding increasing interest from other industrial sectors, particularly for the joining of the aluminum alloy. Despite this interest, the process has experienced limited additional industrial implementation [23], which is partly due to a lack of fundamental scientific understanding of LFW [24].

Furthermore, the LFW process is under development for assembling nickel-based super-alloys [25]. However, the interest in the process is growing, especially for applications where other alloys or non-metallic materials are used. In recent years the LFW process has gained importance because it reduces the material waste of the processing. Consider, an example, to the realization of a piece "L" of a material not weldable. The only way to achieve it would be to extract it from a full piece, but, of course, the amount of unused material would be considerably greater than the one used. However, as is well-known, especially in aviation is the rule Buy to Fly Ratio [26]. This is the reason why this process always has more industrial applications in the recent years [27].

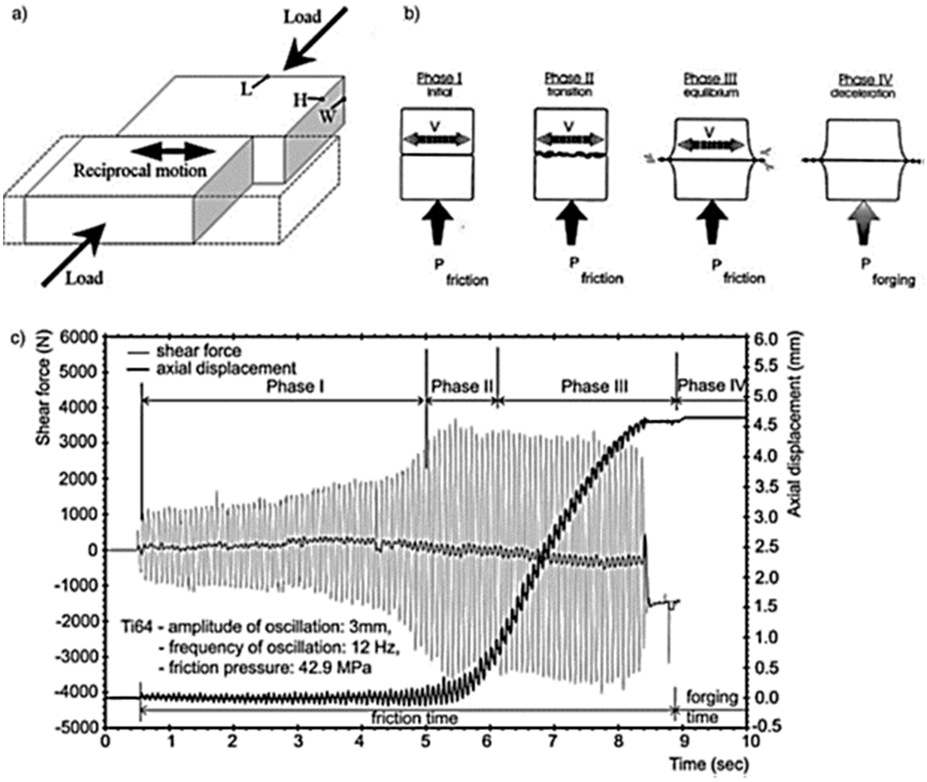

Figure 2.5 a) Schematic of the LFW process, b) its process phases and c) process variables during LFW [10,19,20].

2.1.1.3. Orbital Friction Welding

Orbital friction welding is another method of friction welding, which is particularly suited for the joining of non-circular cross-section components. In this application, neither workpiece rotates about its central axis. The orbital motion provides uniform tangential velocity over the total interface area. When motion ceases, the parts are realigned quickly. Practically it has been recognized that the high-quality welds are produced using this process which is attributed to the constancy of the relative velocity at the rubbing interface [28]. OFW Can be used to join complex geometries. In contrast to the LFW, where the relative speed between the two reversal points Steadily from zero to maximum and again to zero, is with the OFW the Energy input is independent of location and time. The heat is thus developed continuously. Because of the continuous movement, simpler Machine concepts to the LFW since a deceleration of the Moving masses only at the time of compression. The significant of using OFW moved up to minimize the thermal effects, the required energy, and the residual welding stress [29].

Although the process has important advantages, such as a uniform rate of heat generation at the rubbing interface, which produces a uniform thickness of the HAZ, and the cross-section of the components can be of any shape, very limited research works have been published [28-32]. Some introductory works are available [33-38].

The distribution of heat generated across the interface of two rods of circular cross-section and a pair of rods of square cross-section was derived mathematically [28]. It was mathematically shown that the rate of heat generation is uniform over the central part of the rubbing surface and this uniformity provides a good reason why the OFW process produces high quality welds. It was also indicated that the area over which the heat is produced increases with the reduction in offset (amplitude). Furthermore, it was concluded that, in practice, to achieve a good weld quality within a reasonable time on an available OFW machine, the value of offset should be optimized [28].

In orbital friction welding, the energy comes from the relative movement of the joining elements using a circular oscillatory motion of only one part or both joining parts. In multi-orbital friction welding (MOFW) both oscillating heads are rotated in the same direction with a phase offset of 180°. Whereas in the case of single orbital friction welding (OFW), a workpiece describes a circular movement with the resonant circuit diameter DS and the oscillation frequency f, while the other workpiece remains stationary. Due to the reduced resonant circuit and the frequency halved by the omission of a vibrating head, the lowest heat input is achieved by the single orbital friction welding (OFW). For that reason, orbital and multi-orbital friction welding do not have to be restricted to weld components that are rotationally symmetric [29].

The orbital friction welding was originally used to produce plastic window frames. The new process enabled the four profiles of a window frame into a precisely clocked relative movement and so that the corners are simultaneously welded [30]. The suitability of the orbital- friction welding for the joining of metallic materials was carried out at SLV Munich a prototype of a multi-orbital friction welding machine from M-O-SYS investigated. In 2009, the orbital friction welding was used by Rolls-Royce Germany as a joining process to produce blisks for gas turbines [31]. Some investigations have been conducted on orbital friction welding of dissimilar material joints on non-rotationally symmetrical joining cross-sections at SLV Munich [32]. Trommer et al. have conducted Principle tests on the orbital friction welding of the structural steel S355J2 [29].

Maalekian has optimized the OFW parameters for joining of non-circular and large cross-section workpieces of high carbon steel [39]. Using many experimental data and neural network analysis the influence of friction welding parameters on flash formation was investigated. The neural network method is empirical and, hence, requires experimental data to discover the relationships. The obtained experimental data were used to describe the integrity of the weld in terms of weld collar (flash formation). Inputs to the network were the friction welding parameters, namely amplitude, friction force, friction time and rotation speed. The prediction of the influence of welding parameters on the quality of the weld in terms of the size of flash was studied. For instance, the significance of each of the input variables, as perceived by the neural network in influencing the weld integrity concerning the size of the weld collar, is illustrated in **Figure 2.6**. The magnitude of the significance is a measure of the extent to which a particular input explains the variation in the weld shape. As shown in **Figure 2.6** the rotation speed emerges prominently, which is substantiated by the result of Duffin and Bharani [40] for rotary friction welding and Wanjara and Jahazi [41] for LFW. **Figure 2.6** also depicts that the amplitude and the friction time have a large influence on the process. Maalekian et al. have carried out experimental and numerical studies on OFW as well as inverse modelling and simulation of heat generation in friction welding [42-50].

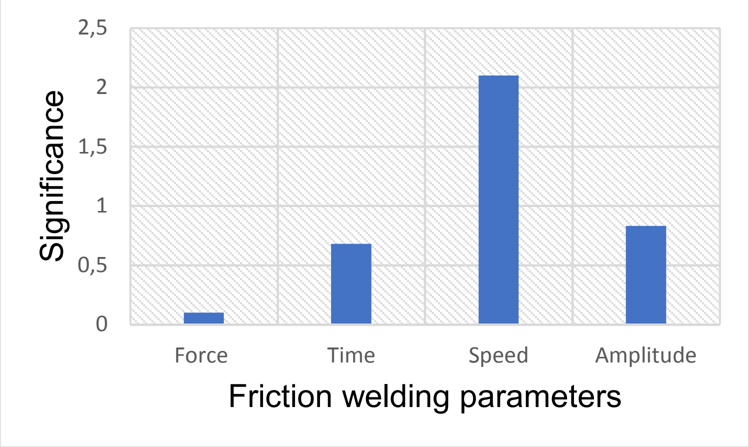

Figure 2.6 Bar chart showing measure of model perceived significance of each of input variables of OFW of high carbon steel bars in influencing weld integrity [39].

Recently, U. Raab et al. have carried out some investigations on orbital friction welding as an alternative process for blisk manufacturing [51-54]. In these studies, the characterization of the Orbital Friction Welding Compounds Ti-6Al-4V / Ti-6Al-4V And Ti-6Al-4V / Ti-6Al-2Sn-4Zr-6Mo has been investigated. Furthermore, a Comparison of heat development during orbital and linear friction welding has been carried out. it was concluded that with similar welding parameters, shorter welding times are achieved with OFW. The reason for the faster heat generation is a continuous relative speed, higher contact pressure and a larger distance covered within one cycle of the process [51].

2.1.2. Thermal energy comparison in LFW and OFW

Rotary friction welding has the constitutional limitation that it cannot be used for non-circular cross-section parts. Another main drawback is that the rate of heat generation is not uniform over the interface (**Figure 2.7**). This gives rise to a non-uniform thickness of the heat affected zone (HAZ), which cannot be the minimum or the optimum thickness at all points across the interface. These disadvantages can be avoided by using LFW or OFW. The two methods can weld noncircular components, and the interfacial energy is generated almost uniformly. **Figure 2.7** represents that the friction heat generation at the interface for orbital compared to the linear method is even more uniform which is attributed to the uniform unidirectional relative velocity between the two elements over the total interface area. The uniform interfacial energy generation present in linear and, particularly, in OFW may account for the higher integrity welds associated with the process. However, in the orbital movement, different components of the contact surfaces undergo different time periods in which they are in contact. Therefore, the center encounters contact at all the time, whereas the edges go through times with no contact during the process. That will result in a non-uniform heat generation. This nonuniformity is sizeable for the large amplitudes. Since usually small amplitudes are used in OFW, consequently, the heat generation can be taken as uniform [7].

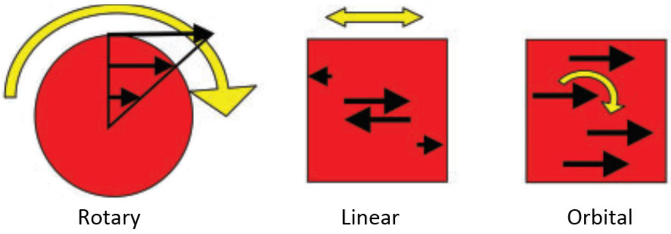

Figure 2.7 Comparison of heat generation over interface for three types of friction welding is shown with black arrows [7].

According to the analysis by Maalekian [7], with the same process parameters for both LFW and OFW, the frictional heat generated in LFW is 63% of that for OFW. Therefore, to produce the same amount of heat flow into the rubbing surfaces, in LFW 58% higher value of process parameters (e.g. speed and/or amplitude) is needed compared to the OFW. Raab et al. [51] have proved experimentally that the improved heat generation affects the resulting dimensions of the welding zone. **Figure 2.8** shows a comparison of central weld zone obtained after LFW and OFW with similar welding parameters. The micrographs show a wider central weld zone obtained after OFW.

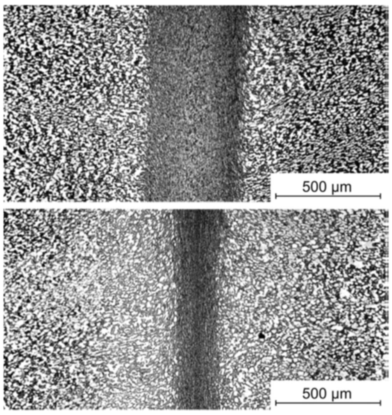

Figure 2.8 Central weld zones of an OFW (up) and a LFW (down) weld [51].

2.1.3. FRW Parameters

2.1.3.1. Rotational Speed

According to Vill [12], the rotational speed is the least sensitive process parameter, and it may vary over a rather wide range without influencing the weld joint quality. However, there are certain optimum speeds for each material combination and application. The main function of rotation is to produce a relative velocity at the friction surfaces. From the standpoint of process intensification and quality improvement of the welded connection (especially metals sensitive to overheating), it is desirable to use relatively low rotational speeds since process efficiency is improved as a result of reduced heat losses, which reduce the amount of energy used for welding. According to Pinheiro et al. [15], at high rotational speeds, deep tearing is replaced by a polishing action. As a result, to achieve the conditions for plastic deformation at the friction surfaces, longer heating times are required allowing thermal energy propagation along workpieces axial direction, and as a consequence a greater volume of material is heated. Therefore, high rotational speeds lead to lower cooling rates, wider heat affected zone (HAZ) and hence lower hardness at the bonding line vicinity. On the other hand, low rotational speeds produce a thinner HAZ with a profile that is much more pinched in comparison with welds produced at higher rotational speeds. Therefore, low rotational speeds lead to higher cooling rates and higher heating times resulting in higher hardness. Generally, an increase in the rotational speed reduces the ultimate tensile strength significantly [15,55,56]. However, Nessler et al. [57] studying parameters influence in two titanium alloys (Ti6Al4V and Ti6Al2Sn4Zr2Mo) showed that neither ultimate tensile strength nor yield strength were affected by any of the parameters analyzed (normal pressure, rotational speed, concentricity, squareness and surface finish). Zhou et al. [58] analyzing aluminum MMCs and AISI304 friction joints showed that when the rotational speed is increased, the tensile strength initially increased and then leveled out.

2.1.3.2. Friction and Forging Pressure

The pressure may vary in wide range and controls the weld zone temperature gradient, the required drive power, and the axial shortening. The specific pressure depends upon metals being joined as well as joint geometry and can be used to compensate for heat loss to a large mass. The heating pressure must be high enough to hold the friction surfaces in intimate contact to avoid oxidation. For a set rotational speed, low pressure limits heating with little or no axial shortening. High pressure causes local heating to high temperature and rapid axial shortening (high burn-off rate). After the heating stage, two different methods of varying axial pressure are usually utilized: keep pressure constant or increase it. The ultimate and the notch tensile strength increases when pressure is increased [15,55,56,58,59]. Such behavior is explained in terms of frictional energy per unit volume. Since this value is maximized when a high frictional pressure is used producing joints with high notch tensile strength [59]; which is confirmed by Shinoda et al. [60] reporting high notch tensile strength when a high energy input (in terms of pressure) was applied. It is recommended that the forging pressure should be at least twice the frictional pressure for production of joints free of unbonded regions [61]. Additionally, increasing the pressure causes an increase in the upset rate, and consequently, the heat input amount is low resulting in higher cooling rates and hardness. For a given burn off, the time from the initial contact of the surfaces to the end of the welding procedure decreases as the normal force increases. The higher the pressure, the faster the material is consumed and the shorter the welding time will be [62].

The axial pressure also influences the HAZ width and shape changing from an almost parallel sided boundary at low pressures to a more "pinched" or double-cone profile at the stud center at high pressures [11]. In the latter, the heat liberated is used to plastify the material and hence does not propagate in the axial direction. According to Ellis [55], the welds made at higher forces show a narrower region where the hardness values are lower than in the parent material. It means that the higher the force is, the more pinched the hardness profile will be in the interface region [62]. **Figure 2.9** presents the effect of the axial pressure and the rotational speed over the HAZ width and shape [16].

2.1.3.3. Heating Time

According to Lebedev and Chernenko [63], the friction welding process may be regulated either by the heating time or the upsetting during heating. Regulation in time is recommended in those cases where the workpiece linear dimensions have large tolerances and joining surfaces are not machined or are machined roughly or inaccurately. Regulation by upsetting value is used in those cases where parts dimensions have to satisfy strict requirements. However, Vill [12] suggested that it would be better to select the heating period duration rather than the upset as the third basic parameter because for a given power of the process (the speed and pressure are given) the duration fully determines the energy to be utilized for welding. The heating time determines the temperature conditions of the process and the plastic deformation of the specimen is derived from the temperature conditions [62]. The heating time is defined as the period from the initial contact of the friction surfaces to the end of the braking phase. It is significantly influenced by the axial pressure and rotational speed as well as the material properties and joint diameter [63].

2.1.3.4. Burn-Off

The burn-off describes the amount of plasticized material and is usually measured as the axial shortening of the rotating workpiece. It can also be expressed regarding the burn-off rate (amount of burn-off per second) and can be considered as a representation of the welding speed. It also has a significant influence on the weldment properties and not only controls the welding cycle. The applied force and rotational speed will affect the time needed to reach the preset amount of burn-off. The time from surfaces initial contact to the end of the burn-off becomes shorter as the force increases and a lower speed results in a higher burn-off rate for the same nominal pressure [55]. According to Vill [12], controlling the process by the burn-off has its disadvantages since it can occur large burrs (central projections remaining on specimen surface) as well as surface defects affecting the weld quality negatively.

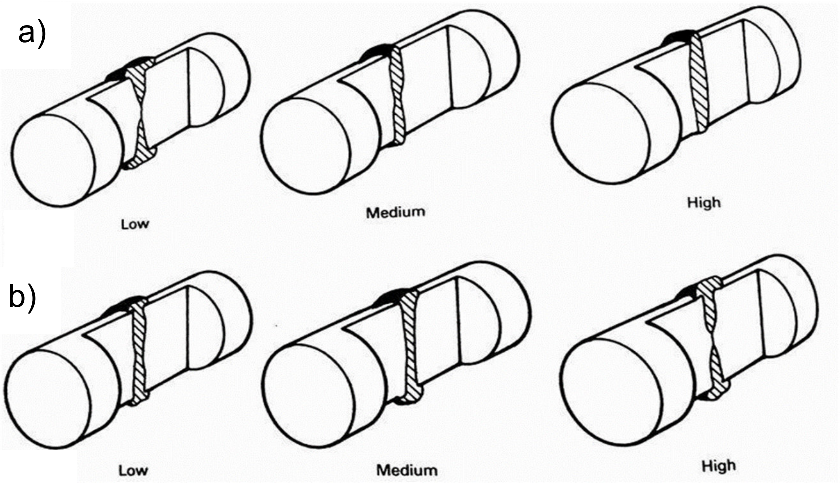

Figure 2.9 Schematic representation showing the effect of the welding parameters on the HAZ shape and width a) Rotational speed and b) axial pressure [16].

2.1.4. FRW Mechanism and HAZ Structure

Considering measured interface temperatures and extrapolated temperatures, combined with metallographic studies, it has been concluded that diffusion is a primary mechanism in friction welding. This is aided by the cleaning action by the relative movement and applied normal pressure, in addition to the probable driving force provided by the forge pressure. The existence of a diffusion layer in friction welding has been demonstrated by some researchers, especially for dissimilar metal joints. Although mutual solubility between the parts to be welded is not a factor when joining similar materials, it has been stated [7] that the ease of making a sound weld is increased as the mutual solubility of dissimilar materials is increased. Therefore, such bonds have been attributed to high temperature solid-state diffusion.

In dissimilar metal joints, diffusion can either improve or deteriorate the weld properties. For instance, when welding a high carbon steel to a medium plain carbon steel, decarburization at the weld interface may increase the ductility of the joint. On the other hand, formation of intermetallic phases when for example joining steel and aluminum, copper and titanium, etc., may cause the joint to become brittle. It has also been proposed that mechanical mixing of a thin layer of material on each side of the interface creates the joints. Metallographic images of weld and HAZ areas for different materials have been studied extensively.

During friction welding, the metal within the HAZ experiences a temperature change and a gradient of strain and strain rate and undergoes a number of microstructural changes. Generally, the HAZ can be divided into different zones as shown in **Figure 2.10** [7].

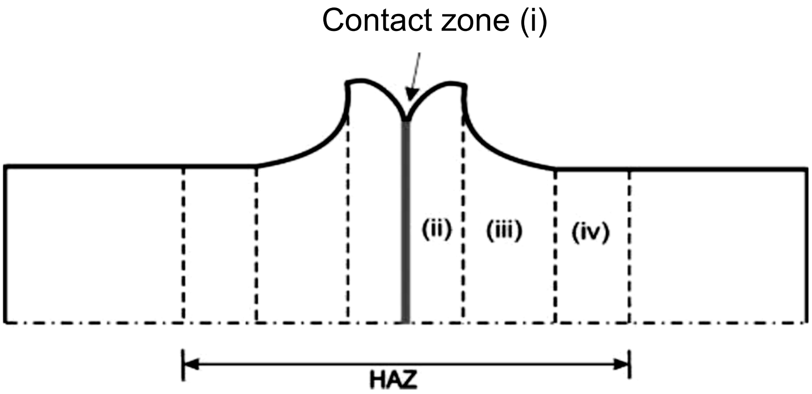

Figure 2.10 Schematic illustration of the different regions in the HAZ of friction welded specimens; i) contact zone; (ii) fully plasticised zone; (iii) partly deformed zone; (iv) undeformed zone [7]

(i) Contact zone (severe plastic deformation zone). This is the zone were rubbing occurs and fragments of metal transfer from one rubbing surface to the other. The strain rate is controlled by the rotational velocity. The material in this zone is subjected to severe plastic deformation. This zone has a very fine grain structure due to severe straining and full recrystallisation.

(ii) Fully plasticised zone (dynamic recrystallisation zone). The material is subjected to a considerable amount of plastic deformation, but it does not participate in the rubbing and material transfer process. Within this region, the dislocation density is increased extremely and, due to the sufficiently high temperature, the material undergoes dynamic recrystallisation. The grains in this zone are fine and equiaxed

(iii) Partly deformed zone. The strain rate, temperature and amount of plastic deformation are lower than those appeared in zone (ii). The microstructure becomes coarser because of the associated reduction in strain and strain rate.

(iv) Undeformed zone. In this region, depending on the maximum temperature, the material doesn’t undergo phase transformation, but plastic deformation does not occur. Grain growth may take place in this zone.

It is well established that when pressure is used to join materials by plastic deformation to produce welds without fusion, there is a localized effect on the microstructure. Such effect depends on the temperature at which the pressure is applied and under which plastic deformation is caused to take place. If the temperature at which the pressure is applied, or to which the material raises because of work converted to heat, exceeds 0.4 T_m for sufficient time, the material in the interface vicinity will undergo plastic deformation and immediate recrystallisation which means that recrystallisation and plastic deformation happen at the same time. Such process is called dynamic recrystallisation and is caused by the movement of the dislocations which pile up or entangle and multiply by generation, therefore increasing the crystal lattice strain energy (which is the driving force for recrystallisation). The recrystallisation process occurs almost at once in a rather rapid sequence [64]. **Figure 2.11** exemplifies the dynamic recrystallisation process.

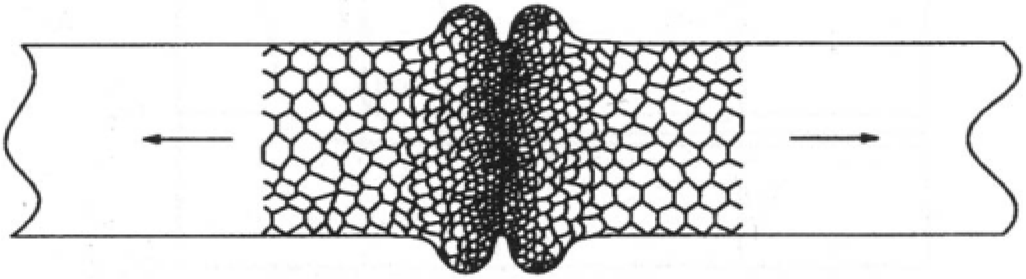

Figure 2.11 Dynamic recrystallisation process with grain refinement in the center region [64].

2.2. RFW of AISI 316L to AISI 1012

2.2.1. Welding of dissimilar materials

Design engineers are frequently faced with the necessity to join dissimilar materials as they are attempting to create new structures or elements with tailor-engineered properties. Sometimes a component needs high-temperature resistance in one zone, good corrosion resistance in another. Structures may require wear resistance or toughness in a zone combined with high strength in another area. Enhancing the ability to join dissimilar materials with engineered properties are facilitating new approaches to light-weighting automotive structures, promoting methods for energy production, creating subsequent generation medical products and consumer devices, and many other constructions and industrial uses. Joining dissimilar materials is usually more complicated than joining the same material or alloys with minor variations in composition; however, many dissimilar materials can be welded successfully with the appropriate joining process and specialized procedures [67].

While many similar-metal FRW joints are produced because of economic considerations, many dissimilar-metal FRW joints are produced because there are no alternative welding methods that can be used. Examples of these types of joints include dissimilar-metal combinations with widely different melting points and dissimilar-metal combinations that form incompatible phases when fusion welded [16].

Problems Common to Welding of Dissimilar Materials. In general, the same problems encountered when welding similar materials must be addressed when welding dissimilar materials. However, some problems are associated only with the welding of dissimilar materials or are greatly magnified during the welding of dissimilar materials. These factors include joint interfaces, low-melting phases, brittle phases, and different thermal expansions [68].

2.2.2. Metal Characteristics

2.2.2.1. Carbon Steel

The American Iron and Steel Institute (AISI) defines carbon steel as follows:

Steel is considered to be carbon steel when no minimum content is specified or required for chromium, cobalt, columbium [niobium], molybdenum, nickel, titanium, tungsten, vanadium or zirconium, or any other element to be added to obtain a desired alloying effect; when the specified minimum for copper does not exceed 0.40 per cent; or when the maximum content specified for any of the following elements does not exceed the percentages noted: manganese 1.65, silicon 0.60, copper 0.60 [69].

Carbon steel can be classified, according to various deoxidation practices, as rimmed, capped, semi-killed, or killed steel. Deoxidation practice and the steelmaking process will have an effect on the properties of the steel. However, variations in carbon have the greatest effect on mechanical properties, with increasing carbon content leading to increased hardness and strength. As such, carbon steels are generally categorized according to their carbon content. Generally speaking, carbon steels contain up to 2% total alloying elements and can be subdivided into low-carbon steels, medium-carbon steels, high-carbon steels, and ultrahigh-carbon steels; each of these designations is discussed below [69].

2.2.2.2. Austenitic Stainless Steel

Austenitic stainless steels (ASSs) were invented in Essen, Germany, in the beginning of the 20th century and represent today more than 2/3 of the total stainless steel world production. Their continuing development has resulted in complex steel compositions with substantial amounts of alloying elements. These alloying elements are of course introduced in the steel for one or more reasons but the final aim is mainly to obtain better mechanical properties (especially high creep strength and high creep-rupture ductility) and/or higher corrosion resistance (especially oxidation resistance in the case of high temperature application) [70,71].

Austenitic stainless steels have better ductility and toughness than carbon and low alloy steels because of the face-centered cubic crystal structure, their notch toughness at cryogenic temperatures is excellent. They are stronger than carbon and low alloy steels at temperatures above 540 °C while maintaining good oxidation resistance. Type 316 stainless steel has the highest stress-rupture capability of the 300 series of alloys. Steels of the austenitic group are characteristically resistant to corrosion and oxidation, primarily because of the chromium. Chromium, when added alone to steel in the range of 16 to 25 percent, forms a solid solution in alpha iron. The addition of one or more strong austenite-forming elements, usually nickel, to the iron-chromium alloy in sufficient proportions suppresses the ferritic structure so that the resulting structure is essentially austenitic. The resultant austenitic alloy is a solid solution of chromium, nickel, and carbon in gamma iron, which is non- magnetic. The nickel addition also increases the high temperature strength and corrosion resistance of the steel [72].

The austenitic stainless steels contain other useful elements. Manganese and nitrogen augment the austenite stabilizing action of the nickel. Molybdenum, columbium, and titanium promote the formation of delta ferrite in the austenitic matrix and form carbides in a manner like that of chromium, the ratio of austenite- and ferrite-forming elements is adjusted to provide suitable properties for the various applications of these steels [73].

The solidification behavior and microstructural development of the weld metal of these alloys are quite complex, and, until recently, were not well understood. In this class of alloys, weldability and subsequent weld performance is often directly related to weld microstructure. Thus, when welding these alloys, a general understanding of the welding metallurgy can be very beneficial in optimizing weld performance. Because chemical composition has the greatest influence on weld microstructure, a number of empirical relationships and constitution diagrams have been developed to predict microstructure based on actual or approximated composition. In all cases, the concept of chromium equivalence (Cr$_{eq}$) and nickel equivalence (Ni$_{eq}$) has been used to normalize the effect of various alloying additions on the ferrite-forming and austenite-forming potency, respectively. Considerable disagreement still exists regarding these equivalency relationships (**Table 2-1**) for austenitic stainless steels [74].

Table 2-1 Chromium- and nickel-equivalency relationships for austenitic stainless steels [74].

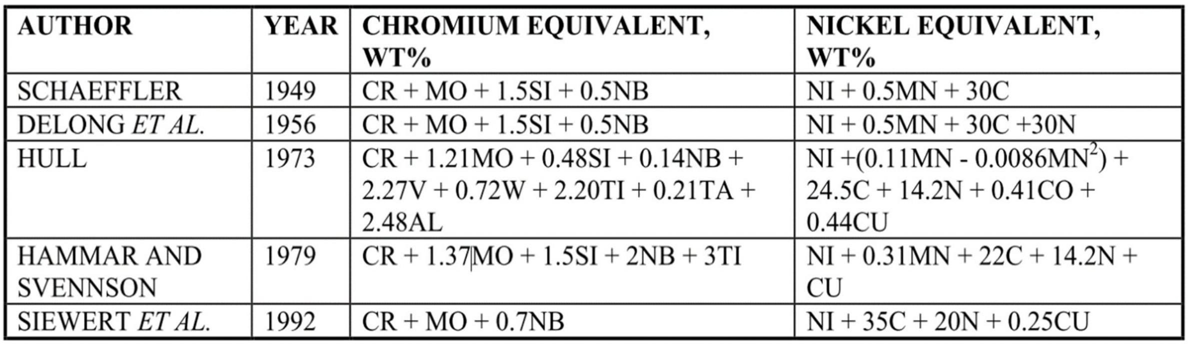

AUTHOR	YEAR	CHROMIUM EQUIVALENT, WT%	NICKEL EQUIVALENT, WT%
SCHAEFFLER	1949	CR + MO + 1.5SI + 0.5NB	NI + 0.5MN + 30C
DELONG *ET AL.*	1956	CR + MO + 1.5SI + 0.5NB	NI + 0.5MN + 30C +30N
HULL	1973	CR + 1.21MO + 0.48SI + 0.14NB + 2.27V + 0.72W + 2.20TI + 0.21TA + 2.48AL	NI +(0.11MN - 0.0086MN^{2}) + 24.5C + 14.2N + 0.41CO + 0.44CU
HAMMAR AND SVENNSON	1979	CR + 1.37MO + 1.5SI + 2NB + 3TI	NI + 0.31MN + 22C + 14.2N + CU
SIEWERT *ET AL.*	1992	CR + MO + 0.7NB	NI + 35C + 20N + 0.25CU

The Schaeffier diagram **Figure 2.12** was developed in the late 1940s in an attempt to predict weld microstructure for a wide range of stainless steels. It has become known as the "roadmap" of stainless steels. The compositional ranges of the ferritic, martensitic, austenitic, and duplex alloys have been superimposed on this diagram [75]. It was refined as the DeLong diagram [76], which pertained to the range of compositions associated with 300-serie stainless steels and filler metals. In 1988, the Welding Research Council introduced a further improvement, when compared with the DeLong diagram, which was called the WRC-1988 diagram [77]. This diagram was further modified in 1992 by adding copper to the Ni$_{eq}$ formula. The WRC-1992 diagram (**Figure 2.13**) allows the amount of weld-metal ferrite to be predicted using newly developed C $_{eq}$ and Ni$_{eq}$ formulas. Weld-metal ferrite content significantly influences both the weldability and service performance of austenitic stainless steels. Weld-metal ferrite content can also be measured using instruments that take advantage of the ferromagnetic characteristics of the ferrite phase.

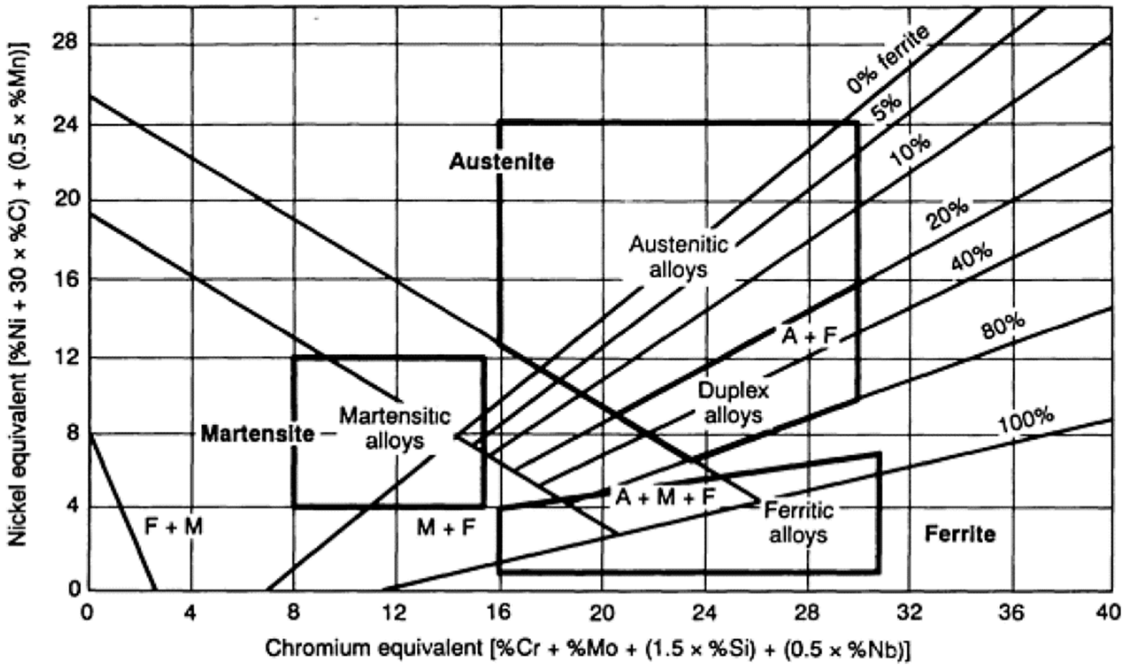

Figure 2.12 The Schaeffler diagram for estimating the microstructure of stainless steel weld metal [75].

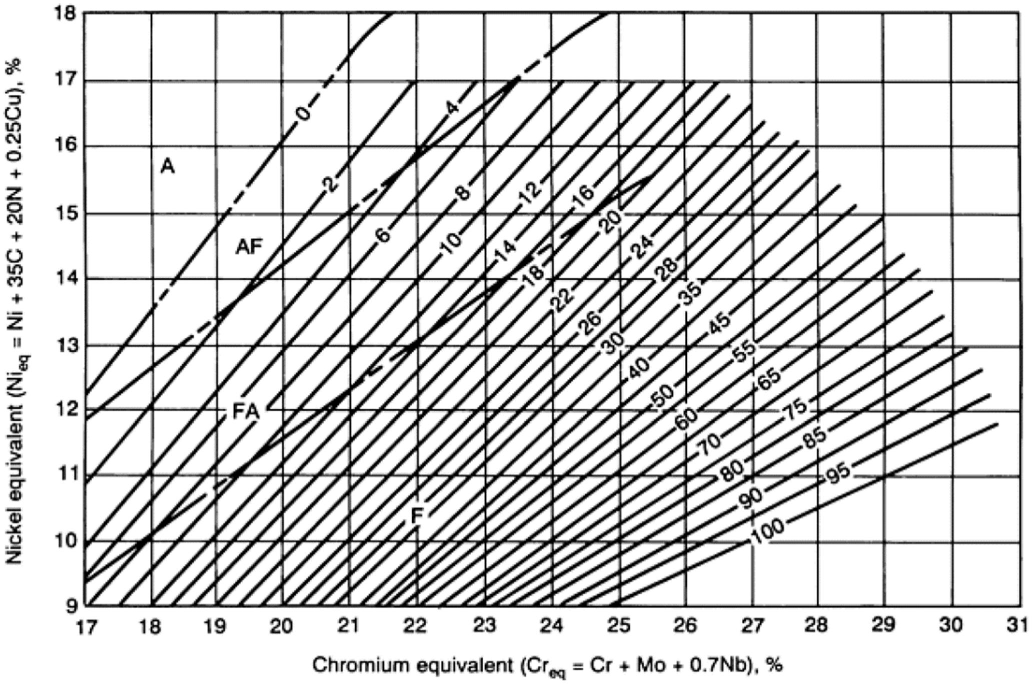

Figure 2.13 WRC-1992 diagram for predicting weld ferrite content and solidification mode [77].

2.2.2.2.1.Stress relieving Heat Treatments

Post-weld heat treatment (PWHT) is often required to relieve RS in austenitic stainless steel weldments. particularly in thick sections. Because the coefficient of thermal expansion (CTE) value and the elevated-temperature yield and creep strengths of austenitic materials are significantly greater than for ferritic materials, the magnitude of RS is generally larger. Although the effect of RS from welding is typically not as severe as when less ductile materials are used, they may still affect mechanical properties and corrosion behavior. PWHT is particularly critical when machining must be performed after welding, because significant distortion may occur [74].

Non-stabilized stainless steels cannot be stress relieved in the sensitizing range without sacrificing corrosion resistance. Extra-low-carbon grades are affected much less, because sensitization is more sluggish. Stabilized grades exhibit minimal chromium carbide precipitation tendencies. Higher stress-relief temperatures can be used for fully austenitic weld metals. For weld metals that contain ferrite, stress-relief temperatures above 650 °C may result in weld embrittlement via σ formation. For austenitic stainless steels, the estimated percentages of RS relieved at various temperatures at the times previously noted are 85% stress relief at 845 to 900 °C and 35% stress relief at 540 to 650 °C. The data compiled by Cole and Jones [78]

The vast majority of austenitic stainless steels present delta ferrite in their microstructure just following its solidification. Apart from Fe, Cr and Ni they contain other chemical elements that are classified as ferrite formers (Cr, Mo, Si) or austenite formers (Ni, N, C, Mn, Cu). The efficiency of these elements as ferrite and austenite stabilizers can be compared to the ones of Cr and Ni (equivalency). Ferrite has a negative influence on hot ductility [79] because ferrite and austenite present different softening mechanisms at high deformation temperatures; while ferrite recovers austenite recrystallizes leading to interface fracture. In most of the cases delta ferrite may be eliminated by long period homogenizing heat treatments [80] in the 1050 °C to 1250 °C temperature range. However, due to economic reasons this is not performed in the steel mills, at least in a complete manner.

2.2.3. Applications and Advantages

Dissimilar metals welding (DMW) of stainless steels to carbon or low alloy steels has a wide application in industry. It is often used in chemical and petrochemical industry (reactors, tubes and pipelines), and in power generation, including nuclear plants (nuclear steam generator channel heads, pressurized water reactors, tube sheets and reheat piping). In nuclear water reactor, dissimilar metal welds are employed to connect the carbon steel reactor pressure and stainless steel pipe systems.

Such joints may involve the combination of low carbon steel-CS (white ferrite) and stainless steel-SS (black austenite) known as black and white joints (BWJ) [81]. The welded BWJ are emerging nowadays due to costs saving and satisfactory service performance. Since dissimilar materials can be joined, a significant cost savings is possible by designing bimetallic parts that use expensive materials only where needed. Engine valve heads made from a nickel-chrome alloy for heat resistance can be welded to an alloy steel stem for wear resistance. A carbon steel shaft welded to a stainless steel stub provides corrosion resistance in pump motors. **Figure 2.14** shows some of application of black and white joints.

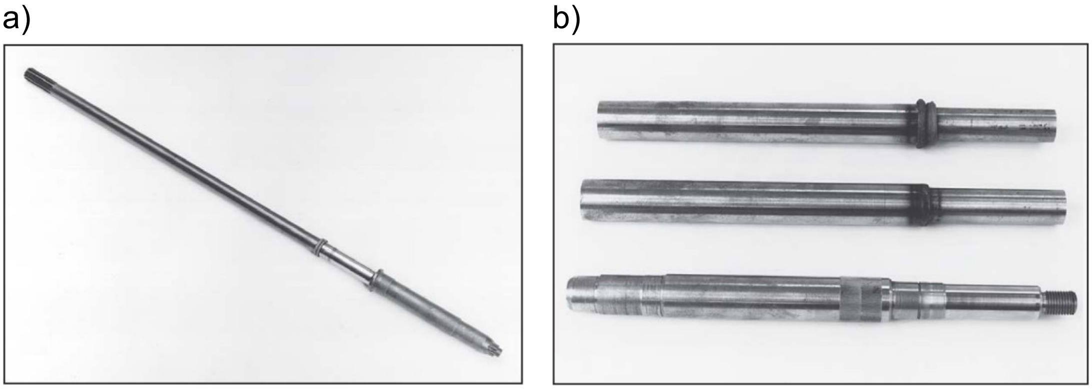

Figure 2.14 a) Carbon steel/stainless steel marine outboard engine drive shaft and b) Bimetallic pump motor shaft.

2.2.4. Precipitations of Carbide

Under certain conditions, austenitic stainless steel welds are subject to intergranular corrosion. When the unstabilized steels are heated or slowly cooled within the temperature range of 400 °C to 850 °C, known as the sensitizing temperature range, carbon is precipitated from solid solution mainly at the grain boundaries where it combines with chromium from the adjacent metal to form chromium-rich carbide ($M_{23}C_6$). The adjacent metal, impoverished in uncombined chromium, exhibits reduced corrosion resistance. Under certain corrosive conditions, localized intergranular attack takes place. The severity of corrosion depends on the time and temperature of exposure, as well as the composition and prior heat treatment of the steel [73].

Figure 2.15 shows that the local chromium depletion is such that the chromium level can become low enough that it has not even enough to be stainless and certainly much lower corrosion resistance than the surrounding area. This zone, because it is lower in chromium, also has very unstable austenite and is quite prone to martensite formation [83].

An example of intergranular corrosion in the HAZ of a weld in type 316L NaOH reactor vessel is shown in **Figure 2.16**. For a given thermal history, the level of precipitation and the associated degree of sensitization are approximately proportional to the carbon content of the austenitic stainless steel. Conventional austenitic stainless steels can retain a maximum of about 0.02 wt% C in solid solution over their service temperature range (up to 600 °C). Thus, as carbon content increases above this level, the driving force for carbide precipitation increases [84].

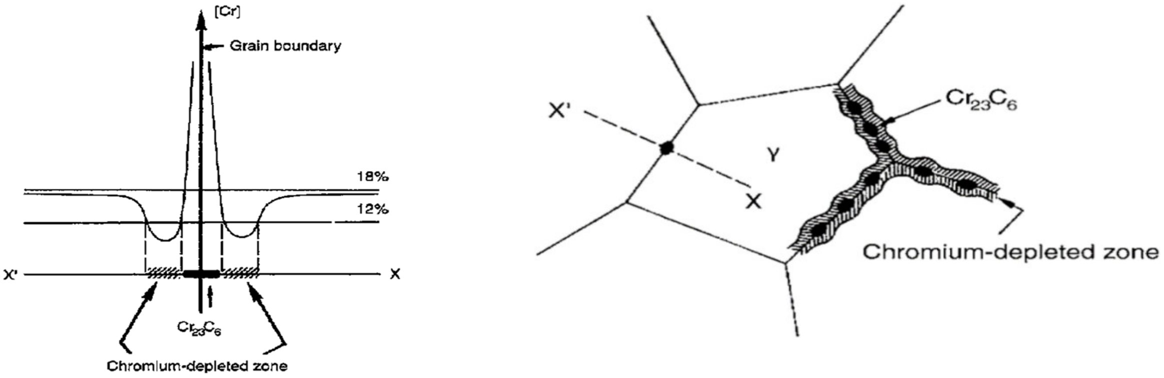

Figure 2.15 Depletion of chromium from the austenite near grain boundaries due to chromium carbide precipitation [83].

This can be illustrated by the time-temperature-transformation/precipitation diagrams (TTT/TTP) curves shown in **Figure 2.17** for an AISI 316 alloy. Because of this, low-carbon grades of stainless steel (the so-called L-grades) are preferred for corrosive service where weldments must be used in the as-welded condition. The most critical temperature range is around 600 to 700 °C, at which 0.08% carbon steels will precipitate carbides in about 2 minutes, whereas 0.02% carbon steels are effectively immune from this problem [74].

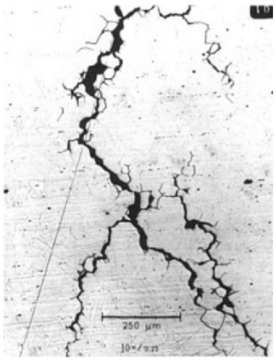

Figure 2.16 Caustic SCC in the HAZ of a type 316L stainless steel NAOH reactor vessel. cracks are branching and intergranular [84].

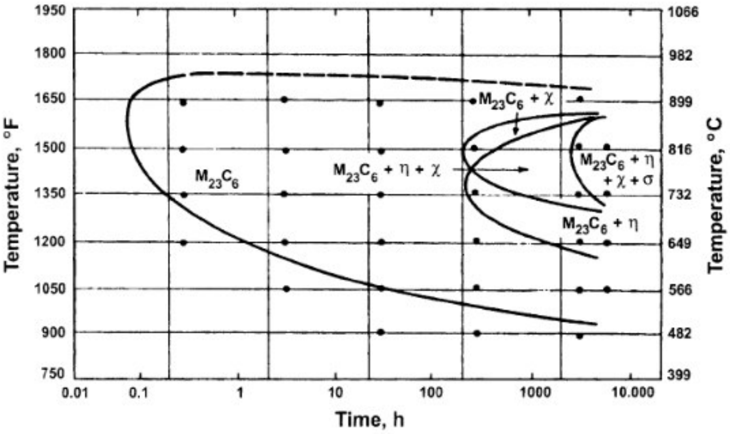

Figure 2.17 TTT diagram of Type AISI 316 austenitic stainless steel, solution annealed for 1.5 h at 1260 °C and water quenched prior to aging. [86].

It is possible to reclaim steel which suffers from carbide precipitation by heating it above 1000 °C, followed by water quenching to retain the carbon and chromium in solution and so prevent the formation of carbides. Most structures which are welded or heated cannot be given this heat treatment and therefore special grades of steel have been designed to avoid this problem. These are the stabilised grades 321 (stabilised with titanium) and 347 (stabilised with niobium). Titanium and niobium each have much higher affinities for carbon than chromium and therefore titanium carbides, niobium carbides and tantalum carbides form instead of chromium carbides, leaving the chromium in solution and ensuring full corrosion resistance. Another method used to overcome intergranular corrosion is to use the extra low carbon grades such as Grades 316L and 304L; these have extremely low carbon levels (generally less than 0.03%) and are therefore considerably more resistant to the precipitation of carbide [85].

2.3. RFW of Commercially Pure Titanium (CP-Ti)

2.3.1. Commercial Pure Titanium

Titanium (Ti) is a low-density metallic element that is plentiful in the earth crust in mineral sands containing ilmenite ($FeTiO_3$) or rutile (TiO_2). Ti could be extracted commercially by reducing titanium tetrachloride ($TiCl_4$) by combining it with the reducing agent magnesium; this process is called the Kroll process as explained with other processes in [87].

$2FeTiO_3 + 7Cl_2 + 6C\ (900\ °C) \rightarrow 2TiCl_4 + 2FeCl_3 + 6CO$

$TiCl_4 + 2Mg\ (1100\ °C) \rightarrow 2MgCl_2 + Ti$

Pure metallic titanium stabilizes to the hexagonal close-pack (HCP) crystal structure, or α-phase, as shown in **Figure 2.18-a)** and exhibits an allotropic transformation at 882 °C to a body-centered cubic (BCC) structure, or β-phase as shown in **Figure 2.18-b)**. The transformation temperature is known as β transus temperature ($T\beta$) and is defined as the lowest equilibrium temperature at which the material is 100% β. However, this temperature is only valid for laboratory-pure titanium; the inevitable presence of oxygen in commercially pure titanium and other alloying elements in different titanium alloys raise this transition temperature [88]. The transformation temperature can be manipulated up or down with varying alloy additions categorized broadly into α and β stabilizers. α stabilizers either increase or have no impact on the β-transus temperature, while β stabilizers decrease the β-transus temperature [89].

Commercially pure (alpha) titanium can be divided into four Grades 1,2,3,4. The mechanical properties of CP titanium are principally controlled by the oxygen and iron content of the grade and are given in **Table 2-2**. Grade 2 is the most widely used specification in all product forms. Grade 1 is specified when superior formability is required. Grades 3 and 4 are used where higher levels of strength are necessary. Commercially pure grades are available with yield strengths ranging from 170 to 480

MPa, with the higher strength grades containing more oxygen. The C grades have good formability, are readily weldable, and have excellent corrosion resistance. The CP grades are supplied in the mill annealed condition which permits extensive forming at room temperature, while severe forming operations can be conducted at 150-450 °C. However, property degradation can be experienced after severe forming if the material is not stress relieved [90,91].

In the present study, I have used commercially pure titanium grade 2 which is the "workhorse" in several industries because it combines excellent formability and moderate strength with superior corrosion resistance. It is used for seawater piping, reactor vessels, heat exchangers, petrochemical, oil and gas markets [90]. Daisuke Terada et al. [92] have investigated the change in microstructure and mechanical properties during annealing of a CP-Ti grade 2 severely deformed by the accumulative roll-bonding (ARB) process. Joining of CP-Ti has become more and more important due to the increased applications.

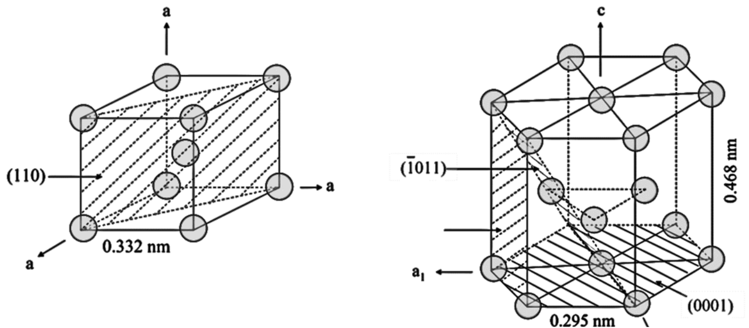

a) bcc

b) hcp

Figure 2.18 Crystal structure of a) β-Ti and b) α-Ti [89].

Table 2-2 Chemical and mechanical requirements of CP titanium [90].

CP Ti Grade	Oxygen max (wt%)	Iron max (wt%)	Ultimate Stress min (MPa)	Yield min (MPa)	Elongation min (%)
Grade 1	0.18	0.2	240	170	24
Grade 2	0.25	0.3	345	275	20
Grade 3	0.35	0.3	445	380	18
Grade 4	0.40	0.5	550	480	15

2.3.2. Applications and Advantages

Prior studies have identified that commercially pure (CP) titanium piping systems can withstand the life cycle conditions of Seawater piping systems [93, 94]. As a result, new ship designs employ the use of titanium piping instead of copper-nickel alloys for seawater piping in offshore industries. Grade 2 is the preferred CP grade since it offers the best combination of strength, ductility, and corrosion resistance. The life of a typical copper-nickel piping system has been approximately 6 to 8 years before refurbishment was required. Titanium piping systems are being engineered that should last the entire 40-year life of a ship providing significant savings through elimination of piping system repair and replacements. Although titanium piping systems are more cost effective over the entire service life of a ship, their initial installation costs are higher than copper-nickel systems due to the higher material cost and stringent fabrication procedures [95].

Several derivatives of these processes have been proposed. In the first, a short length of pipe, or pup piece, is rotated between two stationary pipes. This has the possible advantage of avoiding rotating a whole pipe length, but makes two welds instead of one, needing two flash removal operations. It is also difficult to grip the pup piece in such a way as to transmit the required forces, and the process has not been developed to a commercially viable state. Other process variants have been proposed in which a plate is rotated between two stationary pipes. In one case, the pipe material is supposed to drill through the plate, eventually forming a weld. In a further proposition, the circular plate has teeth machined on the outer diameter to enable the plate to be rotated and welded to the two pipe pieces. Neither of these variants has been fully developed or used for titanium [96].

Figure 2.19-a) shows a continuous drive rotary friction weld made in a Ti-6Al-4V-0.5Pd pipe, of 246mm diameter and 14mm wall thickness. No shielding gas was used. It is emphasized that the procedures used to make this weld were not necessarily those which might be considered as optimum. A macro section through the weld is shown in **Figure 2.19-b)** the area of the weld at and close to the bond line is seen to be completely recrystallized, and to consist of fine equiaxed grains showing the typical Widmanstätten transformation products [97].

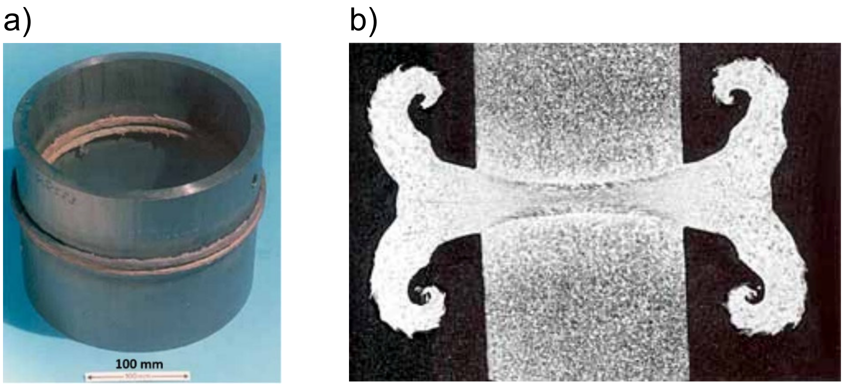

Figure 2.19 a) Rotary friction weld in Ti-6Al 4V-0.5Pd pipe and b) Macro section through rotary friction weld in Ti-6Al-4V-0.5Pd pipe [97].

Nessler et al [98] have described a detailed series of inertia welding tests on rings of Ti-6Al-4V, with additional work on some other alloys. They reported good results, with little dependence of tensile strength on welding parameters, but elongation was slightly reduced at low weld upset values. The rings were 584 mm diameter, 4.75 mm wall thickness. Typical conditions used were reported to be 1500 rev/min rotation speed, with a force of 222 kN, giving an upset of about4mm. The average mechanical properties from many welds was reported. Hutt [99] has referred to preliminary radial friction welds on 100 mm diameter CP titanium pipe, but has not published details of the welds.

2.4. OFW of Ti-6242

2.4.1. Titanium Alloys

Alloying of Ti is controlled by the ability of elements to stabilize either α- or β-phase as illustrated in **Figure 2.20** Elements such as Al and O those dissolve in the α-phase raise the α/β transus. In this system, it is noted that aging of these alloys with an Al content above 5-6% can lead to the formation of a finely dispersed hexagonal phase (α_2) having a general formula Ti_3X. β-stabilizing elements are subdivided into β-isomorphous and β-eutectoid elements.

β-isomorphous elements, such as Mo and V, exhibit complete mutual solubility with β-Ti and progressively depress the transformation showing the martensite start (M_s) and martensite finish (M_f). On the other hand, β-eutectoid elements, such as Cu, Fe and Mn, have restricted solubility in β-Ti and form intermetallic compounds by eutectoid decomposition of the β-phase. Examples are the binary systems Ti-Fe and Ti-Mn and these alloys behave as if they conformed to the β-isomorphous phase diagram; hence the arrows shown in **Figure 2.20**. Furthermore, there are some elements, such as Zr and Sn, behave neutrally. More details are described in [100].

In the present study, Ti–6Al–2Sn–4Zr–2Mo–0.1Si (in the following Ti-6242) which is α-β alloy was used to produce OFW-Joints. Ti-6242 is the workhorse high-temperature Ti-alloys in several industries because it has an outstanding combination of creep strength, tensile strength, toughness and high-temperature stability for long-term applications at temperature up to 425 °C. It is used primarily for gas turbine applications such as high-pressure compressor blades of the jet engine, disks, impellers, engine afterburner structures, hot airframe skin components. Ti-6242 is one of the most creep-resistant Ti-alloys and is recommended for use in elevated temperature applications [101].

2.4.2. Application and Advantages

Friction welding of titanium alloys is widely practiced as a means of obtaining a high integrity joint of materials with α+β processed microstructures. There are three processes, two currently used in production and a third that is under development. For axisymmetric shapes, rotational friction welding is the most commonly used process. linear friction welding is useful for making friction welded joints of non-axisymmetric geometries. An example of the rotor during fabrication by linear friction welding is shown in **Figure 2.21**-a). In this figure, several blades can be seen that are already welded in place and the locations on the hub where two others will be attached. The benefit of using this technique is the cost saving of making a near net shape part and the improved properties of the air foils, since they can be individually forged, and heat treated before attaching them. The third, currently experimental friction welding process is Orbital friction welding. U. Raab et al. have carried out some investigations on orbital friction welding as an alternate method of making this component [51, 54].

An example for the application of Ti-6242 material with bi-modal microstructure is the impeller, which is used as last compressor stage in small, low flow aero-engines and in auxiliary power units (APUs). One more example of application is the GE CF6 high pressure (HP) compressor spool shown in **Figure 2.21-b)**, with five Ti-6Al-4V front stages followed by two Ti-6242 rear stages.

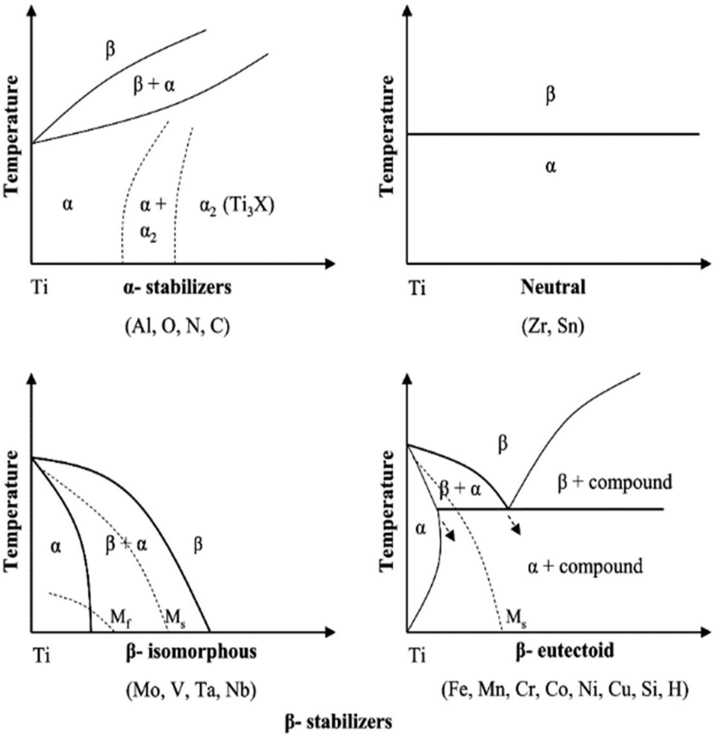

Figure 2.20 Classification scheme of Ti-alloys phase diagrams [100].

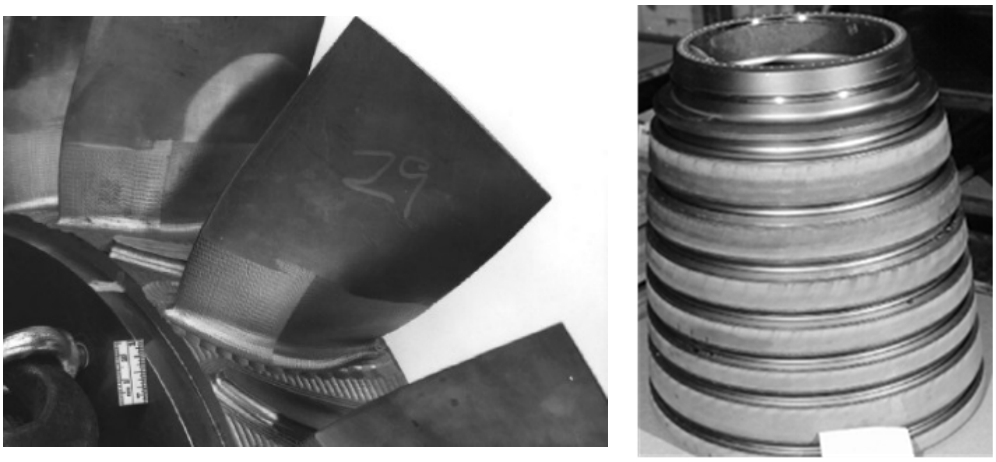

a)

b)

Figure 2.21 a) Close-up photo of the airfoil joint area of an integrally bladed aircraft engine rotor being made by linear friction welding and b) Compressor spool for GE CF6 class engine using inertia welding to connect the individual stages; front stages: Ti-6Al-4V, rear stages: Ti-6242 [90].

2.5. Mechanical Surface Treatments

Mechanical surface treatments such as shot-peening, roller-burnishing and deep-rolling are often performed on high-strength aluminum and titanium alloys to improve fatigue performance [102].The beneficial influence of the mechanical surface treatments on the fatigue performance is often explained by surface strengthening by the process-induced high dislocation densities hindering crack nucleation at the surface and residual compressive stresses which retard microcrack growth from the surface [103]. Generally, the total fatigue life (N_F) of a component can be divided into a crack-free initial stage, i.e. the number of cycles to fatigue crack nucleation (N_I) and the number of cycles for propagating fatigue cracks (N_P) until final fracture: $N_F = N_I + N_P$. All mechanical surface treatments lead to a characteristic surface roughness, increased near-surface dislocation density (cold work) and development of macroscopic RS (**Table 2-3**). A high surface roughness accelerates crack nucleation with no effect on crack propagation. Cold work retards crack nucleation but accelerates crack propagation. Residual compressive stresses have little effect on crack nucleation but can drastically retard crack propagation [104].

Table 2-3 Effects of surface layer properties on the various stages on fatigue life [105].

	Crack nucleation	Crack propagation
Surface roughness	Accelerates	No effect
Cold work	Retards	Accelerates
Residual compressive stress	Minor or no effect	Retards

Many researchers have investigated the fatigue performance enhancement of titanium alloys using shot peening and roller burnishing processes [106-109]. Wolfgang Hennig et al. [110] have utilized shot peening method for Aerofoil Treatment of Blisk Assemblies. **Figure 2.22** shows a scheme of a calliper nozzle for shot peening of aerofoils. Omar Hatamleh et al. have conducted several investigations of the effects of laser and shot peening on the fatigue performance and corrosion resistance of friction stir welded Aluminum joints [111-115].

In present study, the parameters of shot peening and roller burnishing as mechanical surface treatments were optimized to enhance the surface layer properties, fatigue performance as well as the impact toughness of the rotary and orbital friction welded joints.

2.5.1. Shot Peening

Shot peening (SP) is a process used to produce a compressive residual stress layer and modify mechanical properties of metals. The changes in the surface state due to SP are, for examples, changes of the RS, microstructures, hardness by work hardening, surface roughness, and dislocation density. It entails impacting a surface with shot (round metallic, glass or ceramic particles) with a kinetic energy sufficient to create plastic deformation, each piece of shot that strikes the material acts as a tiny peening hammer, imparting to the surface a small indentation or dimple. To create the dimple, the surface of the material must yield in tension. Below the surface, the material tries to restore its original shape, thereby producing below the dimple a hemisphere of cold-worked material highly stressed in compression [102].

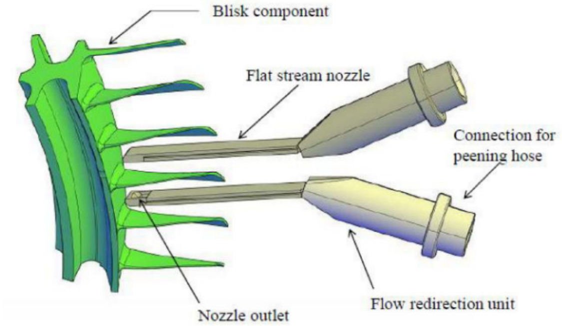

Figure 2.22 Scheme of a calliper nozzle for shot peening of aerofoils [110].

There are many process parameters influencing on the surface characteristics after SP as listed in **Table 2-4**. Due to a large number of these parameters influencing on the results, J. O. Almen (1940) developed a standard process to measure the kinetic energy transferred by a shot stream using Almen strip system. As seen in **Figure 2.23**, an Almen strip is a thin strip of SAE 1070 steel used to quantify the intensity of a shot peening process. They are classified into 3 types: 'N' (0.79 mm thick), 'A' (1.30 mm thick), and 'C' (2.38 mm thick). They differ in their thickness, while they have the same length and width (76 mm long x 19 mm wide). SP specifications refer to this energy as intensity at saturation, which means the earliest point of the saturation curve that, if the exposure time is doubled, the arc height increased by 10% or less [116].

Shot peening coverage is the ratio of the area covered by hits and the complete surface treated by SP. Complete coverage of a shot peened surface is crucial in performing high quality SP. Fuhr et al. [109] have concluded that Low coverage (20 %) resulted in a significant loss of fatigue performance. The major advantage of shot peening is that it covers large areas at low cost, however, care must be taken to ensure that the shot size is small enough to reach the bottom of all undercuts. Typical shot size is in the range of 0.2 to 1.0 mm and the velocities of projection are in the range of 40 to 60 m/s [117].

Table 2-4 Parameters influencing on the results of shot peening treatment.

Device	Shot	Workpiece
Shot velocity	Shape	Geometry
Impact angle	Hardness	Elastic-plastic-deformation behavior
Mass flow rate	Mass	Hardness
Peening time	Size	Crystal structure
Coverage	Material	Temperature
Nozzle diameter	Wear state	Pre-stress
Nozzle clearance		

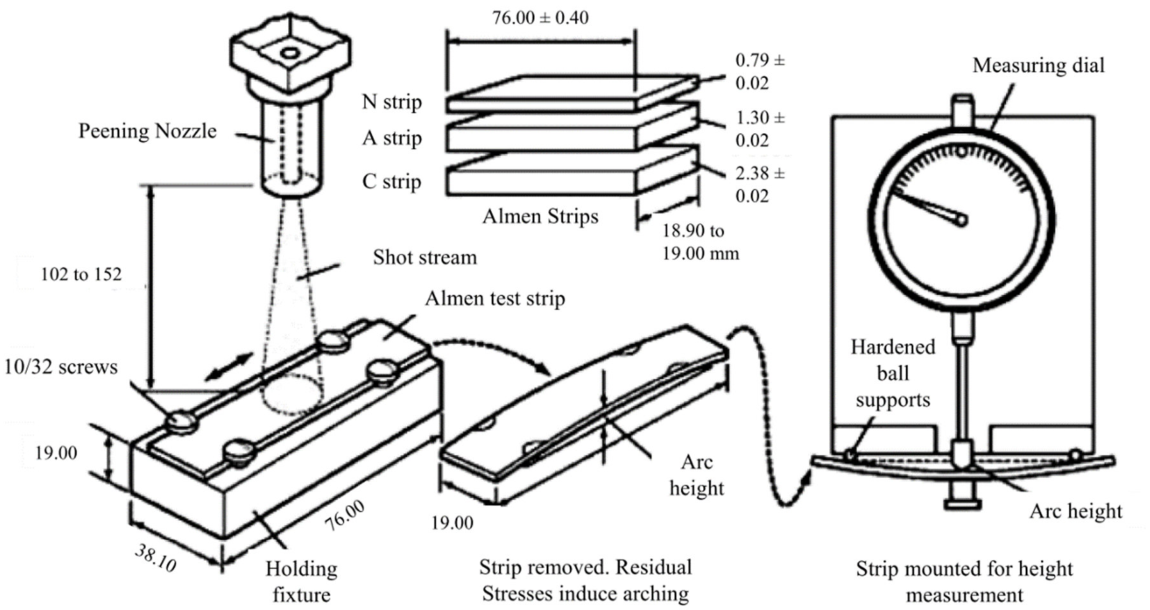

Figure 2.23 Almen strip system (All dimensions in mm) [116].

2.5.2. Roller Burnishing

Burnishing is the most sufficient mechanical process to improve the fatigue strength of dynamically loaded components. This can be performed using either rolls (called roller burnishing) or balls (called ball-burnishing). The burnishing process is applied to cylindrical workpieces of both, external and internal surfaces and does not involve material removal. Under certain conditions, this process provides a manufacturing alternative to grinding, precision turning and honing operations. In most cases, burnishing process is performed on the same lathes where workpieces were machined [118].

Figure 2.24-a) shows how the surface's peaks are pressed down, almost vertically, into the surface and the material then flows into the valleys between the peaks. The resulting smooth surface occurs not because the peaks are bent into the surface, but because the material at the workpiece surface is plastically deformed and the material flows, eliminating surface roughness [119]. The curved arrows pictured at the material's surface demonstrate how the material is displaced into the valleys between the peaks. Plastic deformation increases the roller's contact with the surface in that the applied rolling pressure (or burnishing force) affects the peaks that lie ahead of the roller's current position while causing the peaks at the point of contact to flow. The region found between the arrows labeled "rotation direction" demonstrates how the material's surface is shaped during the burnishing process. The roller suppresses the plasticized material, preventing it from flowing backwards against the feed direction, while clearance angle α ensures that the surface is not over-burnished [119].

Figure 2.24-b) presents a diagram of roller burnishing principle for a spherical roller. The first contact to the machined surface occurs in Section (A). In section (B) the

yield strength of the surface is exceeded, and plastic deformation takes place. Pressurized depth can be seen here as (D). After the material has been subjected to the maximum compressive strain, in section (C) it begins to elastically relieve (E) through the finishing zone finally leaving with a smooth surface and a compressive residual stress of significant peak value. The stresses formed on the material during the compression decrease towards the center. [120]

This process leads to a smoother surface and greater amount of compressive residual stress than SP process. Moreover, compressive residual stress is induced in the surface layer, followed by strain hardening and a series of beneficial effect on mechanical properties leading to improve fatigue and corrosion resistance of different metals under dynamic loads [121].

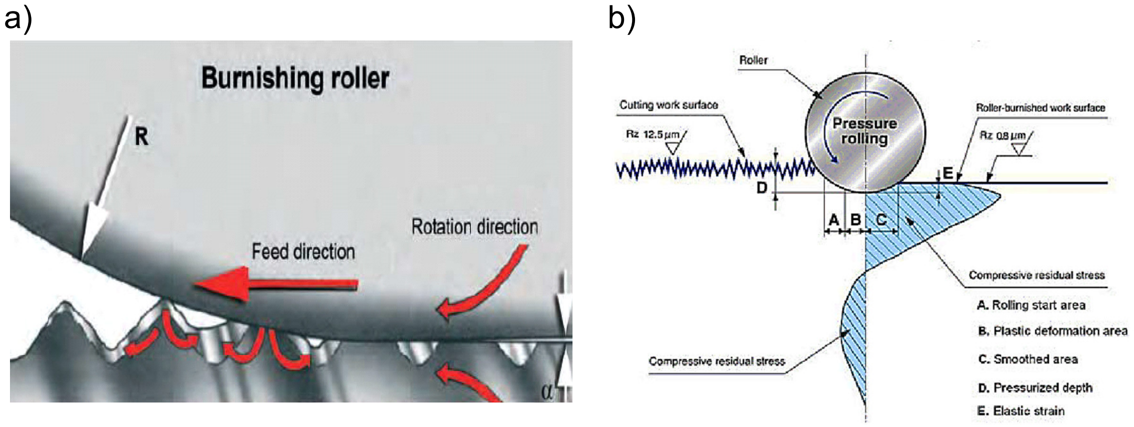

Figure 2.24 a) Roller burnishing process [119] and b) overview of the roller burnishing principle [120].

2.5.3. Weld Fatigue live improvement Techniques

the fatigue life of welded components and structures is dominated by the fatigue crack propagation phase because the initiation phase is insignificant or in some cases nonexistent due to the presence of initial defects resulting from the welding process. Other factors affecting the fatigue strength of welded joints include the presence of tensile residual stresses arising from the welding process. In many cases the fatigue life of welded components and structures can be substantially improved both during initial manufacture and repair by the application of weld improvement methods which reduce or eliminate these effects. In general, the weld fatigue improvement methods can be divided into two main groups, weld geometry modification methods and residual stress methods. A summary of the various improvement residual stress techniques to be considered is shown in **Figure 2.25**. These techniques can be divided into two main groups, mechanical method and thermal method [122].

In the present study, a combination between a mechanical and thermal method has been conducted to enhance the surface layer properties, fatigue performance, as well as the impact toughness of the rotary and orbital friction welded joints. As mechanical methods, SP and RB process have been optimized and as a thermal method, Thermal stress relief (PWHT) has been carried out to investigate the mechanical and metallurgical characterization of welded joints. In other words, the conditions of as-welded (AW), post-weld heat treated (PWHT), as-welded + shot peening (AW SP), as-welded + roller burnishing (AW RB), PWHT SP and PWHT RB have been investigated and the results were compared.

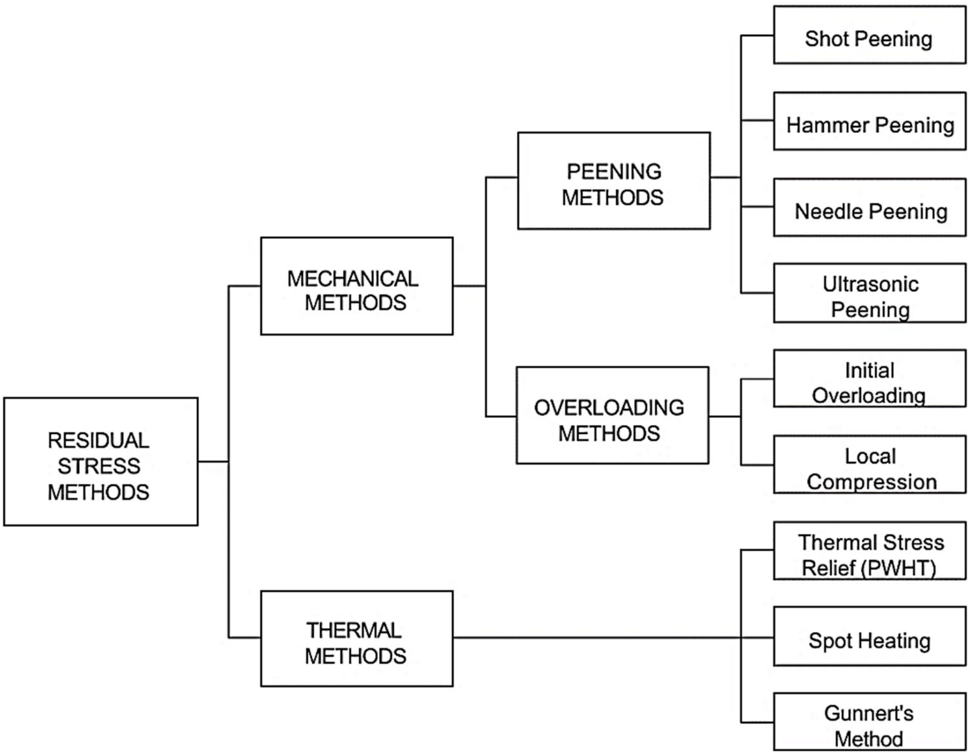

Figure 2.25 Classification of Some Weld Improvement Methods [122].

2.6. Residual Stresses (RS) in Welded Joints

The welding process results in high levels of tensile RS set up in and around the weld as a result of contraction of the metal after it cools down. Chuan LIU et al. [123] have demonstrated the stress distribution in the TC17 alloy LFW joint. They have selected four lines on the cutting surface to evaluate the measured stress as shown in **Figure 2.26-a)**. The Stress distribution along line L1 is shown in **Figure 2.26-b)**. A high tensile stress occurs at the weld line center and decreases sharply to a small peak compressive stress (about 50 MPa) at distance of 11 mm (left side) and 14 mm (right side) from the weld line center, this contributes to a reduction in fatigue strength of welded components and structures. It can be seen from **Figure 2.26-c)** that the through-thickness stress is not uniform from top surface to bottom surface, and the stress near the top and bottom surfaces is smaller than the interior stress. In addition, the stress magnitude decreases sharply with increasing the distance from the weld centerline. At the location of 6 mm from the weld centerline, the stress is compressive through the entire thickness.

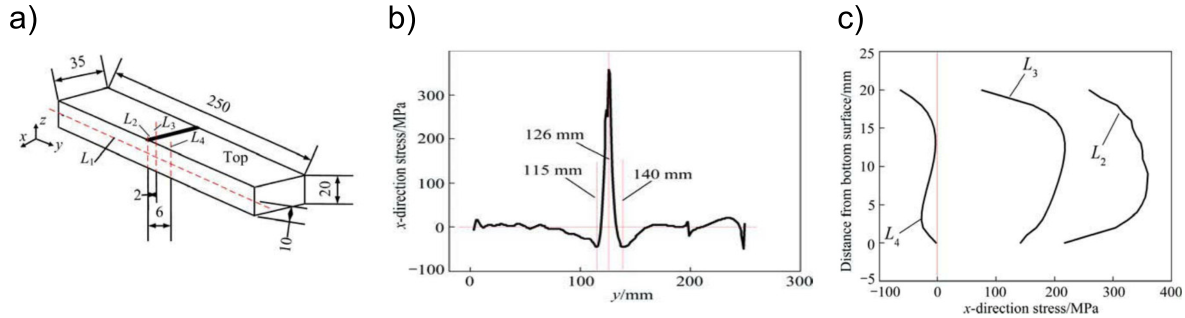

Figure 2.26 a) Schematic diagram of stress evaluation lines (unit: mm), b) stress distribution along line L1 and c) stress distribution along lines L2, L3 and L4 [123].

In circumstances in which a joint is loaded mainly in compression, the fatigue strength can be increased by stress relief which removes residual tensile stresses at the weld [124]. In this sense, post-weld heat treatment (PWHT) or stress relief can be regarded as a fatigue improvement technique. However, it should be noted that in practice local residual tensile stresses of the order of 20% to 30% of the yield strength can still remain after PWHT. As a result, even when the stresses due to applied loads are nominally compressive, stress relief or PWHT may only marginally improve the fatigue strength of a welded joint in a structural assembly. Stress relief has little effect if the applied loading on the detail gives rise only to tensile stresses.

2.6.1. Residual Stresses Determinations

There are many methods to determine RS including mechanical, magnetic, electrical, ultrasonic, thermoelastic, thermoplastic and diffraction methods as explained in [125]. In the present study, the proto laboratory or angle-dispersive X-ray diffraction (proto-LXRD) (as a diffraction method) and the incremental hole drilling technique (as a mechanical method) were used to determine macroscopic or first order residual stress.

2.6.1.1. Proto Laboratory X-ray Diffraction (Proto-LXRD)

In Proto-LXRD using a monochromatic beam, the wavelength (λ) is constant depending on target materials in X-ray tubes (e.g. λ = 1.5418 Å for Cu-tube and λ = 1.7902 Å for Co-tube) and the diffraction angle θ can be varied. The RS can be analyzed by using sin2ψ method. This method is a sensitive and accurate technique to measure RS in a fine grained, polycrystalline material. As shown in **Figure 2.27**, the position of a diffraction peak will shift as the sample is tilted by an angle ψ. The magnitude of the shift will be related to the magnitude of the residual stress. Thus, if there is no residual stress, the shift will be zero. Since the X-ray penetration is extremely shallow using LXRD, a condition of plane-stress is assumed to exist in the diffracting surface layer [126].

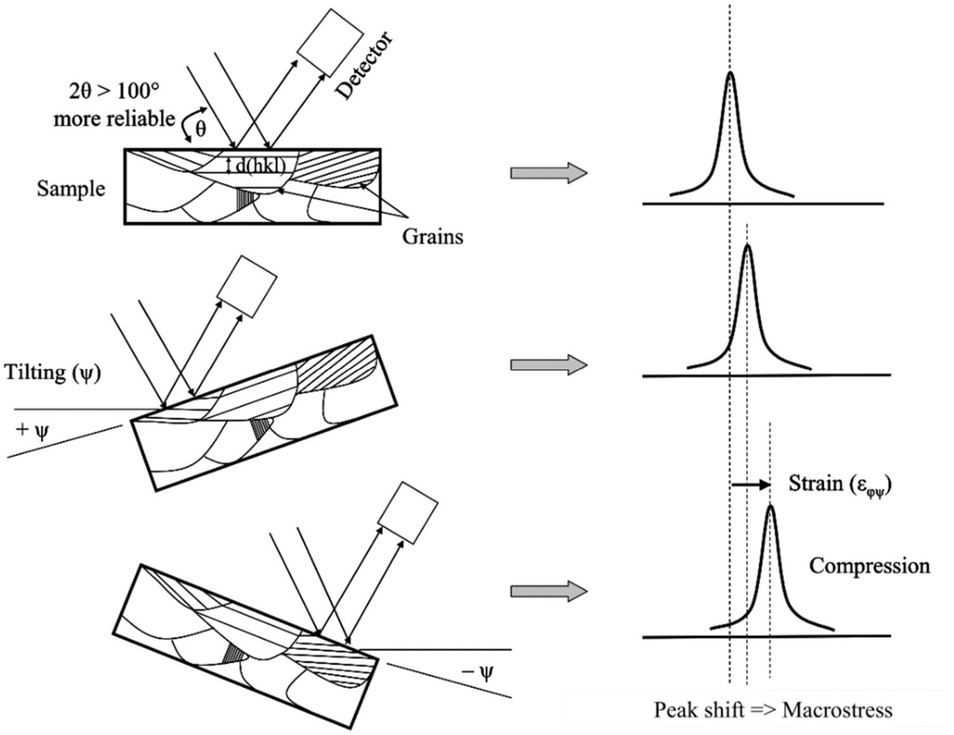

Figure 2.27 Scheme showing shift of diffraction peak with change in tilting angle ψ (d (hkl) = lattice spacing of hkl plane) [126].

2.6.1.2. Incremental Hole Drill Method (IHD)

The principle of IHD involves the introduction of a small hole into a component containing RS and subsequent measurement of the locally relieved surface strains. The residual stress can then be calculated from these strains using formulae and calculations derived from experimental and Finite Element Analyses. In practical terms, a hole is drilled in the component at the center of a special strain gauge rosette. Close to the hole, the strain relief is nearly complete, but the technique suffers from limited strain sensitivity and potential errors and uncertainties related to the dimensions of the hole (diameter, concentricity, profile, depth etc.), surface roughness, flatness, and specimen preparation. Incremental hole drilling improves the versatility of the technique and enables stress profiles and gradients to be measured [127]

In practical terms, there is no point making measurements beyond a depth roughly equivalent to the drill diameter, since no additional strain can be measured. The basic hole drilling analysis assumes that the material is isotropic and linear elastic, that stresses do not vary significantly with depth and the variations of stress within the body of the hole are small. The basic analysis only applies where residual stress values do not exceed half the yield strength of the material.

Figure 2.28 shows a range of residual stress strain gauge geometries currently available. Strain gauge type A is the most commonly used design and is recommended for general purpose measurements, Type B is useful where measurements need to be made near an obstacle or close to a fillet or radius. Type

C, which uses 6 grids, has been introduced recently to give improved strain sensitivity.

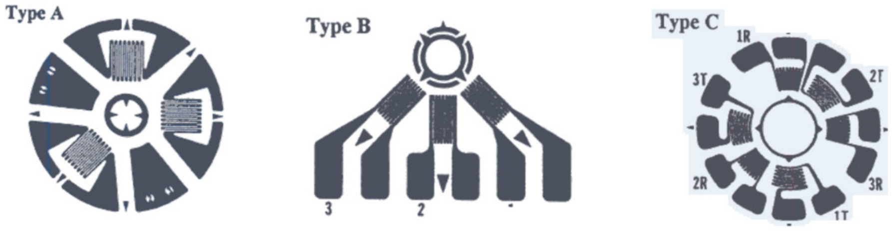

Figure 2.28 Typical residual stress strain gauge rosette geometries [128].

With hole drilling some surface preparation is required to achieve good bonding of the strain gauges, but care must be taken not to remove too much material particularly if the RS close to the surface are important. Choosing a suitable strain gauge and drill size is important (and the two are closely linked) because this will determine the maximum depth of the measurement. Gauge size is important and should be considered in relation to the type of stresses present. Small gauges give a more localized measurement, but are more difficult to handle, only give limited depth information (because of the corresponding small drill size) and are possibly susceptible to larger errors associated with misalignment or surface irregularities [128].

3. Experimental Work

3.1. Research Methodology

Figure 3.1 shows an overview of the research methodology used in this study to deliver improve the fatigue life of orbital and rotary friction welded joints (details in **section 1.1**).

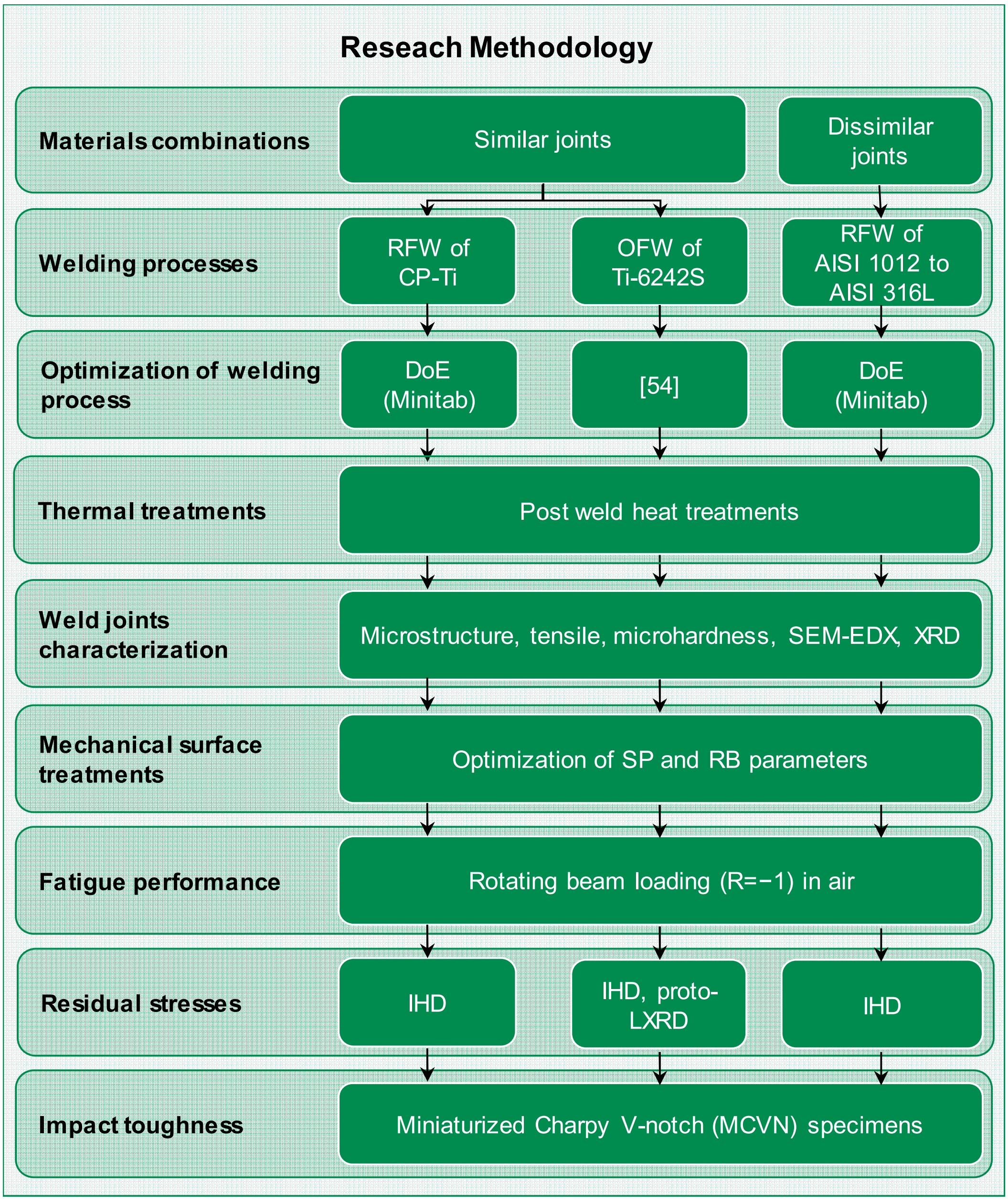

Figure 3.1 An overview of the research methodology used in this study.

3.2. Materials

3.2.1. Commercial Pure Titanium (CP-Ti) Grade 2

The material of CP-Ti grade 2 was received as rods of Ø 32 mm. The chemical composition is listed in **Table 3-1**. **Figure 3.2-a)** shows the microstructure of as-received material which consists of equiaxed grains having an average grain size of 34 µm. The as received rods were swaged from Ø 32 mm down to Ø 10 mm in order to produce a friction welding samples of Ø 8 mm. **Figure 3.2-b)** shows the microstructure after swaging which is characterized by bent and kinked lamellae resulting from the severe plastic deformation. The swaged rods were then annealed for 1 hour at 700 °C to recover the decreased ductility of the deformed materials as shown in **Figure 3.2-c)**. The mechanical properties of the as-received, the swaged and the annealed CP-Ti after swaging are given in **Table 3-2**.

Table 3-1 Chemical composition of as-received material.

Alloying elements	O	Fe	C	N	H	Ti
Wt. %	0.20	0.25	0.08	0.06	0.013	Bal.

Table 3-2 Mechanical properties of as-received, swaged and annealed CP-Ti grade 2.

	YS, MPa	UTS, MPa	EL, %	RA, %	Hardness, HV
As-received	416	546	31	49	174
Swaged	1043	1058	8	31	271
Annealed 700 °C/1h after swaging	462	592	34	65	178

3.2.2. Titanium Alloy Ti-6242

The material employed in orbital friction welding was α-β Ti-6Al-2Sn-4Zr-2Mo-0.1 Si (Ti-6242). It was provided in the form of a forging disk. The welding samples with the dimension of 7 x 14 x 50 mm³ were machined from this disk as shown in **Figure 3.3-a)**. The microstructure and the chemical composition of the as-received material are given in **Figure 3.3-b)** and **Table 3-3**, respectively. The duplex (bi-modal) microstructure shown in **Figure 3.3-b)** consists of globular primary 26 % α-phase (light) with an average grain size of about 17 µm at the triple-points of the β-grain boundaries and α-lamellae (light) within the β-grains (dark). This microstructure is characterized by a high strength, ductility and high fatigue strength in the LCF and HCF range [24]. The mechanical properties of the as-received material are given in **Table 3-4**.

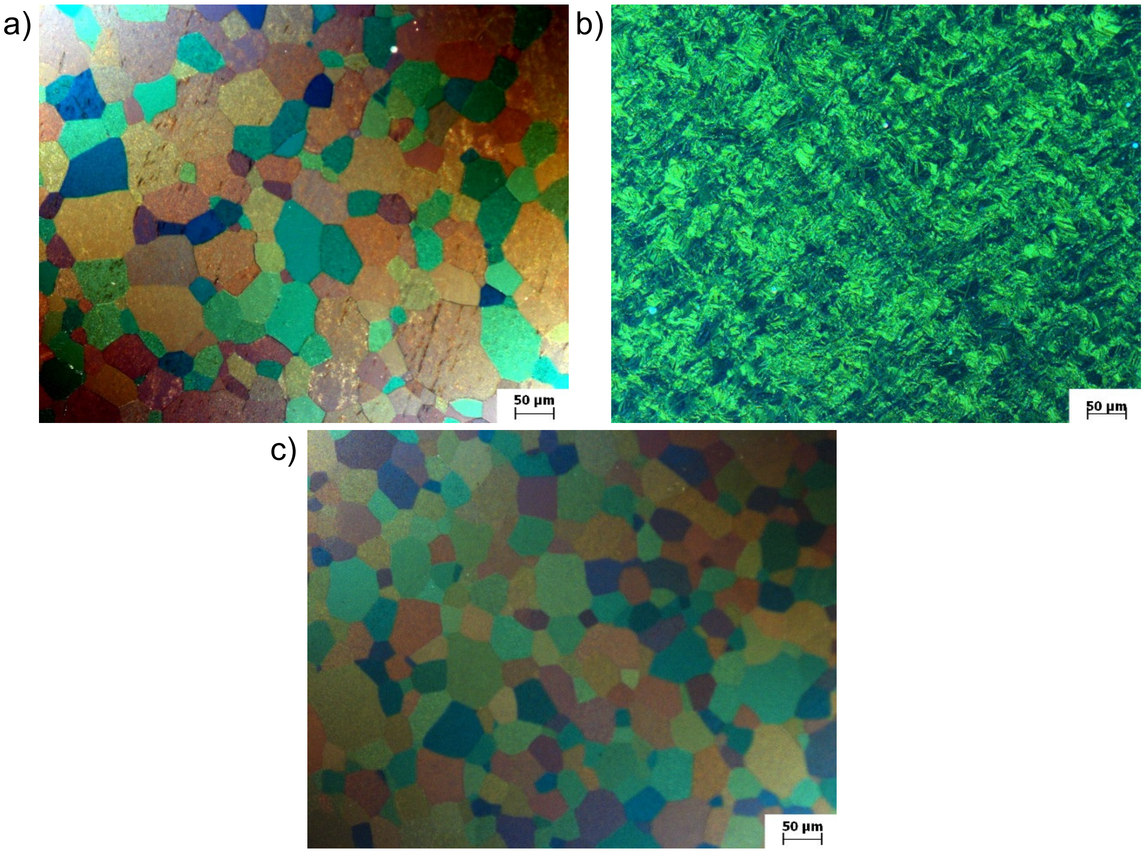

Figure 3.2 Microstructure of a) as-received-, b) swaged- and c) annealed materials. (etched with Kroll's reagent)

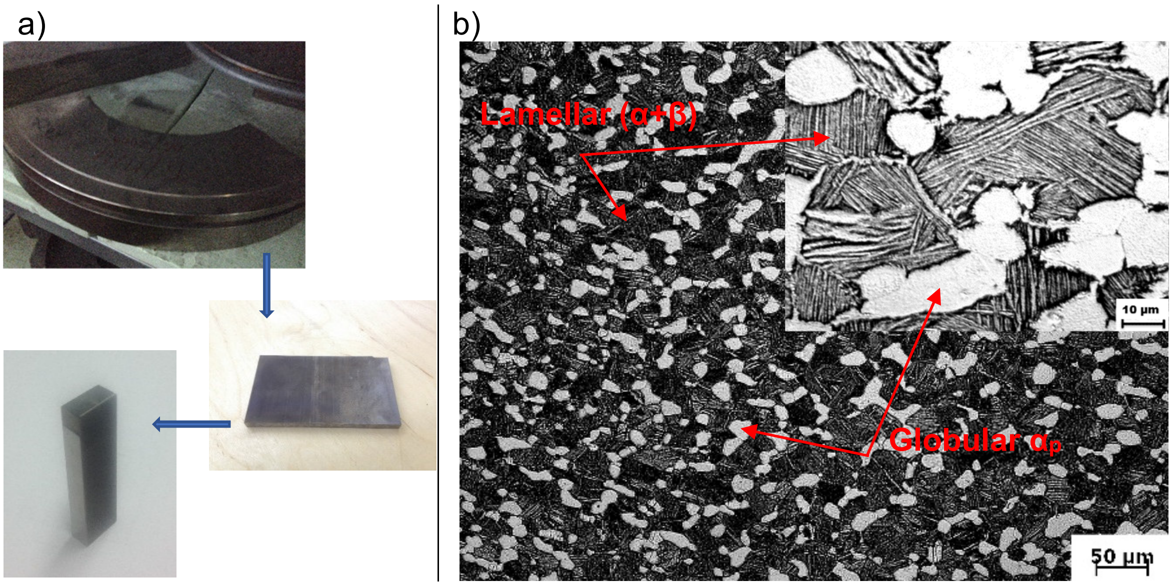

Figure 3.3 a) As-received forging desk and b) microstructure of as-received Ti-6242. (etched with Kroll's reagent)

Table 3-3 Chemical composition of as-received Ti-6242.

Alloying elements	Al	Sn	Zr	Mo	Si	Fe	C	O	Ni
Wt. %	5.63	1.57	4.56	1.43	0.05	0.03	0.02	0.08	0.007

Table 3-4 Mechanical properties of as-received Ti-6242.

Material	YS, MPa	UTS, MPa	EL, %	RA, %	Hardness, HV
Ti-6242 AR	983	1074	17	34	342

3.2.3. AISI 316L to AISI 1012

Dissimilar joints of austenitic stainless steel (AISI 316L) and carbon steel (AISI 1012) specimens of Ø 8 mm and 50 mm length were welded by rotary friction welding without any preheating. **Table 3-5** and **Table 3-6** show the chemical composition and mechanical properties of AISI 1012 and AISI 316L, respectively. **Figure 3.4-a)** shows the microstructure of AISI 1012, which consists of a matrix of ferrite grains (white etching constituent) and pearlite (dark etching constituent). A 5% Nital etching reagent was used to reveal the microstructure of the carbon steel specimens. The indicated high strength and low ductility of the carbon steel may be related to the homogeneously distributed spherical inclusions [129]. The microstructure of the AISI 316L stainless steel (**Figure 3.4-b)**) reveals equiaxed austenite grains with annealing twins etched with V2A reagent (100 mL distilled water + 100 mL hydrochloric acid 32% + 10 mL nitric acid 65% + 0.3 mL Vogel's special reagent). Small pores are visible as dark spots on the BSE micrographs, which are likely to be caused by the pull out of inclusions in the steel during grinding and polishing.

Table 3-5 Chemical composition of the as-received materials.

Materials	Alloying elements, wt.%								
	C	Si	Mn	P	S	Cr	Ni	Mo	Fe
AISI 1012	0.12	0.20	0.47	0.01	0.03	0.10	0.16	0.035	98.6
AISI 316L	0.02	0.50	1.38	0.023	0.014	17.00	9.93	1.93	＜68

Table 3-6 Mechanical properties of the as-received materials.

Materials	UTS, MPa	YS, MPa	EL, %	RA, %	Hardness, HV	Impact toughness, J
AISI 1012	664	624	16	62	216	86
AISI 316L	773	645	41	75	294	119

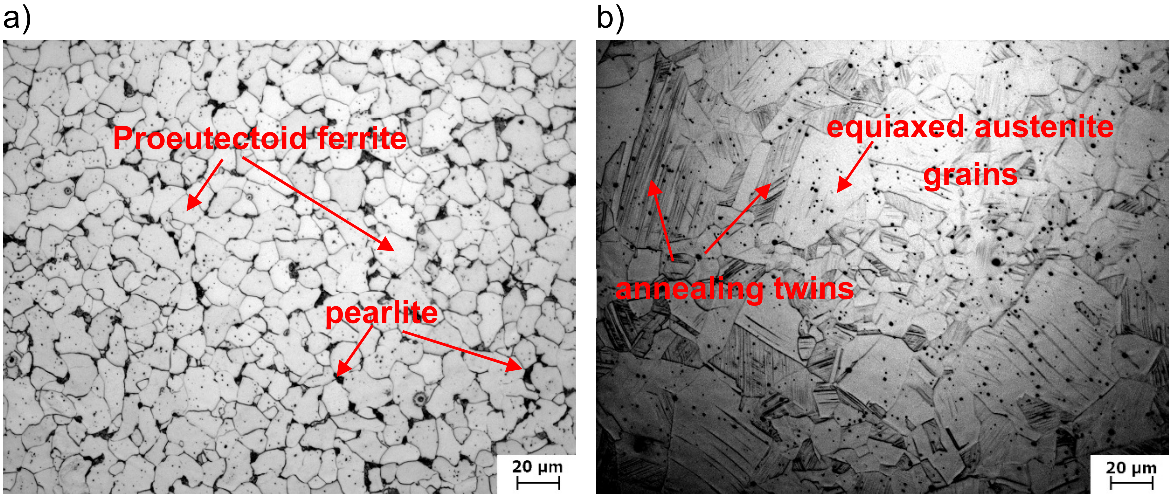

Figure 3.4 The microstructure of a) AISI 1012 etched with Nital 5% and b) AISI 316L etched with V2A reagent.

3.3. Friction Welding Processes

3.3.1. Rotary Friction Welding Equipment

The used rotary friction welding machine is RSM 200 from IWS Service GmbH (**Figure 3.5**). The experiments of welding dissimilar joints of AISI 1012 to AISI 316L as well as welding similar joints of CP-Ti grade 2 are conducted on this machine. The machine is pneumatically driven having 1.85 kW power with an axial load capacity of 18 kN and can run at a speed up to 23000 rpm. The RSM 200 friction welding machine can be classified as a direct drive system in which the friction welding process is controlled by the friction time or by the burn-off distance. Throughout the current experiments, the rotating workpiece (AISI 316 L) was attached to the RSM 200 via a clamping jaw on the spindle. The fixed part (AISI 1012) was attached to the pneumatic collet.

In friction welding, generally surface preparation is not considered as a major requirement because surface irregularities are removed by the scoring action and the debris get removed in flash. However, Hasui et al. [130] reported that the surface preparation can significantly affect the joint strength. In this work, the contact surfaces of the round rods were machined before welding to produce smooth oxide free surfaces and to ensure perpendicularity which are significant for achieving sound weld joints.

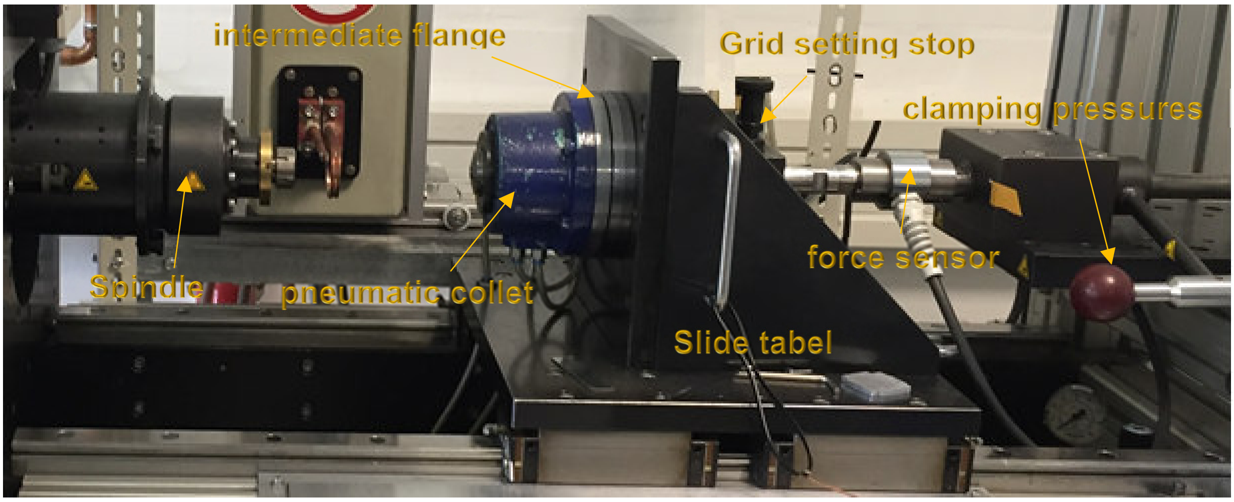

Figure 3.5 The used rotary friction welding machine RSM 200.

3.3.2. Orbital Friction Welding (OFW)

OFW was performed on a multi-orbital friction welding machine dyconn-100, which has a maximum capacity of 100 kN (**Figure 3.6**). The welding process was conducted in the force-displacement mode to weld similar parts of Ti-6242. The machine is equipped with two rotating heads with an oscillating circuit diameter of 1.50 mm and a maximum frequency of 100 Hz. Single orbital friction welding (SOFW) (**Figure 3.7-a)**) has been used in this study for two reasons which are:

1) To minimize the generated heat input in order to obtain a narrow central weld zone, which limit the heat affected zone (HAZ) the surrounding material is not annealed [51].
2) Because in SOFW, the restrictions of the part weight and size on one side of welding process is lifted, which is the required situation for blisk manufacturing [54].

The welding process consisted of four friction phases followed by a single forging phase which was applied after reaching a predetermined displacement (D). The process parameters are listed in **Table 3-7**. Welding specimens with the dimension of 7 x 14 x 50 mm³ were used. The welding surfaces were cleaned with acetone before welding. **Figure 3.7-b)** shows the process parameters versus time. During welding, the high temperature plasticized material is extruded from the interface in the form of flash. The formation of flash can be used as a first quality criterion for a sound friction weld joint [54]. A set of welded joints were post-weld heat treated (PWHT) to relief RS that developed during orbital welding. The stress relief annealing treatment was conducted at 640 °C for two hours followed by air cooling.

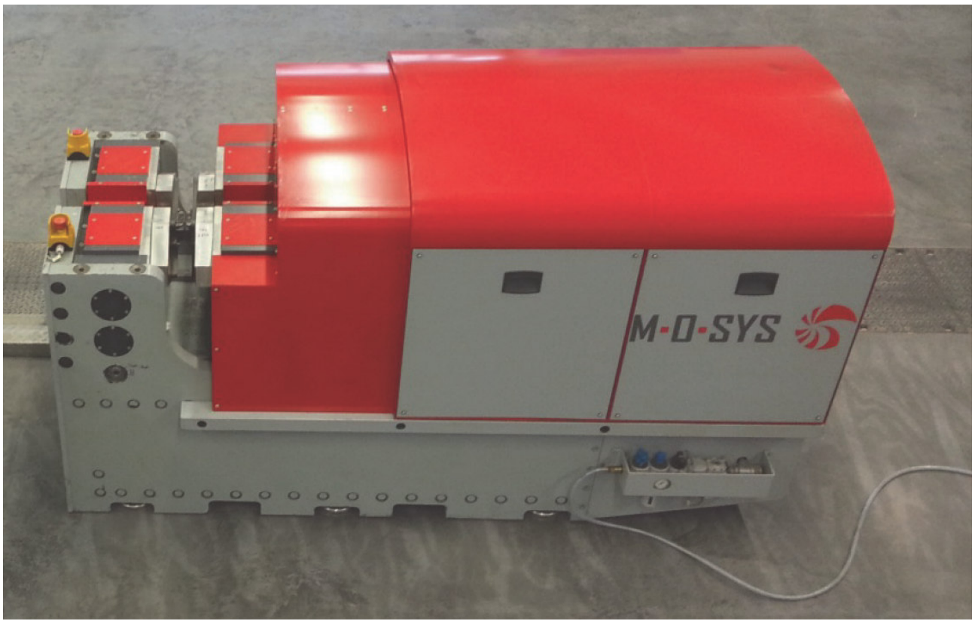

Figure 3.6 Multiorbital-friction welding machine dyconn-100.

Table 3-7 The orbital friction welding parameters.

Parameters			1st Friction phase		2nd Friction phase		3rd Friction phase		4th Friction phase		Forging phase	
LA, mm	w, °/s	Amplitude, mm	F, kN	D, mm	F, kN	D, mm	F, kN	D, mm	F, kN	D, mm	F, kN	t, s
3	20000	1.5	3	0.1	6	0.5	9	1.5	12	1.5	20	10
where: LA: unclamping length of the welding sample, w: angular speed, F: applied force, D: predetermined displacement and t: time												

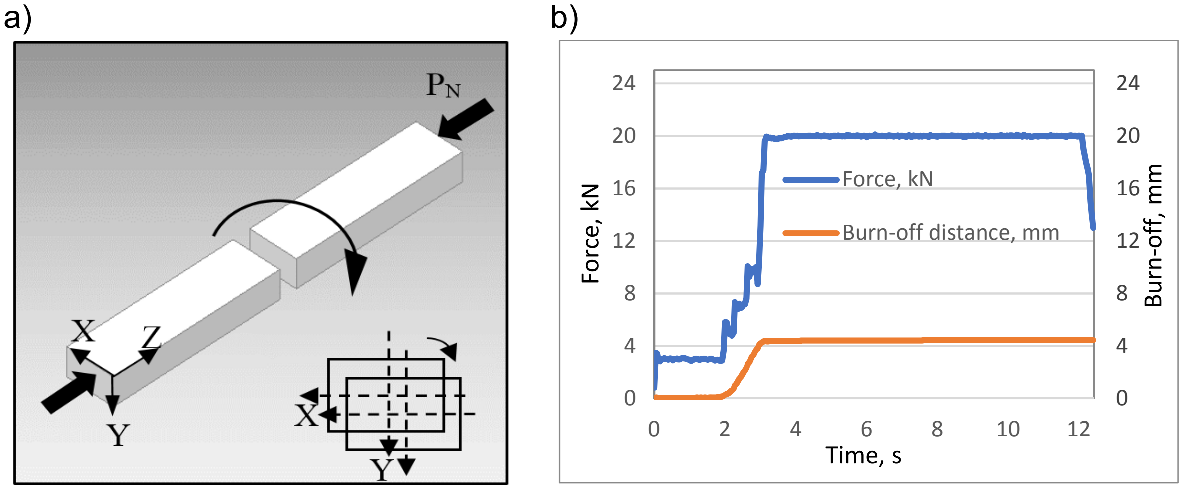

Figure 3.7 a) Single orbital friction welding process and b) process parameters versus time.

3.4. Post-Weld Heat Treatments

After welding, post-weld-heat-treatment PWHT has been carried out. The primary goal of the PWHT is to reduce the tensile residual stresses formed during the welding process [134]. The heat treatment was carried out without protective gas. **Table 3-8** summarizes the parameters for the heat treatment for rotary and orbital friction welded joints.

Table 3-8 The parameters for PWHT of rotary and orbital friction welded joints.

Welding Proccess	Rotary Friction Welding		Orbital Friction Welding
Materials	Cp-Ti to Cp-Ti	AISI 316L AISI 1012	Ti6242 to Ti6242
PWHT	550 °C/30 min AC	900 °C/30 min AC 1050 °C/30 min AC 1050 °C/30 min WQ & 885 °C/ 2h AC	640 °C/30 min AC

3.5. Weld Process Optimization

3.5.1. AISI 1012 to AISI 316L Friction Weld

Design of experiments (DoE) has been used to investigate the effects of input variables (friction welding parameters) such as friction pressure, friction time, forging pressure, forging time and rotational speed on an output variable (response) such as-weld joint tensile strength at the same time. These experiments consist of a series of runs, or tests, in which purposeful changes are made to the input variables. Data were collected at each run. DoE was used to identify the friction welding parameters that affect quality of the weld. The software “Minitab 17” was used to design the welding experiments. It offers four types of designs: factorial designs, response surface designs, mixture designs, and Taguchi designs (also called Taguchi robust designs). The steps to create, analyze, and visualize a designed experiment are similar for all types.

In this part of study, A two-level full factorial design matrix with three replicates has been used to create the designed experiments. The design of experiments methodology was carried out totally in four phases as factorial design, evaluation of data, determination of significance, and parameter optimization as shown in **Figure 3.8**

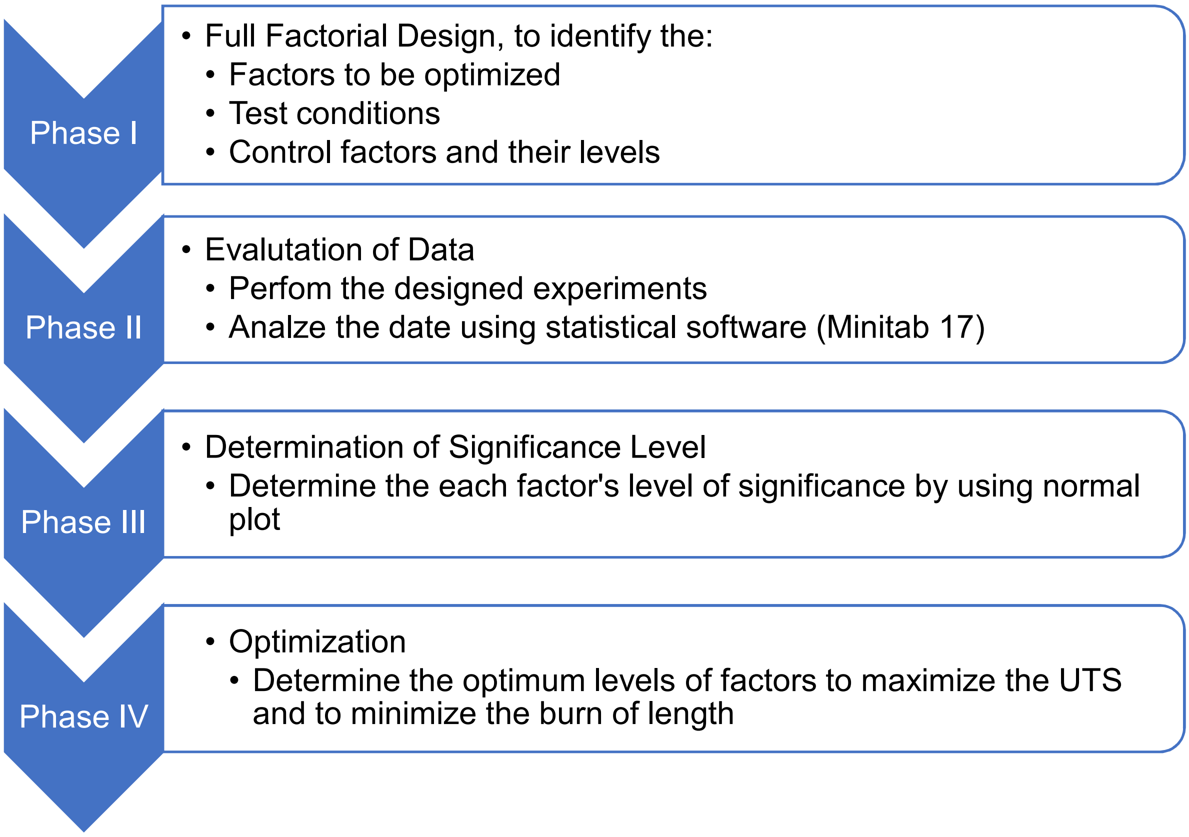

Figure 3.8 Main phases in optimization process.

The quality of the welded joints and particularly the efficiency of the friction welding process depends to a large degree on the relative velocity of the friction surfaces and on the axial force applied during the heating period. The weld quality also depends on the amount of plastic deformation at the ends of the welded pieces. This deformation can be measured by the axial deformation (burn off length). Therefore, the rotational speed (rpm), the axial friction pressure (bar) and friction time (s) were regarded as key parameters of the process. Tensile strength of the weld joints and burn off length were selected as the responses.

3.5.2. CP-Ti Friction Weld

A plan of experiments has been performed by means of testing a selection of appropriate welding parameters for producing satisfactory CP-Ti friction welding. The output variables were the central weld length and flash width of the weld which corresponds to the weld geometry. These output variables were determined according to the input variables, which are the friction pressure (P1), friction time (t1), forging pressure (P2) and forging time (t2) and rotational speed (rpm). The objectives of the optimization are maximization of central weld length and minimization of flash width to minimize the third part region in the friction welded joint. In this part of the investigation, the process parameters have been evaluated viewing the definition of parametric fields leading to suitable weldment quality. Initially, the weldment quality has been established only based on visual examination and a macrostructural evaluation. An optimized parameter matrix has been established and further investigated for the friction welding process.

3.6. Weld Joints Characterization

3.6.1. Microstructure characterization

Following friction welding processes, a microstructural evaluation has been carried out in order to evaluate the metallurgical transformations that have taken place within the joints as well as a base material microstructure evaluation. Several evaluation techniques have been used to analyze the joints and the base material such as Optical Microscopy (OM), Scanning Electron Microscopy (SEM) and Energy-Dispersive X-ray Spectroscopy (EDX). The characterization of the as received structures as well as the microstructural development in the welding zone were carried out in the first step under optical microscope. The samples were taken under cooling water using SiC cutting wheel. The specimens were cut approximately +/- 5 mm from the weld line. The sample was then centrically separated. The sampling is illustrated in **Figure 3.9**.The plain Y-Z to be examined is marked in green. These specimens were also used for microhardness and residual stresses (RS) measurement.

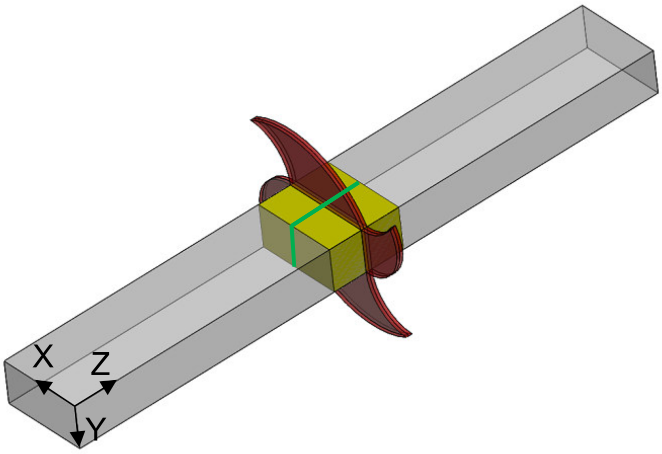

Figure 3.9 Sampling for microstructure analysis, microhardness and RS measurement of Ti-6242.

The mounting was carried out in a hot mounting press at 180 °C. for about 20 minutes and subsequent cooling using Bakelite (polyoxybenzylmethylenglycolanhydride) which can also be used for the scanning electron microscopy analysis due to its electrical conductivity. Subsequent grinding was carried out with SiC abrasive paper. Optimal results could be achieved by grinding grades of 320 up to 2000 grains. Subsequent polishing was done semi-automatically by Struers LaboForce machine. Specimens fixed in sample holder within the polisher were ground on rotating woven cloth plates and further polyester cloth using lubricants (e.g. soft soap) and diamond pastes. The surface polishing was conducted in two stages with a polishing time of 10 minutes and a contact force of 15 kN. In the first polishing step, a textile sheet and a diamond suspension having a particle size of 6 µm were used for pre-polishing. For the second polishing step for fine polishing, a woven cloth plates with a finer silicon oxide polishing suspension (OPS) with a particle size of 0.04 µm was used. Prior to etching, specimens were cleaned in ultrasonic bath for 3 minutes. Then the microstructures of Ti-6242 and CP-Ti were revealed by etching the specimen surfaces with The Kroll's etchant which consists of 92 ml distilled water, 6 ml HNO_3 and 2 ml HF.

Different chemical etchants, 5% Nital and V2A-reagent, were used to reveal the microstructures of AISI 1012 carbon steel and AISI 316L stainless steel, respectively. BI, BII and LBI as color etchant were used to reveal the microstructure of AISI 316L.In addition, δ-ferrite, carbides and manganese sulfate existing in 316L stainless steel were revealed separately by Groesbeck and Mod. Murakami to further investigate its variation. Utilized etchants of AISI 316L and AISI 1012 welded specimens are listed in **Table 3-9**.The microstructure characterization and element diffusion were analyzed by optical microscopy (OM, produced by Carl Zeiss AG), scanning electron microscopy (SEM) with energy-dispersive X-ray spectroscopy (EDX) capability. SEM has been used in this investigation when high resolution and high depth of field images were necessary. Since the depth of field is much greater than in OM, the ability to observe details spread along samples is better.

3.6.2. Tensile Testing

The specimens were precision machined from the friction welding joints as well as from the base material. Tensile tests were performed at room temperature (RT). All tensile specimens share the same geometry (DIN 50125) with gauge lengths and diameters of 20 and 4 mm, respectively as shown in **Figure 3.10-a)**. Three specimens were tested for each condition to get a mean value. Tests were carried out on Instron 5582 universal testing machine at the load of 50 kN, with straining rate of 1 mm/min. Two tensile test specimens have been machined per Ti-6242 orbital welded joint as shown in **Figure 3.10-b)**.

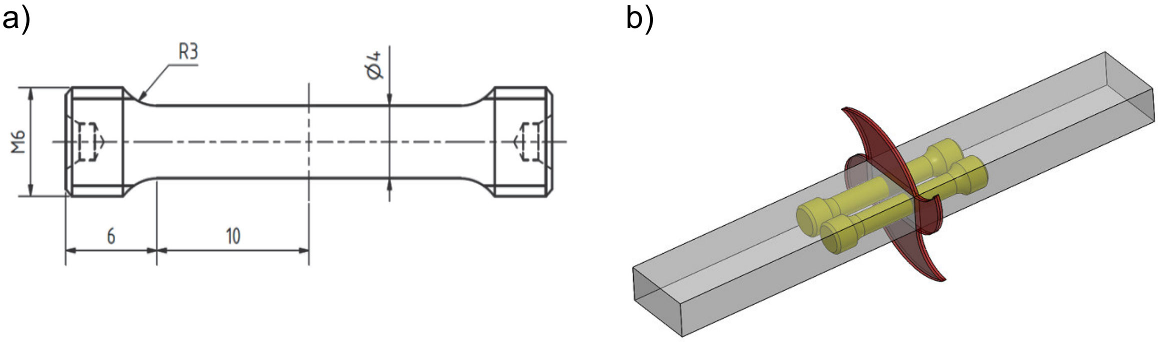

Figure 3.10 a) tensile test sample according to DIN6892 and b) machining position of the round tensile specimens.

Table 3-9 Utilized etchants of AISI 316L and AISI 1012 welded specimens.

Etchant	Composition	Conditions
Nital 5%	100 ml Ethanol 5 ml Nitric acid	Utilized for AISI 1012
BI	100ml stock solution Beraha I 1 g of potassium disulphide ➢ Stock solution of BI (Beraha) • 1000 mL dist. water • 200 mL concentrated hydrochloric acid • 24 g of ammonium bifluoride	Room temp., 5 s.
BII	100ml stock solution Beraha II 1 g of potassium disulphide ➢ Stock solution for B II (Beraha) • 800ml distilled water • 400ml Salt Acid 32% • 48 g of ammonia hydrogen difluoride	15 s immediately after polishing about 2 hours durable
LBI	20g of ammonium hydrogen difluoride 0.5 g of potassium disulfite 100 mL dist. water	30 °C, 5 minutes
Groesbeck	100 mL dist. water 4g of NaOH 4g KMnO4	90 °C, 10 minutes carbids darks, σ phase gray
Mod. Murakami	20 g K3Fe(CN)6 20 g NaOH 100 ml H2Or	Room temp. 60 s for carbides 3 min for σ phase
V2A-reagent	100 ml distilled water 100 mL hydrochloric acid 32% 10 mL nitric acid 65% 0.3 mL Vogel’s special reagent	70 °C, 25 s.

3.6.3. Microhardness profile

Microhardness was determined by means of a Struers Duramin tester using a square base pyramid shaped indenter for testing in a Vickers tester, a nominal force of 100 gf (HV0.1) and a loading time of 10 s. The hardness testers in the Duramin series conform to the standard DIN EN ISO 6507. The average of three measurements was taken at each depth to construct the hardness-depth profiles.

3.6.4. Phases analysis

The phases analysis of rotary friction welded AISI 1012 to AISI 316L specimens at two locations were recorded by X-ray diffractometer operated with CoKα radiation at a scanning rate of 1°/min over a 2θ range of 46-130°. Location 1 is at the weld line and location 2 at a distance 0.8 mm from the weld line in AISI 316L side as shown in **Figure 3.11**. The samples were cleaned with acetone and rinsed with deionized water prior to analysis. The test set-up is schematically shown in **Figure 3.12**.. A z scan was used to position samples at correct heights on the z drive prior to XRD measurement. The experiments were conducted using a Siemens D5000 diffractometer at 40 kV and 40 mA. The diffraction patterns produced were plotted with intensity against 2θ angles, and used for phase transformation and crystallinity analysis.

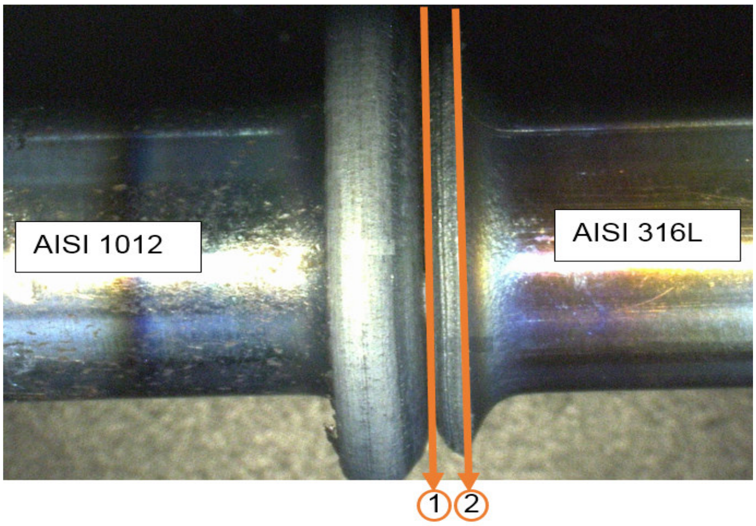

*Location 1 at the weld line

*Location 2 at distance0.8 mm from the weld line

Figure 3.11 XRD measurement locations at the weld specimen.

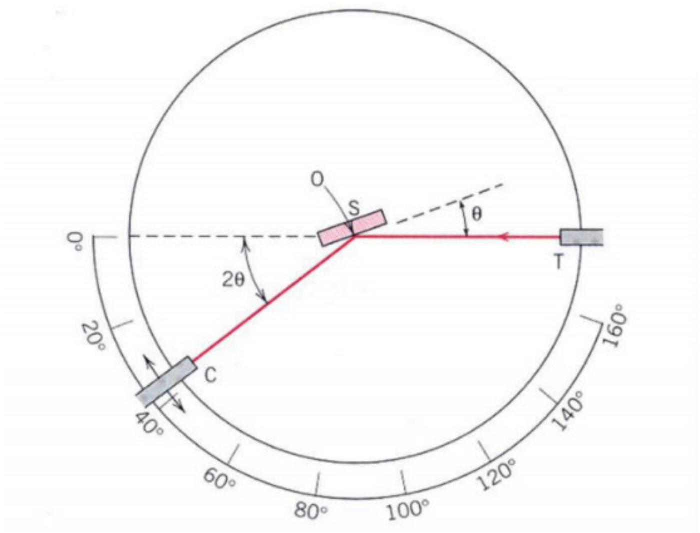

Figure 3.12 Schematic diagram of an x-ray diffractometer, T x-ray source, S specimen, C detector, and O the axis around which the specimen and detector rotate [131].

3.7. Mechanical surface Treatments

3.7.1. Shot Peening (SP)

SP was carried out on a computer-controlled peening machine powered by compressed air (gravitation system), produced by OSK-Kiefer GmbH **Figure 3.13-a)**. The shot media utilized in this study is spherically conditioned (rounded) cut wire shots (SCCW 14) with average size at 0.36 mm. SCCW shots possess spheroidal shapes with slight deviation because of the manufacturing process, showed in **Figure 3.13-b)**. The hardness of shots is around 700 HV. Shots were propelled by air blast system into the path of high pressure air and accelerated through a blasting nozzle which is directed at the specimen. Then each shot functions as a small ball-peen hammer, impinging the specimen surface. (**Figure 3.13-c)**). A recycling system is operated to collect the blasted shots and refuel them back to the nozzle. These cut wire shots could sustain long and be reused due to its conditioned roundness, unlike cast shot which tend to break into pieces that can damage the specimen surface.

The peening coverage is an important quality controlling parameter, exhibiting how completely the specimen surface has been peened by impinging shots. The factors influencing coverage include: number of impacts (shot flow), exposure time, shot properties and work piece properties. Optical monitoring examination was used to determine the coverage. It was ascertained in pretesting that it takes at least 20 s to reach full coverage. So, the peening duration is set up at 25 s to ensure full coverage of all specimens. A duration of 10 s has been applied to shot peen only the weld zone of AISI 1012 to AISI 316L welded specimen, which ensure full coverage of this region. **Figure 3.14** shows the peened region which applied between the two-brown lines for the welded joints. In the process, the distance between the nozzle and the rotating specimen was kept constant to control the uniform coverage of the specimen. **Figure 3.15** shows the shot peening samples manipulator, which is being used to change the peening angle. The major parameters of peening setup are listed in **Table 3-10**. The key parameter to characterize the effect of SP is the peening intensity, which was gauged using Almen-strip A (see **Figure 2.23**) by determining the deformation of peened strip, i.e. the arc height of the bent strip.

The rotary and orbital welded specimens were shot peened at a wide range of Almen intensities to determine the optimum intensity. The aim of optimization process was to obtain the highest enhancement of the surface layer properties, fatigue performance of the rotary and orbital friction welded joints at both as-welded (AW) and post-weld heat treated (PWHT) conditions.

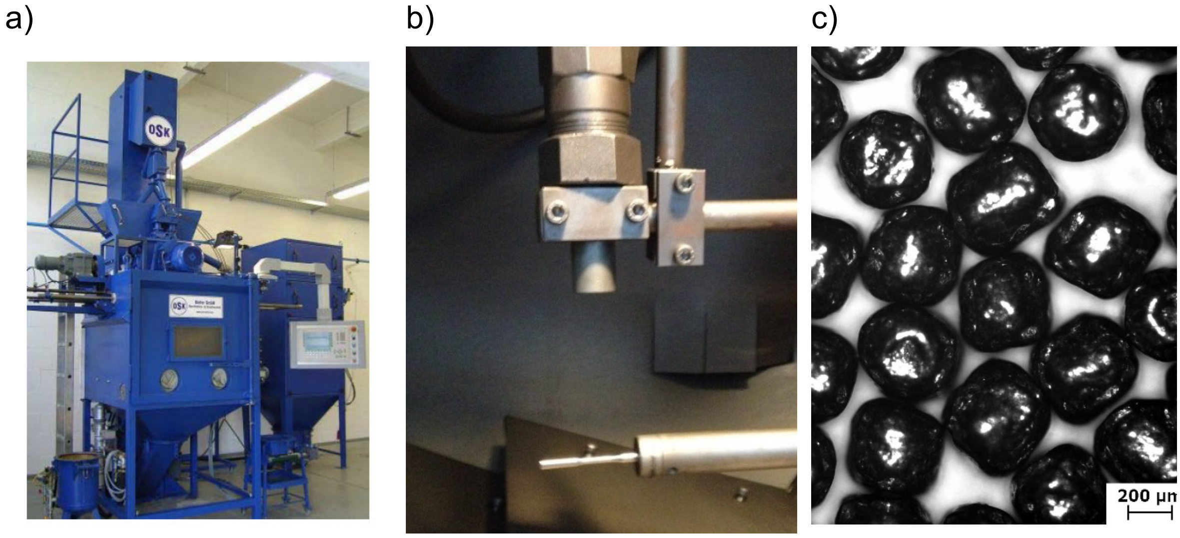

Figure 3.13 a) shot peening machine, b) peening process and c) peening media, spherical conditioned cut wire 14 (SCCW 14).

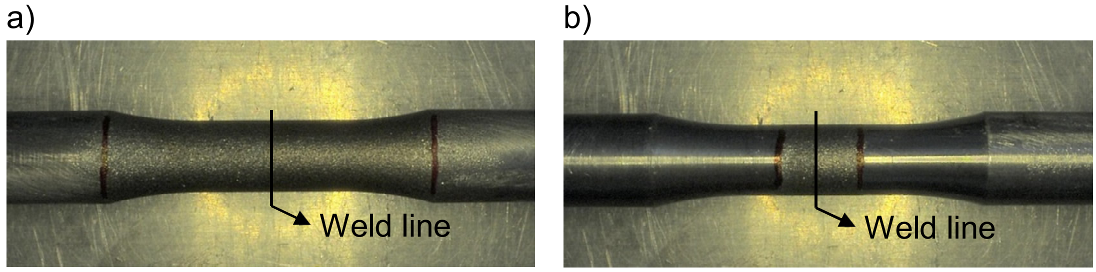

Figure 3.14 The peened region between the two-brown lines for the welded joints a) SP for whole specimen and b) SP for weld zone.

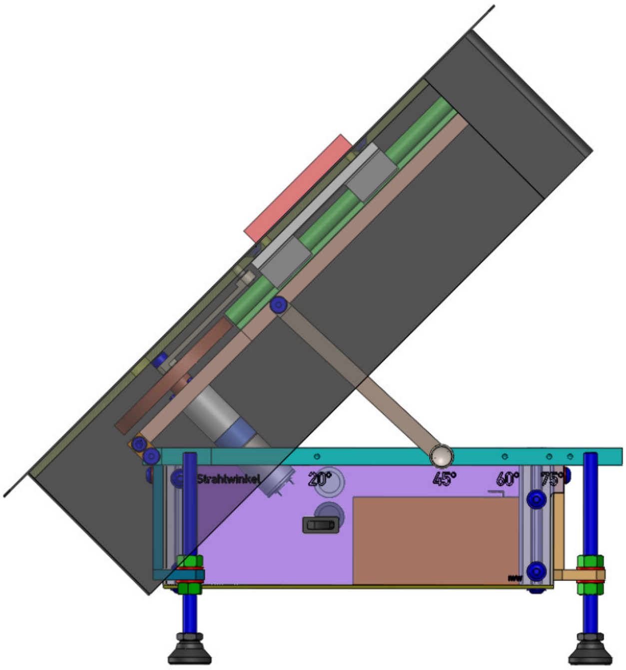

Figure 3.15 Shot peening samples manipulator.

Table 3-10 The applied shot peening parameters.

Peening media	SCCW 14
Distance between nozzle and specimen	90 mm
Specimen rotation	30 rpm
Peening angle	90° or 45°
Peening's time	10 to 25 s
Coverage	100 %
Peening pressure	2 - 7.5 bar
Almen Intensity	0.1 - 0.3 mmA

3.7.2. Roller-Burnishing (RB)

RB was performed by means of a conventional lathe using a hydrostatic tool with a hard metal roller (Ø 40 mm, r 2.5 mm) as shown in **Figure 3.16** with a constant feed rate of 0.17 mm/rev and a rotational speed of 150 rpm. To find out the process parameters for maximum fatigue life enhancements of the welded joints for both AW and PWHT conditions, a range of burnishing pressures (0.4 - 1.8 bar) were applied for roller-burnishing process. As in SP process, the RB process has been applied for the whole specimen and for the weld zone of the welded joints as shown in **Figure 3.17**.

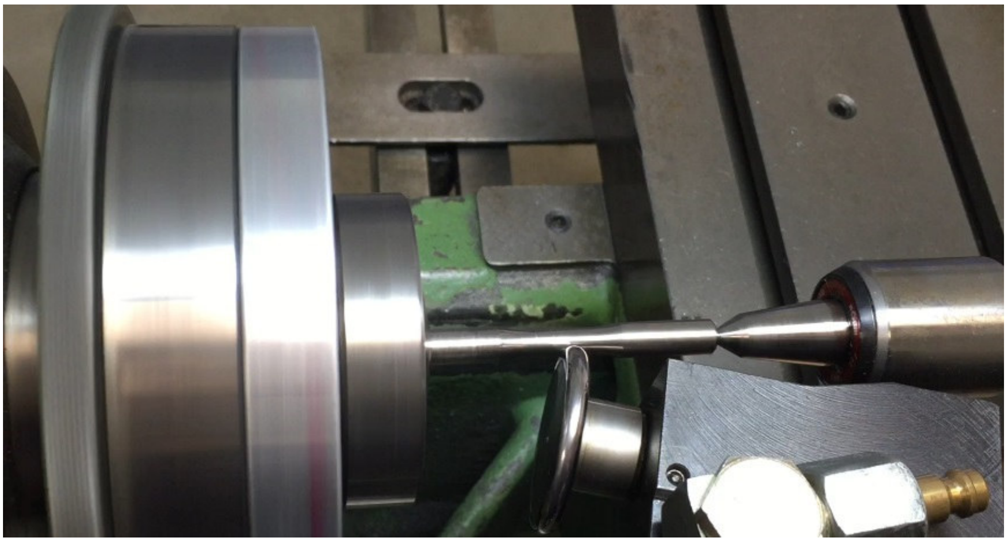

Figure 3.16 Roller burnishing process.

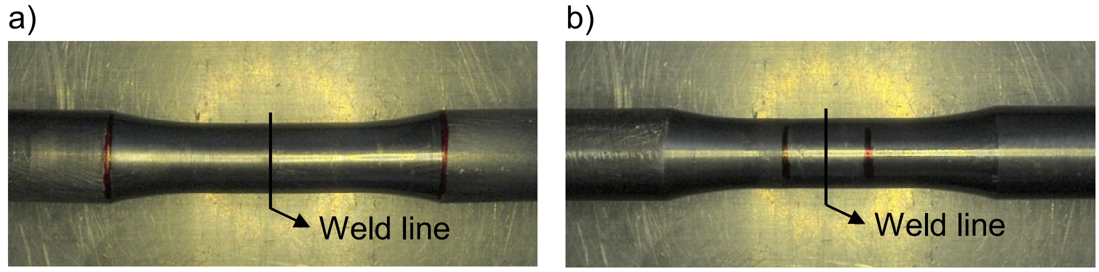

Figure 3.17 The burnished region between the two-red line for the welded joints a) RB for whole specimen and b) RB for weld zone.

3.8. Evaluation of the Mechanical Surface Treatments

3.8.1. Fatigue Performance

Rotating bending fatigue test was performed using Mayes-GTG, Rolls Royce fatigue machine in rotating beam loading (R=−1) on smoothly shaped specimens having minimum gage diameter of 4 mm for Ti-weld and 6 mm for AISI 316L to AISI 1012-weld.as shown in **Figure 3.18**. Tests were conducted at a frequency of 50 Hz. The fatigue specimens were electropolished (EP) or mechanically-polished (MP) to remove any machining effect that could mask the results. All the welded specimens were first ground off about 100 µm by a series of SiC papers with grits ranging from 500 up to 2400. Regarding the Ti-6242 and CP-Ti specimens, they were subsequently electrolytically polished for another 100 µm in a mixed solution of a 920-ml electrolyte solution is used, consisting of 500 ml methanol, 360 ml 1-Butanol and 60 ml perchloric acid. On the other hand, the welded specimens of AISI 316L and AISI 1012 were mechanically-polished. The EP or MP condition is taken as the reference.

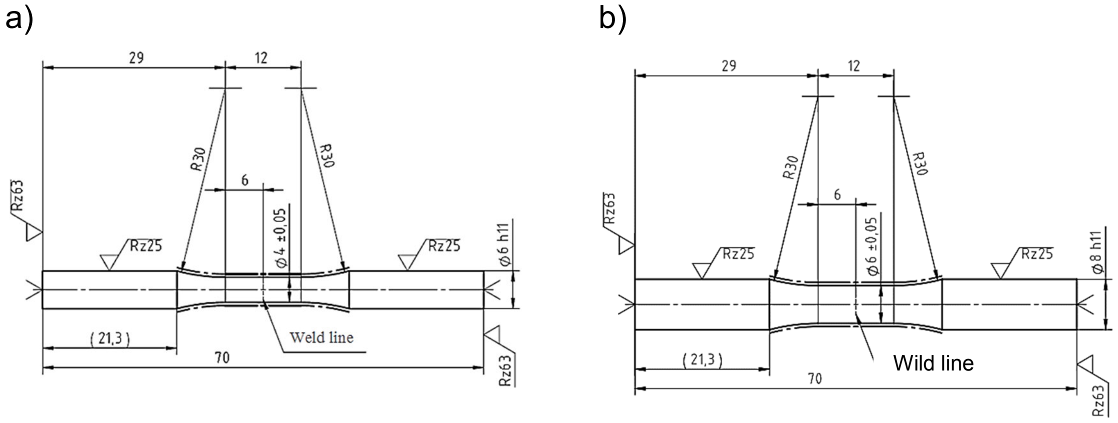

Figure 3.18 Fatigue specimen (dimensions in mm) for a) Ti-weld and b) AISI 316L to AISI 1012-weld.

3.8.2. Surface Roughness

Profile roughness refers to the fine irregularities in the surface texture, usually including those resulting from production processes such as marks caused by machining or surface treatments. As the specimen surface finish plays an important role in fatigue crack initiation, it is very necessary to characterize the difference in roughness resulting from specific surface treatments. In this study, the surface roughness of the various conditions was determined by means of an electronic contact (stylus) profilometer instrument (Perpethometer). The average absolute value of the five highest peaks and the five lowest valleys over the evaluation length (Rz) was reported (DIN 4768). The average of three roughness measurements was taken. The parameter (Rz) was used rather than the average roughness (Ra) comparing all the peaks and valleys to the mean line, since quite different surfaces could have the same Ra and consequently perform in different manner.

3.8.3. Impact Toughness

Impact toughness test was carried out to determine the absorbed energy that was needed for fracture on miniaturized Charpy V-notch (MCVN) specimens according to ASTM E2248-13. **Figure 3.19** shows the dimension of MCVN specimens. The correlation between full-size and MCVN absorbed energies is shown in **Figure 3.20** [132]. An instrumented small-scale impact tester has been used with an impact speed of 3.8 m/s and anvil span of 22 mm. Specimens were sectioned from the weldment with specimen axis transverse to the weld joint then polished on one lateral side and etched before machining the V-notch for the precise alignment of the weld line in the center of V-notch. All tests were performed at both as-welded (AW) and post-weld heat treated (PWHT) conditions at room temperature in air. In addition, the effect of mechanical surface treatment on the impact toughness of the AW and PWHT joints has investigated. Fracture surfaces were investigated by SEM. **Figure 3.21** shows some impact toughness specimens after fracture.

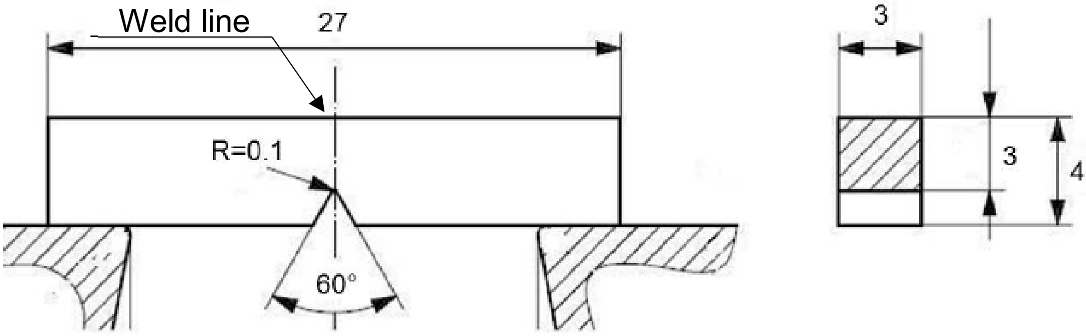

Figure 3.19 MCVN specimen (dimensions in mm).

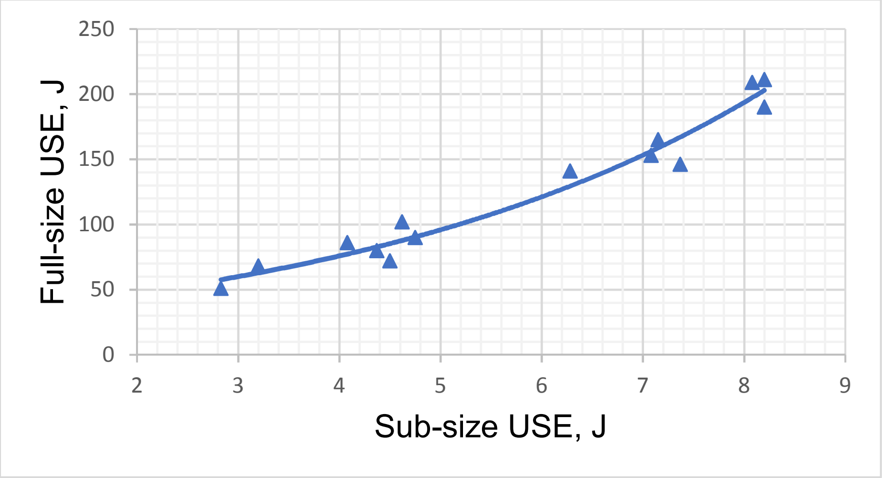

Figure 3.20 Exponential correlation of upper-shelf energies (USE) of full-size and sub-size (MCVN) specimens [132].

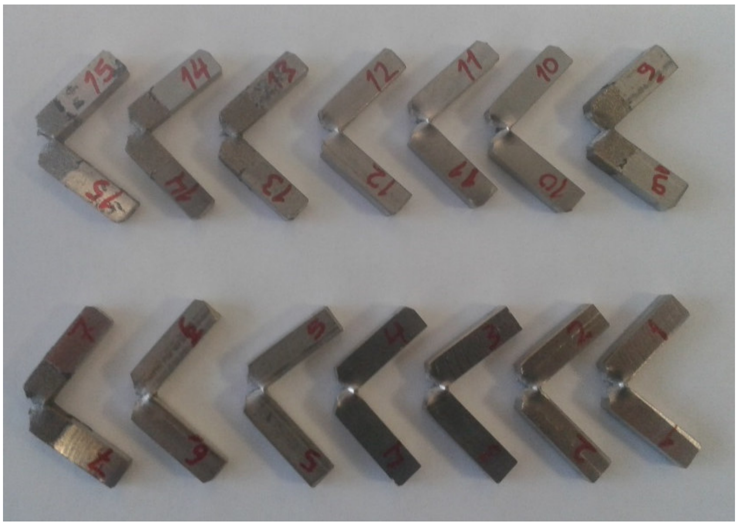

Figure 3.21 Impact toughness specimens after fracture.

3.8.4. Fracture surface Topography

All the fatigue and toughness specimens were first examined after fracture using digital camera for preliminary selection. Specimens with specific features were selected for profound investigation using scanning electron microscopy (SEM) to analyze the failure modes of the fatigue and Charpy fractures.

SEM is a type of electron microscope that generates images of specimens by scanning them with a focused beam of electrons. As incident electrons interact with atoms of the specimen surface, various signals could be produced, including secondary electrons, back-scattered electrons, characteristic X-rays, transmitted electrons. It is rare to detect all the possible signals within a single machine. The signals of characteristic X-ray are also widely applied within SEM, as energy-dispersive X-ray spectroscopy (EDX). The incident beam may excite and eject an electron in an inner shell (low-energy shell), leaving an electron hole. An electron from an outer, higher-energy shell then fills the vacancy, while with emitting X-ray with wave length characteristic of different atomic structures. By means of this the element composition of the specimens could be measured. Both secondary electrons and EDX detection were employed in this study to reveal the local microstructures and element constitutions.

3.8.5. Residual Stresses (RS)

To fully characterize the residual stress levels through orbital friction welding, heat treating (stress relieves) and mechanical surface treatment processes on the Ti-6242 welded joints, two types of residual stress distributions were carried out. Surface residual stress distribution was conducted by using Proto-LXRD (laboratory residual stress measurement system) at Curtiss-Wright Surface Technologies (CWST) in the USA. The measurement relies on Bragg diffraction and the lattice strain is measured corresponding to a strain-free lattice parameter d_0 [133]. In this method, the lattice spacing of the material is utilized efficiently as an atomic strain gauge. When the material is in tension, the d-spacing increases and, when under compression the d-spacing decreases. Stresses can be determined from the measured d-spacings. X-rays diffract from crystalline materials at known angles 2θ according to Bragg's Law: $n\lambda = 2d\sin\theta$, where: n = order of diffraction, λ = wavelength of the x-ray beam, d = distance between lattice planes inside the material and θ = angle of the diffracted beam The surface measurements were evaluated on a line across the weld center (Point 0) on the surface of the specimens with a nominal distance of 2.5 mm right and left the weld center as shown in **Figure 3.22-a)**. **Figure 3.9** shows the cutting surface to evaluate the measured stress. LXRD used parameters are listed in **Table 3-11**. Due to the small sample size and the 2-mm spot size, only 5 points have been evaluated. The components of X-ray diffractometer are shown schematically in **Figure 3.23**.

The depth profile RS were calculated from remaining strains using the incremental hole-drilling method (IHD). The strain gauge rosettes produced by Company Vishay were pasted to the surface as shown in **Figure 3.22-b)**. A hole in the vicinity of the gauges has been drilled using an oscillating drill with 0.9 mm diameter driven by an air turbine with a rotational speed of 200,000 rpm. The induced strains at incremental depth were measured in the surface layers at drilled depths of about every 20 µm. The measurement procedures standardized in ASTM E837–01 could be briefly summarized as the following steps:

1- A strain gage rosette is installed on the as-welded (AW), post-weld heat treated (PWHT), as-welded + shot peening (AW SP), as-welded + roller burnishing (AW RB), PWHT SP and PWHT RB. The gage grids are wired and connected to a multi-channel static strain indicator.
2- A precise drilling set is adjusted perpendicular to the specimen surface and accurately centered over a drilling target on the rosette.

3- After calibration and zero-balancing the gage response, a small shallow hole with a diameter of 0.9 mm is drilled through the geometrical center of the rosette into the material. The drilling process proceeds with a depth increment of 0.02 mm, reaching 0.6 mm beneath the surface.
4- Response of the relaxed strains at each depth of increment was acquired.
5- According to special data-reduction relationships, the principal residual stress and the angular orientation are calculated from the measured strains.

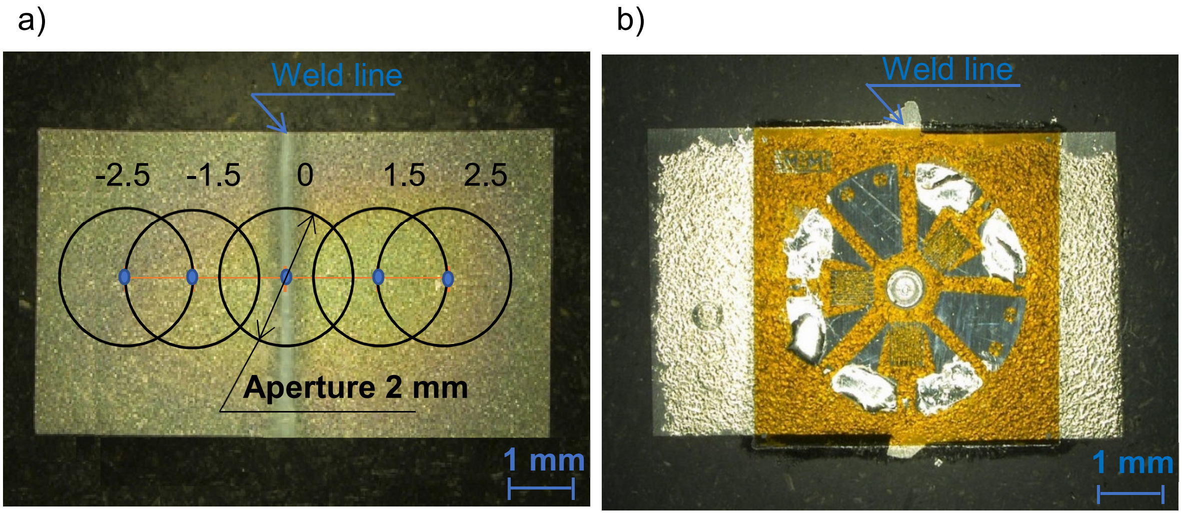

Figure 3.22 a) stress evaluation line on proto-LXRD with representation of x-ray spot size and locations on the friction welded joints and b) Strain gauge rosette arrangement for determining residual stress using IHD after shot peening.

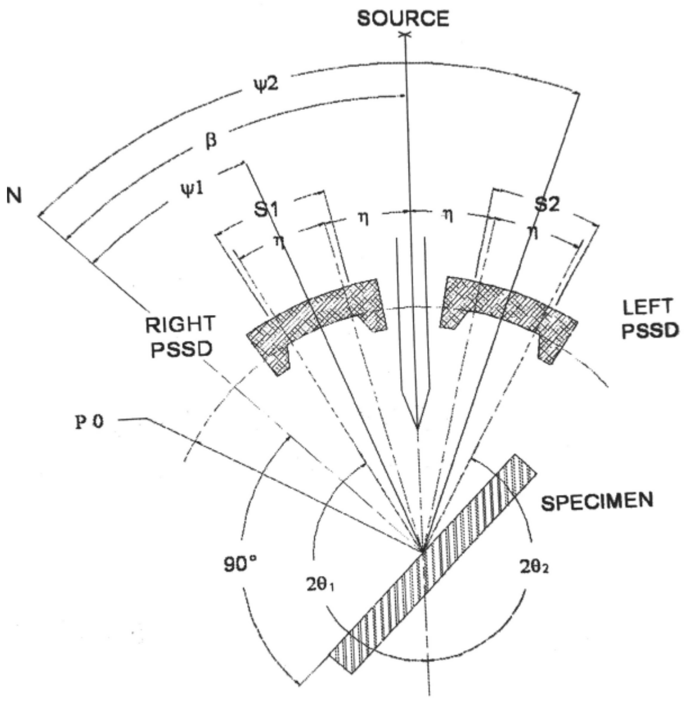

Figure 3.23 Schematic layout of energy-dispersive (laboratory) X-ray diffractometer at Curtiss-Wright Surface Technologies (CWST).

Table 3-11 LXRD parameters used for the stress measurement on the orbital welded joints.

Item	Condition
Equipment	Proto LXRD
Target	Cu Tube (λ = 1.541 Å)
Bragg Angle, 2θ	140°
Aperture (spot size)	2 mm, Ni filter
Collection Time	4s
Oscillation, °	3
Psi (ψ) Tilts	15 tilts
Tilts, ° (±)	(0, 30.00, 25.25, 19.50, 15.59, 10.35, 4.48, 2.80)

4. Characterization of AISI 1012 to AISI 316L Weld Joints

In this chapter, the effect of welding parameters on the performance characteristics of AISI 316L - AISI 1012 friction welded joints are presented and accordingly their optimized welding parameters are determined. A plan of experiments was designed based on DoE method using Minitab 17. The output variables are the tensile strength and metal loss of the weld. These output variables were determined experimentally according to the input variables, which are the friction pressure (P1), friction time (t1), and rotational speed (rpm). Forging pressure (P2) and forging time (t2) were set to be constant throughout this study. The optimization objectives are achieving of maximum tensile strength and minimum burn off length (metal loss). By statistical analysis, an optimal level of combination of processing parameters were achieved, which were validated through conducting an experimental study at the same previously found parameters. The results were analyzed and interpreted in terms of estimated effects, analysis of variance (ANOVA), normal probability plots, and main effects plots. Based on these analyses, the significant factors were determined, and predictive models were formulated.

Furthermore, the evaluation of the mechanical and metallurgical characterization of the dissimilar joints under as-welded AW state and post-weld heat treated PWHT state were presented and compared to analyze the effect of AW and PWHT on the microstructures, element diffusion and mechanical properties of the friction welded joint, and their influence on the fracture mechanism and mechanical properties of the AW and PWHT joints before and after applying the mechanical surface treatment by either shot peeing (SP) or roller burnishing (RB).

4.1. Process Parameters Optimization

Based on the preliminary welding trials, two levels were considered for each of the process parameters. Working range of each parameter was decided only based on visual examination and a macroscopic evaluation. **Table 4-1** shows the range of parameter values for low and high-level settings for each parameter (factor), which were coded as -1 and +1, respectively. The forging pressure and the forging time were set to be constant throughout the study at 3.5 bar and 2 s, respectively. That’s because the forging pressure and forging time exhibited insignificant influence on the properties of the joints by preliminary experiments. Data analysis was conducted to identify the significant parameters that affect the tensile strength and burn off length between AISI 316L and AISI 1012. The statistical significance of each parameter and the two-level interaction effects to the output responses were then evaluated using the Minitab software at 5% significance level.

A full factorial design of 2^3 with three replicates was conducted, which means that twenty-four treatment combinations should be carried out. The design matrix and results with three parameters (rotational speed, friction pressure P1 and friction time t1) and two responses (tensile strength of the weld joints UTS and burn off length) are summarized in **Table 4-2**. The experimental sequence (Std Order) was randomized to minimize the unexpected variability in the observed response. The significant effect of each parameter was evaluated by a normal probability plot of standardized effect at 5% significance level as shown in **Figure 4.1-a)** and **Figure 4.1-b)** for the ultimate tensile strength of the weld joints (UTS) and burn off length, respectively. It is clear from **Figure 4.1-a)** that the main effects such as the friction pressure A, as well as the interaction effect of (friction pressure A x rotational speed C), (friction pressure A x friction time B) and (friction time B x rotational speed C) are the influential parameters for the development of the ultimate tensile strength of the weld joints. On the other hand, it is obvious in **Figure 4.1-b)** that the main effects such as the friction time B, as well as the interaction effects of (friction pressure A x friction time B) are the influential parameters for the development of burn off length.

The main effects of friction pressure, friction time and rotational speed on the UTS and burn of length are shown in **Figure 4.2-a)** and **Figure 4.2-b)**, respectively. According to these figures, it could be concluded that to obtain maximum UTS, the friction pressure should be set at the high level, friction time and rotational speed should be set at low levels. The increase in tensile strength can be attributed to the increase of both of heat input and plastic deformation occurring at the interface of the joined steels. While, the main factors affecting the burn off length (metal loss) are the rotational speed and frictional time, which should be set at low levels to minimize the metal loss of the welded joints. **Figure 4.3** shows the interactions plot between all factors and UTS and burn off length. It was observed that all tensile samples failed in the area adjacent to the HAZ on the AISI 1012 side.

Table 4-1 Input process parameters and their levels.

	symbols	units	Level	
			-1	+1
Friction pressure, P1	A	bar	1.5	3
Friction time, t1	B	s	1	3
Rotational speed, rpm	C	rpm	12000	16000

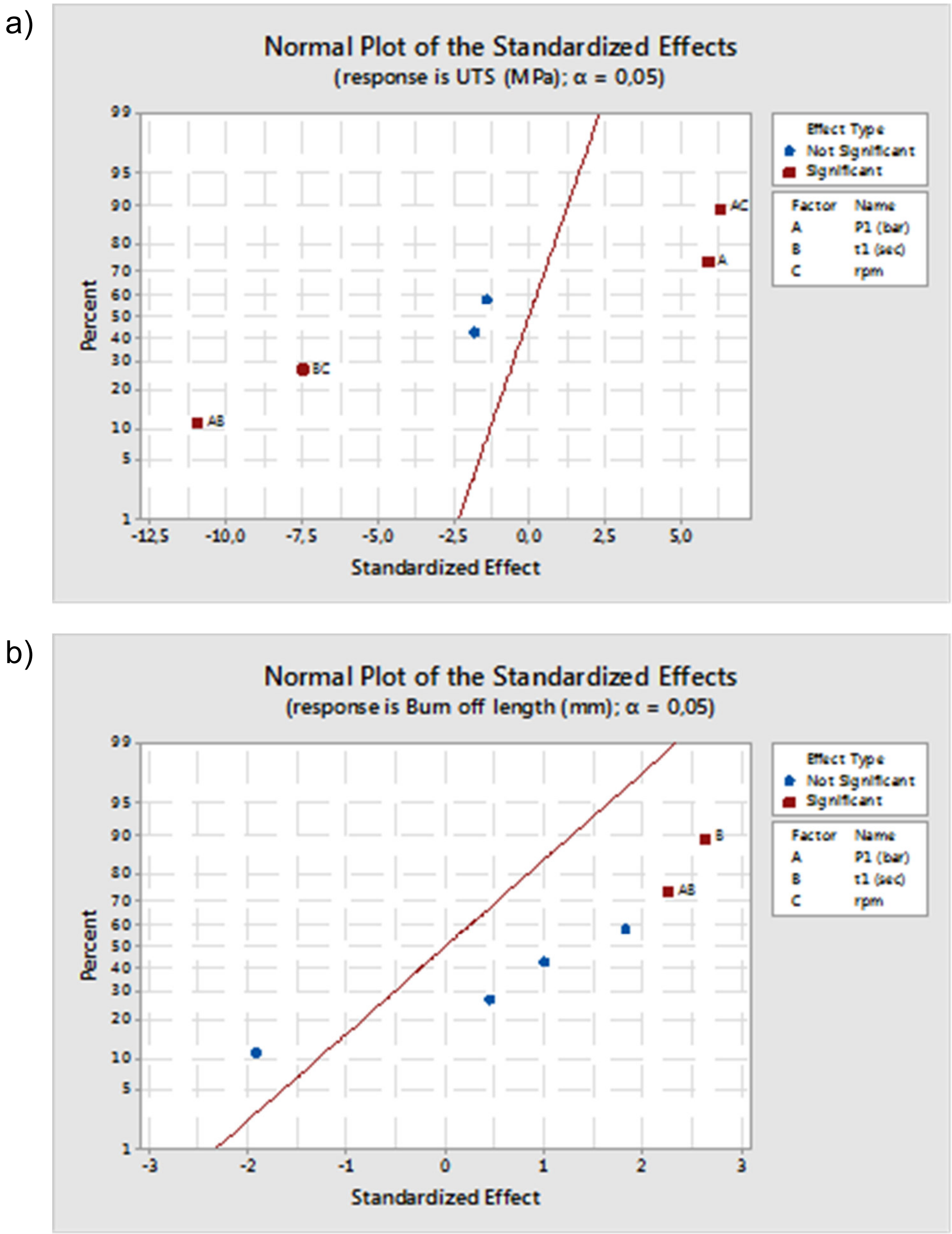

Figure 4.1 Normal probability plot of standardized effects for a) tensile strength of the weld joints UTS (MPa) and b) burn off length (mm).

Table 4-2 The DoE matrix and corresponding results of the full factorial design of 2^3 with three replicates.

Input process variables	Std Order	Run Order	P1, bar	t1, s	Rotational speed, rpm		Experimental results	Burn off length, mm	UTS, MPa
	3	1	1.5	3	12000			3.00	623
	21	2	1.5	1	16000			4.00	595
	5	3	1.5	1	16000			3.80	588
	4	4	3	3	12000			3.25	605
	1	5	1.5	1	12000			2.15	599
	23	6	1.5	3	16000			3.20	593
	17	7	1.5	1	12000			2.05	593
	10	8	3	1	12000			3.20	610
	8	9	3	3	16000			4.20	599
	11	10	1.5	3	12000			2.85	615
	7	11	1.5	3	16000	➔		3.10	595
	15	12	1.5	3	16000			3.30	599
	18	13	3	1	12000			3.35	615
	16	14	3	3	16000			5.00	600
	22	15	3	1	16000			1.65	631
	19	16	1.5	3	12000			3.10	626
	6	17	3	1	16000			1.85	627
	12	18	3	3	12000			3.10	601
	9	19	1.5	1	12000			1.85	588
	20	20	3	3	12000			3.15	600
	24	21	3	3	16000			4.50	596
	13	22	1.5	1	16000			4.05	598
	14	23	3	1	16000			1.70	635
	2	24	3	1	12000			3.05	609

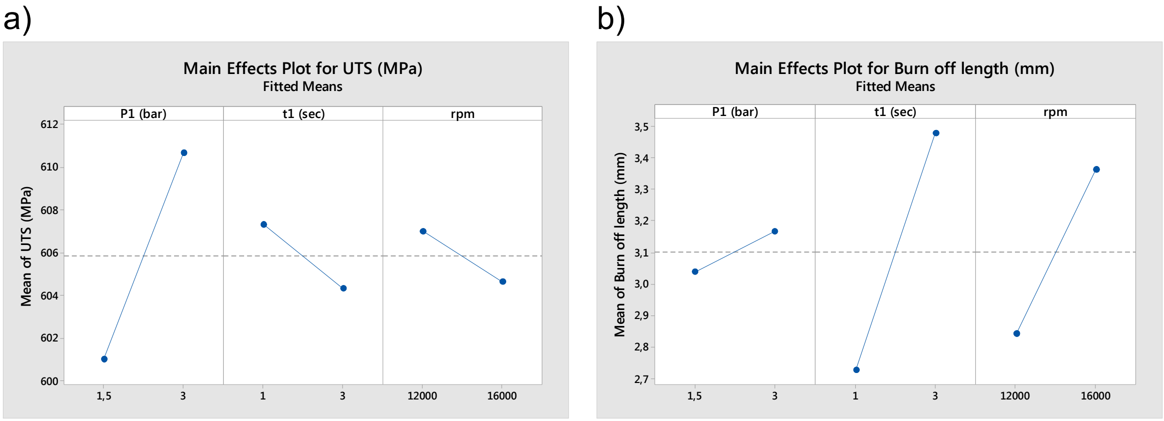

Figure 4.2 Main effect plot for a) tensile strength of the weld joints UTS, MPa and b) burn off length, mm.

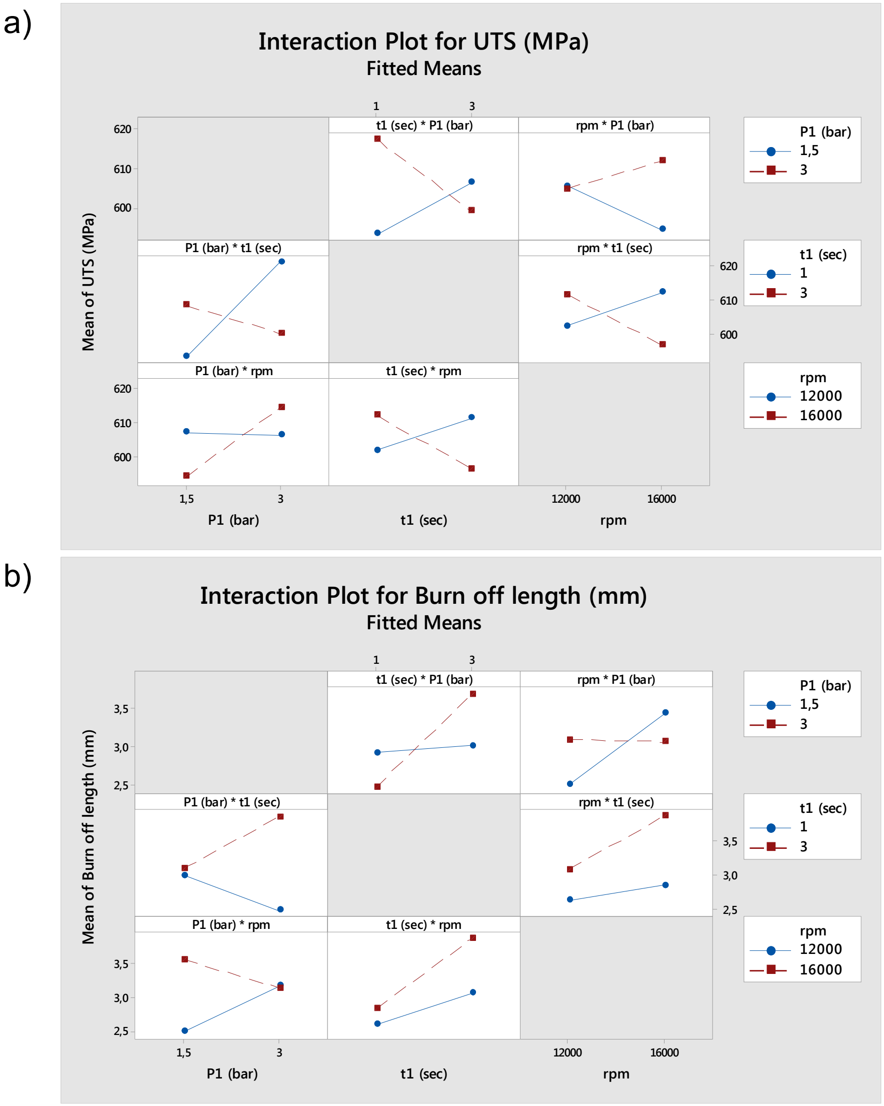

Figure 4.3 Interaction effects of parameters for, a) tensile strength of the weld joints UTS, MPa and b) burn off length, mm.

4.1.1. Final Regression Models

From the ANOVA results, the predicted first-order models were formulated. The correlation between the factors is determined from the linear regression equations (4.1) and (4.2). The normal probability plots of the residuals versus the predicted response for UTS and burn off length are plotted in **Figure 4.4-a)** and **Figure 4.4-b)**, respectively. Based on that, it is revealing that the data closely follows the straight line. That is the data obeying the normal distribution law, which is observed when the p value is greater than the level of significance and it implies that the models proposed are satisfactory.

$$UTS = 605.8 + 4.8 * \text{Friction pressure} - 1.5 * \text{Friction time} - 1.2 * \text{Rotational speed} - 9.0 * \text{Friction pressure} * \text{Friction time} + 5.2 * \text{Friction pressure} * \text{Rotational speed} - 6.2 * \text{Friction time} * \text{Rotational speed} \tag{4.1}$$

$$\text{Burn off length} = 3.10 + 0.06 * \text{Friction pressure} + 0.38 * \text{Friction time} + 0.26 \text{ Rotational speed} + 0.32 * \text{Friction pressure} * \text{Friction time} - 0.28 * \text{Friction pressure} * \text{Rotational speed} + 0.14 * \text{Friction time} * \text{Rotational speed} \tag{4.2}$$

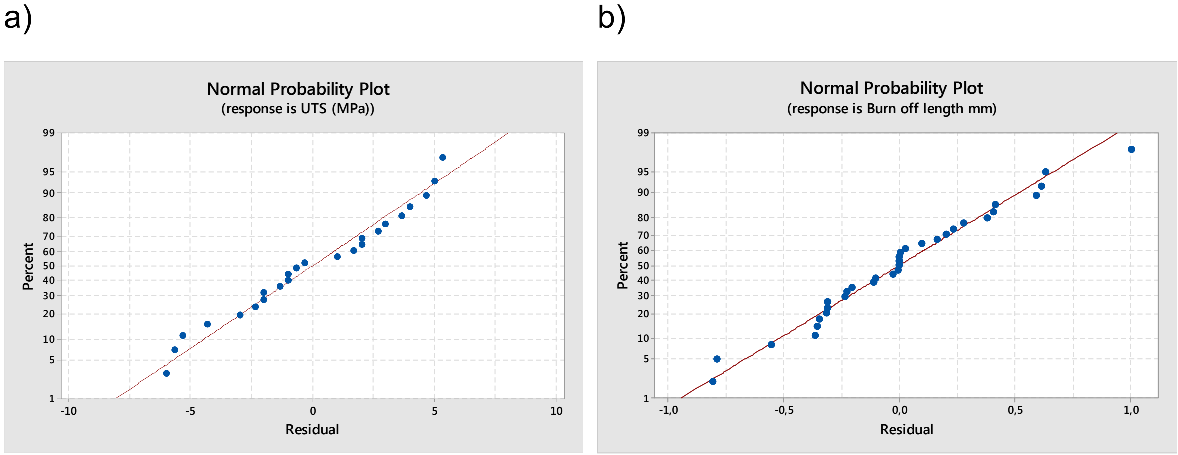

Figure 4.4 Normal probability plot of standardized residuals for a) tensile strength of the weld joints UTS, MPa and b) burn off length, mm.

4.1.2. Determination of Optimum Parameters

An optimization study is conducted to determine the optimal parameters for simultaneous maximization of UTS and minimization of the metal loss (burn off length). In fact, once the model has been developed and checked for adequacy, the optimization criteria can be set to find the optimum conditions. Response optimizer was used to identify the combination of input variables settings that jointly optimize a set of responses (UTS and burn of length). The proposed optimum parameters were, friction pressure at 3 bars, friction time of 1 s and rotational speed of 16000 rpm which give a composite desirability of 0.86.

Validation experiment has been conducted at the previously-mentioned parameters as a final step to check the model validity. The values obtained experimentally were compared to the predicted values from the developed model. The process parameters used for confirmation tests and the results are illustrated in **Table 4-3**. The fracture locations were outside the weld zone on the AISI 1012 side as shown in **Figure 4.5** (the reasons are discussed in **section 4.4.1**). From this comparison, it can be stated that model equations (4.1) and (4.2) correlating the process parameters to the output responses are reliable with reasonable degrees of approximation.

Table 4-3 Results of the validation experiment.

Welding Parameters					Responses					
					Burn of length, mm			UTS, MPa		
P1	P2	t1	t2	rpm	Exp.	Model	Error	Exp.	Model	Error
3	3.5	1	2	16000	2.1	2.306	0.206 (9.8 %)	625	631.33	6.33 (1 %)

Figure 4.5 The fracture location after tensile test.

4.2. Weld Joint Characterization

4.2.1. Macro- and Microscopic Characterization

The different thermal and physical properties of the dissimilarly-welded materials (heat capacity, thermal conductivity, relation between hardness and temperature) result generally in an asymmetrical deformation [135]. Austenitic stainless steel AISI 316L has lower thermal conductivity and greater hardness at higher temperatures compared to AISI 1012. For this reason, austenitic stainless steel does not undergo extensive deformation while carbon steel specimen undergoes extensive deformation.

Visual examination of the welded specimens showed uniform and good welded joints. The flash obtained was also symmetric and even which indicates plastic deformation on both carbon steel and stainless steel side. The flash formed on the stainless steel side is smaller than that on the carbon steel side. The more formation of upset collar (flash) on the carbon steel side is due to low strength of AISI 1012. **Figure 4.6** shows the macrograph of the welded specimen under optimum welding conditions.

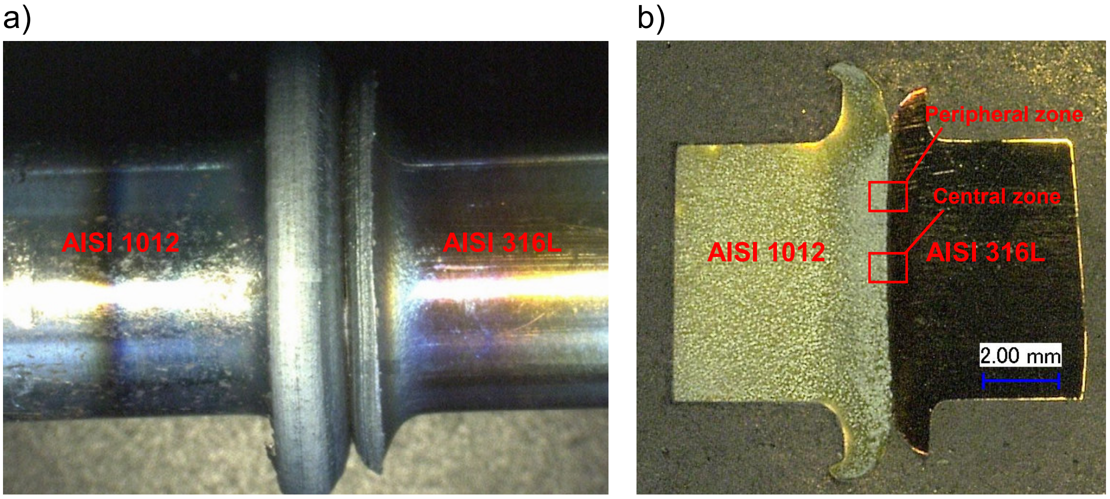

Figure 4.6 The macrograph of the welded specimen under optimum welding conditions a) whole weld specimen and b) cross sectional view.

Different characteristic zones, such as-weld interface, thermo-mechanically affected zone (TMAZ) and heat affected zone (HAZ) on both sides are analyzed in detail on etched cross-section of the joint. The microstructure variations of different zones on 1012 carbon steel side and 316L stainless steel side are discussed in section 4.2.1.1 and **4.2.1.2**, respectively.

4.2.1.1. Microstructure on AISI 1012 Carbon Steel Side

Figure 4.7-a) illustrates typical macrographs in various zones geometry of the weld across the interface. The width of these regions is illustrated in **Figure 4.7-b)**. Zone 1, 2 and 3 represent the heat affected zone (HAZ) of AISI 1012 weld side. The microstructure of friction-welded carbon steel side revealed four different zones across the specimens, which can be identified as severe plastic deformed zone (SPDZ) (Zone 1), transformed and recrystallized fully plasticized deformed zone (FPDZ) (Zone 2), partially deformed zone (PDZ) (Zone 3), and parent metal (PM) (Zone 4) [136-139].

The most microstructural changes took place in the SPDZ (Zone 1). Ji et al. and Hong Ma et al. [140, 145] tested the friction welding thermal cycle in the central zone of the final weld interface of carbon steel to stainless steel dissimilar metals joint. They reported that the peak temperature at the weld interface can reach up to 1300 °C which is high enough for the recrystallization of the metal. Thus, the process temperature in SPDZ is high enough to austenitize and coarsen the grains on the AISI 1012 side, subsequently, the relatively high cooling rate results in the coarse pearlite grains and less ferrite precipitating at pearlite grain boundaries. Moreover, some ferrites also exist in the Widmanstätten structure owing to the overheated

SPDZ near the weld interface, which means the microstructure is quite heterogeneous in SPDZ as shown in **Figure 4.8-a)**.

It is well known that pressure used to bring joint pair together by plastic deformation results in dynamic recrystallization leading to a grain refinement in fully plasticized deformed zone (FPDZ) [141] as shown in **Figure 4.8-b)**. The lower temperature reached in zone 3 (PDZ) leads to the fact that the ferrite content is higher than that in any other zone. Moreover, the amount of plastic deformation is lower than those appeared in zone 1 and 2. Thus, the microstructure becomes coarser (**Figure 4.8-c)**) because of the associated reduction in strain and strain rate [7]. **Figure 4.8-d)** shows the microstructure in zone 4 which represent the parent AISI 1012 showing a matrix of proeutectoid ferrite grains (white etching constituent) and pearlite (dark etching constituent). This zone is an unaffected zone in which neither heating nor plastic deformation affect the microstructure of the material.

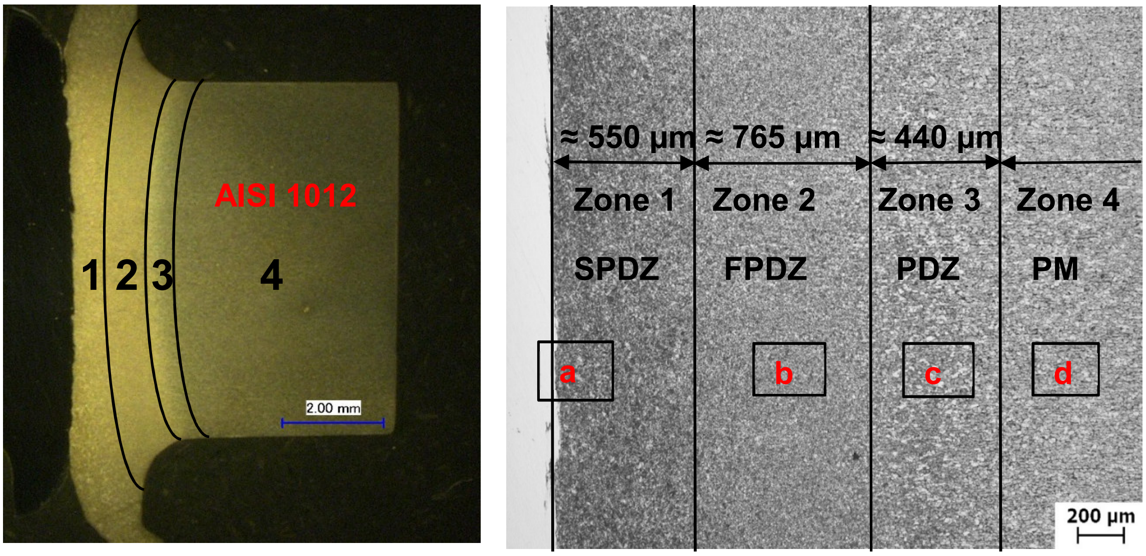

a)

b)

Figure 4.7 AISI 1012 weld side a) macrograph and b) micrograph of different weld zones.

In the peripheral zone, AISI 1012 and AISI 316L interlock with each other due to the severer plastic flow compared with the central zone, resulting in the mechanical mixed zone as shown in **Figure 4.9** [142].

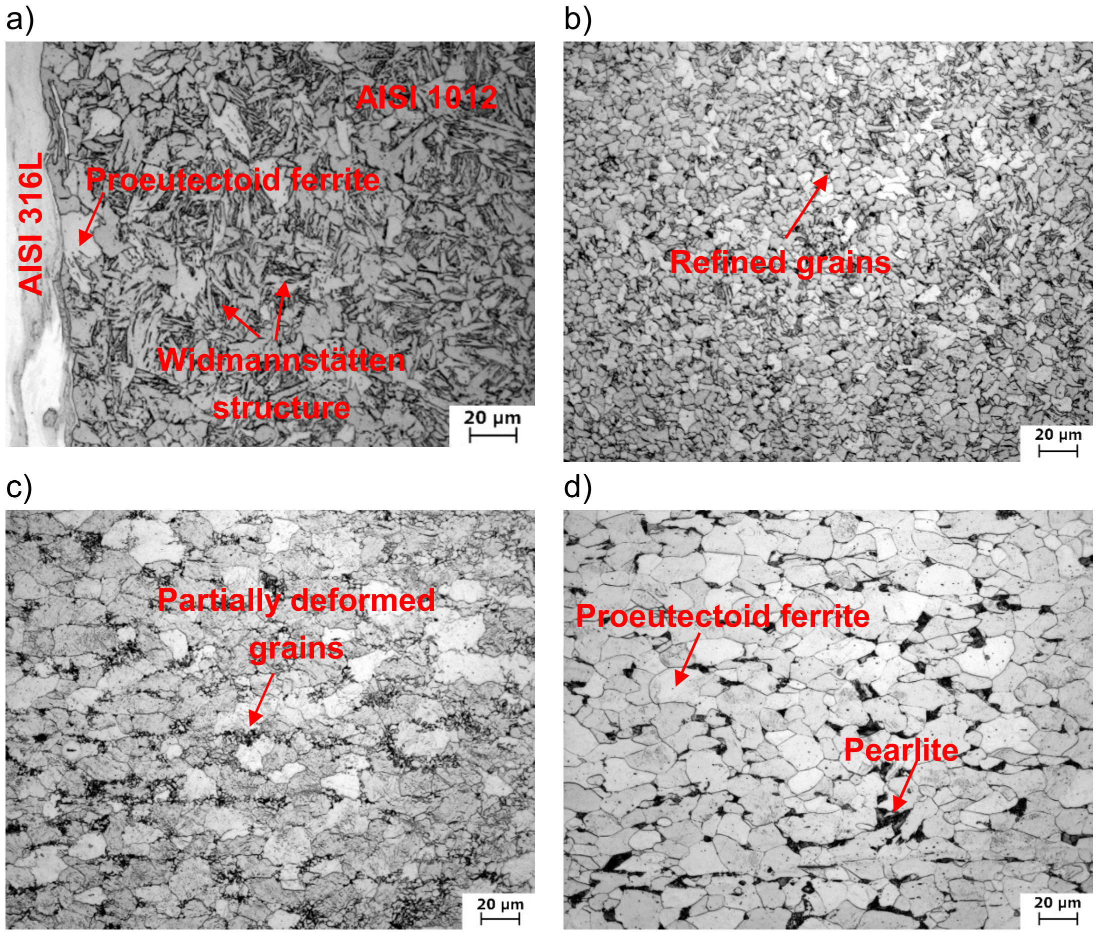

Figure 4.8 AISI 1012 weld side a) severe plastic deformed zone SPDZ, b) fully plasticized deformed zone FPDZ, c) partially deformed zone PDZ and d) parent metal PM.

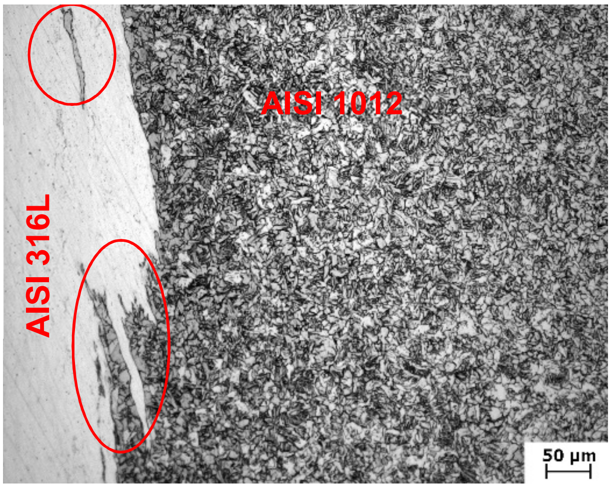

Figure 4.9 Typical microstructure of the peripheral zone.

4.2.1.2. Microstructure on AISI 316L Stainless Steel Side

The microstructure in different zones on AISI 316L side is shown in **Figure 4.10**. The microstructure of friction-welded AISI 316L side revealed different zones across the specimens that can be identified as, weld interface, partially deformed zone (PDZ), fully plasticized deformed zone (FPDZ), and parent metal (PM). In the central zone of the weld interface (shown in **Figure 4.11-a)**), the concurrent effects of frictional heating and severe plastic deformation result in the recrystallization of crushed austenite grains caused by mechanical friction with a significant grain refinement at the weld interface. Severer plastic flow and higher temperature in the peripheral zone lead to a more distinct recrystallization phenomenon shown in **Figure 4.11-b)**.

In PDZ, austenite grains under the effects of the plastic flow and high temperature are deformed slightly but a large amount of grain refinement had not taken place, and carbide also forms in austenite grains (**Figure 4.11-a)** and **Figure 4.11-b)**). No δ-ferrite is observed in PDZ near the weld interface. δ-ferrite behavior will be covered later in **section4.2.3.1**. The austenite grains in FPDZ on AISI 316L side just become finer than those in the parent material with lower formation of annealing twins as shown in **Figure 4.11-c)**, leading to the merging of austenite grains. The areas of grain refinement and deformation are, collectively, commonly termed the thermo-mechanically affected zone (TMAZ) [142]. Beyond the FPDZ the parent material microstructure appeared to be sustained as shown in **Figure 4.11-d)**.

The reasons why the PDZ comes before FPDZ in AISI 316L weld side is still an area of ongoing research. It is likely that the microstructures are produced as a result of a complex interaction among heat input, heat losses (due to conduction, convection and flash expulsion) and applied force.

Due to both of the great difference in chemical composition of the base metals (see **Table 3-1**) and the relatively high temperature during the welding process, the elements diffusion occurs inevitably. To evaluate the elements diffusion at the weld interface, the EDX line scanning is performed in the central zone of the joint, across the weld line as shown in **Figure 4.12-a)** and parallel to the weld line as shown in **Figure 4.12-b)**. The analysis of the records clearly indicates a diffusion of Cr and Ni through the interface from AISI 316L to AISI 1012. As a result of the diffusion, a gradual reduction of Cr in stainless steel while approaching the interface has been observed which causes the formation of δ-ferrite free zone (more details in **section 4.2.3.1**).

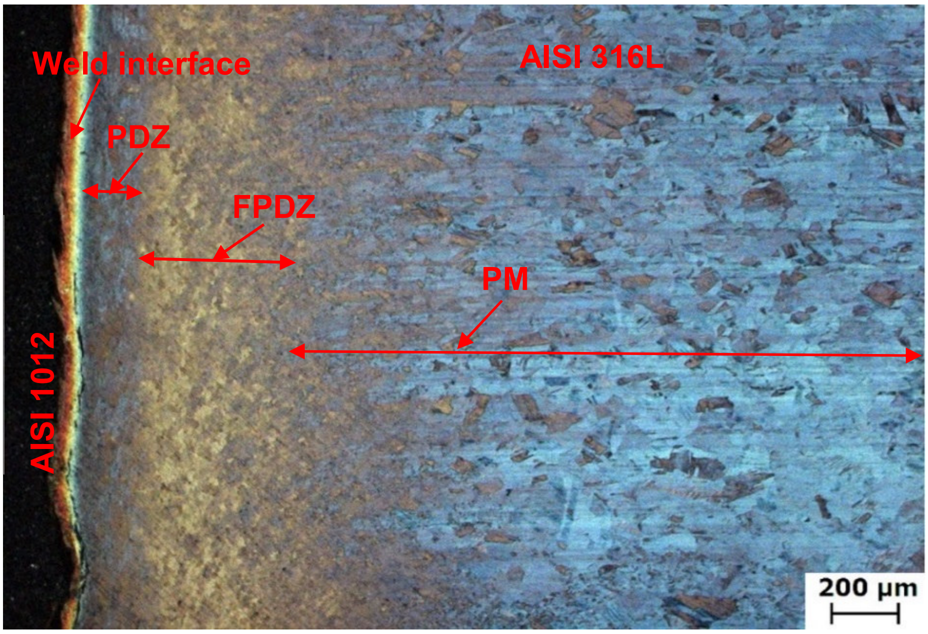

Figure 4.10 Typical microstructure in different zones on AISI 316L side of the joint revealed using color etchant Beraha II.

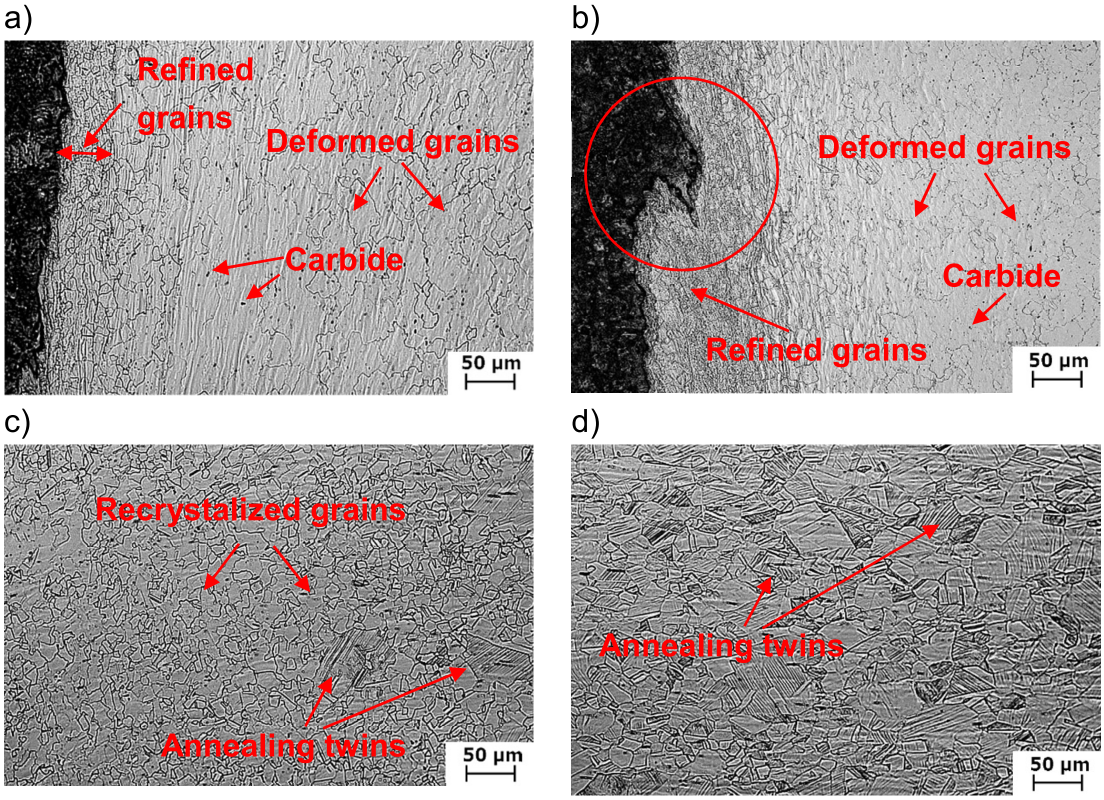

Figure 4.11 Typical microstructure in different zones on AISI 316L side of the joint, a) weld interface and PDZ of the central zone, b) weld interface and PDZ of the peripheral zone, c) FPDZ and d) parent metal PM (etched with V2A etchant)

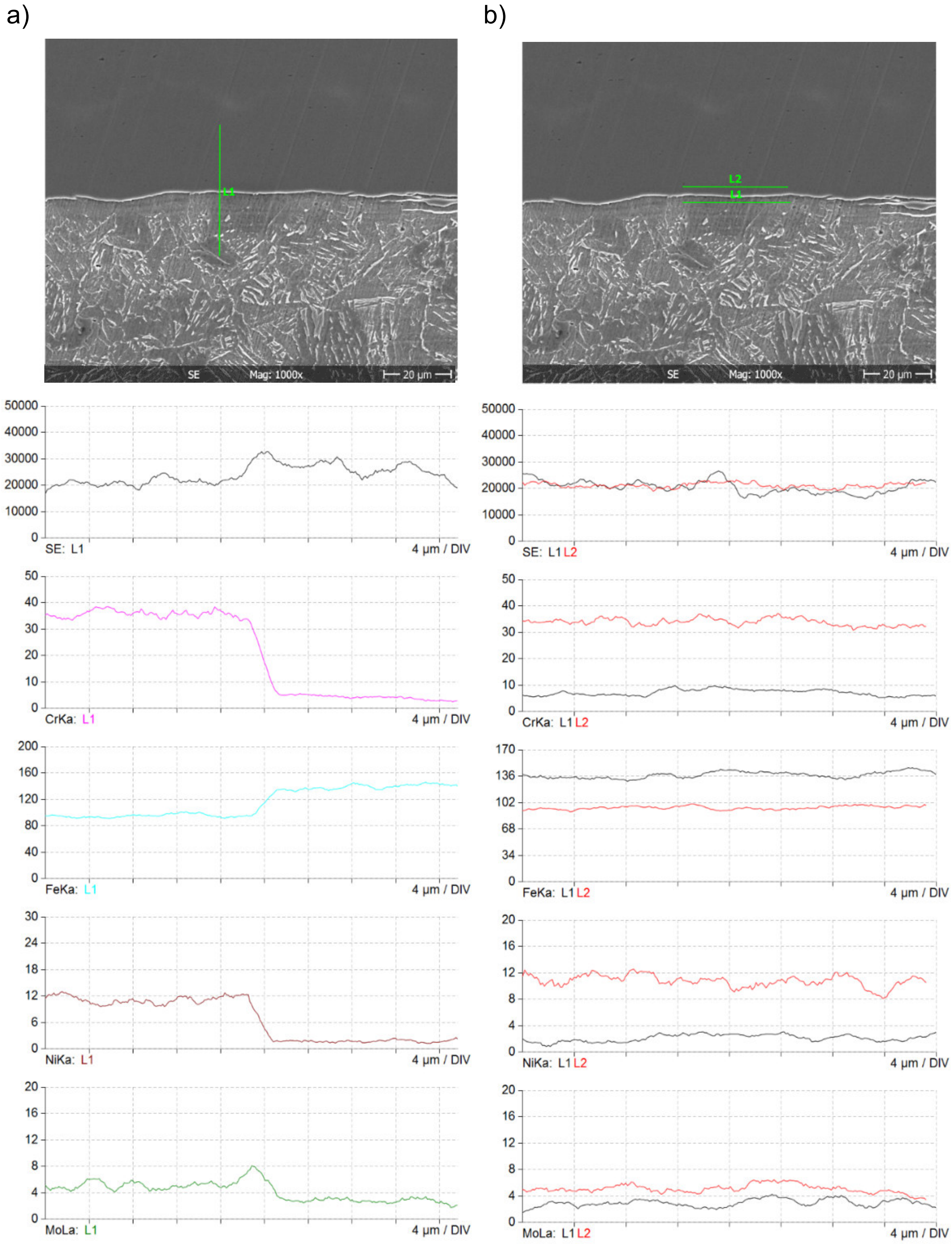

Figure 4.12 EDX line scanning in the central zone of the joint a) across the weld line and b) parallel to the weld line in both sides (L1 in AISI 1012 and L2 in AISI 316L).

Scanning electron microscopy (SEM) and energy dispersive X-ray (EDX) analysis were performed to investigate the elements at the welding interface in AISI 1012 side. SEM microstructure of interface region and EDX analysis results are given in **Figure 4.13**. The results confirm the diffusion of Cr and Ni through the interface from AISI 316L to AISI 1012. R. Winiczenko et al. [143] proved using EDX analysis that the carbon diffuses from ductile iron into stainless steel during friction welding. This had been proved and reported in **section 4.2.3.2** by using different etchant reagents.

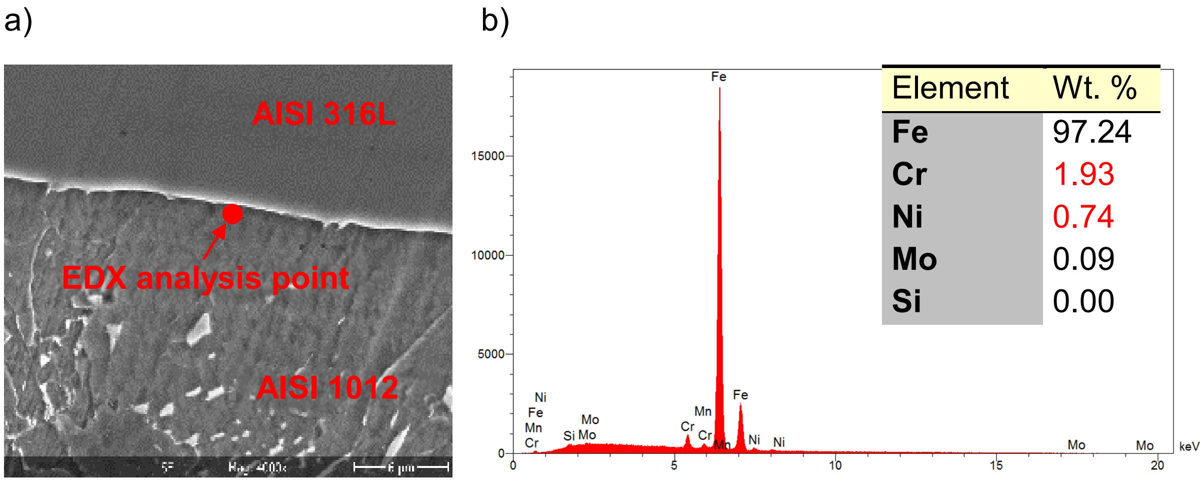

Element	Wt. %
Fe	97.24
Cr	1.93
Ni	0.74
Mo	0.09
Si	0.00

Figure 4.13 a) SEM microstructure of the interface region of friction welded AISI 316L- AISI 1012 joint. and b) EDX analysis result taken from AISI 1012 weld interface side represented to SEM image.

4.2.2. Post-Weld Heat Treatments

The post-weld heat treatment process was conducted after welding. Considering different annealing temperatures had great impact on the variation of the microstructure. Different PWHT temperatures (**Table 4-4**) were employed on the welded joint. The PWHTs were used to relieve most of the internal RS which are induced during the welding process. Additionally, the effect of combining thermal and mechanical treatment on the fatigue performance of the welded joints will be investigated later.

Table 4-4 Different PWHT conditions - AC: air cooled, WQ: water quenched.

Symbol	Post-weld heat treatment
A	900 °C/30 min. AC
B	1050 °C /30 min. AC
C	1050 °C /30 min. WQ + 885 °C /2h AC

4.2.2.1. Characterization of the Treated Materials

A comparison between the microstructure of the AISI 1012 in as received condition and at different heat treatment conditions is shown in **Figure 4.14**. The mechanical properties of the treated AISI 1012 and AISI 316L materials are listed in **Table 4-5**. It is clearly observed that the heat treatments A and C showed little effect on the ferrite grain size and have restored the microstructure of AISI 1012, which consists of a few pearlite plates dispersed among grains of blocky ferrite. After heat treatment B, an increase in the ferrite grain size has been observed and bainite grains can be seen in the space between the ferrite-pearlite structure as shown in **Figure 4.14-c)**. All heat treatment conditions have increased the ductility and decreased the strength compared to the as received AISI 1012. **Figure 4.14-d)** shows the laths martensitic microstructure of the intermediate stage of heat treatment C after water quenching.

Figure 4.15 shows the comparison between the microstructure of the AISI 316L in as received condition and at different heat treatment conditions after etching with LBI and BII reagents. After all heat treatments, an increase in the austenite grain size has been observed. Moreover, all heat treatment conditions have increased the ductility and decreased the strength compared to the as received AISI 316L.

Table 4-5 Mechanical properties of the treated materials.

	Heat treatment	UTS,MPa	YS, MPa	EL, %	RA, %	Hardness, HV10
AISI 1012	AR	664	624	16	62	216
	900 °C/30min AC	497	368	34	75	142
	1050 °C/30min AC	486	315	33	64	158
	1050 °C/30min WQ	987	815	12	46	358
	1050 °C/30min WQ +885 °C/2h AC	460	297	39	68	142
AISI 316L	AR	773	645	41	75	294
	900 °C/30min AC	750	530	58	75	199
	1050 °C/30min AC	643	350	69	81	152
	1050 °C/30min WQ	628	350	71	77	147
	1050 °C/30min WQ +885 °C/2h AC	631	357	70	72	149

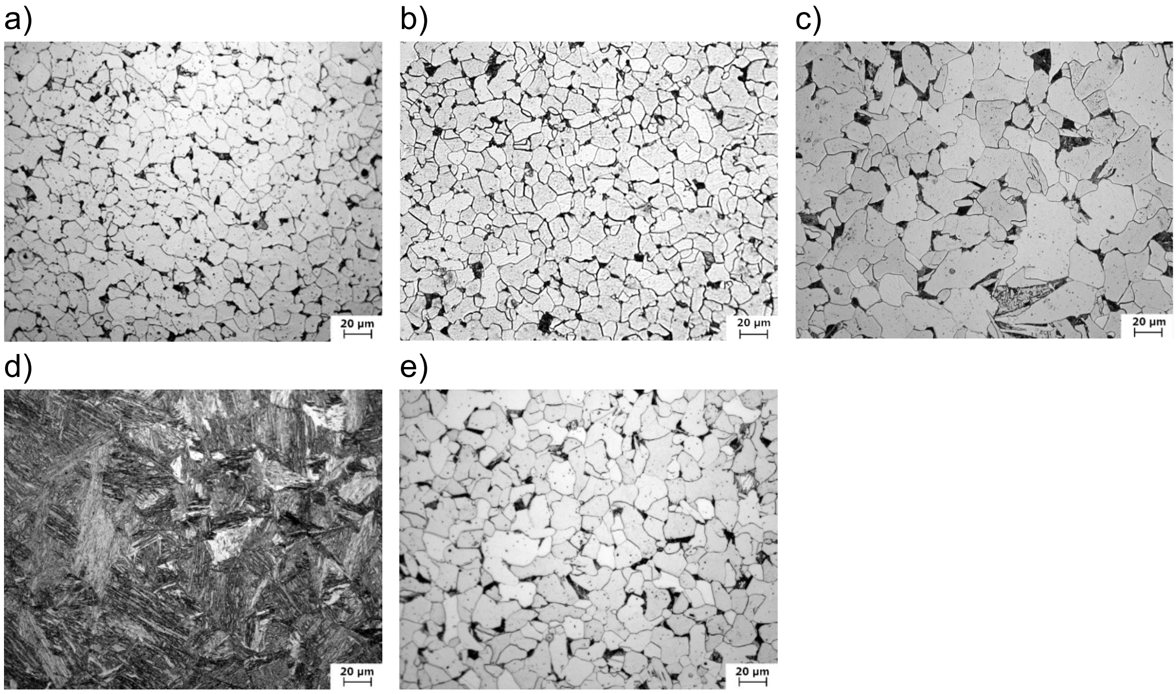

Figure 4.14 Typical microstructure of AISI 1012 a) as received, b) 900 °C/30 min. AC, c) 1050 °C/30 min. AC, d) 1050 °C/30 min. WQ and e) 1050 °C/30 min. WQ + 885 °C/2h AC.

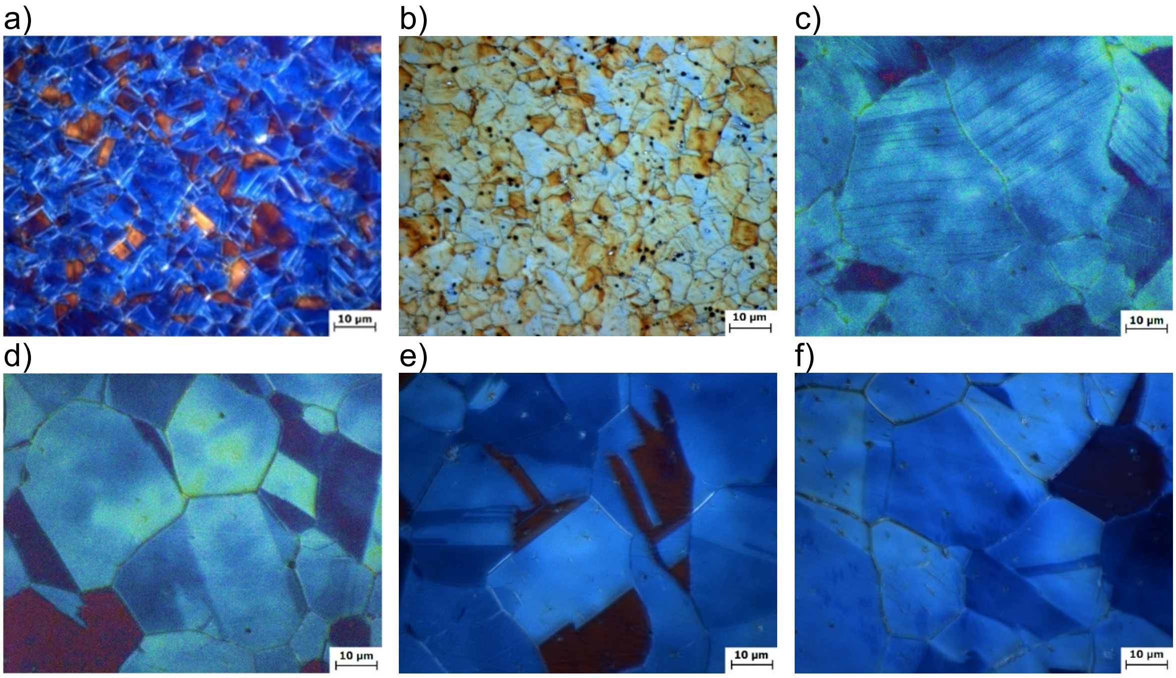

Figure 4.15 Typical microstructure of AISI 316L a) as received revealed with BII, b) as received revealed with LBI c) 900 °C/30 min. AC, d) 1050 °C/30 min. AC, e) 1050 °C/30 min. WQ and f) 1050 °C/30 min. WQ + 885 °C/2h AC.

4.2.2.2. Microstructure of the Welded Joints

The microstructure of the AW joint along the central line on AISI 1012 side is shown in **Figure 4.16-a)**. As mentioned previously, some ferrites exist in the Widmanstätten structure owing to the over-heat near the weld interface, which means that the microstructure is quite heterogeneous in this area. The microstructures of joints at different heat treatment conditions A, B and C on AISI 1012 side are shown in **Figure 4.16-b)**, **-c)** and **-d)**, respectively. After PWHT, a significant modification of the weld microstructure from Widmanstätten ferrite/pearlite structure to an equiaxed ferrite structure containing some pearlite has been taken place. A thin proeutectoid ferrite layer forms close to the weld interface on AISI 1012 side both in central and peripheral zone.

It could be observed that at a heat treatment temperature of 900 °C (**Figure 4.16-b)**), the weld interface became distinct, the Widmanstätten structure transformed to proeutectoid ferrite, and a layer of fine equiaxed ferrite grains formed near the weld interface with absence of pearlite grains due to carbon diffusion from AISI 1012 to AISI 316L. After applying heat treatment condition B, it could be noted that the structure still consists of some Widmanstätten ferrite on the prior austenite grain boundaries and the ferrite layer near the weld interface became a little wider and coarser than that in heat treatment condition A and in as-welded state as shown in **Figure 4.16-c)**. After the heat treatment condition C was applied, the weld interface became rather distinct and a much wider and coarser ferrite layer formed along the weld interface as shown in **Figure 4.16-d)**.

Since the microstructure of as-welded joint was quite heterogeneous in TMAZ, the successive heat treatment process led to separation of a little more ferrite along the pearlite grain boundary, which results in improving the homogeneity of the microstructure in this heat-treated state to some extent. In TMAZ near the weld interface which is shown in **Figure 4.16-d)**, the content of ferrite decreased compared to that of the joint heat treated at conditions A and B, which could be related to the increasing pearlite content by the formation of the wide ferrite layer. The severer element diffusion is responsible for the wider proeutectoid ferrite layer [145]. The effect of this ferrite layer formation on the mechanical properties of the welded joints will be discussed later in **section 4.2.3.1**.

The microstructures of as-welded joint along the central line on AISI 316L side are shown in **Figure 4.17-a)**. At weld interface, the crushed austenite gains were recrystallized on account of concurrent effect of frictional heating and severe deformation with a significant grain refinement (layer thickness about 100 µm). In TMAZ, the grains were oriented to the radial direction by severe plastic deformation, especially the grains near the weld interface, which might have a strong (111) and <112> texture [144].

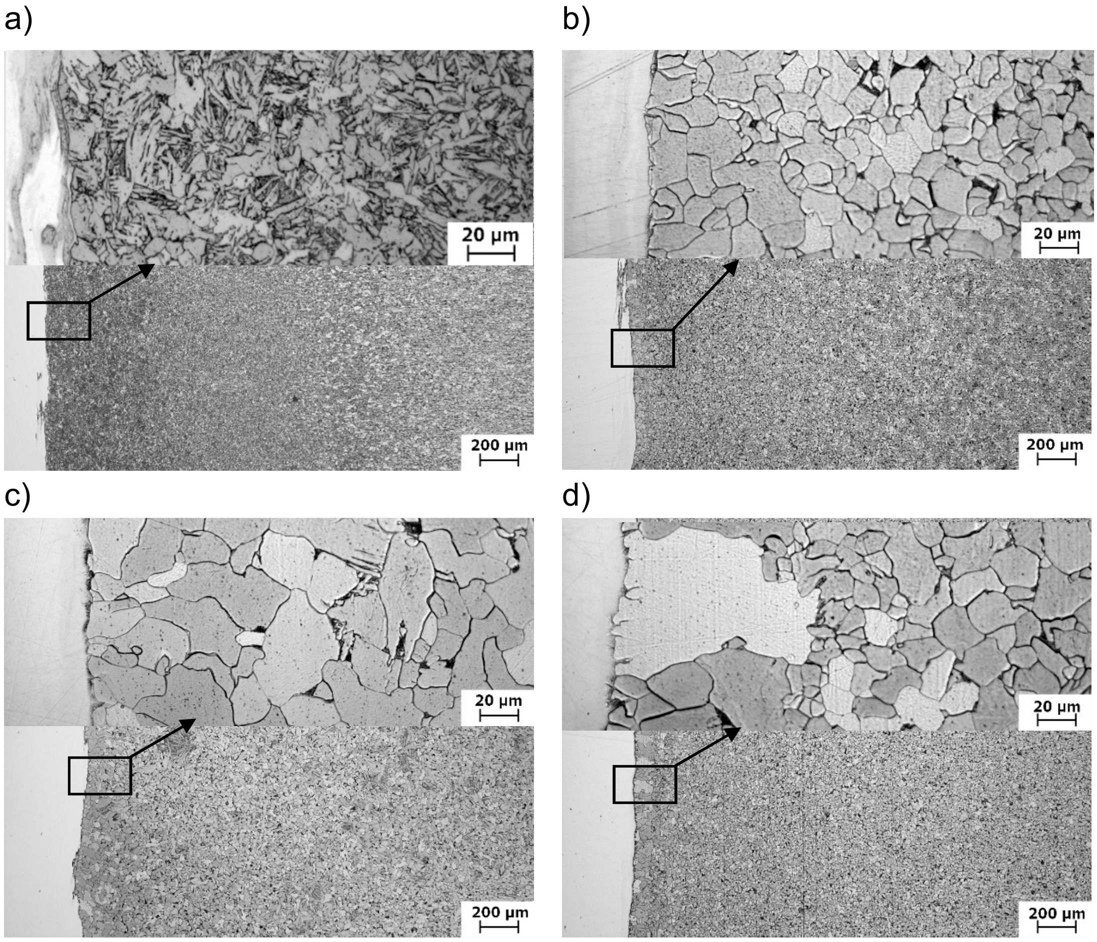

Figure 4.16 Typical microstructure of the welded joint along the central line on AISI 1012 side a) as-welded (AW), b) 900 °C/30 min. AC, c) 1050 °C/30 min. AC and d) 1050 °C/30 min. WQ + 885 °C/2h AC.

The microstructures of the weld interface after heat treatment at different temperatures are shown in **Figure 4.17-b)**, **-c)** and **-d)**. There was little change in the size of austenite grains at weld interface and TMAZ in heat treated joints except that the austenite grains became distinct near the weld interface specially at heat treatment condition C as shown in **Figure 4.17-d)**.

Figure 4.18 shows the microstructures of the weld flash on AISI 1012 side of as-welded joint and at different heat treatment conditions. **Figure 4.18-a)** shows the weld flash on as-welded condition which consists mainly of Widmanstätten ferrite and little proectuoid ferrite. It was remarkable that at 1050 °C/AC the microstructure contains some of Widmanstätten ferrite on the prior austenite grain boundaries as shown in **Figure 4.18-c)**. Whereas, at heat treatment conditions A and C, the microstructure contains pearlite grains in a matrix of ferrite grains as shown in **Figure 4.18-b)** and **-d)**, respectively. **Figure 4.19** shows the microstructure and EDX analysis of the inclusions detected in the welded joint on AISI 316L side after PWHT. Based on the EDX analysis, elongated MnS inclusions are fusiform or stripe shape with sizes up to 30 μm [146].

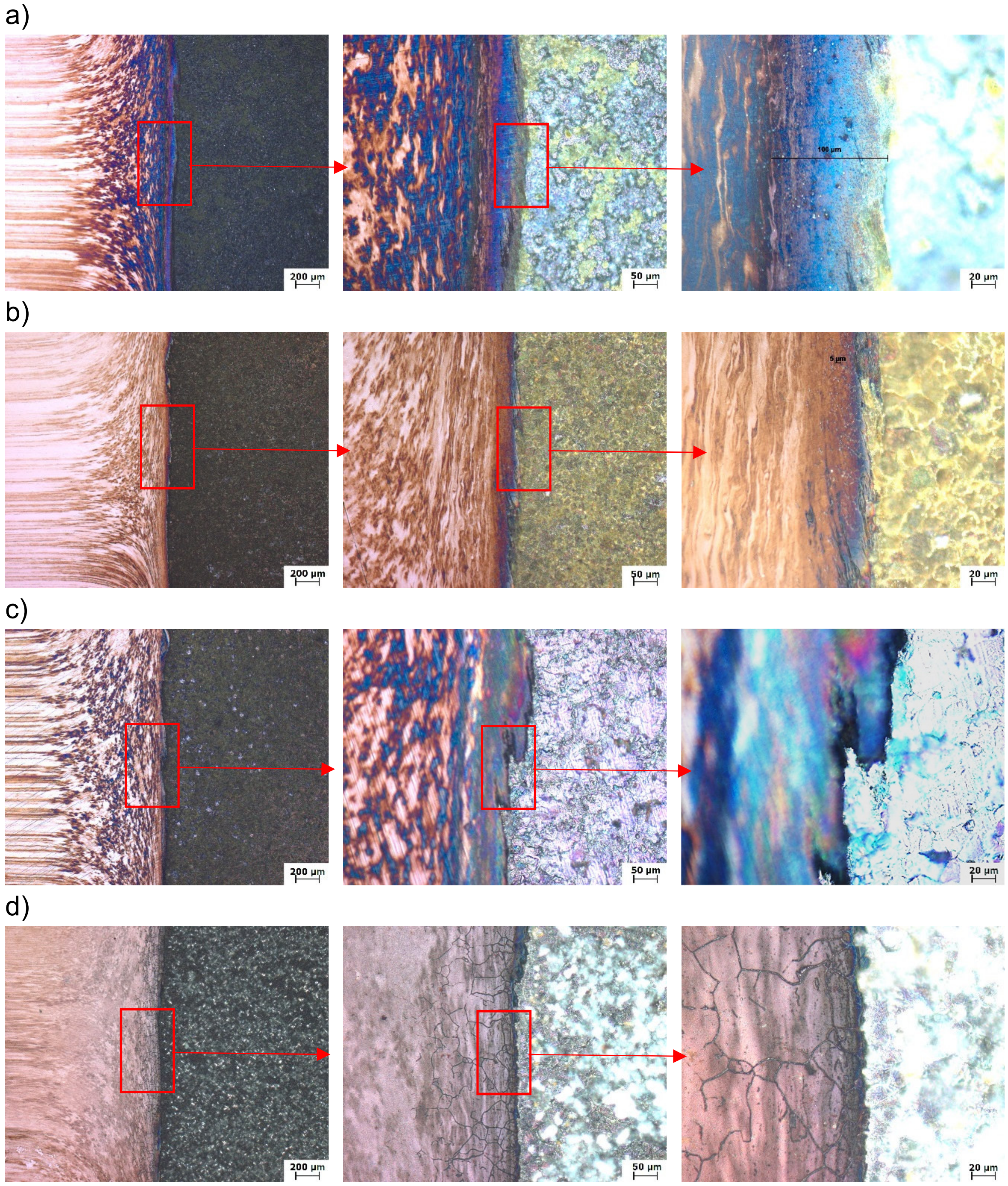

Figure 4.17 Typical microstructure of the welded joint along the central line on AISI 316L side revealed with LBI a) as-welded (AW), b) 900 °C/30 min. AC, c) 1050 °C/30 min. AC and d) 1050 °C/30 min. WQ + 885 °C/2h AC.

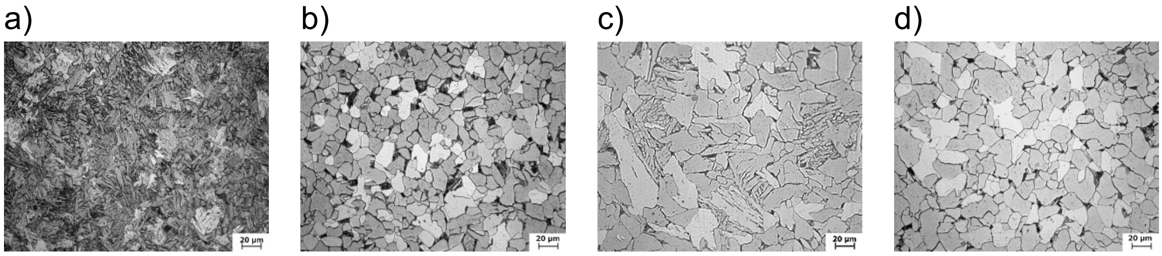

Figure 4.18 Typical microstructure of the weld flash on AISI 1012 side a) as-welded (AW), b) 900 °C/30 min. AC, c) 1050 °C/30 min. AC and d) 1050 °C/30 min. WQ + 885 °C/2h AC.

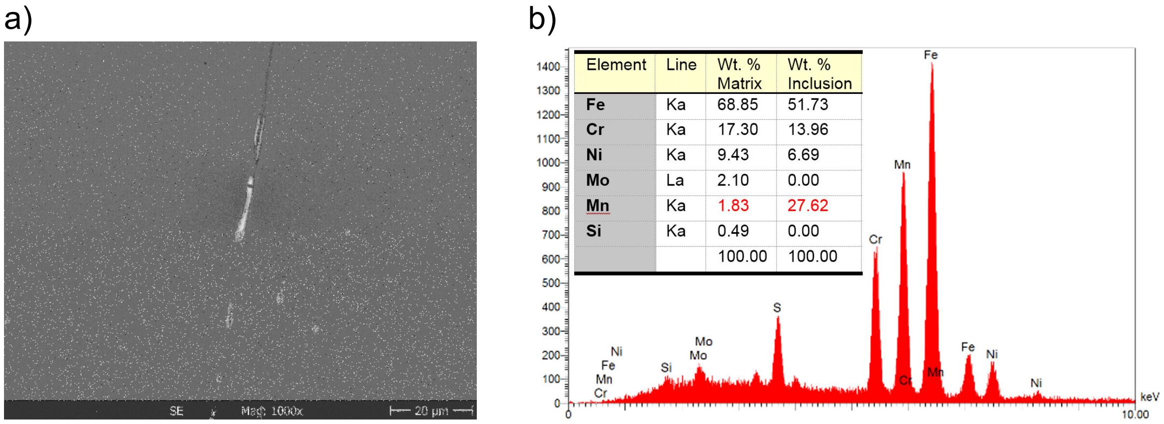

Element	Line	Wt. % Matrix	Wt. % Inclusion
Fe	Ka	68.85	51.73
Cr	Ka	17.30	13.96
Ni	Ka	9.43	6.69
Mo	La	2.10	0.00
Mn	Ka	1.83	27.62
Si	Ka	0.49	0.00
		100.00	100.00

Figure 4.19 The microstructure and EDX analysis of the inclusions detected in the welded joint on AISI 316L side.

4.2.3. Phase Composition and Element Diffusion at Weld Interface

To identify the phases formed at the weld interface and at HAZ, a trail has been conducted using quantitative X-ray diffraction analysis. For this purpose, polished specimens were scanned using a Siemens D5000 diffractometer which has a goniometric diameter of 600 mm. The experiments were conducted using a Fe-filtered Co-Kα radiation diffractometer at 40 kV and 40 mA. The peak intensities of the whole patterns were collected by the step scanning technique utilizing small step size of $\Delta(2\theta) = 0.025°$ and a period of 3 s at each fixed value of 2θ in the range between 46° and 130°.

The XRD-patterns for the as received (AR) AISI 316L, as-welded (AW) and post-weld heat treated (PWHT) at the weld interface of AISI 316L side are represented in **Figure 4.20-a)**. The XRD-patterns taken at distance of 0.8 mm from the weld interface of AISI 316L side in **Figure 4.20-b)**. The figures reveal the high austenitic stability of the base material, even with high strain rate hot deformation in the welding process.

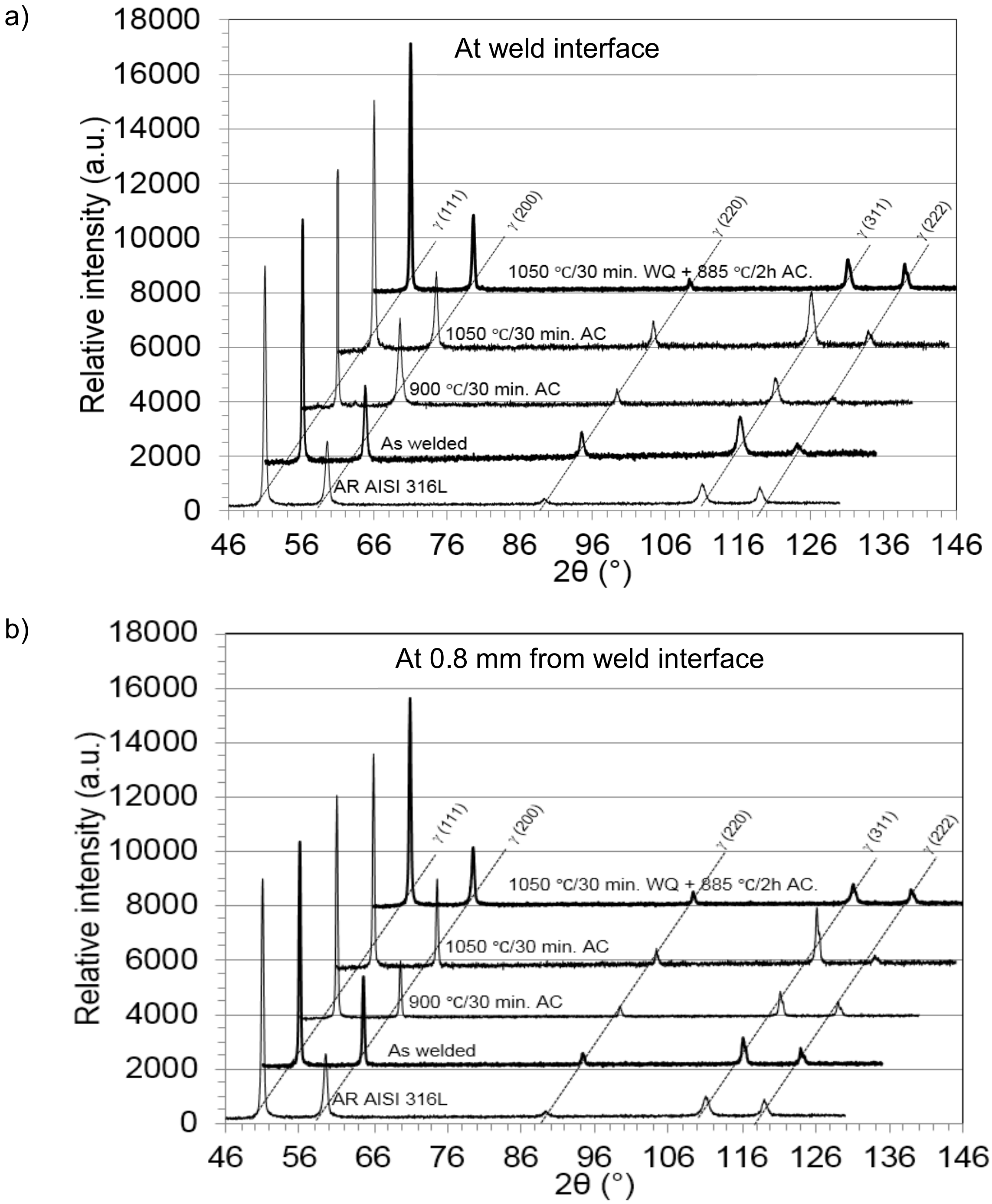

Figure 4.20 Representative XRD-patterns for the prescribed condition a) at weld interface and b) at 0.8 mm from weld interface.

It can be noted from these figures that the peaks of (111), (200), (220), (311) and (222) planes of FCC austenite are revealed alone without any emergence of ferrite or carbides peaks. However, Hong Ma et al. [147] have proved the existence of carbides at the weld interface in both as-welded and PWHT state using the micro-spot XRD. Therefore, further investigations using specific etchants - as Groesbeck's and mod. Murakami's reagents- have been conducted to be able to detect the presence of δ-ferrite and carbides in the welded joints.

4.2.3.1. δ-Ferrite Behavior

δ-ferrite varies significantly in different characteristic zones on stainless steel weld side [147]. The δ-ferrite near the weld interface is totally disappeared and no stripe-like δ-ferrite existed near the weld interface, resulting in the formation of δ-ferrite free zone as shown in **Figure 4.21-a)**. In addition, a great reduction of δ-ferrite content in TMAZ in as-welded joint could be observed in **Figure 4.21-a)**. **Figure 4.21-b)** shows the morphology of δ-ferrite in base metal after etching with mod. Murakami's reagent. It could be noticed that the δ-ferrite decreased from BM to the weld interface and no δ-ferrite existed in the TMAZ near the weld interface.

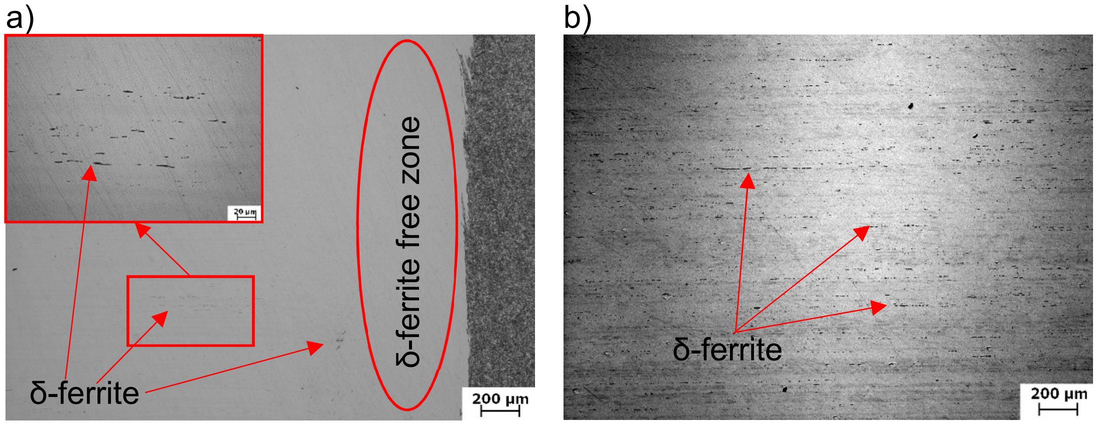

Figure 4.21 The morphology of δ-ferrite in different zones a) weld zone in as-welded state and b) base metal. (etched with mod. Murakami's reagent)

The original δ-ferrite in stainless steel base metal can dissolve under the combined effects of thermal cycle and plastic deformation. The dissolution of δ-ferrite is a eutectoid decomposition which mainly happens in two forms. One is the transformation from δ-ferrite to $M_{23}C_6$ and secondary austenite ($\delta \rightarrow M_{23}C_6 + \gamma_2$), the other is the transformation from δ-ferrite to σ-phase and secondary austenite ($\delta \rightarrow \sigma + \gamma_2$) [148]. However, the lattice mismatch between σ-phase and austenite phase leads to the retarded nucleation of σ-phase, causing the transformation from δ-ferrite to σ-phase and secondary austenite lags the transformation from δ-ferrite to $M_{23}C_6$ and secondary austenite. Thus, the transformation of $\delta \rightarrow M_{23}C_6 + \gamma_2$ dominates the dissolution of δ-ferrite during friction welding which is also proven by the formation of carbide shown in **Figure 4.22**.

Lo et al. [149] and Mateša et al. [150] reported that δ-ferrite could be fully dissolved by a long-time heat-treatment (above 1 hour) at 500-900 °C since δ-ferrite was unstable in this temperature range. However, the temperature should play a less prominent role because of the process time in friction welding is rather short (only several seconds from the thermal cycle) compared to the long-time heat-treatment; therefore, it was supposed to have another factor that was responsible for the reduction of δ-ferrite in TMAZ. In friction welding, TMAZ was encountered severe plastic deformation, thus the grain boundary migration was greatly enhanced, which accelerated the dissolution of δ-ferrite existed at grain boundary. Therefore, the plastic deformation may play a predominant role in the rapid dissolution of δ-ferrite in TMAZ, while in HAZ, δ-ferrite only decreased slightly due to the lack of plastic deformation and the rather low temperature. Thus, the dissolution of δ-ferrite could be accelerated by the severe plastic deformation at a relatively high temperature. For the joint in PWHT state, it was just at a relatively high temperature with no plastic deformation, which resulted in little changes of δ-ferrite.

4.2.3.2. Carbide Behavior

Despite the absence of carbides peaks in XRD pattern in **Figure 4.20**, the proeutectoid ferrite layer formation at the weld interface after PWHT (**Figure 4.16**) suggests the presence of carbides [145]. Since this layer is formed as a result of the concentration of carbon (carbon rich layer) at the weld interface. Groesbeck's reagent has been used to reveal the carbide layer at the weld interface. **Figure 4.22** shows the formation of carbide layer at different heat treatment temperatures. It can be noted that with increasing the PWHT temperature, element diffusion became severer and the diffusion distance of carbon became longer, and more chromium carbides formed at the grain boundary, hence the width of distinct austenite grains increased as can be clearly observed in **Figure 4.22**.

$Cr_{23}C_6$ is a common carbide phase that can easily form in the process of welding austenitic stainless steel due to the element diffusion [151]. Thus, in friction welding of stainless steel to carbon steel, C and Cr can more easily react with each other to form $Cr_{23}C_6$ at weld interface. Hong et al. have testified the existence of $Cr_{23}C_6$ with face-centered cubic (FCC) structure (a=b=c=10.67 Å) by the selected area diffraction (SAD) [145]. The formations of $Cr_{23}C_6$ also verify the existence of the carbon rich layer. It should be noticed that Ni also diffuses to weld interface which can form other phases such as Ni_3C, CrNiFe, as revealed by friction welding of AISI 304 to AISI 4140. Thus, the carbon rich layer is a complex carbide layer which may consist of other phases besides $Cr_{23}C_6$ and CrC [152].

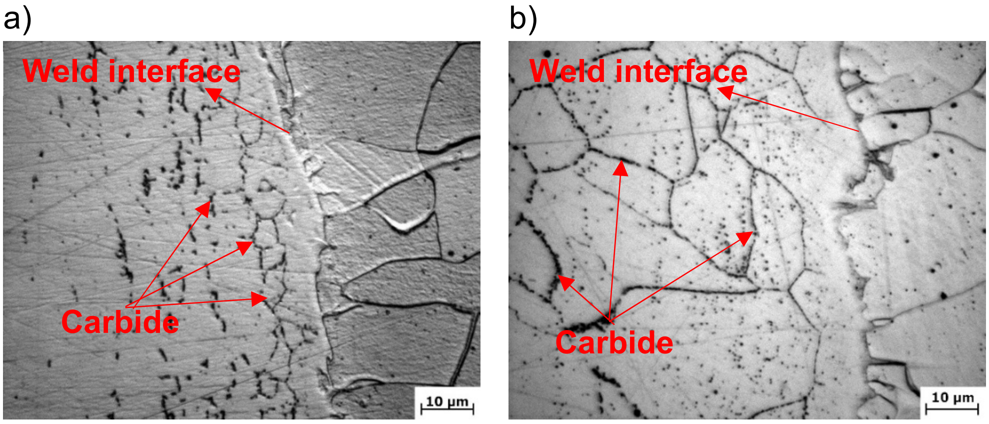

Figure 4.22 Morphology of carbides at the weld interface of the joint with different heat treatment temperature on AISI 316L (lift side on the microstructure image) a) 900 °C/30 min. AC and b) 1050 °C/30 min. WQ + 885 °C/2h AC. (etched with Groesbeck's reagent)

Hong et al. [147] have illustrated the diffusion process at the weld interface of stainless steel to carbon steel joints after PWHT (shown in **Figure 4.24-a)**). They reported that element diffusion in PWHT not only prompted the formation of chromium carbides and more ferrite at the weld interface of carbon steel side but also led to the variation of stainless steel. They reported that the diffusion coefficient of the grain-boundary was much higher than that of intra-grain diffusion. Therefore carbon (C) was more likely to cross the weld interface and diffused along the austenite grain boundary to form chromium carbides with Cr. Thus, a large amount of chromium carbides formed at the austenite grain boundary, which lowered corrosion resistance of stainless steel near the weld interface. This could be proved by the distinct austenite grains near the weld interface, as presented in **Figure 4.23-b)**.

Since C could easily produce chromium carbides with Cr, and the diffusion coefficient of C was much higher than that of Cr and Ni, C was supposed to agglomerate at the weld interface and form chromium carbides with Cr in friction welding. However, in friction welding process, the combination of short friction time and a high temperature at the weld interface was not enough to cause severe element diffusion in the as-welded state. Hence the content of C at the weld interface was not much higher than that in carbon steel base metal, and the reason of no visible agglomeration of C detected by optical and scanning electron microscope in the as-welded state. However, with increasing the heat treatment temperature agglomeration of C has been observed at the weld interface as shown in **Figure 4.23-b)**. This could be attributed to the element diffusion became severer, and the temperature was high enough to form carbide.

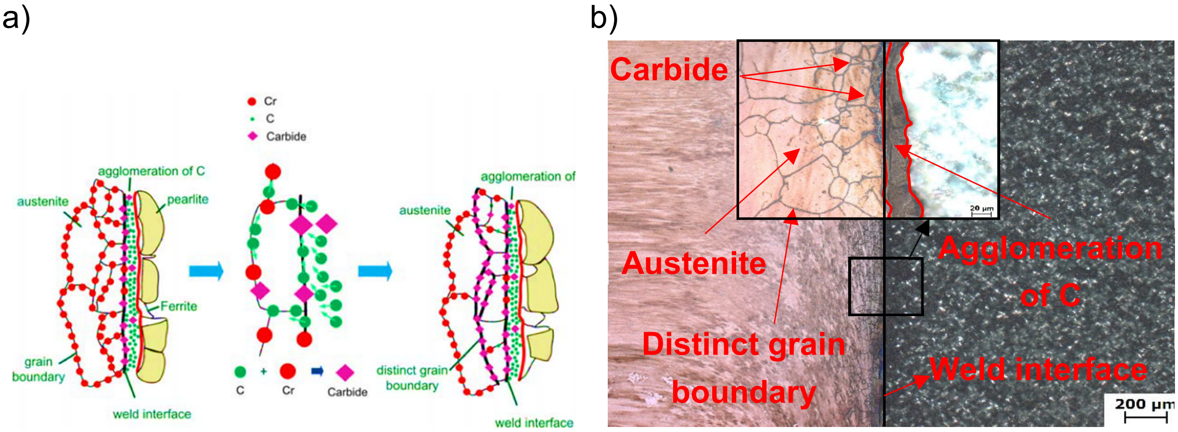
a)
b)

Figure 4.23 a) Schematic illustration of the diffusion process at the weld interface of stainless steel to carbon steel joints after PWHT [147] and b) Morphology of carbides and C agglomeration at the weld interface of the joint on AISI 316L side at 1050 °C/30 min. WQ

4.2.4. Microhardness-Depth Profiles

Micro-hardness distributions along the central line of AW and PWHT joints are shown in **Figure 4.24**. In the AW joint, the weld interface was harder than TMAZ and HAZ, which should be correlated to the formation of chromium carbides. From the weld interface to the base metal, the micro-hardness endured a drop and eventually to the minimum micro-hardness, indicating both AISI 1012 and AISI 316L sides softened in HAZ after welding. The reduction of micro-hardness on AISI 1012 side could attribute to the increasing content of ferrite in HAZ. On AISI 316L side, the reduced dislocation density and coarse austenite might be the cause for the descending trend in HAZ.

As for the heat-treated joints, it could be remarked that the micro-hardness at weld interface of the joint heat-treated at 1050 °C/30 min. AC and at 1050 °C/30 min. WQ + 885 °C/2h AC varied little compared to that of the as-welded joint. Although the formation of the highest amount of chromium carbides at 1050 °C/30 min. WQ + 885 °C/2h AC observed, however, the micro-hardness at the weld interface was not the greatest. That can be attributed to excessive austenite grain growth at the weld interface (**Figure 4.17-d)**). At a PWHT of 900 °C, the micro-hardness at the weld interface was the highest due to the increased amount of chromium carbides and the form of fine austenite grains. **Figure 4.25** shows the variation of micro-hardness at weld interface of the as-welded and heat-treated states.

The minimum micro-hardness on both weld side decreased after PWHT compared to the as-welded state. A sudden drop in micro-hardness on AISI 1012 side could be recognized. The lowest value of micro-hardness obtained after treatment at 1050 °C/30 min. WQ + 885 °C/2h AC. The wider and coarser ferrite layer formed along the weld interface (**Figure 4.16-d)**) might be related to this trend. The micro-hardness of carbon steel base metal after PWHT at all condition had little variation, while on AISI 316L side, after PWHT at 900 °C, the micro-hardness increased compared to the other PWHT conditions, which should attribute to the formation of finer austenite grains.

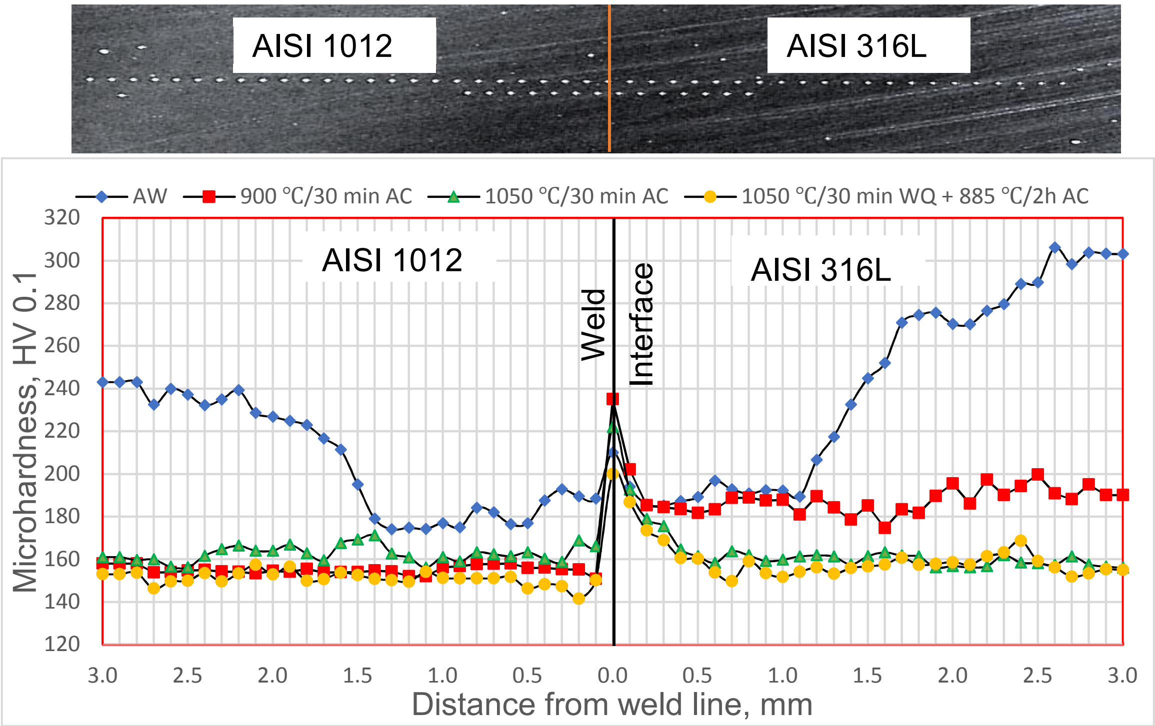

Figure 4.24 Vickers micro-hardness distribution along the central line of joints in as-welded and heat-treated states.

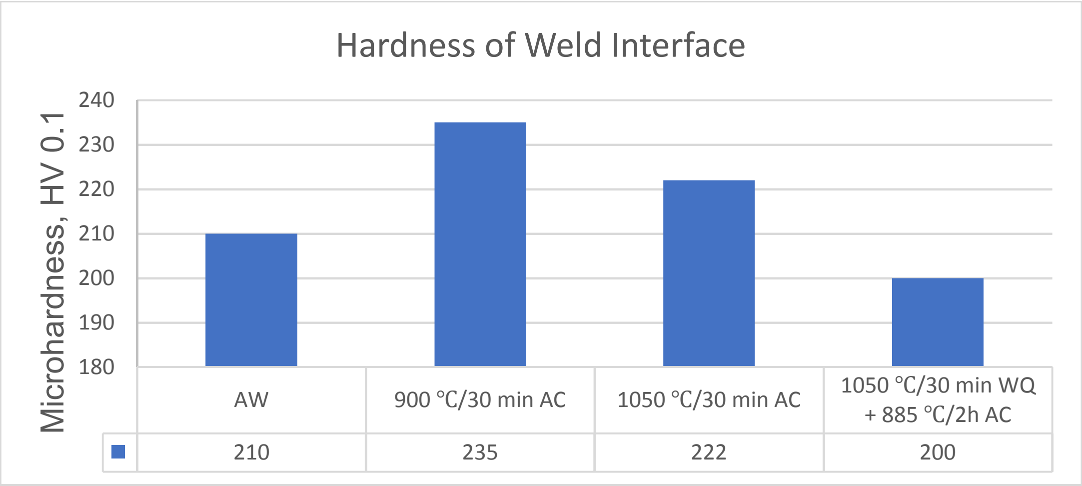

Figure 4.25 Variation of micro-hardness at weld interface of the as-welded and heat-treated states.

4.3. Mechanical Surface Treatments

4.3.1. Shot Peening Optimization

The optimization of the shot peening parameters was conducted for AISI 1012 to AISI 316L friction welded joints in the as-welded state. The optimization process was carried out at a wide range of different peening pressures adjacent to variable Almen intensities as listed in **Table 4-6**. All other parameters remain constant during the shot peening process, such as impingement angle of 90°, shots of type SCCW 14 with average size 0.36 mm. The peening duration is set up at 25 s to ensure full coverage of all specimens. A time of 10 s has been applied to shot peen only the weld zone (distance 5 mm right and left the weld line) of AISI 1012 to AISI 316L welded samples, which ensure full coverage of this region. The peened samples in the weld zone designated as SP WZ. In the SP process, the distance between the nozzle and the rotating specimen was kept constant (90 mm) to control the uniform coverage of the specimen.

The Almen intensity is determined as the saturation value of the arc height measured on so-called Almen strips peened for progressively longer exposure times on one side of the strips. This Almen value is the most important process parameter that characterizes the intensity of the SP treatment [153]. The SSCS program (Saturation Curve Solver by Shock form Aeronautique Inc.) was employed to process the data of the arc height of the Almen strip of type A and the time to determine the Almen intensity values.

Table 4-6 Correlation between the peening pressure and Almen intensity.

Peening pressure, bar	1	2	4	6	7.5
Almen intensity, mmA	0.1	0.15	0.2	0.25	0.3

The effect of SP using a wide variation in Almen intensity on fatigue life at a stress amplitude (σa) of 450 MPa in AISI 1012 to AISI 316L welded joint is given in **Figure 4.26**. Mechanically polished (MP) condition was used as a reference. It could be noted that the fatigue life in the shot-peened welded joints depends sensitively on Almen intensity. Optimum life improvement is observed after SP only if higher Almen intensities are used leading to subsurface fatigue crack nucleation. Peening pressure of 7.5 bar which corresponds to 0.3 mmA is the maximum provided pressure on the shot peening machine. Therefore, Almen intensity of 0.3 mmA was utilized as the optimum value for further investigations.

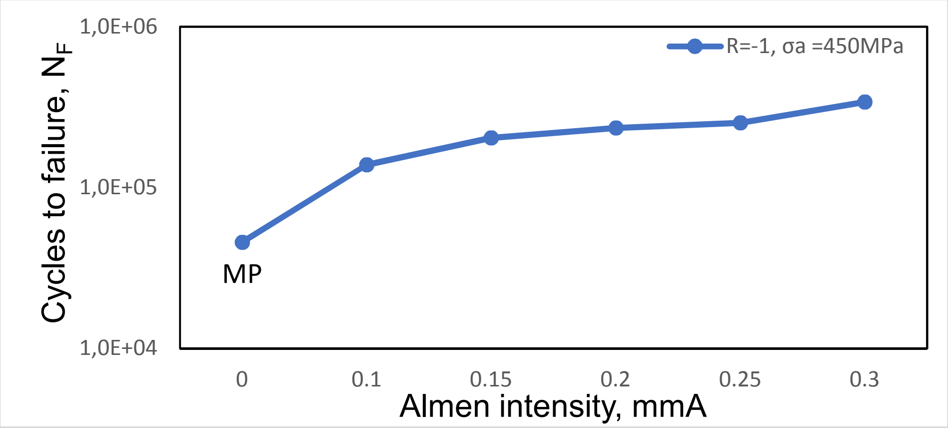

Figure 4.26 Fatigue life versus Almen intensity (σa = 450 MPa) in AISI 1012 to AISI 316L welded joint after SP.

4.3.2. Roller Burnishing Optimization

The optimization of roller burnishing (RB) pressure was carried out at constant feeding rate of 0.17 mm/rev using a hard metal Roller (Ø 40 mm, r 2.5 mm) with a constant rotating speed 150 rpm. The burnishing pressure was varied from 0.5 to 2.3 bar. **Figure 4.27** shows the effect of various roller-burnishing (RB) pressures on the fatigue life of the welded joint. Starting with condition MP, the fatigue life first increases with increasing the burnishing pressure and then slightly decreases after burnishing with higher burnishing pressures. In other words, there is a slight over-burnishing effect in RB on fatigue life by varying the burnishing pressure, consequently, with increasing the burnishing pressure, the fatigue life of welded joint is slightly decreased. For further fatigue testing, a burnishing pressure of 1 bar was chosen because at this pressure, the maximum number of cycles to failure for the welded joints was observed.

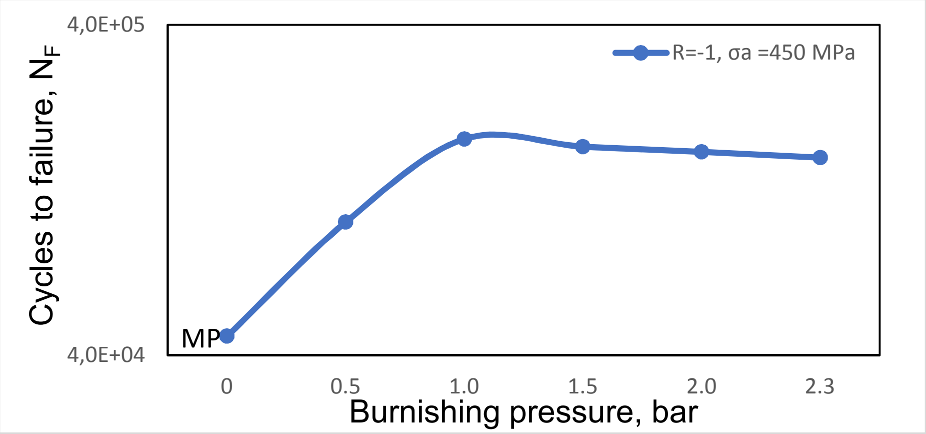

Figure 4.27 Effect of various roller-burnishing (RB) pressures on the fatigue life of the welded joint.

4.4. Evaluation of the Mechanical Surface Treatments

4.4.1. High Cycle Fatigue Performance

Figure 4.28 shows the S–N curves of the as-welded mechanically polished (AW MP), shot peened- and roller burnished-joints. As mentioned previously, SP and RB have been applied for the whole specimen (AW SP and AW RB) and the weld zone (AW SP (WZ) and AW RB (WZ)). Fatigue results of AW MP were included as a reference to compare with the shot peened and burnished data. The arrows in the figure represent specimens that did not break throughout the tests. The fatigue life is improved by SP and RB at all stress amplitudes. The most improvement of the fatigue life obtained after SP and RB for the whole weld joint which increases from 320 to 410 and 400 MPa, respectively, the enhancement is about 30%.

It was observed that the AW MP samples cracked in the weld zone after fatigue test, most probably because of tensile RS developed during welding [153-154]. The fracture location can be moved to the base metal of AISI 1012 by applying SP and RB on the weld zone. That could be attributed to the reinforcement of weld zone which means replacement of welding tensile RS with local compressive RS at the weld zone [124]. Consequently, the fracture location moved the weakest part which is BM-AISI 1012 in this case. Therefore, the fatigue behavior of AW SP (WZ) and AW RB (WZ) is slightly identical. However, after applying SP and RB on the whole fatigue specimen, the fracture location moved again to the weld zone. That may be ascribed to the reinforcement of the whole specimen after SP and RB which means that the minimum induced compressive RS will be at the weld zone. Nevertheless, the fatigue life of AW SP and AW RB is significantly higher than that of AW SP (WZ) and AW RB (WZ). That probably because of higher weld zone strength than the BM of AISI 1012. From these results, it can be concluded that the mechanical surface treatment (SP and RB) can control the fracture location either in the weld zone or in the lower strength base metal of the welded joints. Schematic graph -based on literature [124,187] clarifies the expected behavior of the welding tensile RS after conducting the mechanical surface treatments on the whole part and the weld zone (**Figure 4.29**). This graph illustrates how the fracture location can be controlled by distinguishing the reinforcement zone.

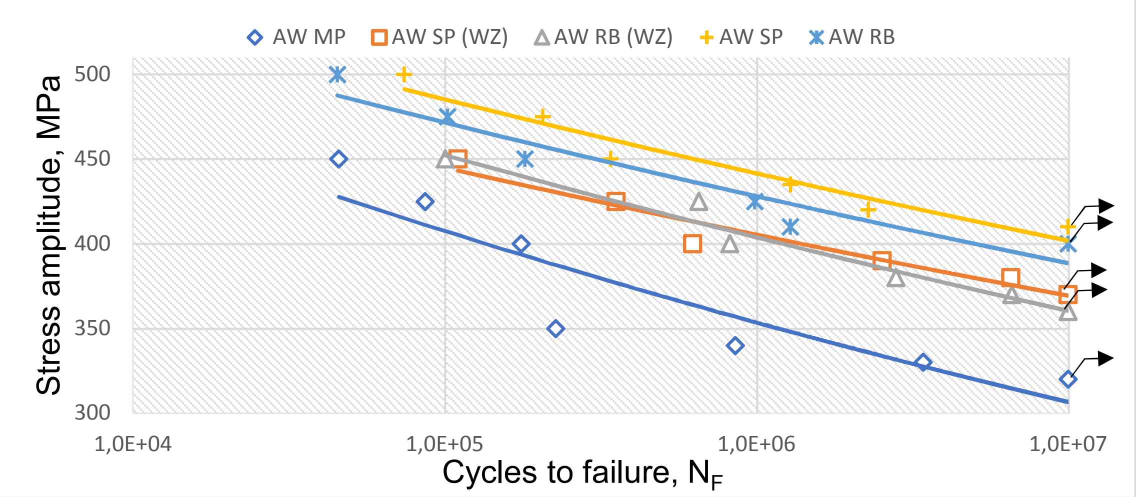

Figure 4.28 S–N curves for as-welded joint after various surface treatments.

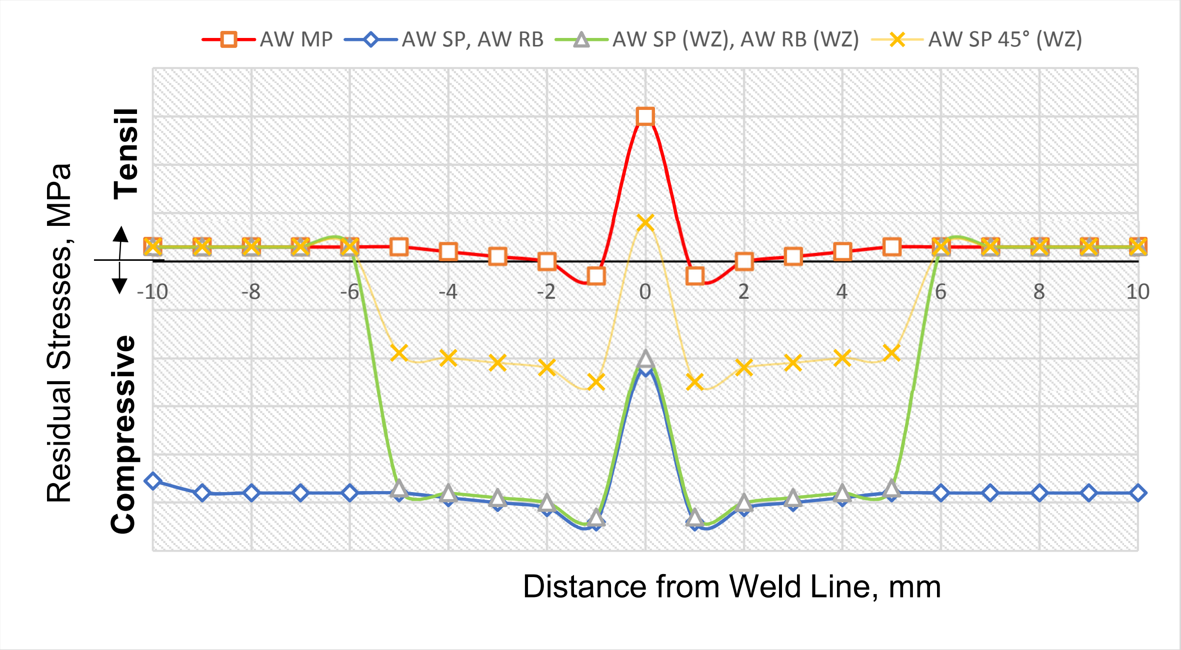

Figure 4.29 Schematic graph clarifying the expected behavior of the welding tensile RS after conducting the mechanical surface treatments on the whole part and weld zone.

The RB and SP-induced residual compressive stresses play an important role to enhance the fatigue performance because it significantly retards the fatigue micro-cracks propagation [155,156]. As a result, the fatigue cracks nucleation site changes from the surface to subsurface region. The subsurface crack nucleation sites in AW SP specimen are represented in **Figure 4.30-a)**. While fatigue cracks in AW MP specimen, always nucleated at the specimen surface as shown in **Figure 4.30-b)**. Remarkably, the fatigue limit after SP was higher than that after RB despite markedly lower roughness values of RB than SP as illustrated in **Figure 4.31**. This could be attributed to the higher induced compressive RS after SP than that after RB as shown in **Figure 4.32**. The subsurface (depth) residual stress distribution could be realized by pasting the strain gauge rosettes to the rounded-surface of the fatigue specimens as shown in the bottom right corner of **Figure 4.32**.

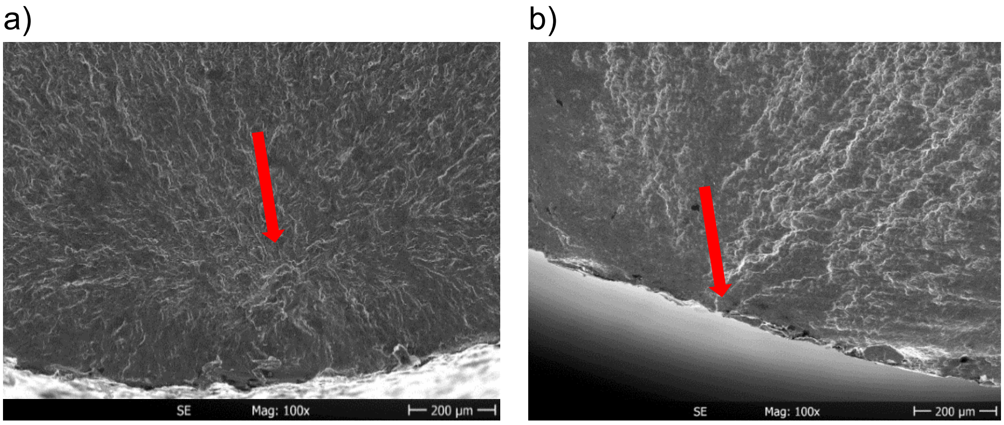
a)

b)

Figure 4.30 HCF crack nucleation sites a) AW SP and b) AW MP.

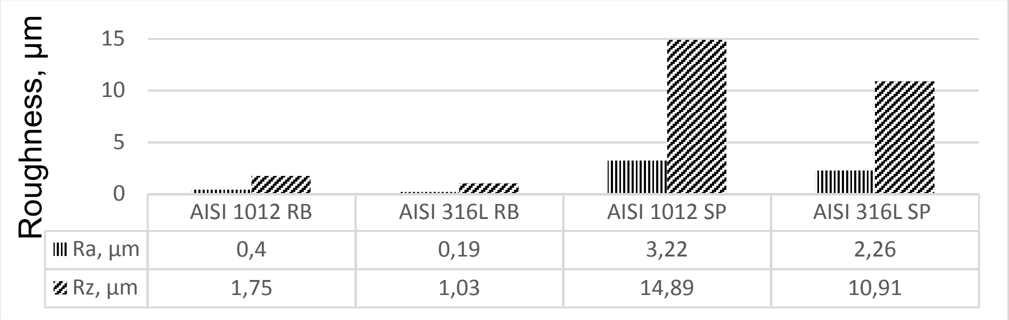

	AISI 1012 RB	AISI 316L RB	AISI 1012 SP	AISI 316L SP
▥ Ra, µm	0,4	0,19	3,22	2,26
▨ Rz, µm	1,75	1,03	14,89	10,91

Figure 4.31 Roughness values of the various surface treated conditions in both weld side

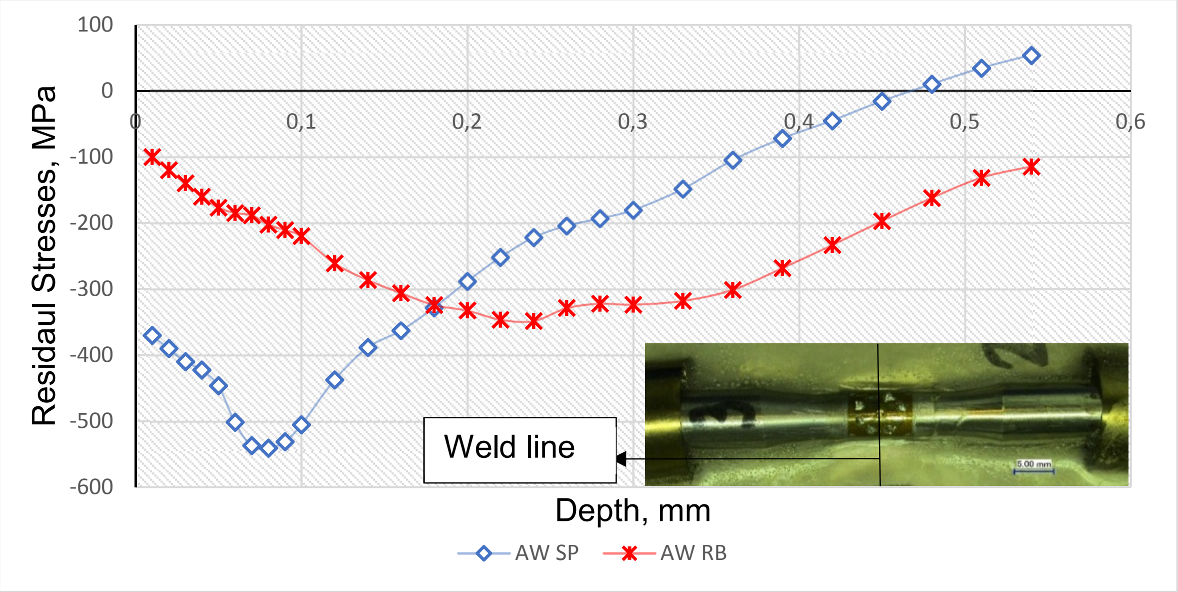

Figure 4.32 Residual stress-depth profile after SP and RB for AW state.

Figure 4.33 shows the effect of shot peening angle on the fatigue performance of the welded joints. The peening angle of 90 and 45 degrees has been applied at the same pressure of 7.5 bar, which means different Almen intensities to simulate some SP circumstances' in industry. The peening pressure of 7.5 bar corresponds to 0.3 mmA Almen intensity at 90°and 0.15 mmA at 45° degrees. It could be clearly observed that the fatigue performance of the welded joint negatively affect by reducing the peening angle at the same peening pressure. Whereas no significant effects on the resulting fatigue life has been reported when utilizing different peening angle at the same Almen intensity [109].

Interestingly, the fracture location after fatigue test did not change in AW SP 45° and AW SP 45° (WZ), where the sample was broken in the welding zone in both cases. That could be probably because of lower utilized Almen intensity (0.15 mmA) which was not high enough to completely convert the welding tensile RS at weld zone to compressive stresses (**Figure 4.29**). Therefore, the fatigue behavior in both cases is slightly identical. **Table 4-7** summarizes the endurance limit and fracture location in all applied conditions. According to these results, a trail has been conducted to increase the endurance limit of welded joint as well as the control of fracture location through shot peening of the weld zone at 0.3 mmA Almen intensity and shot peening of the base metal in both sides at 0.15 mmA Almen intensity. The result shows an improve in endurance limit to 390 MPa and the location of fracture remains at base metal of AISI 1012 side.

Table 4-7 The endurance limit and fracture location in prescribed conditions.

Treatment process	Endurance limit, MPa	Fracture location
AW MP	320	WZ-AISI 1012
AW SP 90°	410	WZ-AISI 1012
AW SP 90° weld zone	370	BM-AISI 1012
AW SP 45°	330	WZ-AISI 1012
AW SP 45° weld zone	340	WZ-AISI 1012
AW RB	400	WZ-AISI 1012
AW RB weld zone	360	BM-AISI 1012

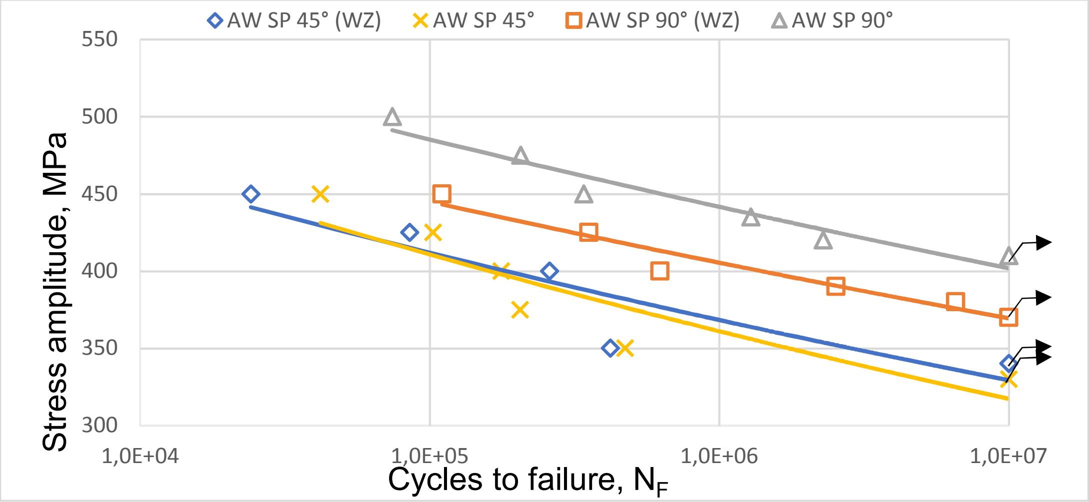

Figure 4.33 The effect of Peening angle on the fatigue performance of welded joint.

Figure 4.34 shows the effect of post-weld heat treatment on the fatigue performance of the welded joint. Thereof the fatigue life of AW state is higher than of that after PWHT. That may be attributed to the formation of the Widmanstätten structure owing to the overheated SPDZ near the weld interface on AISI 1012 side (**Figure 4.8-a)**) and the finer austenitic grains on AISI 316L side. It can be also noted that with increasing the PWHT temperature the fatigue life is retarded because of the formation of a wider and coarser ferrite layer along the weld interface (**Figure 4.16-d)**).

Figure 4.35 shows the effect of SP and RB on the fatigue performance of PWHT joint. An enhancement of the fatigue life has been achieved after mechanical surface treatments on weld zone of all PWHT conditions. It was observed that the fatigue performance of RB joints was more improved than of SP joints. That could be attributed to deeper penetration depth of compressive RS and lower surface roughness. On the other hand, high surface roughness in SP could lead to an early crack nucleation [157]. **Table 4-8** summarize the endurance limit and fracture location of PWHT conditions after different surface treatments. Noteworthy, the fatigue fracture is located at or close to the weld interface for MP condition. Probably because of the formation of proeutectoid ferrite layer close to the weld interface on AISI 1012 side after PWHT.

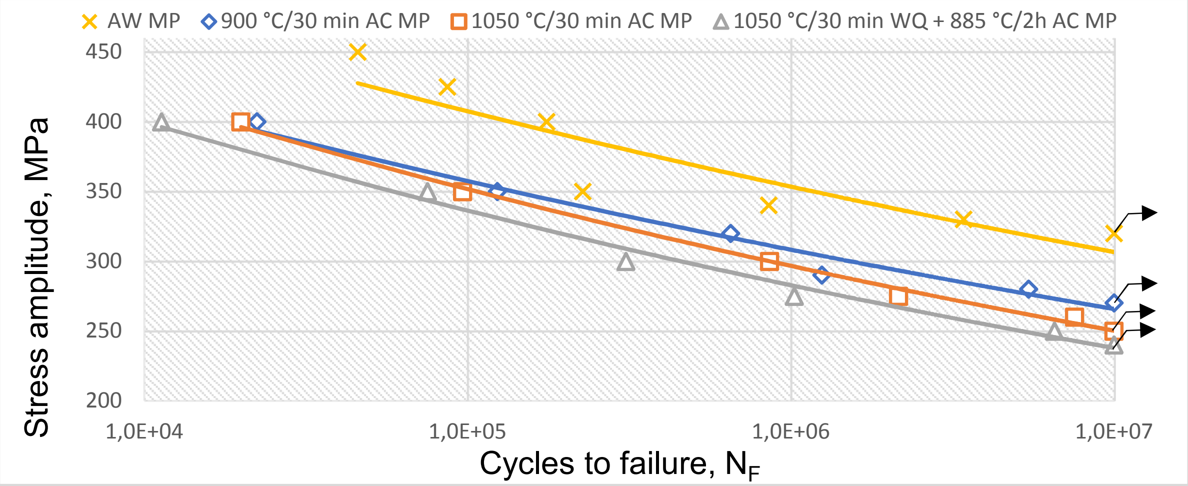

Figure 4.34 The effect of PWHT on the fatigue performance of the welded joint.

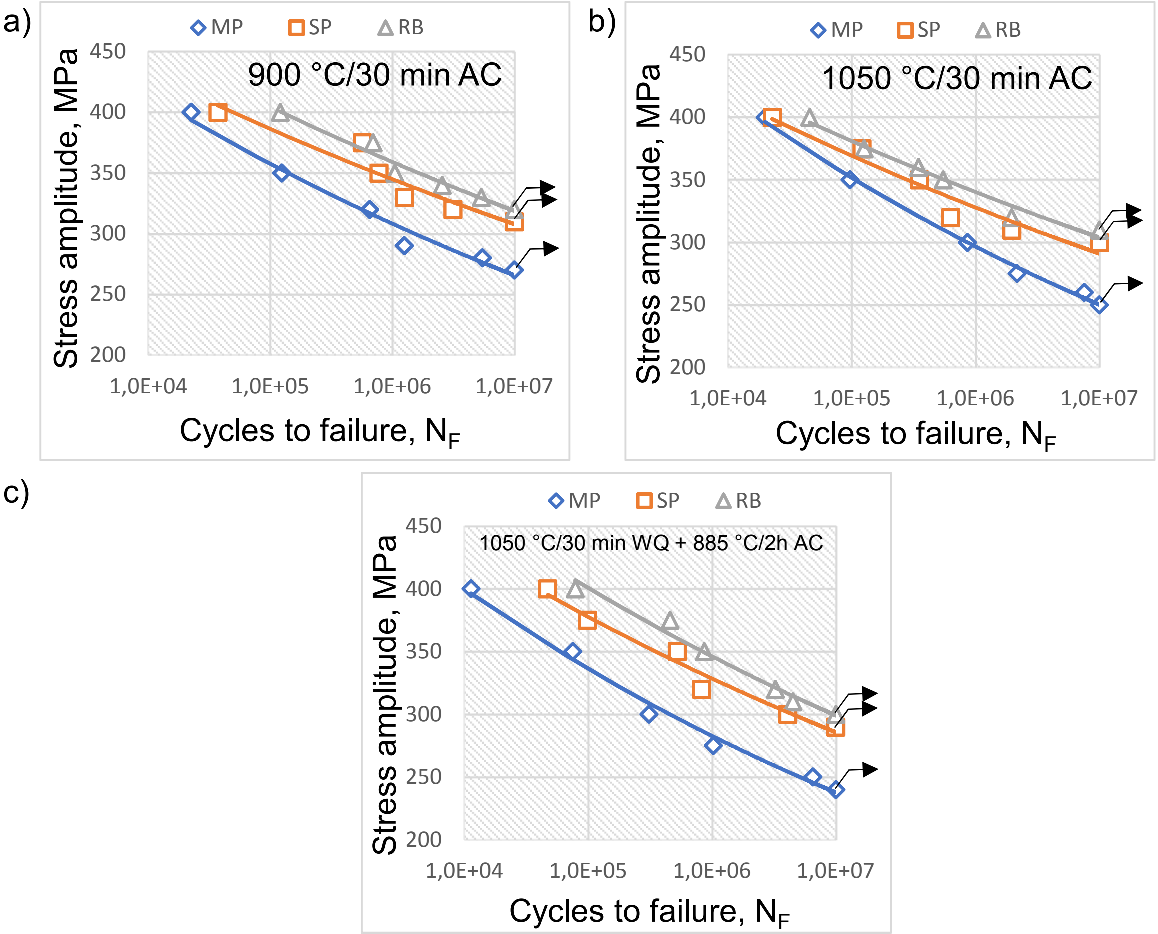

Figure 4.35 The effect of SP and RB on the fatigue performance of PWHT joint.

Table 4-8 The endurance limit and fracture location of PWHT conditions after different surface treatments.

Heat treatment	Surface treatment	Endurance limit, MPa	Fracture location
900 °C/30 min AC	MP	270	WZ-AISI 1012 (@ ≈ 0.1 mm from weld interface)
	SP	310	BM-AISI 1012
	RB	320	BM-AISI 1012
1050 °C/30 min AC	MP	250	WZ-AISI 1012 (@ ≈ 0.1 mm from weld interface)
	SP	300	BM-AISI 1012
	RB	310	BM-AISI 1012
1050 °C/30 min WQ + 885 °C/2h AC	MP	240	WZ-AISI 1012 (@ ≈ 0.2 mm from weld interface)
	SP	290	BM-AISI 1012
	RB	300	BM-AISI 1012

4.4.2. Impact Toughness

To evaluate the impact toughness values of the welded joint, a series of Charpy V-notch tests were performed on parent metals (AISI 1012 and AISI 316L) and friction-welded joints at room temperature. The test data are average values obtained from three specimens. The average impact toughness values are presented in **Table 4-9**. And **Figure 4.36**. The sub-size impact toughness has been correlated to the full-size impact toughness according to ASTM STP 1380 [132]. The impact toughness of both base metals AISI 316L and AISI 1012 was 119 J and 86 J, respectively. The impact energy in AW state decrease considerably. Probably because of the brittleness of the chromium carbide layer at and close to the weld interface [158]. Despite the improvement of fatigue life after SP, the impact energy of the peened weld joint is decreased compared to AW state. That could be attributed to elevated dislocation density and the higher roughness values after SP which cause a stress concentration at the V-notch [159].

Table 4-9 Impact toughness values of the base metals and friction welded joints at room temperature.

	Avg. sub-size impact toughness, J	Avg. full-size impact toughness, J
AISI 316L	5.97	119
AISI 1012	4.53	86
AW	4.1	78
AW SP	3.53	68

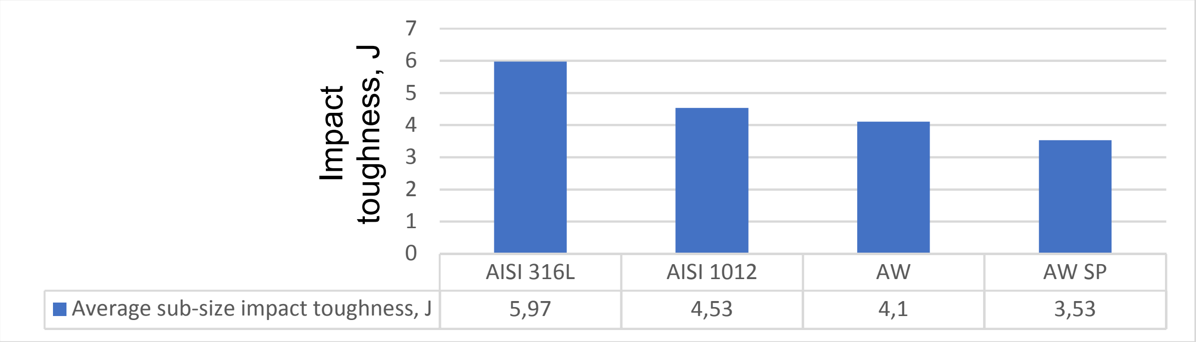

Figure 4.36 Avg. sub-size impact toughness of the prescribed conditions.

the fracture behaviors of the parent metals, peened-, and unpeened-welded joints after impact testing were analyzed in detail. SEM analysis of fracture surface of prescribed conditions is shown in **Figure 4.37**. A typical ductile Charpy failure with desired lateral expansion for parent metals as well as-welded joints. Shear deformation, crack initiation, and crack propagation are the consecutive evolution stages for plastic deformation and fracture of materials [159]. The fracture pattern can be divided into different characteristic zones, such as shear region (I), shear lips (II), zone of subcritical crack growth (III), zone of final fracture (IV) as shown in **Figure 4.37-a)**. This figure indicated that ductile dimples fracture was the fracture mode of AISI 316L, while AISI 1012 failed by transgranular fracture, which is characterized by quasi-cleavage and a small quantity of dimples on tear ridges as shown in **Figure 4.37-b)**. The fracture surface of as-welded joint, shown in **Figure 4.37-c)**, can be classified into two zones, the central and peripheral zone. In central zone (above the red dashed line), quasi-cleavage fracture with a small quantity of dimples dominates the fracture mode. While dimples fracture occurs in the peripheral zone (below the red dashed line). From the flow direction of river pattern (yellow arrows in **Figure 4.37-c)** in region A) and from crack path investigation in **Figure 4.38**, it can be seen that the cracks initiated from the central zone at AISI 1012 side. That could be attributed to the heterogeneous microstructure at AISI 1012 side [147]. It is clearly observed after SP that the higher roughness values accelerate the cracks initiation on the fracture surface as shown in **Figure 4.37-d)** in region A, which probably was the responsible for the reduction of impact toughness after SP.

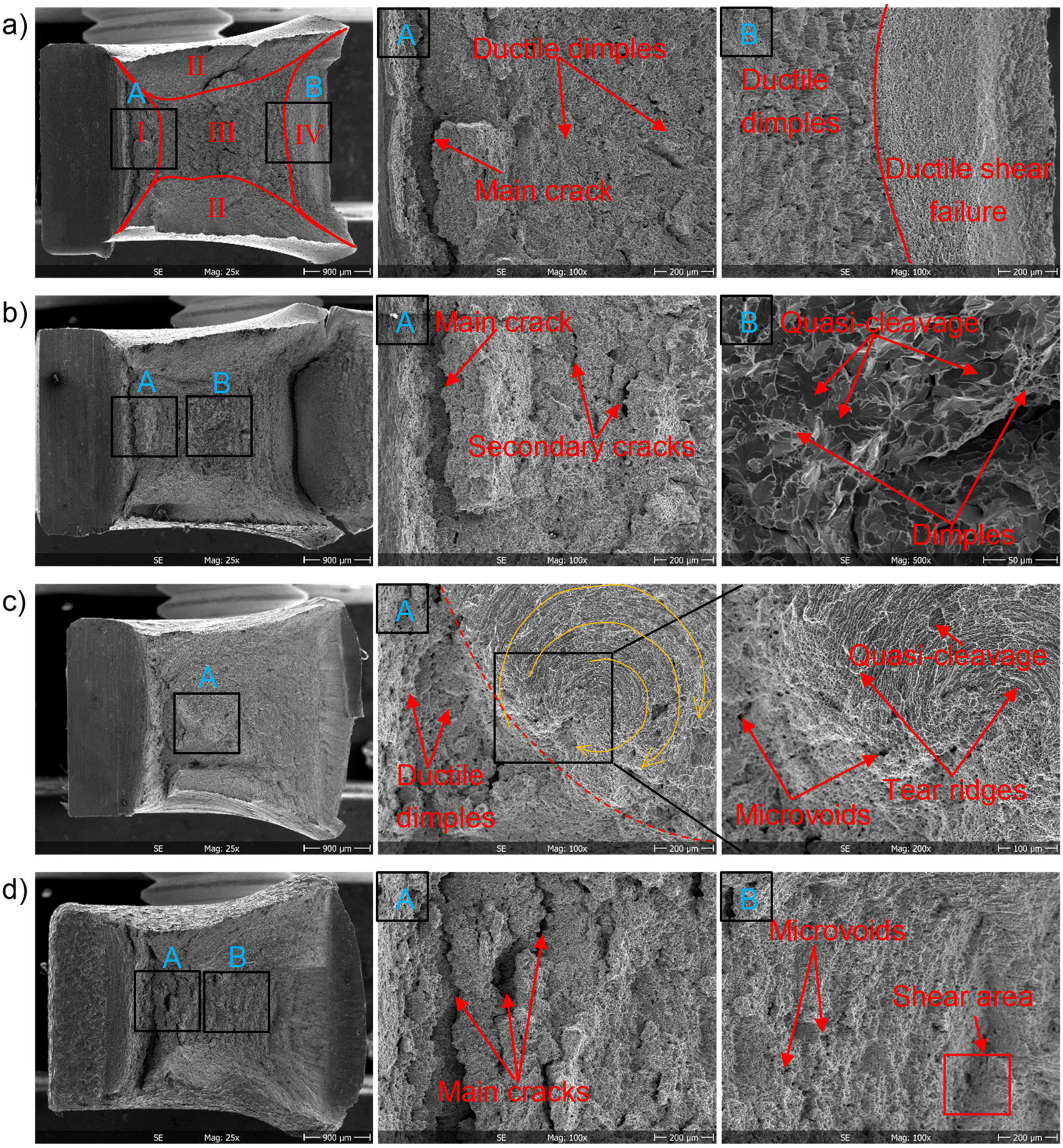

Figure 4.37 Fracture appearances after impact testing for a) AISI 316L, b) AISI 1012, c) AW and d) AW SP. Regions A and B are magnified right to the fracture pattern.

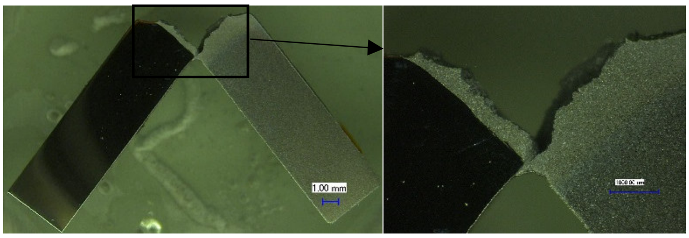

Figure 4.38 Cross-sectional view of the fractured AW samples after impact test which shows that the fracture occurred at AISI 1012 side.

5. Characterization of Similar Weld Joints

5.1. Characterization of CP-Ti Weld Joints

In this part, the results of the welding parameters optimization and their effect on the metallographic, weld geometry and strength-related aspects of the CP-Ti welded joints are presented. In this regard, a selection of proper friction welding parameters was tested as an optimization procedure aiming at producing sound weld joints. The objectives of the optimization are maximizing the central weld length and minimizing the flash width to reduce the third part region in the friction welded joint. Therefore, the weld joint has been mechanically and metallurgically characterized through tensile testing, micro-hardness and impact toughness measurement, and microstructure of the welded joints namely the as-welded (AW) and the post-weld heat treated (PWHT) conditions. The welded joints were then mechanically surface treated by either shot peeing (SP) or roller burnishing (RB). SP and RB are expected to enhance the surface layer properties, fatigue performance as well as the impact toughness of both AW and PWHT conditions. The RS depth profile at the weld line has been measured using the incremental hole-drilling method (IHD).

5.1.1. Process Parameters Optimization

Trial runs were carried out by changing one of the process variables and keeping the others constant. All friction welding parameters have been varied to check the material response over the different friction welding conditions and heat inputs. **Table 5-1** shows the initial welding parameters utilized in the primary characterization with the following parameters: friction pressure (P1), forging pressure (P2), friction time (t1), forging time (t2) and rotational speed (rpm). All friction welding parameters have been varied to check the material response over the different friction welding conditions and heat inputs. Initially, the weld quality has been established only based on visual examination and macro- and microstructural evaluation. The evaluated factors were weld distortion, amount and formation of flash, weld geometry as well as-weld defects (lack of bonding and cracks). The used procedures to investigate the initial parameters matrix are shown in **Figure 5.1**.

Table 5-1 The friction welding parameters of the initial experimental matrix.

	Exp. No.	P1 (bar)	P2 (bar)	t1 (s)	t2 (s)	Rotational speed (rpm)
Group 1	1	0.7	3	0.5	2.5	8000
	2	1	3	0.5	2.5	8000
	3	2	3	0.5	2.5	8000
	4	2.5	3	0.5	2.5	8000
Group 2	5	0.7	1	0.5	2.5	8000
	6	0.7	2	0.5	2.5	8000
	7	0.7	4	0.5	2.5	8000
	8	0.7	5	0.5	2.5	8000
Group 3	9	0.7	3	0.2	2.5	8000
	10	0.7	3	0.5	2.5	8000
	11	0.7	3	1	2.5	8000
	12	0.7	3	1.5	2.5	8000
Group 4	13	0.7	3	0.5	1	8000
	14	0.7	3	0.5	2	8000
	15	0.7	3	0.5	4	8000
	16	0.7	3	0.5	5	8000
Group 5	17	0.7	3	0.5	2.5	6000
	18	0.7	3	0.5	2.5	10000
	19	0.7	3	0.5	2.5	12000

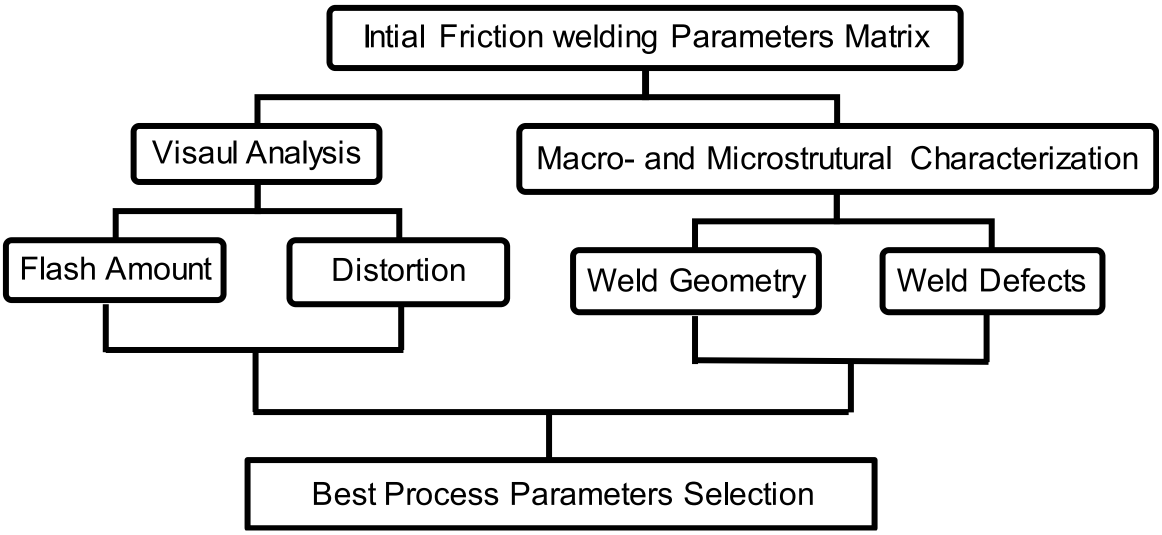

Figure 5.1 Flowchart showing the procedure used to investigate the initial parameter matrix.

Figure 5.2 shows the macrographs of some welded specimens at different friction pressures and rotational speed values. It can be observed that the flash width decreased by increasing the friction pressure as a result of the reduced plastic deformation of the material [160,161]. Also, a significant effect of the rotational speed on the amount and formation of flash has been observed for the welded joints. It was observed that the flash width increased at higher value of rotational speed as shown in **Figure 5.2-e)** to **-h)**. On the other hand, excessive specimen deformation has presented with increasing the forging pressure as shown in **Figure 5.3**. The micrographs in **Figure 5.4** refer to a longitudinal crack on Exp. 4 and Exp. 12 at high friction pressure and high friction time, respectively. Lack of bonding has been observed for Exp. 5 with a low value of forging pressure (1 bar) as shown in **Figure 5.5**.

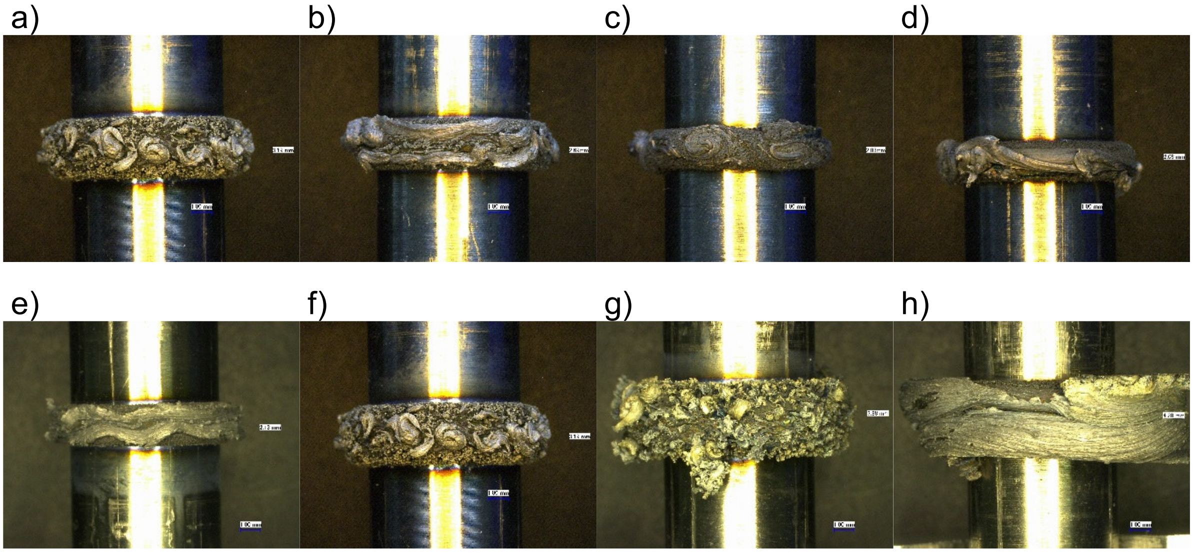

Figure 5.2 Macrographs of the welded specimens for different friction pressure and rotational speed values: a) Exp. 1 (P1= 0.7 bar), b) Exp. 2 (P1= 1 bar), c) Exp. 3 (P1= 2 bar), d) Exp. 4 (P1= 2.5 bar), e) Exp. 17 (6000 rpm), f) Exp. 1 (8000 rpm), g) Exp.18 (10000 rpm) and h) Exp. 19 (12000 rpm).

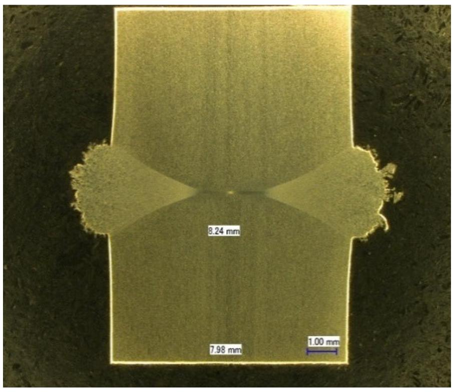

Figure 5.3 Macrograph of the welded specimen demonstrates excessive deformation at forging pressure of 5 bar (Exp. 8).

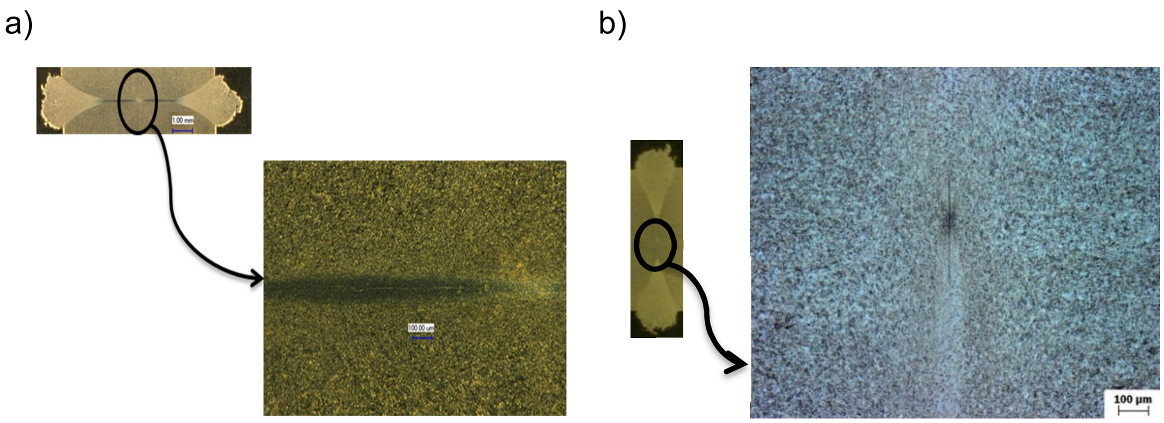

Figure 5.4 Longitudinal crack on weld line at high friction pressure and friction time a) Exp. 4 at P1= 3 bar and b) Exp. 12 at t1= 1.5 s.

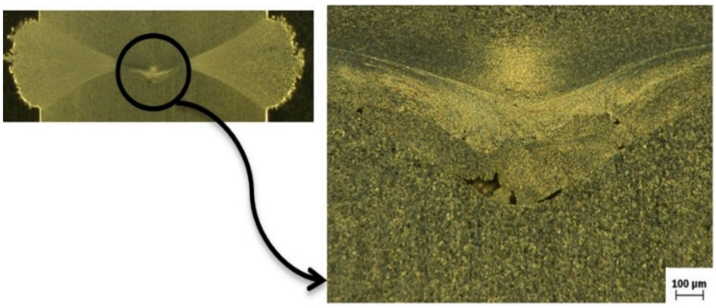

Figure 5.5 Lack of bonding for Exp. 5 at low forging pressure of 1 bar.

The primary goal of parameter optimization was set to achieve weld strength above the strength of the base materials in addition to minimizing the weld zone geometry. That means to keep the secondary heat input and the heat affected zone as low as possible. Therefore, further investigations have been conducted to evaluate the geometry of the weld.

Table 5-2 shows the determined values of weld width (µm), flash width (mm) and central weld length (mm) of the first run welded joints. It was observed that the central weld length increased at higher values of friction pressure. During parameter optimization, all welded joints in AW state are broken outside the weld zone. Although there were defects within the welding zone, such as a longitudinal crack in Exp. 4, 12 and lack of bonding in Exp. 5, the welding strength was not affected because of these flaws. The results of tensile tests are listed in Table 5-3. It is evident that there was no reduction in the strength of Exp. 5 and Exp. 12 despite the existence of welding defects. In fact, all failure occurred away from the weld zone. In General, there was no noticeable difference in the mechanical properties of the welded joints and parent material. Therefore, the strength aspect was not considered in the further optimization procedures'.

Table 5-2 The determined weld geometry of the first run welded joints.

Exp. No.	Weld Geometry			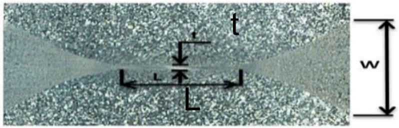
	W (mm)	t (µm)	L (mm)	
1	3.03	75	1.89	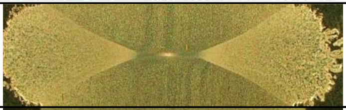
3	2.01	-	3.38	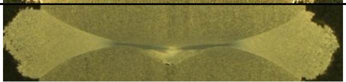
4	1.86	47	3.11	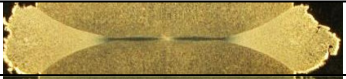
5	2.73	-	2.11	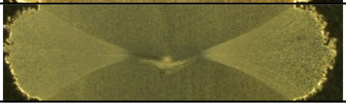
6	2.97	39	2.18	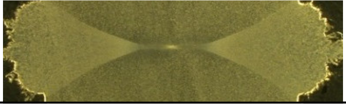
8	2.83	50	2.20	
9	2.77	75	1.85	
10	3.03	75	1.89	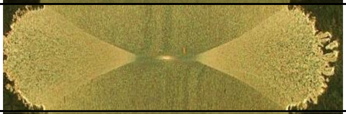
11	2.9	79	2.01	
12	2.91	72	2.1	
13	3.14	35	2.06	
16	2.75	78	1.86	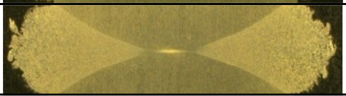
17	2.2	75	1.72	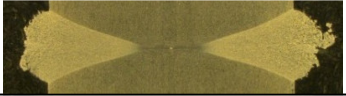
18	3.25	45	1.5	
19	3.07	30	1.44	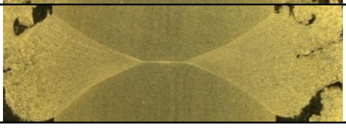
t: Weld width,W: Flash width, L: Central weld length				

Table 5-3 Results of the tensile tests performed for the defected weld joints.

Base metal	UTS, MPa	YS, MPa	EL, %	Fracture Location
	546	416	31	
Exp. 3	580	441	31	
Exp. 5	581	443	29	
Exp. 12	571	442	31	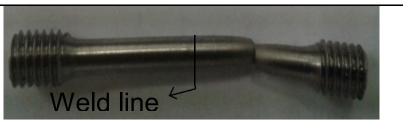

Minitab 17 has been utilized to investigate the significance of the weld parameters on the flash width and central weld length of the welded joints. The significant effect of each parameter was evaluated by a normal probability plot of standardized effect at 5% significance level as shown in **Figure 5.6-a)** and **Figure 5.6-b)** for the central weld length the weld joints (mm) and flash width (mm), respectively. From **Figure 5.6-a)**, it was observed that the friction pressure is the influential parameter for the development of central weld length of the weld joints. From **Figure 5.6-b)**, it was observed that the friction time and rotational speed (rpm) are the significant parameters for the development of the flash width of the welded joints. The influence of the friction pressure and rotational speed on the central weld length and flash width is shown in **Figure 5.7**. The friction pressure and rotational speed should be optimized to maximize the central weld length and minimize the flash width. Therefore, a second trial with a different combination of P1 and rotational speed has been conducted.

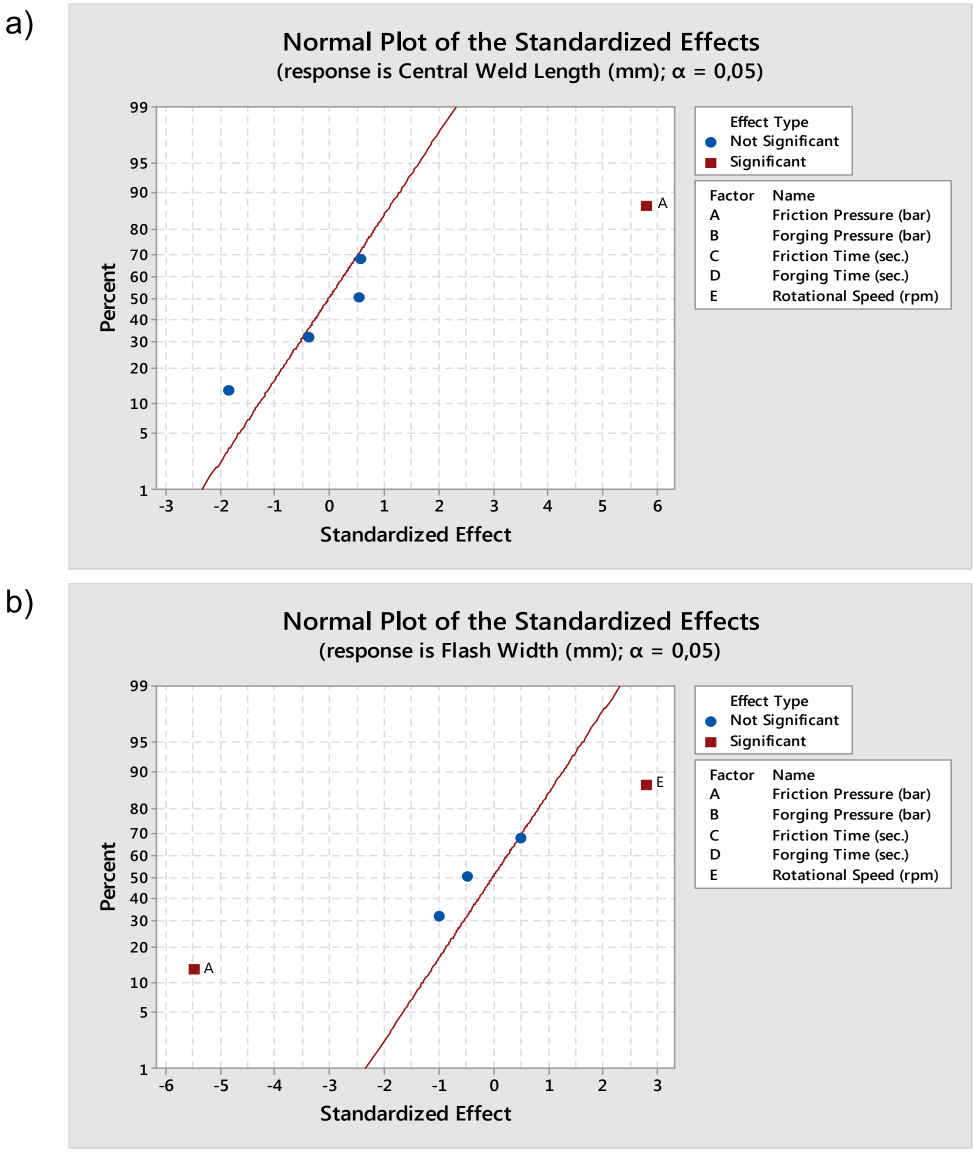

Figure 5.6 Normal probability plot of standardized effects for a) central weld length and b) flash width (mm).

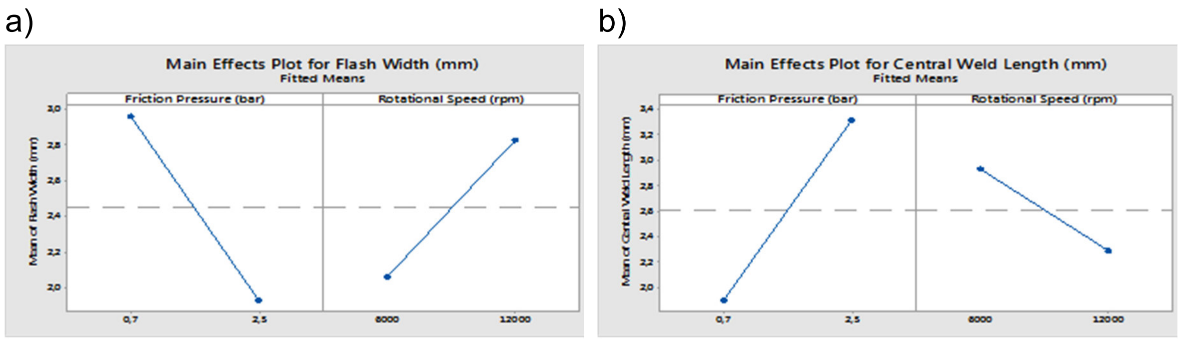

Figure 5.7 Main effect plot for a) central weld length and b) flash width (mm).

After the initial optimization step, the most significant parameters (friction pressure and rotational speed) have been chosen for further investigations (metallurgical and mechanical evaluation) for a second run. In this run, P1 and rotational speed have been varied while the other three parameters (P2, t2 and t1) were kept constant.

Table 5-4 shows an experiment matrix of the friction welding parameters used in the second DoE run. All experiments have been welded with a forging pressure of 3 bar, forging time of 2.5 s and friction time of 0.5 s. The optimization process has been carried to maximize the central weld length and minimize the flash width to minimize the metal loss in the friction welding process.

Table 5-4 The experimental matrix for the second optimization run of the friction welding parameters. All conditions have been applied with a forging pressure of 3 bar, forging time of 2.5 s and friction time of 0.5 s.

Exp. No.	20	21	22	23	24	25
P1, bar	2.5	2.5	2	2	1.5	1.5
Rotational speed, rpm	12000	10000	10000	12000	12000	10000

Table 5-5 presents the determined values of weld geometry (weld width, flash width, and central weld length) for the second run welded-joints. The data indicates that the higher values of friction pressure and rotational speed increased the central weld length increased and the flash width. decreased the observed increase in central weld length (**Figure 5.8**) could be attributed to the generated heat at the higher applied pressure (Exp. 20 or Exp. 21), this heat is mainly used to plastify the material and consequently does not propagate in the axial direction; therefore, high pressures lead to thinner transformed regions [161].

Table 5-5 The measured weld geometry of the second run.

Exp. No.	**Weld Geometry**		
	W (mm)	t (µm)	L (mm)
20	2.36	81	3.88
21	2.46	122	3.63
22	2.62	136	3.4
23	2.64	111	3.65
24	3.1	121	3.64
25	2.72	119	3.24
W: Flash width, t: Weld width, L: Central weld length (approx.)			

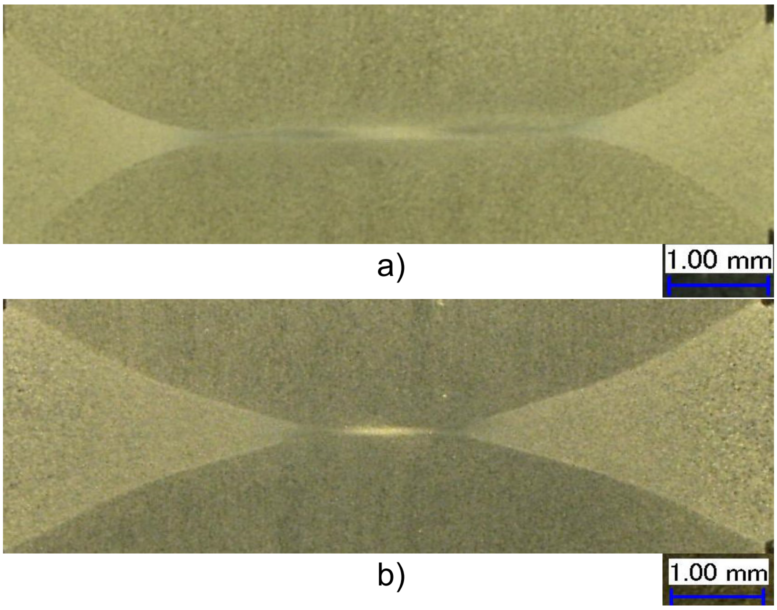

Figure 5.8 The weld geometry of a) Exp. 21 b) Exp. 16.

Furthermore, the microhardness profiles were determined across the friction welded joints. All welding conditions have shown the same behavior. **Figure 5.9** shows the microhardness distributions across the weld line for the second run specimens for some experiments. It can be observed that the highest hardness values are located at the central weld zone (CWZ). This could be attributed to the very fine grains at the weld interface induced by the dynamic recrystallization as a result of the hot-heavy plastic deformation. The coarser grain in the thermo-mechanical zone (TMAZ) led to a reduction in the hardness (**Figure 5.13**). It was also observed that the weld-interface hardness decreased at lower value of friction pressure (Exp. 25).

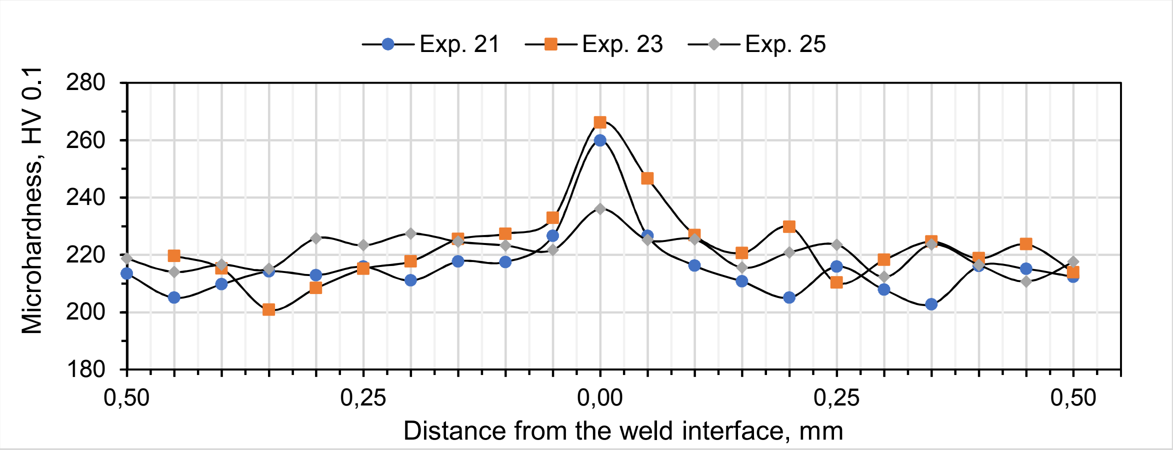

Figure 5.9 Microhardness distributions across the weld line for the second run specimens.

By statistical analysis using Minitab 17, an optimal level of combination of processing parameters is achieved. A contour plot is produced to display the region of the optimal factor settings. **Figure 5.10** and **Figure 5.11** present the contour plot of central weld length and flash width vs. friction pressure and rotational speed, respectively. It could be stated that the higher values of central weld length (dark green zone in **Figure 5.10**) could be achieved when utilizing higher values of P1 and rotational speed. However, the lower values of flash width could be attained when applying higher values of P1 and lower values of rotational speed. By analyzing the contour plots, the maximum achievable central weld length value was 3.88 mm, and the minimum flash width value was 1.86 mm. The optimized parameters that yielded the minimum metal loss were: friction pressure of 2.5 bar, forging pressure of 3 bar, friction time of 0.5 s, forging time of 2.5 s, and rotational speed of 12000 rpm.

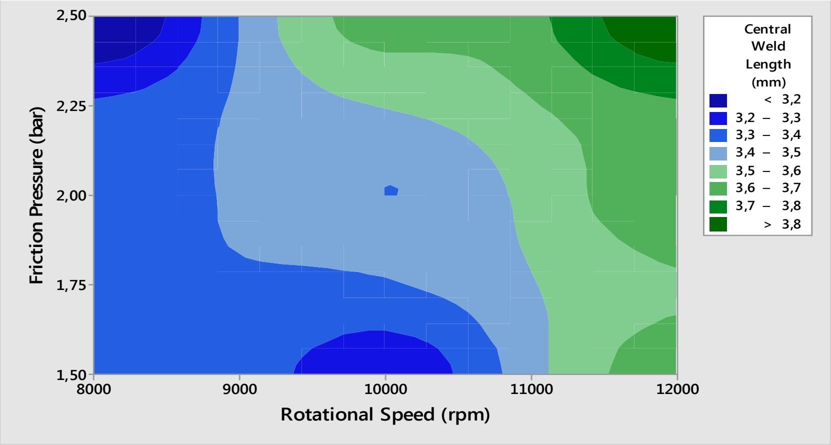

Figure 5.10 The contour plot of the central weld length vs. the friction pressure and rotational speed.

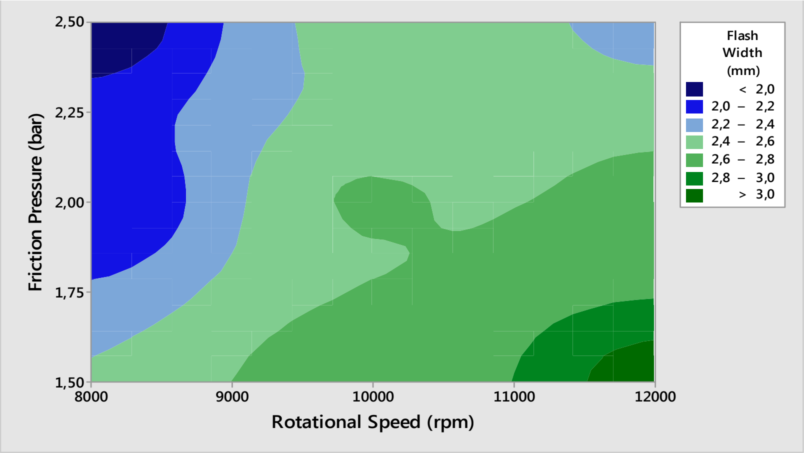

Figure 5.11 The contour plot of the flash width vs. the friction pressure and rotational speed.

5.1.2. Weld Joint Characterization

5.1.2.1. Macro- and Microscopic characterization

The rotary friction welding process leads to a drastic change of the microstructure. **Figure 5.12** shows the microstructure of cross-sectional view of CP-Ti friction welded joint. The central weld zone (CWZ) in the middle of the picture. Next to the CWZ the thermo-mechanical affected zone (TMAZ) (Zone II) is formed. A heat affected zone where grain coarsening may have occurred, cannot be found in the weld. Zone III is base material (BM) and consisted of undeformed equiaxed grains.

It can be seen that the microstructure is gradually changed toward the weld interface. The microstructure was clearly divided into CWZ, TMAZ and BM zones. In CWZ zone, the material is subjected to severe plastic deformation, therefore the grains close to this zone were completely recrystallized and consisted of very fine grain structure. Because of that, this region is also called as the transformed and recrystallized zone (TRZ). In TMAZ zone, the material is subjected to a considerable amount of plastic deformation. Moreover, the dislocation density is extremely increased due to the sufficiently high temperature, the material undergoes dynamic recrystallisation [12,13]. The grains in this zone are fine and elongated deformed grains. In BM zone, the strain rate, temperature and plastic deformation had no effect on the microstructure.

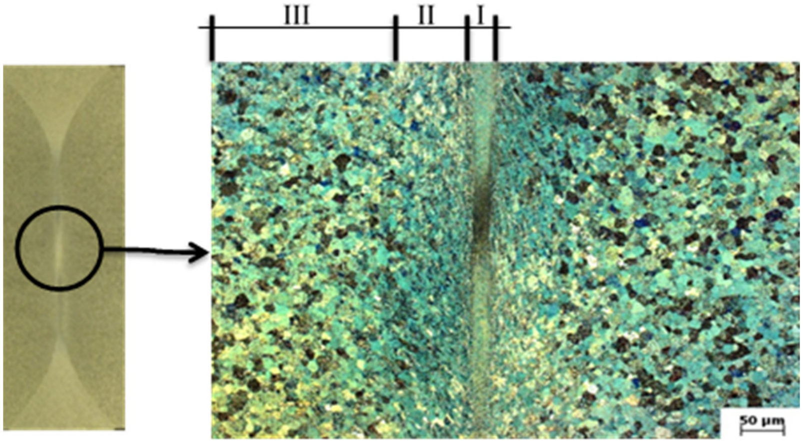

Figure 5.12 The microstructure of cross-sectional view of friction welded joint at AW state (zone I: CWZ, zone II: TMAZ and zone III: BM).

The post-weld heat treatment process was conducted at 550 °C/30 min air cooling (AC) to relieve most of the internal tensile RS induced during the welding process and to investigate later the effect of combining the thermal and/or mechanical treatment on the fatigue performance of the welded joints. The variation of the microstructure after PWHT was examined on the welded joint. The microstructure of the AW joint at higher magnification is shown in **Figure 5.13-a)**. The central weld zone (CWZ) is characterized by very fine grains that developed due to dynamic recrystallization during welding. The grains on TMAZ are extremely deformed because of severe plastic deformation. It was observed that after PWHT the grains in CWZ and TMAZ have been recrystallized to fine equiaxed grains and coarse equiaxed grains, respectively as show in **Figure 5.13-b)**, which means that recovery and recrystallization occurred during PWHT.

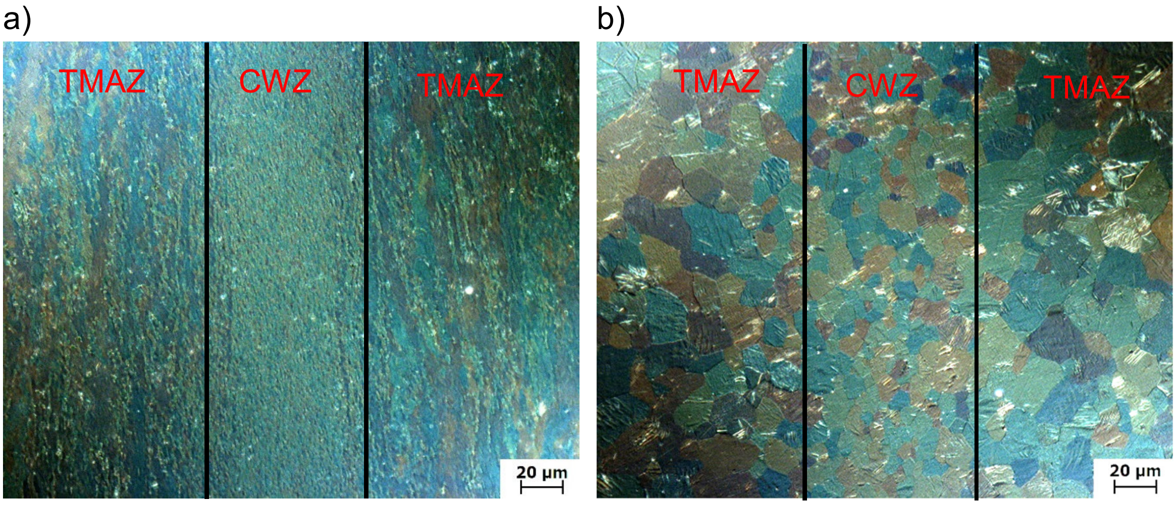

Figure 5.13 Typical microstructure of the different zones of a) AW and b) PWHT.

5.1.2.2. Microhardness-Depth Profiles

Figure 5.14 presents the microhardness distributions across the weld line of as-welded (AW) and post-weld heat treatment (PWHT) joints. The test data are average values obtained from three specimens. In the AW joint, the weld interface was harder than TMAZ and BM, which should be correlated to the formation of very fine grains at CWZ. It was observed that after PWHT the hardness of base metal (BM) and TMAZ did not change but hardness of CWZ decreased slightly. The reduction of micro-hardness on CWZ for PWHT could attribute to that grains became sparingly coarser than that of AW state due to recrystallization process (**Figure 5.13-b)**) [162].

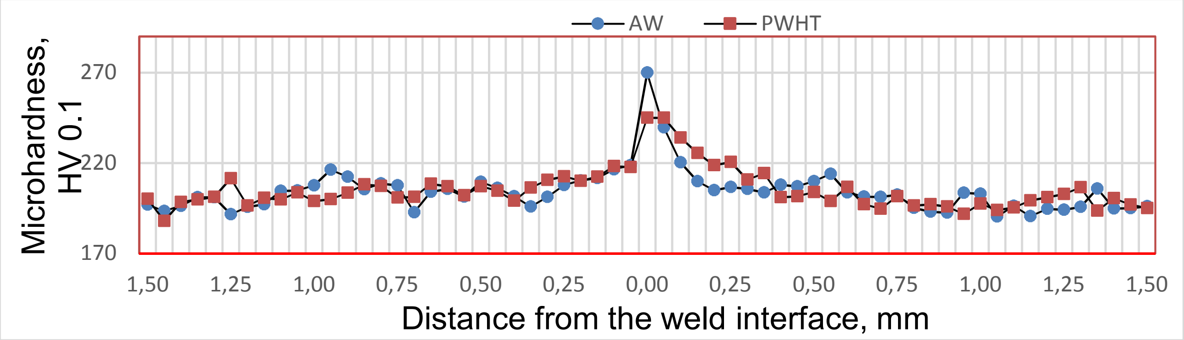

Figure 5.14 The microhardness distributions across the weld line of AW and PWHT CP-Ti joints.

5.1.3. Mechanical Surface Treatments

On one hand, the welded specimens were shot peened at an Almen intensity of 0.2 mmA using shot media of SCCW14 having an average shot size of 0.36 mm to full coverage. On the other hand, roller burnishing was performed on a conventional lathe and hydrostatic tool for the welded specimens using a hard metal roller (Ø 40 mm, r 2.5 mm) with a constant feed rate of 0.17 mm/rev, a rotational speed of 150 rpm and rolling pressure of 0.4 bar (rolling force 260 N). To identify the effect of SP and RB on the AW and PWHT joints, RS measurements, high cyclic fatigue (HCF) performance, surface roughness and impact toughness have been evaluated.

5.1.3.1. Residual Stress-Depth Profiles

The RS depth profile was determined from remaining strains using the incremental hole-drilling method (IHD). The subsurface (depth) residual stress distribution could be realized by mounting the strain gauge rosettes to the rounded-surface of the friction welded specimens after removing the flash as shown in the top left corner of **Figure 5.15**. Technical Note TN 503 by the Measurement Group [163] has clarified that the residual stress determination by the hole drilling method involves a higher number and variety of procedures and parameters than conventional experimental stress analysis. Therefore, the potential for error is correspondingly higher. Paul Barsanescu et al. [164] have reported that the accuracy of the hole-drilling strain-gage technique is directly related to the eccentricity between the hole center and rosette center. Although the drilling tool is optically adjusted, the eccentricity always cannot be zero, especially over the rounded surface. This eccentricity was probably the responsible for the unreasonable values of RS from the weld surface to a depth of 0.3 mm. In spite of that, **Figure 5.15** illustrates the relieving of tensile residual stress induced after welding by means of PWHT. While, these tensile stresses have been totally converted to compressive RS after utilizing SP process. It could be observed that the combination of PWHT and SP induces the highest compressive RS.

5.1.3.2. High Cycle Fatigue Performance

The S-N curves in rotating beam loading in air of SP, RB and electropolished (EP) friction-welded joints in AW state are shown in **Figure 5.17-a)**. Fatigue results of AW EP were included as a reference. The arrows in the figure represent specimens that did not break throughout the tests. SP and RB led to an apparent improvement of the fatigue performance of the friction welded joint compared to EP condition. Apparently, the 10^7 cycles fatigue strength of AW EP significantly increased from 240 MPa to 410 MPa and 400 MPa after SP and RB, respectively. This resulted in an enhancement of the fatigue life of welded joints by about 71% after SP and by 66% after RB. It was observed that the AW EP samples had been broken in the weld zone after fatigue test. This could be explained by the developed tensile RS during welding [153-154]. After SP and RB, the fracture of the fatigue samples occurred outside the weld zone in the base metal. This could be attributed to the converting of welding tensile RS with local compressive RS at the weld zone as indicated in **Figure 5.15**. Such improvements have revealed that failure is associated with subsurface fatigue crack nucleation.

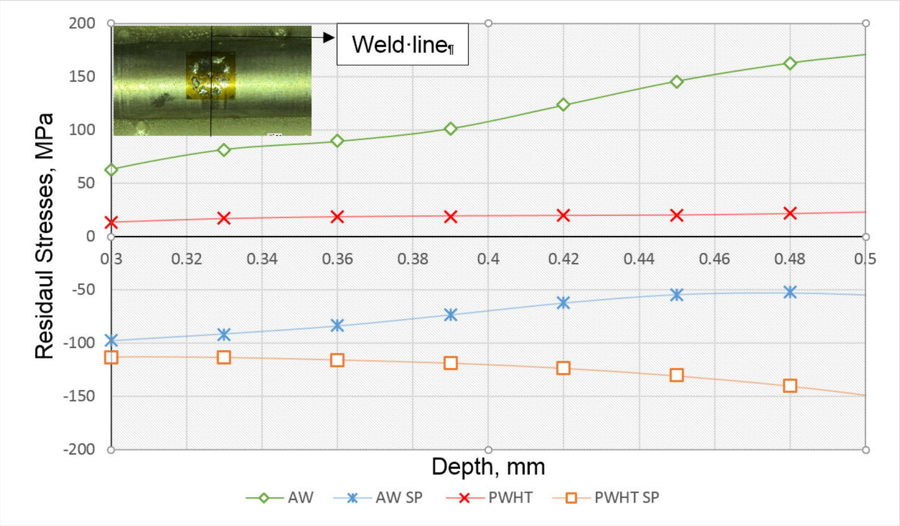

Figure 5.15 Subsurface residual stress distribution of CP-Ti welded joints at various treatments.

Figure 5.17-b) shows the effect of post-weld heat treatment on the fatigue performance of the welded joint. Obviously, the endurance limit of PWHT increased from 260 MPa to 450 and 400 MPa after SP and RB, respectively. This resulted in improvement of fatigue life of PWHT joints by 73% after SP and 53% after RB. It can be seen that the improvement of the high cycle fatigue (HCF) after SP was superior to that after RB. That may be attributed to the higher compressive RS induced by shot peened joints, in view of that the failure in HCF controlled by crack propagation [165]. The lower compressive RS induced in RB joints may be as a result of using low rolling pressure (0.4 bar) during the RB process. On the other side, it was observed that the low cycle fatigue (LCF) performance of RB joints was more improved than of SP joints. That could be attributed to the lower surface roughness of the RB joints than SP joints as shown in **Figure 5.16**, where the failure in LCF controlled by crack initiation [166]. As seen in **Figure 5.16**, the surface roughness of shot peened welded joints is much higher than that of the EP reference, while a remarkable improvement on the surface roughness was observed after RB compared to that after SP. Also, it could be noted that roughness of SP and RB after PWHT is slightly lower than that after AW.

Figure 5.17-c) shows S-N curves of all combined treatments. A slight enhancement of the fatigue life has been established after PWHT without utilizing mechanical surface treatments, because the PWHT has probably reduced the tensile RS formed during the welding process [134]. In additions, the fatigue life of PWHT SP and PWHT RB is higher than that of AW SP and AW RB. Probably because of SP and RB for AW state required first to remove the welding tensile RS and then induce compressive RS if applicable, while SP and RB for PWHT state may directly induce compressive RS owing to PWHT has already reduced or relieved the welding tensile stresses. The most improvement of the fatigue life obtained after a combination of SP and PWHT from 240 MPa to 450 MPa by about 87% enhancement. It could be

concluded that the combination of thermal and mechanical treatments effectively improves the fatigue performance of the welded joints.

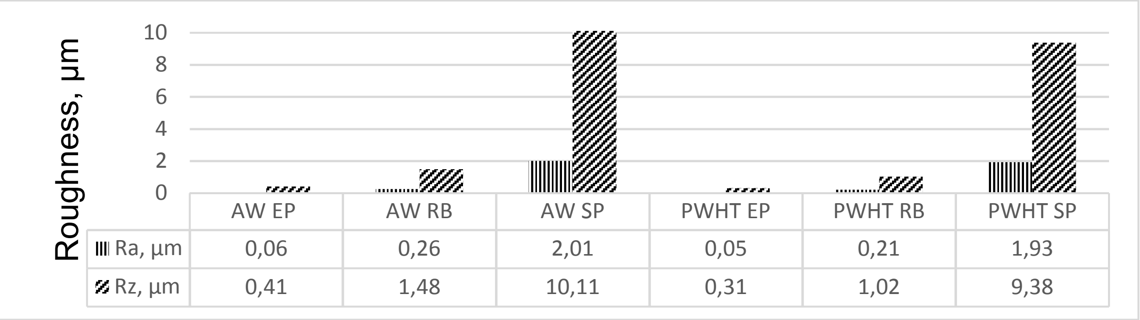

Figure 5.16 Surface roughness after various surface treatments.

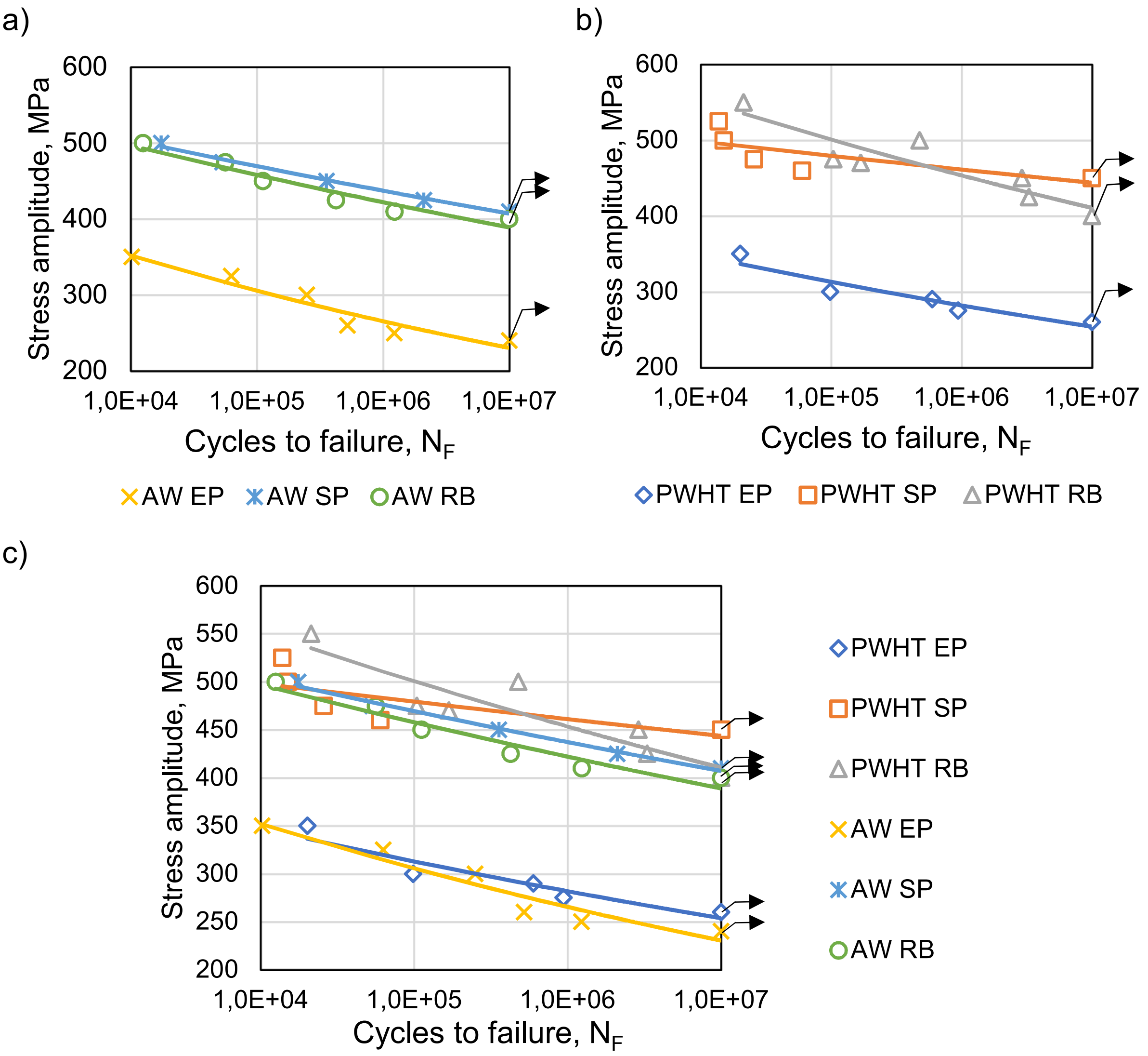

Figure 5.17 S–N curves after various surface treatments for a) as-welded joint, b) PWHT joint and c) comparison of all pairs of treatments.

5.1.3.3. Impact Toughness

Charpy impact energy data for the base metal as well as for friction welds for varying treatment conditions are presented in **Figure 5.18** and **Table 5-6**. As mentioned in **section 4.4.2**, the sub-size impact toughness has been correlated to the full-size impact toughness according to ASTM STP 1380 [132]. The notched impact tests a quality control test does allow comparison within the prescribed conditions. An examination of the results indicates that the Charpy energy increases for AW state and decreases for PWHT state as compared with BM. In addition, the impact toughness values of AW were observed to be reduced after applying SP. However, impact energy of PWHT increases after SP.

This may be proved by observing the fractographs for the base metal and welds with various treatments, as shown in **Figure 5.19**. The ductile behavior was verified accompanied by lateral expansion of the fractured surfaces. One can observe the presence of large, elongated fracture features and the much larger void sizes in base metal of CP titanium as shown in **Figure 5.19-a)**. That probably due to extensive plastic flow during crack extension and relatively low number of boundaries (mostly α/α grain boundaries) that are barriers to slip transmission [168]. From **Figure 5.19-b)**, a very clear evidence of the reduced toughness in case of welded samples can be observed; whereas, the AW joint fractures in a quasi-cleavage mode with radial fan-shaped tear ridges around the impact initiation area (crack origin). This fracture occurs along the basal plan (0001) when the local normal stress across the cleavage plane exceeds a critical value [169]. That can be explained that the crack front is deviated in the direction of expansion due to the different resistance so that the crack begins to grow along a series of planes with a height variation, and the different fracture surfaces intersect to form a step. These steps establish the characteristic morphology of the radial fan-shaped tear ridges on the impact fracture [170]. The reduction in impact energy of AW after SP probably because of surface crack initiation as shown in **Figure 5.19-c)**.

Figure 5.19-d) shows an example of ductile stretching and tearing fracture after PWHT. Ductile dimples, large void size and main cracks can be observed on the fractured surface. That probably the responsible for the reduction of impact energy compared to AW. In additions, the recrystallized equiaxed grains (**Figure 5.13-b)**) in CWZ and TMAZ during PWHT can be another reason for the lack of impact toughness. Interestingly, after SP, ductile dimples fracture with a small quantity of quasi-cleavage fracture dominates the fracture mode of PWHT SP specimens as shown in **Figure 5.19-e)**, which in turn caused the toughness to improve. Furthermore, the crack path shows that the impact failures occurred in the base metal of AW (**Figure 5.20-a)** and **b)**). While, the failure of PWHT occurred in weld zone (**Figure 5.20-c)** and **d)**), which illustrate the reduction in impact toughness of PWHT.

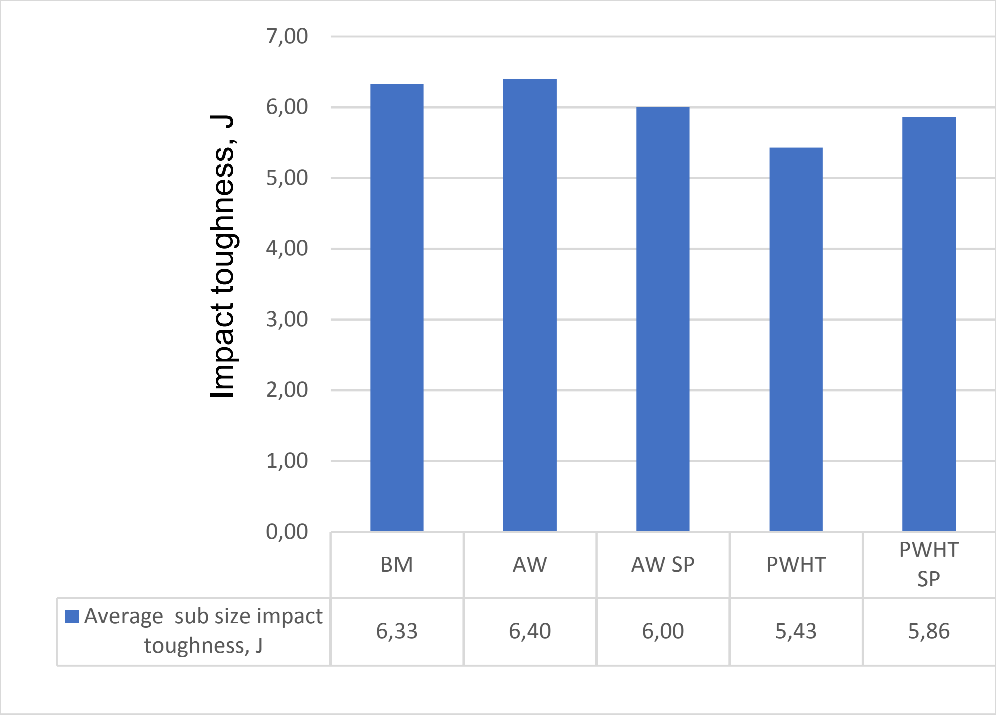

Figure 5.18 Average sub-size impact toughness of the prescribed conditions.

Table 5-6 Impact toughness values of the base metals and friction welded joints at room temperature.

	Impact toughness, J	Avg. sub-size impact toughness, J	Avg. full-size impact toughness, J
BM	6.5	6.33	130
	6.2		
	6.3		
AW	6.3	6.4	135
	6.4		
	6.5		
AW SP	6.4	6	120
	6		
	5.6		
PWHT	5.3	5.43	108
	5.6		
	5.4		
PWHT SP	5.9	5.86	115
	6		
	5.7		

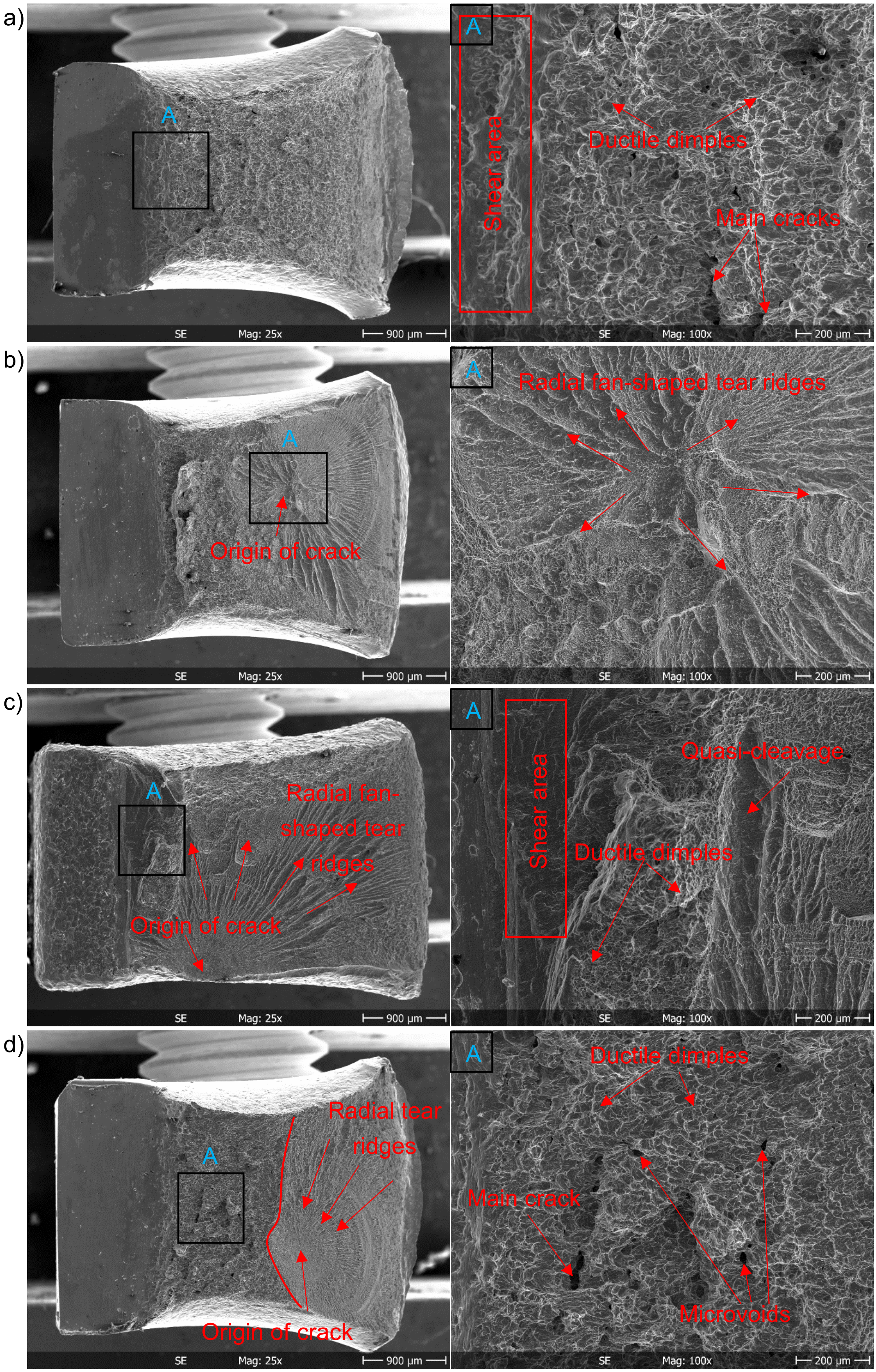
a)
A
SE Mag: 25x 900 µm
A
Shear area
Ductile dimples
Main cracks
SE Mag: 100x 200 µm
b)
A
Origin of crack
SE Mag: 25x 900 µm
A
Radial fan-shaped tear ridges
SE Mag: 100x 200 µm
c)
A
Radial fan-shaped tear ridges
Origin of crack
SE Mag: 25x 900 µm
A
Shear area
Quasi-cleavage
Ductile dimples
SE Mag: 100x 200 µm
d)
A
Radial tear ridges
Origin of crack
SE Mag: 25x 900 µm
A
Ductile dimples
Main crack
Microvoids
SE Mag: 100x 200 µm

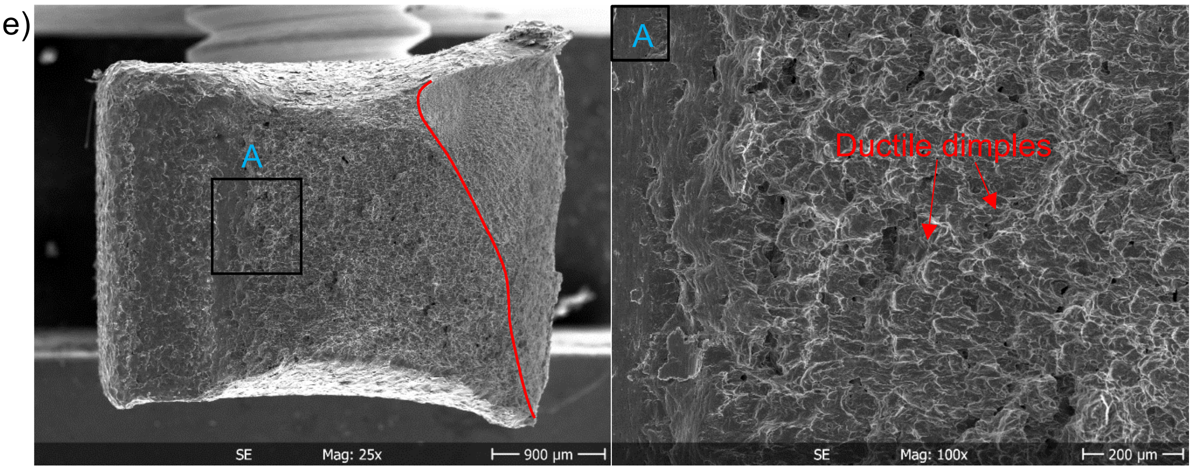

Figure 5.19 Fracture appearances after impact testing for a) BM, b) AW, c) AW SP, d) PWHT, e) PWHT SP. Region A is magnified right to the fracture pattern.

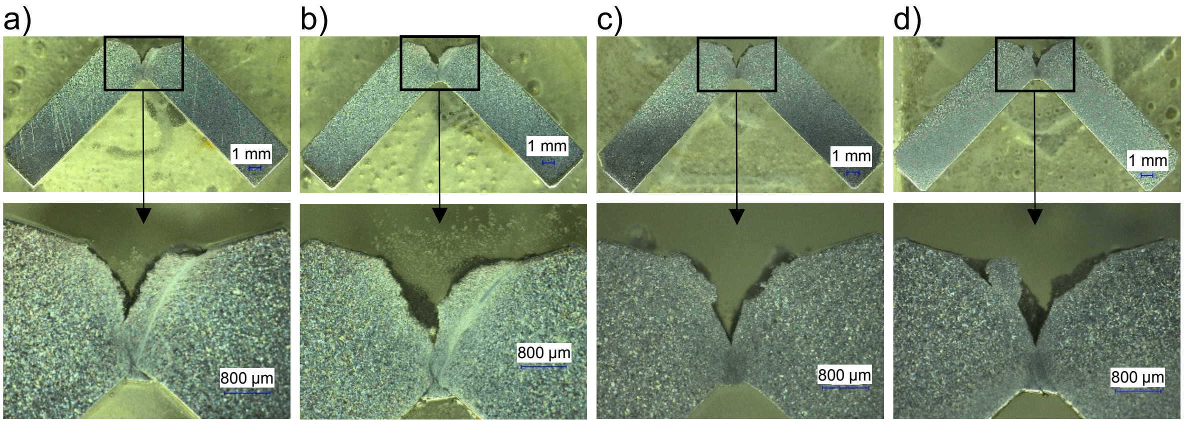

Figure 5.20 Cross-sectional view of the fractured samples after impact test a) AW, b) AW SP, c) PWHT and d) PWHT SP.

5.2. Characterization of Ti-6242 Orbital Weld Joints

In this part, the orbital friction welding was performed in the force-displacement mode on multi-orbital friction welding machine. The optimized orbital friction welding parameters have been taken from a previous study [54]. The optimized weld joint characterizations have been conducted through the tensile test, micro-hardness, impact toughness, and microstructure to investigate the mechanical and metallurgical characterization of welded joints. An attempt was made to optimize the shot peening (SP), and roller burnishing (RB) parameters of the Ti-6242 orbital friction welded joints. The aim was to enhance the surface layer properties, fatigue performance, as well as the impact toughness at both as-welded (AW) and post-weld heat treated (PWHT) conditions. The fatigue behavior of AW and PWHT joints before and after SP and RB were compared. Fatigue crack nucleation sites were investigated by scanning electron microscopy (SEM). The depth profile RS and surface residual stress distribution across the weld line has been measured using the incremental hole-drilling method (IHD) and Laboratory X-Ray Diffraction (LXRD), respectively.

5.2.1. Weld Joint Characterization

5.2.1.1. Microscopic characterization

OFW was performed on a multi-orbital friction welding machine dyconn-100 (see details in **section 3.3.2**). From visual inspection of the interface region in the OFWed Ti-6242, an obvious flash from all four sides of the joint was observed which is sometimes reflects the quality of weld [171]. **Figure 5.21** illustrates that material was expelled in all directions. Hence, it can be assumed that a sound welding of the entire cross section was generated. The axial shortening of welded specimens was estimated to be about 3 mm, which is enough to form a sound weld according to Raab et al.'s results [51,52].

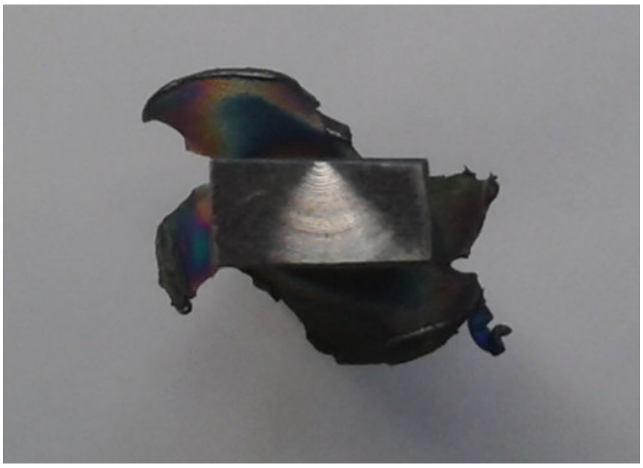

Figure 5.21 Top view of the formed flash during welding.

The orbital friction welding process leads to a severe change of the microstructure. **Figure 5.22** shows the cross-sectional microstructure of a OFW Ti-6242 sample along the oscillation direction in as-welded (AW) and post-weld heat treated (PWHT) conditions. The microstructure shows a gradual change from the weld interface towards the parent materials. The central weld zone (CWZ) in the central of the picture stands out less textured and a bit lighter microstructure than that of base metal. Next to the CWZ the thermo-mechanical affected zone (TMAZ) shows a bit darker microstructure than CWZ and lighter than the base metal. A heat affected zone cannot be recognized in the weld.

From **Figure 5.22-b)**, it can be observed that the CWZ and TMAZ has slightly darkened by the heat treatment. An explanation for this could be a lower content of α-stabilizers in the matrix. Due to the heat of the welding, the CWZ and parts of the TMAZ come to dissolve the primary α-phases due to temperatures in the upper α-β range. As a result, the α-stabilizing aluminum goes into solution, resulting in a higher corrosion resistance of the β-matrix. Due to the heat treatment, the aluminum atoms agglomerate and form secondary α-precipitation particles, which reduces the resistance to Kroll etchant [54].

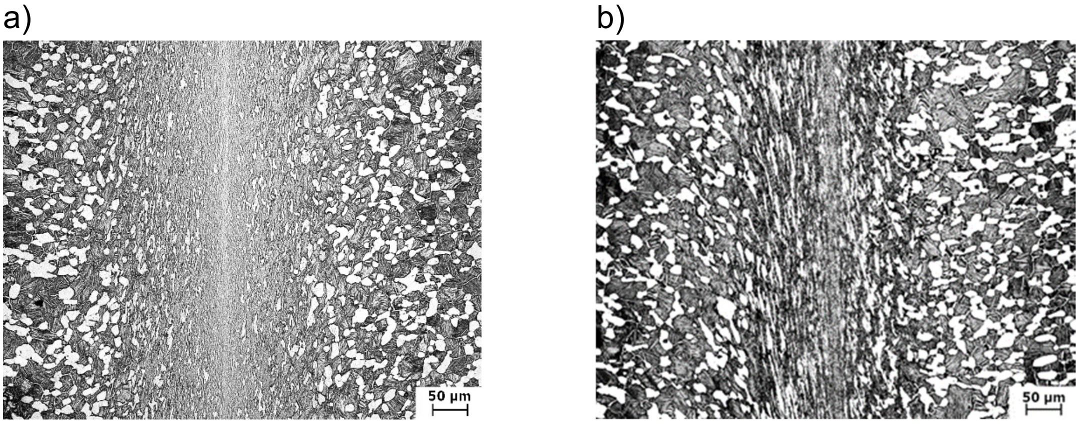

Figure 5.22 Cross-sectional microstructure of OFW Ti-6242 sample along the oscillation direction in a) as-welded (AW) and b) post-weld heat treated (PWHT).

A comparison of the microstructure in the center of the weld at higher magnifications of AW and PWHT is shown in **Figure 5.23**. From this Figure, it can be found that the width of CWZ can be limited to about 30 µm before it merges into the partially recrystallized area of the TMAZ. The TMAZ extended for about 112 µm from CWZ on both sides. It is noticeable here that the TMAZ has slightly darkened after PWHT owing to a lower content of α-stabilizers in the matrix. The central weld zone (CWZ) is characterized by a grain fined microstructure that developed due to dynamic recrystallization during welding. Next to the CWZ the thermo-mechanical affected zone (TMAZ) shows severe plastic deformation of the parent material. Between CWZ and TMAZ the primary alpha phase dissolved completely. In the TMAZ partially dissolved primary alpha grains are visible. These finding give rise to the assumption that the welding temperatures exceeded the beta transus of Ti-6242 (995 °C) [51].

The microstructure close to the weld zone shows highly deformed α_p nodules, elongated following the friction movement direction as shown in **Figure 5.24**.

Figure 5.23 Microstructure in the center of the weld at higher magnifications of a) AW and b) PWHT.

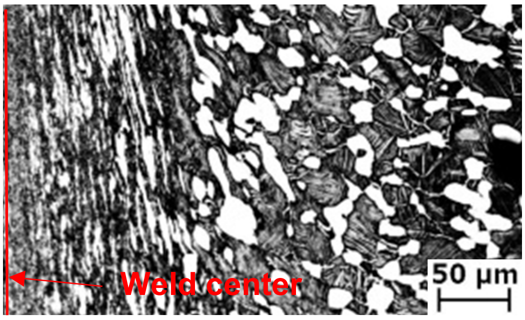

Figure 5.24 Microstructure in one side when approaching the weld center.

The microstructure development in the CWZ can be significantly influenced by the welding process. Greatest temperature at weld interface, cooling rate, joining surface and pressure have a strong influence on the configuration of the microstructure in the CWZ [54]. A very fine-grained structure is typical of microstructures in this region, which is related to the material being exposed to high temperature and strain resulting in dynamic recrystallisation. Directly in the CWZ the microstructure is too fine to be resolved by optical microscope. Therefore, more powerful technique, such as SEM was used. **Figure 5.25** shows a higher magnification picture of the microstructure at CWZ of AW condition. This very fine microstructure (about 2 µm) is characteristic of OFW and evolves from the fact that the temperature during the process exceeds the β -transus in a small volume of material and the cooling rate for this small volume is very high [172].

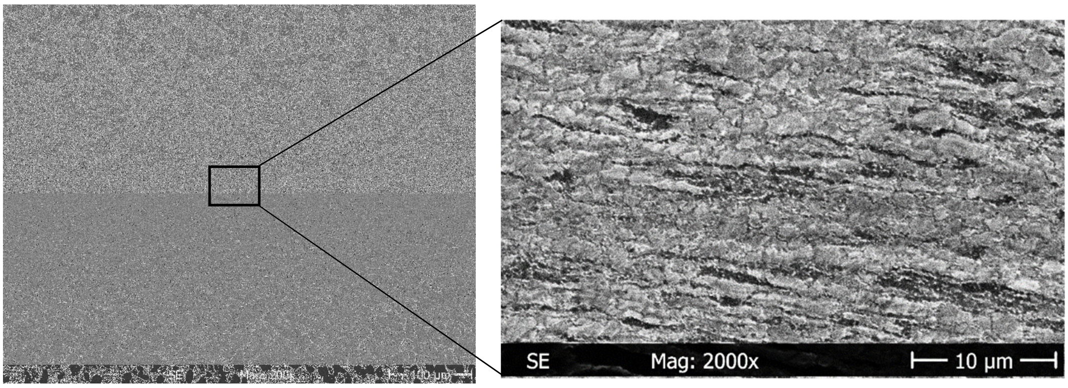

Figure 5.25 A SEM picture of the weld zone of AW condition.

5.2.1.2. Tensile Test

Tensile testing was performed on both the as-received and the welded specimens in AW and PWHT conditions. The average yield strength (YS), ultimate tensile strength (UTS), elongation (EL) and reduction of area (RA) are summarized in **Table 5-7**. It is worth noting that all the fractures of AW and PWHT specimens occurred in the base metal. This fact suggests that the weld yielded a higher strength than the corresponding base metal in both AW and PWHT conditions, which also agrees with the microstructure observation of CWZ which strengthened owing to the very fine-grained structure. Moreover, the result also means that the TMAZ has little effect on the strength of welded specimens, not like that in FSW process [173]. Therefore, it can be concluded that OFW of Ti-6242 could be successfully carried out without the introduction of some defects into the weld. The PWHT specimens show slightly higher ductility than that of the base metal and AW specimens.

Table 5-7 Tensile tests Results of Ti-6242 for as-received, AW and PWHT conditions.

	YS, MPa	UTS, MPa	EL, %	RA, %	Fracture location
as-received	890	975	16.4	34	
AW	946	1037	16.1	36	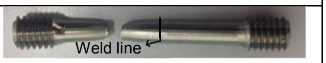
PWHT	940	1024	17.5	37	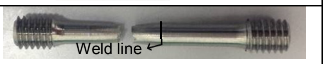

5.2.1.3. Microhardness-Depth Profiles

The measurement of the microhardness is a standard method for the characterization of friction welded joints. Owing to hardness variations between the base metal and the weld zone, the HAZ can be identified as well as strengthening and softening processes by the microstructure development in the weld zone can be detected. Therefore, hardness variations with the microstructure development in CWZ, TMAZ and HAZ are related [54].

The microhardness profiles obtained from AW and PWHT welds are presented in **Figure 5.26**. The average of three measurements was taken at each point across the weld line. The Ti-6242 base metal has an average hardness value of about 360 HV. For the AW specimen, the hardness of the weld interface is generally of about 60 HV higher than that of the parent material attributed to the grain refinement by dynamic recrystallization in CWZ, which provide improved strength at the wild line relative to the base metal. This increase in hardness give rise to the assumption that α`` Martensites are not precipitated from β phases in CWZ, which normally resulting in reducing the microhardness of weld zone [174]. Owing to the partially recrystallized region of the TMAZ, a hardness drop from CWZ towards base metal occurs. After PWHT, the hardness of Ti-6242 shows a slight increase in the weld region and the highest hardness value which is consistent with Li et al. results [175].

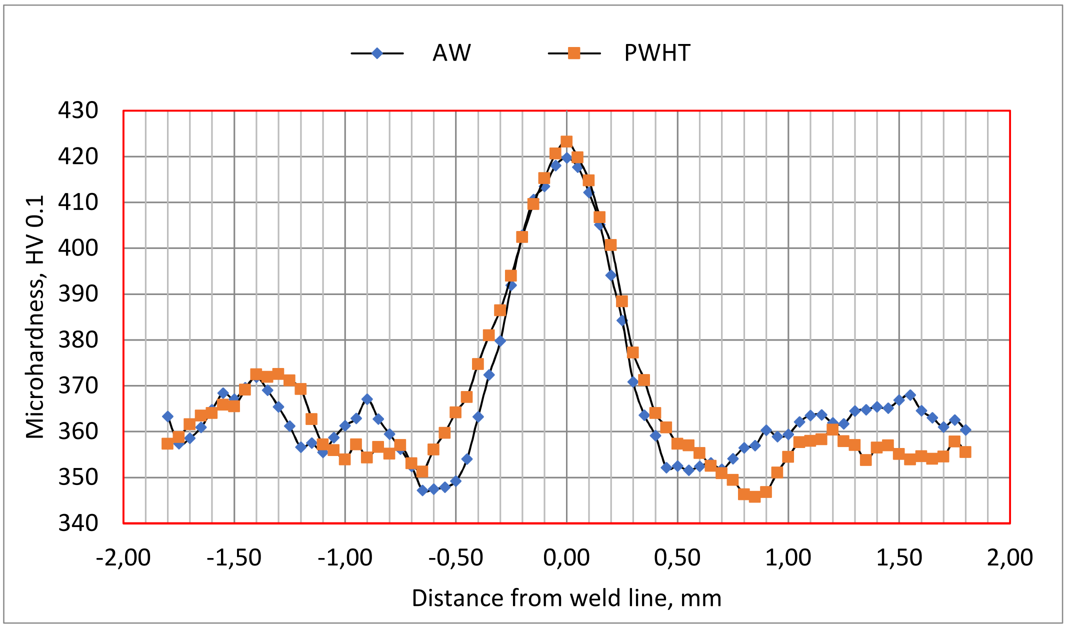

Figure 5.26 Microhardness distributions across the weld line of AW and PWHT Ti-6242 joints.

5.2.2. Mechanical Surface Treatments

5.2.2.1. Shot Peening (SP) Optimization

SP parameters optimization were carried out for Ti-6242 orbital friction welded joints on the AW and PWHT state. The optimization process was performed at a wide range of peening pressures next to variable Almen intensities. **Figure 5.27** shows the effect of Almen intensity on fatigue life at a stress amplitude (σa) of 600 MPa in AW and PWHT joints. It can be seen that the cycles to failure in Ti-6242 welded joints depend on Almen intensity. Compared to the reference EP welded specimens, the fatigue life first dramatically increases, then drops slightly at higher Almen intensity. Regarding the fatigue performance, the Almen intensity of 0.2 mmA is taken as the optimum in both AW and PWHT, which stands for a very common intensity for the present shot media (SCCW14) to be applied on aerospace components made of Ti alloys [109].

Noticeably, SP of Ti-6242 welded joints after PWHT increases the fatigue behavior at all Almen intensities more than that after AW.

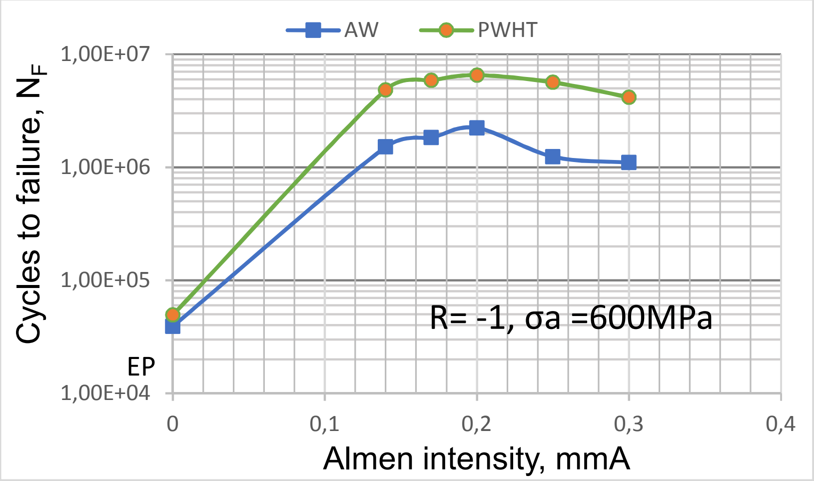

Figure 5.27 Fatigue life versus Almen intensity (σa = 600 MPa) in Ti-6242 welded joints after SP.

Figure 5.28 shows the effect of various Almen intensities on near-surface microhardness depth profile of welded joints for AW and PWHT conditions. AW EP and PWHT EP were included as a reference to compare with the peened data. Hardness profiles revealed the existence of a work hardened layer in the peened specimens. Owing to the induced plastic deformation after SP the surface layer hardness increases for all Almen intensities of both AW and PWHT conditions followed by a gradual decrease in hardness towards the interior. The bulk hardness value was about 360 HV0.1, while the hardness values at the surface reached about 390 HV0.1 after SP. It can be seen that the microhardness close to the surface increased with increasing Almen intensity. Therefore, the most increase in surface hardness was found at 0.3 mmA for both AW and PWHT conditions. However, the fatigue behavior is negatively affected by increasing the Almen intensity (**Figure 5.27**). It is well known that the heavier shot peening not only results in lower near surface residual compressive stresses, but also increases roughness and induces microcracks [166]. Therefore, the drop in fatigue life can be attributed to the increase of surface roughness with increasing Almen intensity [104,105]. In additions, the significant overlapping and microcrack formation. on the surface at higher Almen intensity (**Figure 5.29**) acts as crack nucleation during the fatigue test.

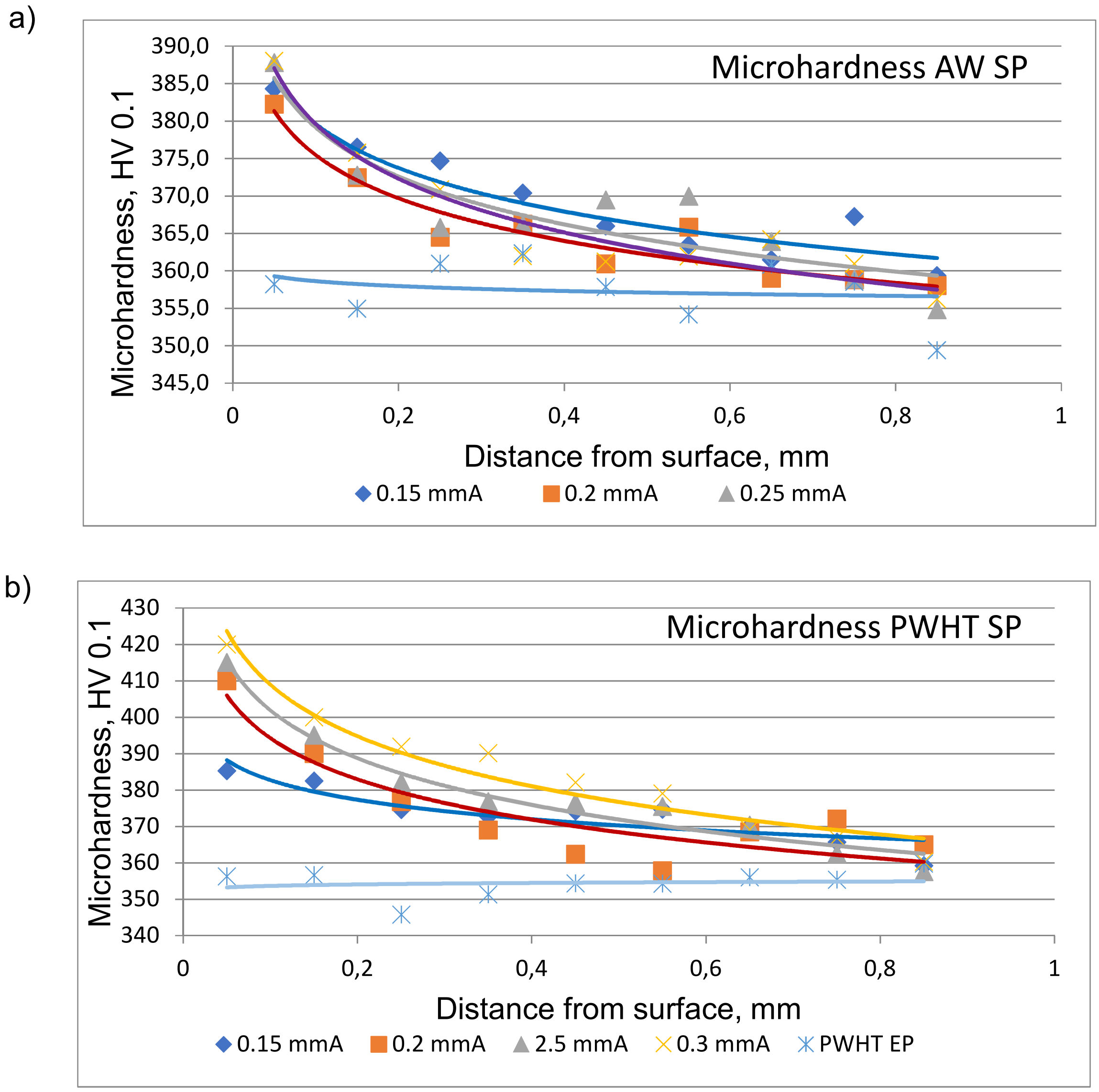

Figure 5.28 Near-surface hardness depth profiles at various Almen intensities of a) AW and b) PWHT.

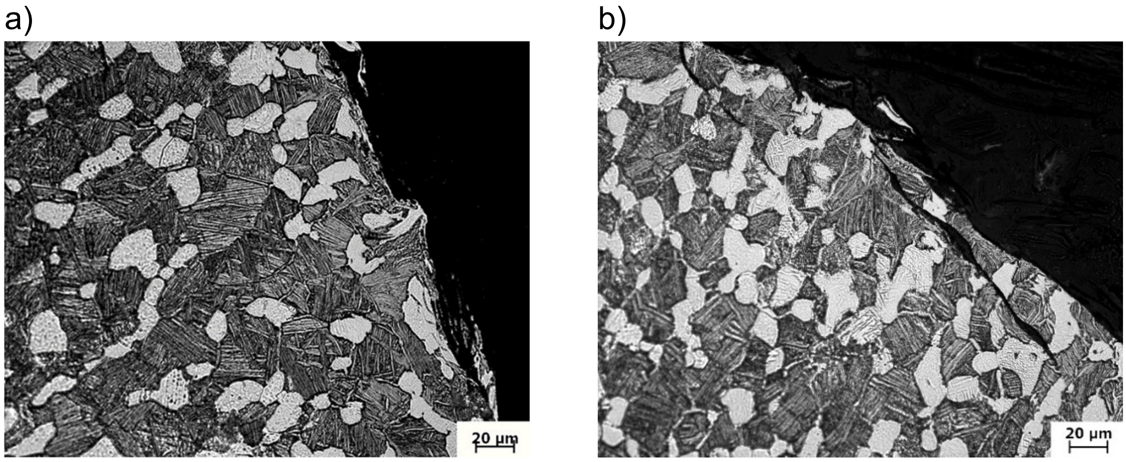

Figure 5.29 Section topographies of peened AW specimens at high Almen intensities a) 0.25 mmA and b) 0.3 mmA.

5.2.2.2. Roller Burnishing (RB) Optimization

The burnishing pressure was varied from 0.4 to 1.8 bar on Ti-6242 Welded joints. **Figure 5.30** shows the fatigue life as a function of burnishing pressures at stress amplitude of σa = 600 MPa for the AW and PWHT joints. Unlike SP, AW and PWHT conditions have almost the same fatigue behavior after applying RB. The cycles to failure first increases with increasing the burnishing pressure and then drops drastically after burnishing with higher burnishing pressures. The fatigue life drop may be attributed to the occurrence of surface layers flaking due to the shear failure of the layers after using high burnishing pressure values [176]. This flaking was also responsible for the reduction of near-surface microhardness at burnishing pressure of 1.8 bar in both AW and PWHT conditions as shown in **Figure 5.31-a)** and **-b)**, respectively. This Figure illustrates the effect of various burnishing pressure on near-surface microhardness depth profile of welded joints for AW and PWHT conditions. Like SP, RB results in marked hardening in the surface layer. However, it can be noted that the microhardness increased with burnishing pressure up to certain extent and then decreased, which is consistent with the results from previous reports [177,178]. N. Rao et al. [177] reported that higher work hardening of surface layer will lead to flaking effect, which is the main cause for decrease in surface hardness with higher and higher burnishing pressures.

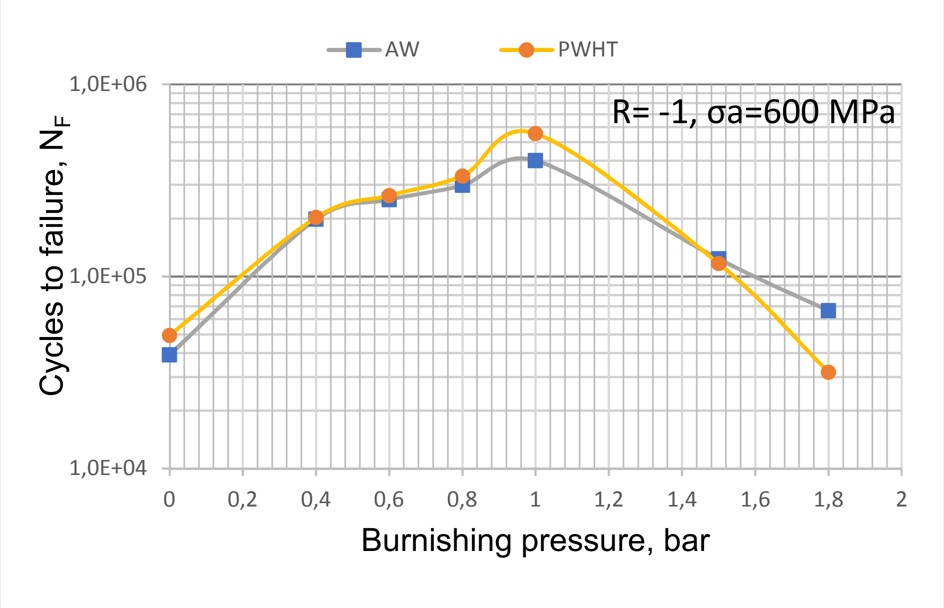

Figure 5.30 Fatigue life versus burnishing pressures (σa = 600 MPa) in Ti-6242 welded joints after RB.

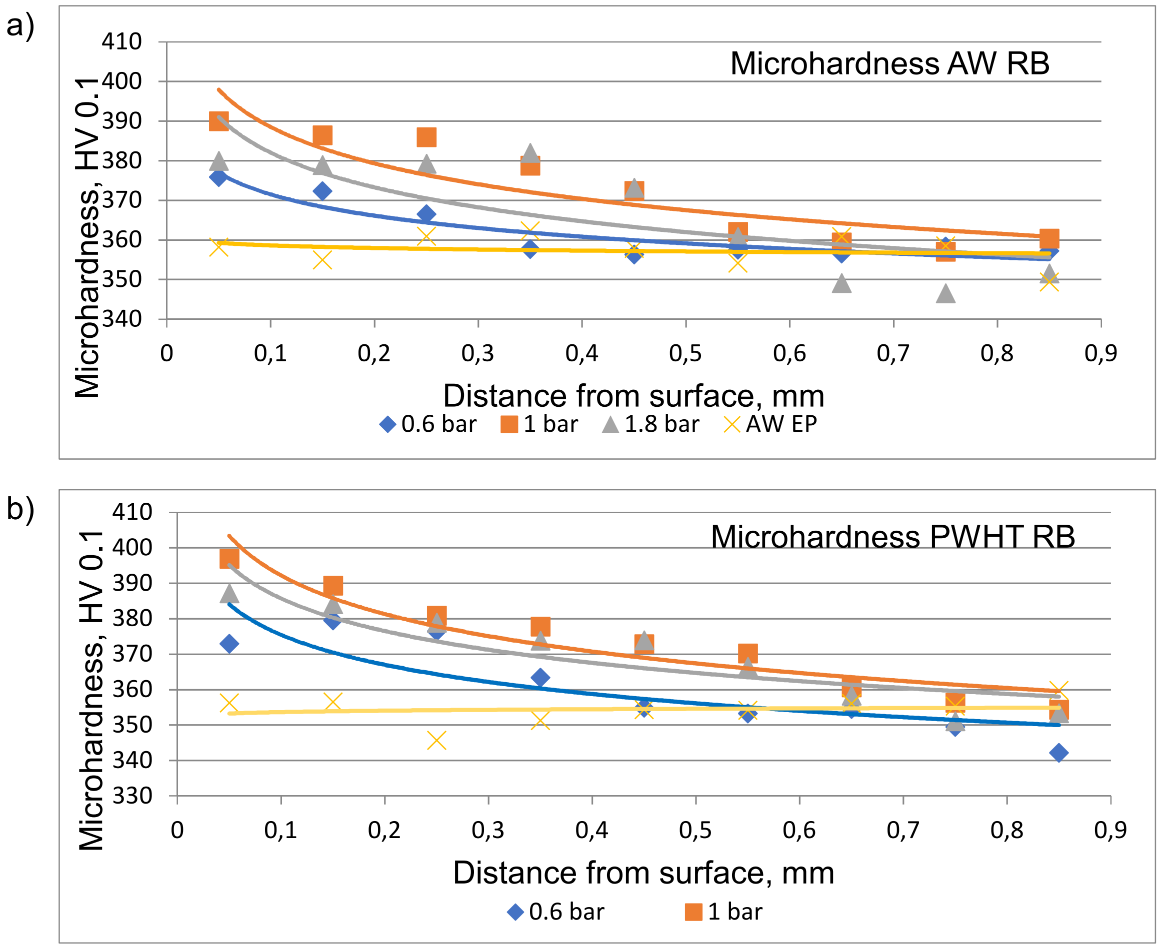

Figure 5.31 Near-surface hardness depth profiles at various burning pressures of a) AW and b) PWHT.

5.2.3. Evaluation of the Mechanical Surface Treatments

This beneficial effect of the mechanical surface treatments on the HCF performance was interpreted by microhardness, surface roughness, surface morphology, compressive residual stress in the surface layers and crack nucleation site.

5.2.3.1. Microhardness-Depth Profiles

Figure 5.32 compares the near-surface hardness depth profiles at various optimized surface treated conditions on parent material. It was found that the bulk hardness in PWHT EP condition is slightly lower than that of AW EP, which is consenting with the tensile test results (**Table 5-7**). This decrease of the hardness after PWHT is explained by the recovery influence. The maximum microhardness induced by SP and RB for AW and PWHT conditions was observed at the surface which gradually decreased in the near-surface regions. The microhardness at the SP surface after PWHT increases approximately by 50 HV0.1 as opposed to the bulk material. The observed surface layer strengthening in both PWHT SP and PWHT RB is much greater than of AW SP and AW RB. This result being related to the more marked strain hardening capability of PWHT condition compared to AW condition. That can explain later the lower fatigue performance of AW condition after SP and RB (see **section 5.2.3.3**).

The near-surface hardness depth profiles on the weld interface at various optimized surface treated conditions is represented in **Figure 5.33**. unlike the microhardness-depth distributions of parent material, it was seen that the microhardness at the surface was lower than at the near-surface regions. In addition, the mechanical surface treatments did not have the same effect on increasing the weld interface hardness, whereas the microhardness at the weld interface after SP and RB increases approximately by 20 HV0.1 as opposed to the weld interface after EP. That could be attributed to the higher hardness value at weld interface due to the grain refinement in CWZ as illustrated in **Figure 5.26**.

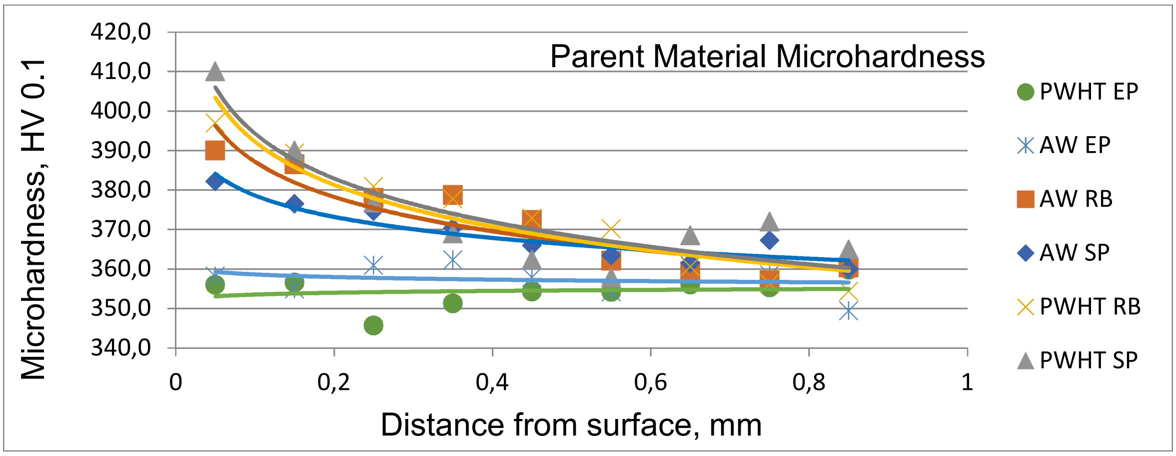

Figure 5.32 Near-surface hardness depth profiles at various optimized surface treated conditions on parent material.

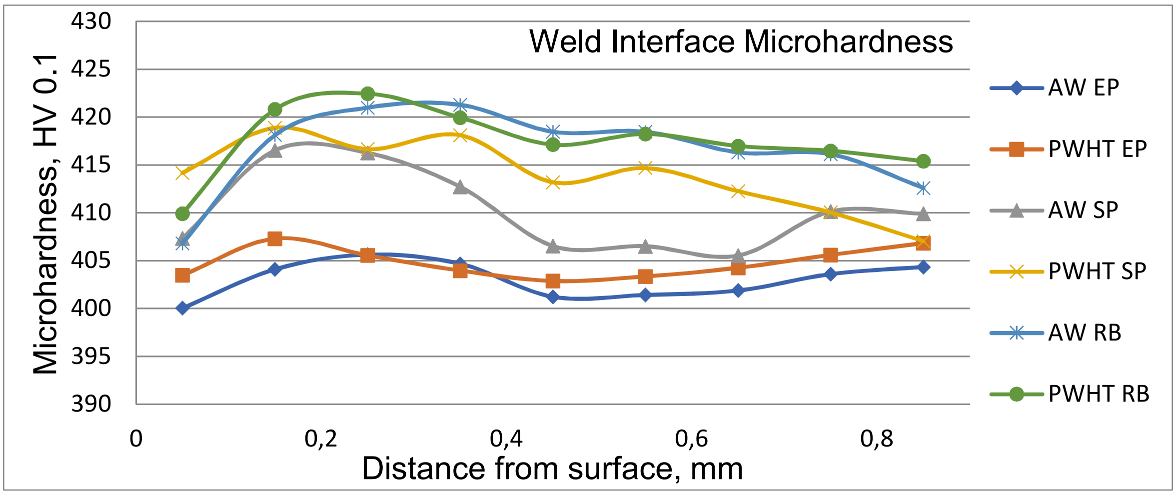

Figure 5.33 Near-surface hardness depth profiles on the weld interface at various optimized surface treated conditions.

5.2.3.2. Residual Stresses

Even though no melting is involved in friction welding processes and thus the local heat input is lower than for conventional fusion welding methods, they are also characterized by significant RS [179]. The origin of the strain development during OFW is caused by the combination of thermomechanical deformation, and the constraints to thermal expansion. The formation of flash is directly correlated with the presence of tensile strains in the weld plane [180]. Therefore, the effect of PWHT and mechanical surface treatments (SP and RB) or combination of them on residual stresses in the orbital friction welded joints was examined. Surface residual stress distribution was conducted by using Proto-LXRD (laboratory residual stress measurement system) at Curtiss-Wright Surface Technologies (CWST) in the USA. While, the depth profile RS were calculated from remaining strains using the incremental hole-drilling method (IHD). (More details in **section 3.8.5**)

5.2.3.2.1.Proto-LXRD

The surface RS near the weld line (± 2.5 mm) for the as-welded, PWHT, AW SP and PWHT SP are shown in **Figure 5.34**. The residual stress profiles of AW and PWHT conditions show a characteristic shape typical of linear friction welds [180-182]. High tensile stresses arise within CWZ of AW joint. Notably, this tensile region is relieved after PWHT. It can be seen that 100% of the tensile stress is not removed by stress relieving. However, any reduction of tensile stresses is beneficial from a fatigue standpoint. This figure proves the large stress reversal induced by SP. The 300 MPa tensile stresses has been converted to about 670 and 780 MPa compressive stresses for AW SP and PWHT SP, respectively. Meanwhile less tensile/more compressive stress is better, one can see noticeable benefits from shot peening welds. Remarkably, the induced compressive stresses on parent material is higher than of that on CWZ for AW SP condition. This can explain later the reason for cracking the fatigue specimens in the welding zone for AW SP conditions

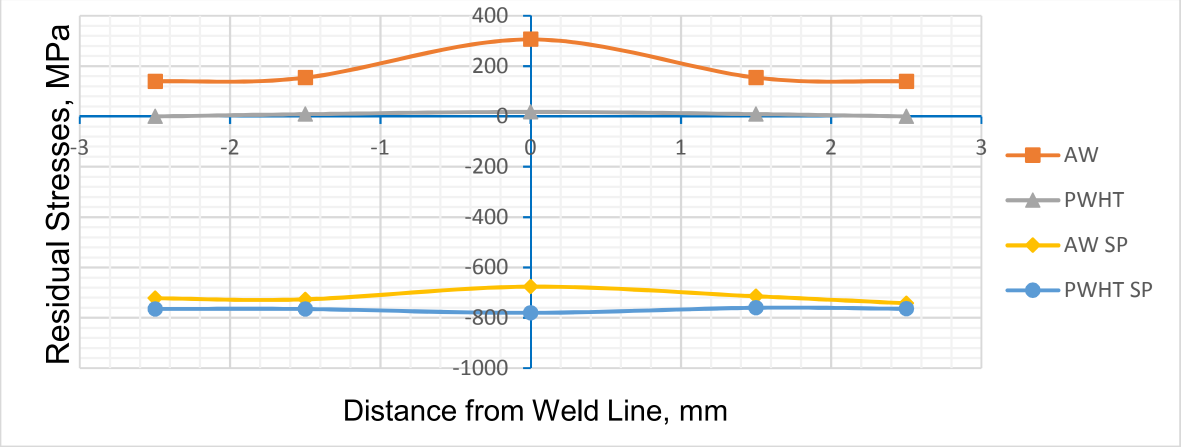

Figure 5.34 Surface RS for the as-welded, PWHT, AW SP and PWHT SP.

5.2.3.2.2.IHD

The depth profile RS at the weld interface of PWHT, PWHT RB and PWHT SP are illustrated in **Figure 5.35**. Both SP and RB result in compressive RS with pronounced maxima below the surface. In SP, the maximum values are clearly higher than that of RB. The residual stress profiles indicate lower near-surface compressive stresses but greater depths for RB compared to SP. **Figure 5.36** demonstrates the induced compressive stresses after PWHT RB for parent material, HAZ and weld interface compared to PWHT condition. One can see that the induced compressive stresses at weld line is higher than of that at HAZ and parent material. That could be attributed to the different microstructures and work hardening capability for each zone.

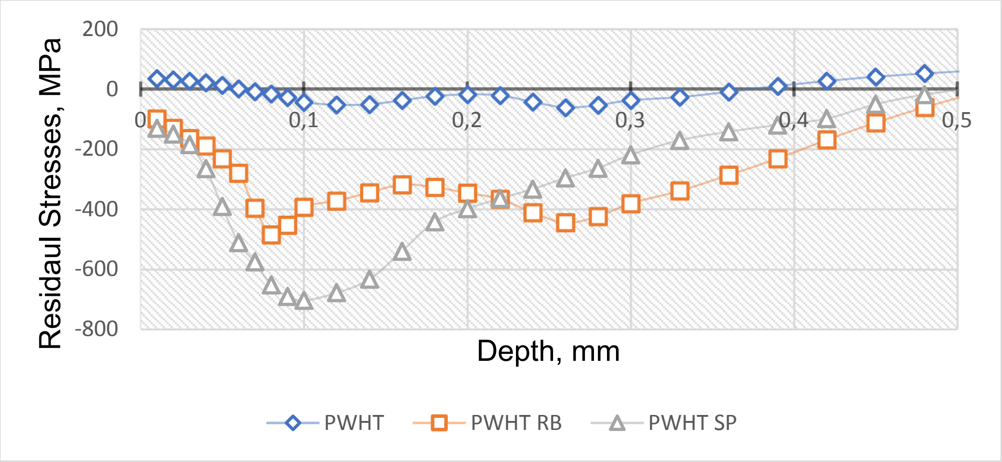

Figure 5.35 Depth profile residual stresses for PWHT after SP and RB.

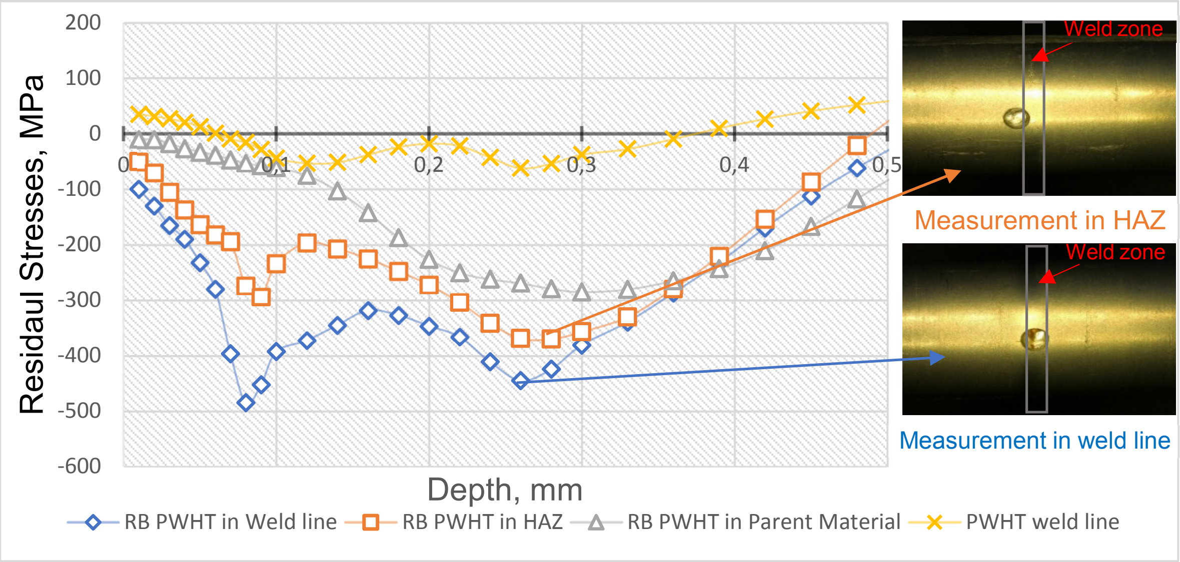

Figure 5.36 Depth profile residual stresses for the prescribed conditions.

5.2.3.3. High Cycle Fatigue Performance

The S–N curves of all pairs of treatments at the optimum treated conditions for Ti-6242 welded joints are shown in Figure 4.36. the EP specimens of AW and PWHT conditions are taken as a reference. A slight improvement of the fatigue performance has been seen after PWHT without applying mechanical surface treatments. The fatigue limit increases from 350 to 375 MPa after PWHT. Apparently, the 10^7 cycles fatigue strength of TI-6242 joints significantly increased from 350 MPa for AW EP to about 450 MPa for AW RB or PWHT RB, 460 MPa for AW SP and 550 MPa for PWHT SP. That means that the enhancement of fatigue life after combination of PWHT and SP is about 55%. Regarding the improvement of fatigue life, one can see that for Ti-6242 weld, PWHT SP is superior to PWHT RB. That could be attributed to the lower induced compressive stresses in case of RB than that in case of SP (see **Figure 5.35**).

Notably, the fracture location of the fatigue specimens is observed in parent materials in all treatment condition except AW EP and AW SP. The high tensile RS at the weld line of AW EP specimens is the reason behind the fraction at the weld interface in case of AW EP. While the lower induced compressive stresses on weld zone than on parent material for AW SP condition (see **Figure 5.34**) is the responsible for the fraction at the weld interface in case of AW SP. The higher induced compressive RS (**Figure 5.34**) and the lower surface roughness (**Figure 5.38**) of PWHT SP than that of AW SP could explain the reduction of fatigue life of AW SP compared with PWHT SP.

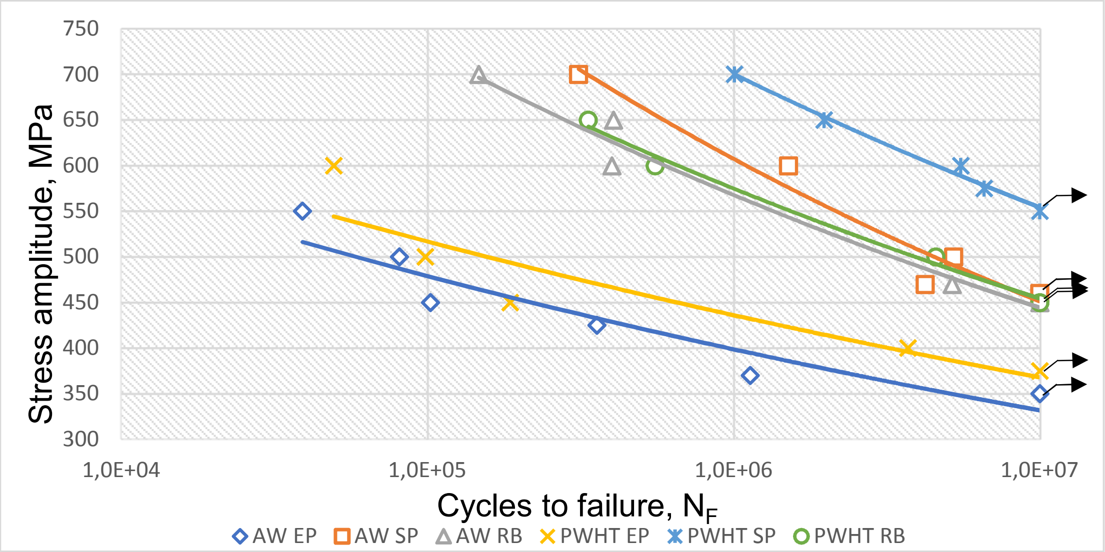

Figure 5.37 S–N curves for as-welded and PWHT joints after various surface treatments.

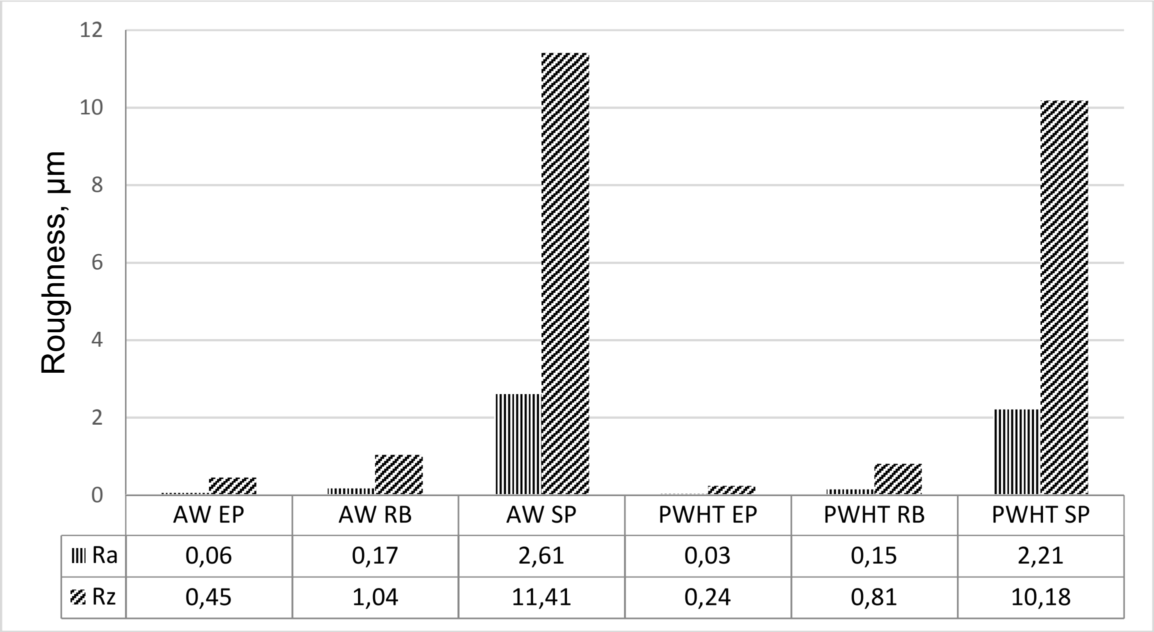

	AW EP	AW RB	AW SP	PWHT EP	PWHT RB	PWHT SP
▥ Ra	0,06	0,17	2,61	0,03	0,15	2,21
▨ Rz	0,45	1,04	11,41	0,24	0,81	10,18

Figure 5.38 Roughness values of the various surface treated conditions.

Both SP and RB lead to a drastic reduction in the microcrack growth from the surface to interior [183], this decrease being a direct consequence of the compressive stresses induced by SP and RB. As the stress amplitude decreases, so-called nonpropagating fatigue cracks are observed, presumably because the local stress intensity factor has decreased below that required for microcrack growth. Moreover, with a further decrease in stress amplitude, the fatigue crack nucleation site changes from the surface, as observed for AW EP (**Figure 5.39-a)**, to subsurface regions in mechanically surface treated specimens as shown in **Figure 5.39-b)** and **-c)**. RB leads to a higher depths of crack nucleation site than that of SP. This could be attributed to the relatively deeper residual compressive stresses in the near-surface region caused by RB (**Figure 5.35**) while SP induces higher surface roughness that leads to early crack nucleation.

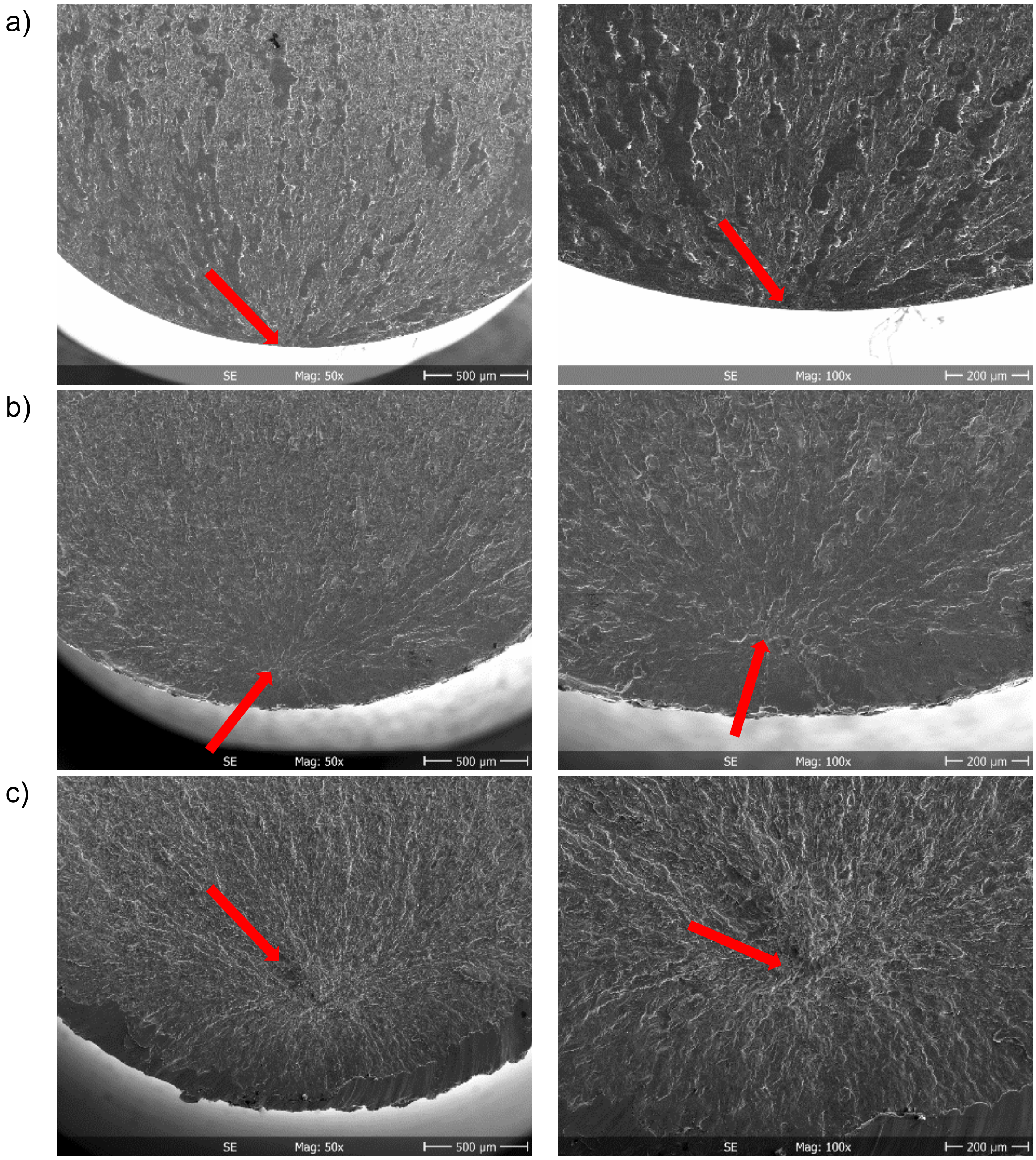

Figure 5.39 Fracture surfaces of fatigue failed Ti-6242 weld joints of a) PWHT EP, b) PWHT SP and c) PWHT RB. (Arrow indicates crack nucleation site) larger magnification right to the fracture pattern.

The fracture location can be moved to the parent materials of Ti-6242 weld joints by applying SP and RB on the weld zone. **Figure 5.40** illustrates how the fracture location can be controlled by distinguishing the reinforcement zone. In **Figure 5.40-a)**, the fatigue specimen has fractured at weld interface after SP for AW state. While, fracture location moved to the parent material after applying SP on the weld zone for AW state. (More explanation see **section4.4.1**)

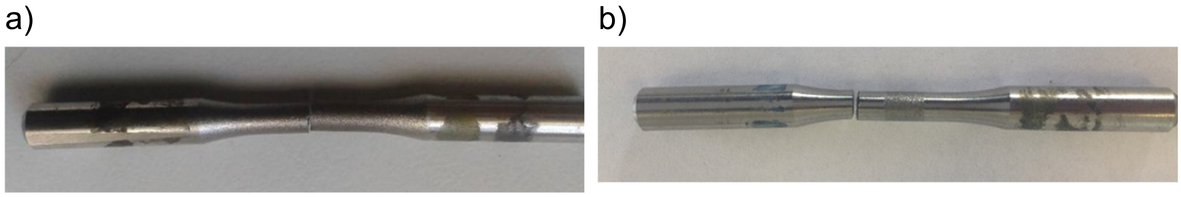

Figure 5.40 Fracture location after fatigue test for a) AW SP and b) AW SP on weld zone.

5.2.3.4. Impact Toughness

A series of Charpy V-notch tests were carried out on parent metals and Ti-6242 friction-welds joints at room temperature for varying treatment conditions. The test data are average values obtained from three specimens. The average impact toughness values are presented in **Figure 4.40**. Because of the small values of the sub-size impact toughness it could not be correlated to the full-size impact toughness (see **Figure 3.20**). The sub-size impact toughness of base metal was 0.9 J and SP has almost no effect on the impact toughness of base metal. The impact energy in AW state increases considerably and decreases for PWHT state as compared with BM. Like CP-Ti weld, the impact toughness values of AW were found to be reduced after applying SP. However, impact energy of PWHT slightly increased after SP. Marushchak et al. [159] reported that the elevated dislocation density and the higher roughness values reduced the impact toughness, which give a cause of toughness reduction after SP for AW state. The obvious reduction in impact energy after PWHT compared to AW probably because of the recovery effect and formation of coarser equiaxed grains. The observation of the crack path clearly shows that all the failures occurred in the base metal as shown in **Figure 5.42**. This fact suggests that the impact toughness of the weld is higher than that of the parent metal [65].

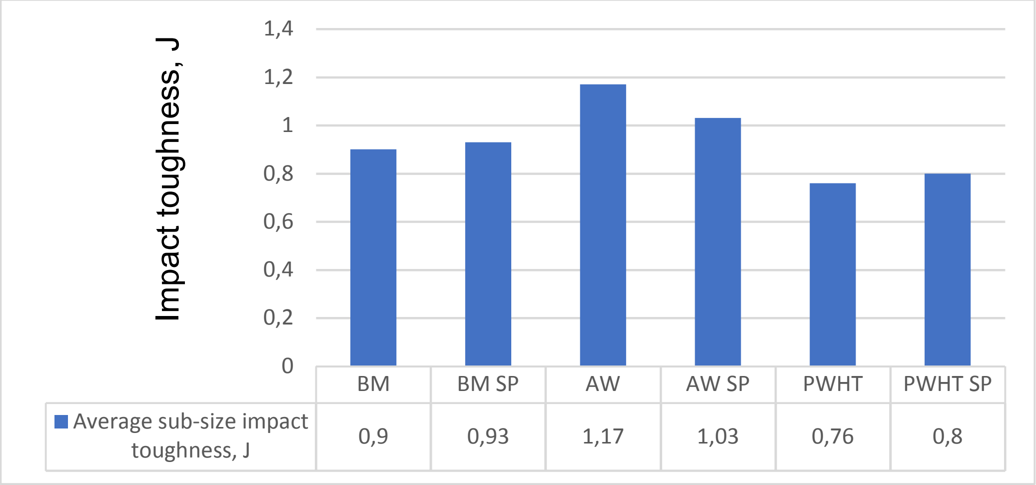

Figure 5.41 Average sub-size impact toughness of the prescribed conditions.

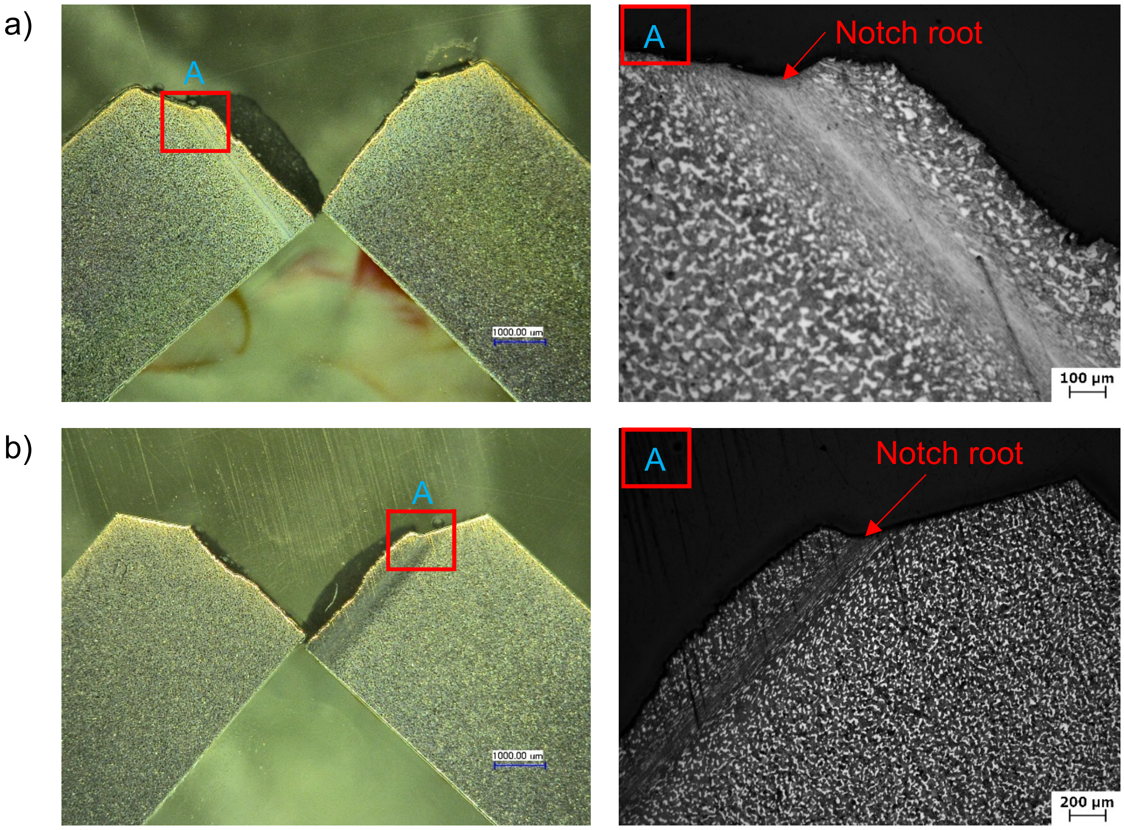

Figure 5.42 Cross-sectional view of the fractured samples after impact test a) AW and b) PWHT.

The fractographs for the base metal and welds with various treatments are shown in **Figure 5.43**. The brittle behavior was verified with almost no lateral expansion of the fractured surfaces. The brittle fracture is believed to take place in three stages. First plastic deformation that causes dislocation pile-ups at obstacles. Second the nucleation of micro-crack because of build-up of shear stresses. Third eventual crack propagation under applied stress aided by stored elastic energy [66]. The appearance of fracture surface of base metal of Ti-6242 before and after SP (**Figure 5.43-a)** and **-b)**) indicated transgranular (quasi-cleavage) fracture with a small quantity of intergranular fracture dominates the fracture mode. For AW and PWHT, one can see the presence of both intergranular and transgranular features as well. **Figure 5.43-e)** shows the presence of microcracks after PWHT which probably beside the recrystallized equiaxed grains after PWHT the responsible for the reduction of impact energy compared to AW. The presence of both intergranular and transgranular features indicates a mixed mode fracture morphology for Ti-6242 orbital weld which can be clearly seen in the cross-sectional view of the fracture surface of impact specimens in **Figure 5.44**.

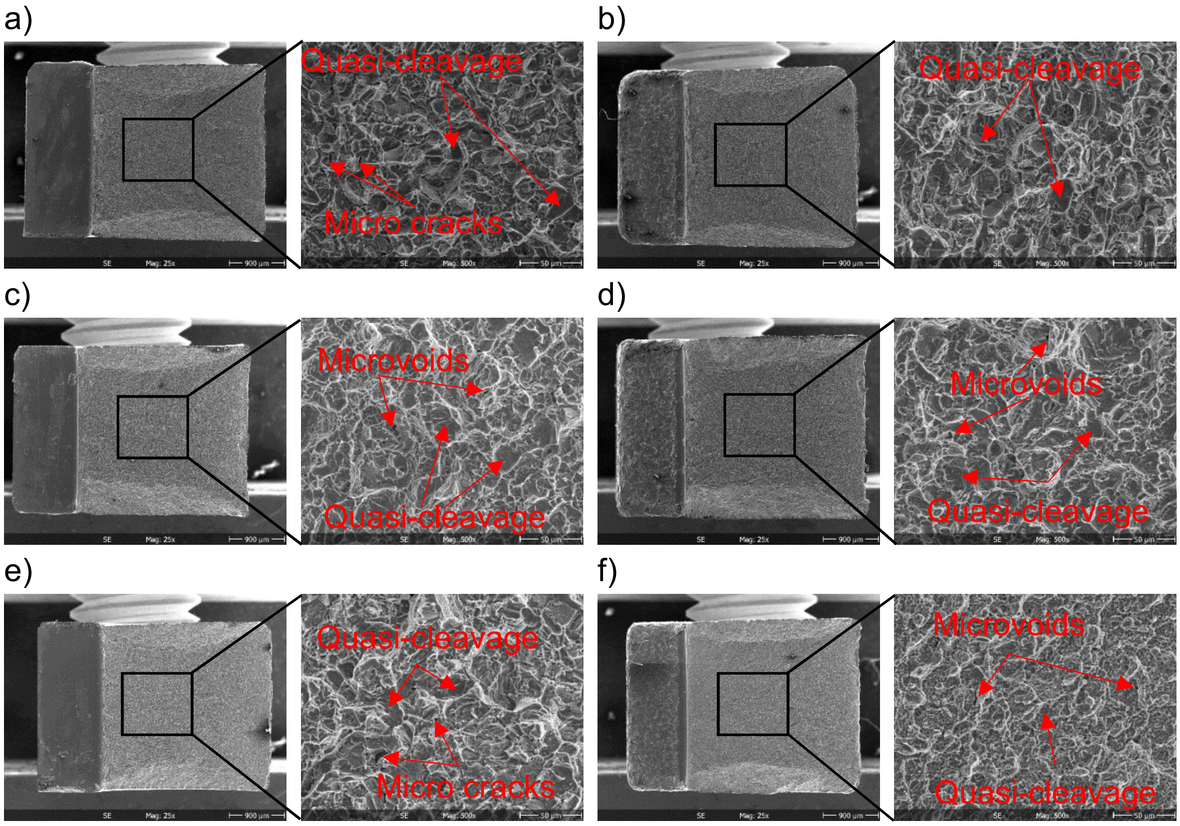

Figure 5.43 Fracture appearances after impact testing for a) BM, b) BM SP, c) AW, d) AW SP, e) PWHT and f) PWHT SP.

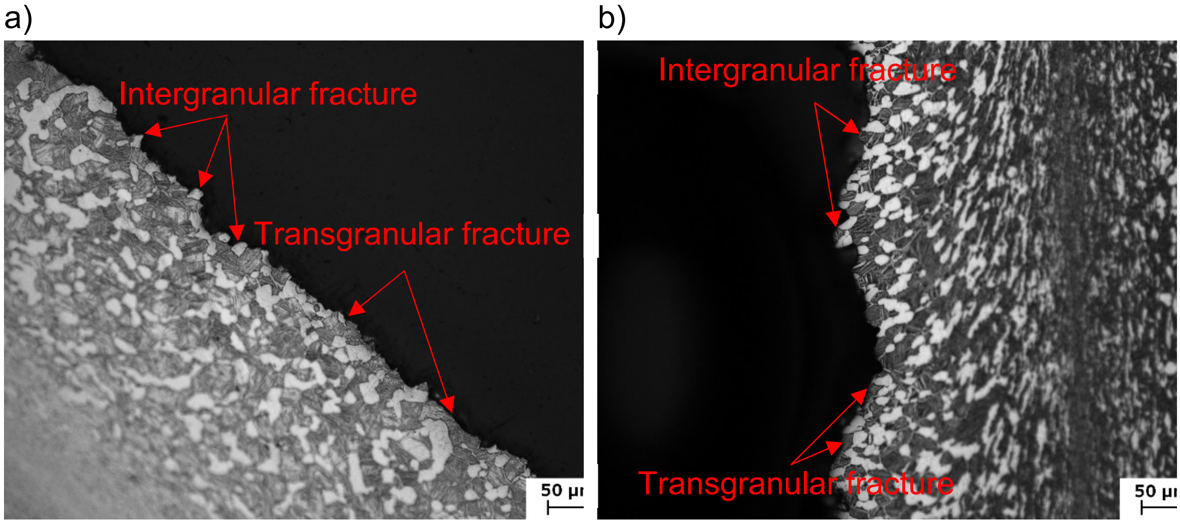

Figure 5.44 Cross-sectional view of the fractured samples after impact test showing a mixed mode fracture morphology a) AW and b) PWHT.

This page intentionally left blank

6. Summary and Conclusions

A detailed research activity on the solid-state welding techniques called rotary friction welding and orbital friction welding has been carried out. A combination of thermal and /or mechanical treatment techniques such as SP together with PWHT have been conducted to enhance the fatigue performance of rotary and orbital friction welded joints. The applied combined treatments lead additionally to the enhancement of the surface layer properties and maintain or even improve the impact toughness of the friction welded joints. This research aims to provide treatment guidelines for enhancement the fatigue life of orbital and rotary friction-welded joints. In particular the research has been developed in three main parts:

- RFW of AISI 316L to AISI 1012
- RFW of CP-Ti
- OFW of Ti-6242

6.1. RFW of AISI 316L to AISI 1012

Using the design of experiments (DoE) method, dissimilar friction welded joint between AISI 1012, and AISI 316L were optimized with respect to its UTS and burn of length. The effects of PWHT on the welded joint were examined in detail. After that, an attempt was made to optimize the shot peening (SP), and roller burnishing (RB) parameters to improve the surface layer properties, fatigue performance, as well as the impact toughness at both AW and PWHT conditions. The main conclusions were summarized as follows:

- A two-level full factorial design with three replicates has been conducted to create the designed experiments to obtain a sound dissimilar metal joint between AISI 1012 and AISI 316L by continuous drive friction welding. The tensile strength of joint was maximized, and the metal loss was minimized.
- A predicted first-order regression models were formulated, and the correlation between the factors was determined from the following linear regression equations
    - $UTS = 605.8 + 4.8 \ast \text{Friction pressure} - 1.5 \ast \text{Friction time} - 1.2 \ast \text{Rotational speed} - 9.0 \ast \text{Friction pressure} \ast \text{Friction time} + 5.2 \ast \text{Friction pressure} \ast \text{Rotational speed} - 6.2 \ast \text{Friction time} \ast \text{Rotational speed}$
    - $\text{Burn off length} = 3.10 + 0.06 \ast \text{Friction pressure} + 0.38 \ast \text{Friction time} + 0.26\ \text{Rotational speed} + 0.32 \ast \text{Friction pressure} \ast \text{Friction time} - 0.28 \ast \text{Friction pressure} \ast \text{Rotational speed} + 0.14 \ast \text{Friction time} \ast \text{Rotational speed}$

- The weld interface is easily recognized in the central zone, while two elements interlock with each other in the peripheral region. After PWHT, the weld interface became straight and obvious, because it separated AISI 1012 and AISI 316L distinctly, and a ferrite layer formed along the weld interface.
- There is a significant decrease of δ-ferrite from AISI 316L base metal to the weld interface. High plastic deformation plays a predominant role in the rapid dissolution of δ-ferrite compared to the high temperature.
- Carbon diffusion dominates the element diffusion process, which leads to the formation of a chromium carbide layer at the weld interface. The quantity of chromium carbide increased with increasing the heat treatment temperature.
- SP and RB improve the fatigue life at all stress amplitudes. The most improvement of the fatigue life obtained after SP and RB for the whole weld joint which increases from 320 to 410 and 400 MPa, respectively, the enhancement is about 30%.
- The mechanical surface treatment (SP and RB) can control the fracture location either in the weld zone or the lower strength base metal of the welded joints.
- Conducting different Almen intensities on weld zone and base metal leads to further enhancement in endurance limit of weld joints, while the location of fracture remains outside the welding zone.
- Impact toughness fracture mechanism of AW joints is a combination of quasi-cleavage and dimple fracture. SP impaired the impact toughness of the welded joints.

6.2. RFW of CP-Ti

Rotary friction welded joints between CP-Ti were optimized. Testing a selection of proper friction welding parameters applied as an optimization procedure for producing sound weld joints. Minitab 17 has been utilized to investigate the significant of weld parameters on the flash width and central weld length of the welded joints. The effect of combination of thermal (PWHT) and mechanical treatments (SP and RB) on the surface layer properties, fatigue performance, as well as the impact toughness of the welded joints were examined. The main conclusions were summarized as follows:

- There is a wide range of the operating parameters to produce satisfactory CP-Ti friction-welded joints concerning the mechanical and metallurgical properties.
- Weld defects such as lack of bonding and/or longitudinal cracks of the friction welded-joints did not affect the tensile strength of the CP-Ti welded-joints. Excessive deformation during rotary friction welding has presented with increasing the forging pressure. Friction welding at high rotational speeds with high friction pressure led to thinner flash zone width.

- Minimum metal loss welds were obtained at a rotational speed of 12000 rpm, friction pressure 2.5 bar, forging pressure 2.5 bar, friction time 0.5 s and forging time 2.5 s.
- An increase of the hardness at transformed and recrystallized zone (TRZ) has been detected for all welding conditions. After PWHT, the hardness of base metal (BM) and TMAZ did not change but hardness of CWZ decreased slightly by about 10%.
- The fatigue performance of CP-Ti friction welded joints was improved by applying SP and RB due to the induced compressive residual compressive.
- The welding tensile stresses has been converted to compressive residual stresses after utilizing SP process. It could be observed that the combination of PWHT and SP induces the highest compressive residual stresses. The most improvement of the fatigue life could be obtained after a combination of SP and PWHT from 240 MPa up to 450 MPa, i.e. about 87% enhancement. Therefore, it could be concluded that the combination of thermal and mechanical treatments effectively improved the fatigue performance of the CP-Ti weld joints.
- The Charpy energy increases for AW state and decreases for PWHT state as compared with BM. In addition, the impact toughness values of AW reduced after applying SP. However, impact energy of PWHT increases after applying SP.
- Impact toughness fracture mechanism of AW joints is a quasi-cleavage mode with radial fan-shaped tear ridges.

6.3. OFW of Ti-6242

Orbital friction welded joints between Ti-6242 were carried out. The shot peening (SP), and roller burnishing (RB) parameters were optimized at both as-welded (AW) and post-weld heat treated (PWHT) conditions. The effect of combination of thermal (PWHT) and mechanical treatments (SP and RB) on the surface layer properties, fatigue performance, as well as the impact toughness of the welded joints were examined. The depth profile residual stresses and surface residual stress distribution across the weld line has been measured using the incremental hole-drilling method (IHD) and Laboratory X-Ray Diffraction (LXRD), respectively. The main conclusions were summarized as follows:

- The orbital friction welding process leads to a severe change of the microstructure. The width of CWZ is about 30 µm and the TMAZ extended for about 112 µm from CWZ on both sides.
- The microstructure at CWZ of AW condition consisted of very fine equiaxed grains with about 2 µm in size.
- Slightly higher ductility has been obtained after PWHT than that of the base metal and AW specimens

- An increase of the weld interface hardness is found because of the grain refinement by dynamic recrystallization process in CWZ, which provide improved strength at the wild line relative to the base metal.
- Notwithstanding that, the most increase in surface hardness was found at 0.3 mmA for both AW and PWHT conditions. However, the fatigue behavior is negatively affected by increasing the Almen intensity because of the induced microcracks and the higher roughness values.
- Higher burnishing pressures lead to fatigue life drop as a result of the occurrence of surface layers flaking due to the shear failure of the layers.
- Tensile residual stress at the weld interface has been detected for AW conditions. This tensile region is partially relieved after PWHT and completely converted to compressive stresses by SP. The 300 MPa tensile stresses has been converted to about 670 and 780 MPa compressive stresses for AW SP and PWHT SP, respectively.
- The fracture in weld zone for AW SP specimens after fatigue test attributed to that the induced compressive stresses on parent material is higher than of that on weld zone.
- Like CP-Ti weld, the combination of PWHT and SP induces the highest compressive residual stresses and provides the most enhancement of the fatigue life from 350 to 550 MPa by about 57% improvement.
- The impact toughness increases for AW state and decreases for PWHT state as compared with BM. Moreover, the absorbed energy values of AW reduced after applying SP. However, increases for PWHT after applying SP.
- The impact failures occurred in the base metal for all conditions which suggest that the impact toughness of the weld is higher than that of the parent metal.
- The presence of both intergranular and transgranular features on fracture surface morphology indicates a mixed mode fracture mechanism for Ti-6242 orbital weld.

7. References

[1] G. Çam and M. Koçak, “Progress in joining of advanced materials”, GKSS Report: GKSS 98/E/55, **1998**.

[2] R. Dixon, “Introduction to solid-state welding”, Welding Brazing and Soldering ASM Handbook, Vol. 6, pp. 141–142,**1995**.

[3] J. Guo, “Solid state welding processes in manufacturing”, In: Andrew Y. C. Nee (ed) Handbook of manufacturing engineering and technology. Springer London, pp. 569-592, **2015**.

[4] G. Linnert, “Welding metallurgy carbon and alloy steels”, Vol. 1 Fundamentals, (AWS, Miami, Florida), pp. 1–940, **1994**.

[5] O. Midling, Ø. Grong, “A process model for friction welding of Al-Mg-Si alloys and Al—SiC metal matrix composites-II. HAZ microstructure and strength evolution”, Acta Metall. Mater., Vol. 42, pp. 1611–1622, **1994**.

[6] J. Squires, “Thermal and mechanical characteristics of friction welding mild steel”, Br. Weld. J., Vol. 13, pp. 652–657, **1966**.

[7] M. Maalekian, “Friction welding – critical assessment of literature”, Sci. Technol. Weld. Join., pp. 738–759, **2007**.

[8] D. Spindler, “What industry needs to know about friction welding”, Weld. J., pp. 37–42, **1994**.

[9] J. Searle, “Friction welding non-circular components using orbital motion” Welding & Metal Fabrication, Vol. 39, pp. 294–297, **1971**.

[10] L. Wenya, V. Achilles, P. Michael, M. Tiejun, “Linear and rotary friction welding review”, International Materials Reviews, Vol. 61, pp. 1–30, **2016**.

[11] ANSI/AWS C6.1-89 American National Standard, "recommended practices for friction welding", pp. 1–27, **1989**.

[12] V. Vill, “Friction welding of metals”, (AWS, New York, New Jersey), pp. 1–114, **1962**.

[13] American Welding Society (AWS), Welding Handbook Vol. 2, (AWS, Miami, Florida), pp. 740–763, **1989**.

[14] R. Messler, “Principles of welding processes”, Physics, Chemistry and Metallurgy, (John Wiley and Sons Inc., New York, New Jersey), pp. 1–662, **1999**.

[15] G. Pinheiro, A. Meyer, J. dos Santos, “A literature review on friction welding”, GKSS Internal Report (Materials Research - Joining Technology), pp. 1–47, **2000**.

[16] J. Elmer, D. Kautz, S. Tsang: in ‘ASM handbook’, Vol. 6, “Welding, brazing and soldering”, Materials Park, OH, ASM International, pp. 150-155, pp. 315–317, **1993**.

[17] A. Vairis, “High frequency linear friction welding”, PhD thesis, University of Bristol, Bristol, UK, **1998**.

[18] A. Vairis, M. Frost, “On the extrusion stage of linear friction welding of Ti-6Al-4V”, Mater. Sci. Eng. A, Vol. 271, pp. 477–484, **1999**.

[19] A. Vairis, M. Frost, “Modelling the linear friction welding of titanium blocks”, Mater. Sci. Eng. A, Vol. 292, pp. 8–17, **2000**.

[20] A. Vairis, M. Frost, “High frequency linear friction welding of a titanium alloy”, Wear, Vol. 217, pp. 117–131, **1998**.

[21] S. Caldara, “Blisks-an Investigation into the Linear Friction Welding of Titanium Alloy IMI 318”, department of mechanical and manufacturing engineering University of Bristol, Bristol, **1987**.

[22] A. Addison, “Linear friction welding information for production engineering”, TWI Ltd, Cambridge, UK **2010**.

[23] A. Mateo, “On the feasibility of BLISK produced by linear friction welding”, Revista de Metalurgia, Vol. 50, pp. e023, **2014**.

[24] W. Suo, T. Ma, Y. Feng, K. Kim, “Abnormal microstructure in the weld zone of linear friction welded Ti-6.5Al-3.5Mo-1.5Zr-0.3Si titanium alloy joint and its influence on joint properties”, Materials Science and Engineering A, Vol. 599, pp. 38–45, **2014**.

[25] M. Molzen, D. Hornbach, “Evaluation of welding residual stress levels through shot peening and heat treating”, SAE Paper No. 2000-01-2564, **2000**.

[26] N. Nasir, M. Razab, S. Mamat, M. Ahmad, “Review on welding residual stress”, ARPN Journal of Engineering and Applied Sciences, Vol. 11, pp. 6166–6175, **2016**.

[27] S. Kanchidurai, P. Krishanan, K. Baskar, K. Saravana, “A review of inducing compressive residual stress – shot peening; on structural metal and welded connection,” IOP Conference Series: Earth and Environmental Science, Vol. 80, pp. 012033, **2017**.

[28] R. Craine, A. Francis, “Frictional heat generated in the early stages of an orbital friction welding process”, Wear, Vol. 114, pp. 355–365, **1987**.

[29] I. Martinek, H. Goldau, F. Trommer, “Grundsatzuntersuchungen zum Orbitalreibschweißen des unlegierten Baustahls S355JR”, Innovationspreis Reibschweißen 2011, www.raiser.de, accessed 10 Feb. **2016**.

[30] L. Crasser, “Multi-head friction welding method” U.S. Patent 10/072,386, issued Feb 7, **2002**.

[31] Europäische Patentanmeldung (EP 2 106 873 A1): Verfahren zur Herstellung integral beschaufelter Rotoren durch Verwendung des kreisförmigen Reibschweissen, Rolls-Royce Deutschland Ltd & Co KG.

[32] F. Zech, H. Cramer, L. Appel, M. Serve, “Orbital friction welding of metallic materials and dissimilar material joints on non-rotationally symmetrical joining cross-sections”, The 4th International Conference – Innovative technologies for joining advanced materials, TIMA 10 Timisoara, **2010**.

[33] A new concept in friction welding, Press Release, University of Leeds, April 30, **1970**.

[34] B. Cole, C. Young, “Design and make project report-friction” Welding Machine, University of Leeds, February 7,**1969**.

[35] A. Burton, R. Craven, “Preliminary research of friction welding machine”, University of Leeds, April 27, **1970**.

[36] C. Dawes, “An examination of orbital friction welding using axial offset”, Weld. Inst. Res. Bull., pp. 161–167, **1971**.

[37] J. Searle, “Friction welding non-circular components using orbital motion”, Weld. Met. Fabr., Vol. 39, pp. 294–297, **1971**.

[38] J. Searle, “The orbital friction welding process for non-circular components”, Eng. Dig. London, Vol 32, pp. 33–36, **1971**.

[39] M. Maalekian, “Friction welding of high carbon steel in large cross-section”, PhD thesis, Graz University of Technology, Graz, Austria, **2007**.

[40] F. Duffin, A. Bahrani, “Frictional behavior of mild steel in friction welding”, Wear, Vol. 26, pp. 53–74, **1973**.

[41] P. Wanjara, M. Jahazi, “Linear friction welding of Ti-6Al-4V: processing, microstructure, and mechanical-property interrelationships”, Metall. Mater. Trans. A, X, Vol. 36, pp. 2149–2164, **1973**.

[42] M. Maalekian, “Characterization and optimization of orbital friction welding of high carbon steel bars”, Welding in the World, Vol. 53, pp. 109-123, **1973**.

[43] M. Maalekian, H. Cerjak, “Thermal-phase transformation modelling and neural network analysis of friction welding of non-circular eutectoid steel components”, Welding in the World, Vol. 53, pp. 44–51, **2009**.

[44] M. Maalekian, “Thermal modelling of friction welding”, ISIJ International, Vol. 10, pp. 1429–1433, **2008**.

[45] M. Maalekian, E. Kozeschnik, H. Brantner, H. Cerjak, “Comparative analysis of heat generation in friction welding of steels bars”, Acta Materialia, Vol. 56, pp. 2843-2855, **2008**.

[46] M. Maalekian, E. Kozeschnik, H. Brantner, H. Cerjak, “Finite element modelling of orbital friction welding of eutectoid steel bars”, Metallurgical and Materials Transactions, Vol. 39A, pp. 844–852, **2008**.

[47] M. Maalekian, E. Kozeschnik, H.P. Brantner, H. Cerjak, “Inverse modelling and simulation of heat generation in friction welding”, Mathematical modelling of weld phenomena 8, H. Cerjak, H.K.D.H. Bhadeshia, E. Kozeschnik (Eds.), Verlag der Technischen Universität Graz, pp. 881–890, **2007**.

[48] M. Maalekian, H. “Cerjak, “Modelling the orbital friction welding of pearlitic steel bars”, Trends in Welding Research, Proceedings of the 8th International Conference, S.A. David et al (editors), pp. 736–741, **2009**.

[49] M. Maalekian, E. Kozeschnik, H. Cerjak, “Heat generation in friction welding”, Thermal Forming and Welding Distortion”, F. Vollertsen, J. Sakkiettibutra (Eds.), Strahltechnik, Vol. 31, pp. 375–384, **2008**.

[50] M. Maalekian, H. Brantner, Y. Ghanimi, H. Cerjak, “Experimental & numerical studies on orbital friction welding of high carbon steel”, PA, USA, Symposium: Joining of Monolithic Structures and Components”, MS&T **2005**.

[51] U. Raab, S. Levin, L. Wagner, C. Heinze, “Orbital friction welding as an alternative process for blisk manufacturing”, Journal of Materials Processing Technology, Vol.215, pp. 189–192, **2015**.

[52] U. Raab, S. Levin, L. Wagner, C. Heinze, “Orbital Friction Welding of Titanium-Blisks: Process Characteristics and Microstructure Development” 13th World Conference on Titanium, August Manchester Grand Hyatt San Diego, California, **2015**.

[53] U. Raab, C. Becker, L. Wagner “Influence of shot peening on the fatigue behavior of orbital friction welded titanium joints” 12th International Conference on Shot Peening, Goslar, Germany, September **2014**.

[54] U. Raab, “Untersuchungen zum Orbital-Reibschweißen als alternatives Herstellungsverfahren von Titan-Blisks im Vergleich mit dem Linear-Reibschweißen“, PhD thesis, TU-Clausthal, Clausthal-Zellerfeld, Germany, **2016**.

[55] C. Ellis, “Continuous drive friction welding of mild steel”, Welding Journal, Vol. 51, pp. 183–197, **1972**.

[56] M. Futamata, A. Fuji, “Friction welding of titanium and SUS 304L austenitic stainless steel”, Welding International, Vol. 4, pp. 768–774, **1972**.

[57] C. Nessler, D. Rutz, R. Eng, P. Vozzela, “Friction welding of titanium alloys”, Welding Journal, Vol. 50, pp.379–385, **1971**.

[58] Y. Zhou, Z. Fuji, T. North, “Mechanical properties of particulate MMC/AISI 304 friction joints”, ISIJ International, Vol. 35, pp. 1315–1321, **1995**.

[59] Y. Zhou, J. Zhang, T. North, Z. Wang, “The mechanical properties of friction welded aluminum-based-metal-matrix composite materials”, Journal of Materials Science, Vol. 32, pp. 3883–3889, **1995**.

[60] T. Shinoda, K. Tanada, Y. Katoh, T. Shimizi, “Study of thermal phenomena during friction welding and the mechanical properties of an aluminium alloy”, Welding International, Vol. 8, pp. 349–353, **1994**.

[61] Z. Maldonando, T. North, B. Altshuller, “Mechanical and metallurgical properties of MMC friction welds”, Welding Journal, Vol. 76, pp. 367–373, **1997**.

[62] A. Meyer, “Friction hydro pillar processing – bonding mechanism and properties”, GKSS Forschungszentrum Geesthacht GmbH, Geesthacht, **2003**.

[63] V. Lebedev, I. Chernenko, “Friction welding”, Sov. Tech. Rev. C. Weld. Surf., pp. 59–168, **1992**.

[64] R. Messler, “Principles of welding processes”, Physics, Chemistry and Metallurgy, John Wiley and Sons Inc., New York, New Jersey, pp. 1–662, **1999**.

[65] T. Ma, W. Li, S. Yang, “Impact toughness and fracture analysis of linear friction welded Ti–6Al–4V alloy joints”, Materials and Design 30, pp. 2128–2132, **2009**.

[66] M. Maleque, M. Salit, “Mechanical failure of materials”, Materials Selection and Design. Springer Briefs in Materials. Springer, Singapore, **2013**.

[67] R. Tenaglia, “News from EWI – dissimilar materials joining”, EWI, Rebecca Gurk, ewi.org/dissimilar-materials-joining/. (https://ewi.org/dissimilar-materials-joining/), accessed 23 Nov. **2016**.

[68] Metals Handbook, 9th Ed., American Society for Metals, Vol. 2, pp. 204–209, **1979**.

[69] J. Davis, ASM specialty handbook – Carbon and alloy steels, ASM International, Material Park, OH, **1996**.

[70] A. Padilha, R. Plaut, P. Rios, Steel heat treatment handbook, 2nd Ed., Boca Raton, FL, USA, CRC Press, Totten GE, pp. 695–739, **2007**.

[71] A. Padilha, P. Rios, “Decomposition of austenite in austenitic stainless steels”, ISIJ International (Japan), Vol.42, pp. 325–337, **2002**.

[72] M. McGuire, “Stainless steels for design engineers”, ASM International, Materials Park, OH, pp. 1–10, **2008**.

[73] AWS Welding Handbook, “Metals and their weldability”, Vol 4, 7th Ed., pp. 98–102, **1982**.

[74] J. DAVIS, “ASM specialty handbook stainless steels”, ASM International, Materials, Park, OH, USA, pp. 340–400, **1994**.

[75] A. Schaeffler, “Constitution Diagram for Stainless Steel Weld Metal”, Met. Prog., Vol. 56, pp. 680–688, **1949**.

[76] W. DeLong, “A modified phase diagram for stainless steel weld metals”, Met. Prog, Vol. 77, pp. 98–100, **1960**.

[77] D. Kotecki, T. Siewert, “WRC-1992 constitution diagram for stainless steel weld metals: A modification of the WRC-1988 diagram”, Welding J., Vol. 71, pp. 171–179, **1992**.

[78] R. Tobler, T. Siewert, H. McHenry, “Strength-toughness relationship of austenitic stainless steel welds at 4 K”, Cryogenics, Vol. 26, pp. 392–395, **1698**.

[79] B. Mintz, A. Cowley, R. Abushosha, “Importance of columnar grains in dictating hot ductility of steels”, Metals Science and Technology, Vol. 16, pp. 1–5, **2000**.

[80] S. Kim, H. Moon, T. Kang, C. Lee, “Dissolution kinetics of delta ferrite in AISI 304 stainless steel produced by strip casting process”, Materials Science and Engineering, Vol. 356, pp. 390–398, **2003**.

[81] Z. Sun, “Feasibility of producing ferritic/austenitic dissimilar metal joints by high energy density laser beam process”, Int. J. Pres. Ves. & Piping, Vol. 68, pp. 153–160, **1996**.

[82] J. Donohue, “Meeting pump shaft manufacturing challenges using friction welding”, American friction welding, inc. https://www.teamafw.com/wp-content/uploads/2015/03/white-paper-pump-shafts.pdf, accessed 17 Sep. **2017**.

[83] M. McGuire, “Stainless steels for design engineers”, ASM International, Materials Park, OH, pp. 69–90, **2008**.

[84] J. Davis, “Corrosion of weldments”, ASM International, Technology & Engineering, **2006**.

[85] Atlas Steels Technical Department, The Atlas Steels Technical Handbook of Stainless Steels, Melbourne, **2010**.

[86] B. Weiss, R. Stickler, Metallurgical Transactions, Vol. 3, pp. 851–866, **1972**.

[87] J. Gambogi, S. Gerdemann, “Titanium metal: extraction to application”, DOE/ARC, 060, **1999.**

[88] L. Wagner, J. Gregory, “Thermomechanical surface treatment of titanium alloys”, 2nd ASM Heat Treatment and Surface Engineering Conference in Europe, Dortmund, ASM, Materials Park, Ohio **1993**.

[89] M. Peters, J. Hemptenmacher, J. Kumpfert, C. Leyens (Eds.), “Structure and properties of titanium and titanium alloys”, Weinheim, pp. 1, **2003**.

[90] G. Lüterjing, J. Williams, “Titanium”, Springer, pp. 149–175, **2003**.

[91] F. Campbell, “Manufacturing processes for advanced composites”, Elsevier Ltd, pp. 119–174, **2004**.

[92] D. Terada, M. Inoue, H. Kitahara, “Change in mechanical properties and microstructure of ARB processed Ti during annealing”, Materials Transactions, Vol. 49, pp. 41–46, **2008**.

[93] W. Adamson, R. Schutz, “Application of titanium in shipboard seawater cooling systems”, Naval Engineers Journal, pp. 124–134, **1987**.

[94] J. Mountford, “Basics and benefits of titanium for sea service - A review”, The Annual Surface Ships Corrosion Control Conference”, K. Louisville, **1996**.

[95] J. Talkington, D. Harwig, H. Castner, A. Joseph, R. Spencer, B. Grimmett, “Advances in titanium pipe welding and inspection”, Technology for Navy Ships, Ship Production Symposium, June **2001**.

[96] P. Threadgill, “The potential for solid state welding of titanium pipe in offshore industries”, Symposium on the Right Use of Titanium, Stavanger, Norway, **1997**.

[97] F. Froes, P. Allen, M. Niinomi, “Non-Aerospace applications of titanium”, TMS, Warrendale, PA, pp. 3–18, **1998**.

[98] C. Nessler, D. Rutz, R. Eng, P. Vozzella, “Friction welding of titanium alloys”, Welding Journal Research Supplement, pp. 379–385, **1971**

[99] G. Hutt, “Titanium dynamic riser systems”, Titanium World, Vol. 2, pp. 25–27, **1995**.

[100] I. Polmear, “Light alloys, metallurgy of light metals”, 2nd Ed., New York, pp. 211, **1989**.

[101] M. Donachie, “*Titanium: A technical guide”,* ASM International, Ohio, USA, **2000**.

[102] L. Wagner, G. Lütjering, “Shot peening”, A. Niku Lari (Ed.), Pergamon Press, City, pp. 453, **1982**.

[103] E. Maawad, S. Yi, H. Brokmeier, L. Wagner, “Residual stress-induced subsurface fatigue crack nucleation in shot peened titanium alloys”, 10th Int. Conference on Shot Peening, K. Tosha (Ed.), Tokyo, Japan, pp. 499–504, **2008**.

[104] L. Wagner, “Surface performance of titanium alloys”, J.K. Gregory, H.J. Rack, D. Eylon (Eds.), TMS, City, pp. 199, **1997**.

[105] L. Wagner, “Mechanical surface treatments on titanium, aluminum and magnesium alloys”, Mater. Sci. Eng. A, Vol. 263, pp. 210–216, **1999**.

[106] A. Drechsler, J. Kiese, L. Wagner, “Effect of shot peening and roller-burnishing on fatigue performance of various titanium alloys”, Proc. ICSP-7, pp. 145–152, **1999**.

[107] M. Kocan, A. Ostertag, L. Wagner, “Shot peening and roller-burnishing to improve fatigue resistance of the (α+β) titanium alloy Ti-6A1- 4%”, Shot peening, (L. Wagner, ed.) WILEY-VCH- Verlag, Weinheim, pp. 461–467, **2003**.

[108] M. Basha, U. Raab, A. Ahmed, M. Mhaede, M. Wollmann, L. Wagner “Effect of shot peening and roller-burnishing on the fatigue performance of cp-ti friction-welded joints” 13th World Conference on Titanium, Manchester Grand Hyatt * San Diego, California, **2015**.

[109] J. Fuhr, M. Basha, M. Wollmann, L. Wagner “Coverage and peening angle effects in shot peening on HCF performance of TI-6AL-4V”, International Conference on Surface Modification Technologies (SMT30), Milan, Italy, **2016.**

[110] W. Hennig, G. Feldmann, T. Haubold, “Shot peening method for aerofoil treatment of blisk assemblies”, Procedia CIRP, Vol. 13, pp. 355–358, **2014**.

[111] O. Hatamleh, J. Smith, D. Cohen, R. Bradley, “Surface roughness and friction coefficient in peened friction stir welded 2195 aluminum alloy” Applied Surface Science, Vol. 255, pp. 7414–7426, **2009**.

[112] O. Hatamleh, J. Lyons, R. Forman, “Laser and shot peening effects on fatigue crack growth in friction stir welded 7075-T7351 aluminum alloy joints”, International Journal of Fatigue, pp. 421–434, **2007**.

[113] O. Hatamleh, R. Mishra, O. Oliveras, “Peening effects on mechanical properties in friction stir welded AA 2195 at elevated and cryogenic temperatures” Materials and Design, pp. 3165–3173, **2009**.

[114] O. Hatamleh, A. DeWaldb, “An investigation of the peening effects on the residual stresses in friction stir welded 2195 and 7075 aluminum alloy joints”, Journal of Materials Processing Technology, Vol. 209, pp. 4822–4829, **2009**.

[115] O. Hatamleh, “A comprehensive investigation on the effects of laser and shot peening on fatigue crack growth in friction stir welded AA 2195 joints” International Journal of Fatigue,.Vol. 31, pp. 974–988, **2009**.

[116] T. Shives (Ed.), “Advanced technologies in failure prevention”, Cambridge University Press, Cambridge, pp. 92, **1991**.

[117] S. Baiker (Ed.), “Shot peening, A dynamic application and its future”, 1st Ed., Switzerland, **2006**.

[118] S. Swirad, “The surface texture analysis after sliding burnishing with cylindrical elements”, Wear -Lausanne, Vol. 271, pp. 576–581, **2010**.

[119] Ecoroll catalogue, http://www.ecoroll.de, accessed 24 Sep **2017**.

[120] http://www.yamato.com.tr/documents/en/176/176/art-of-roller-burnishing, accessed 24 Sep **2017**.

[121] N. Loh, S. Tam, “Effects of ball burnishing parameters on surface finish—a literature survey and discussion”, Precis. Eng., Vol. 10, pp. 215–220, **1988**.

[122] K. Kirkhope, R. Bell, L. Caron, R. Basu, K. Ma, “Weld detail fatigue life improvement techniques part1 review”, Marine Structures, pp. 447–474, **1999**.

[123] C. Liu, C. Dong, “Internal residual stress measurement on linear friction welding of titanium alloy plates with contour method”, Trans. Nonferrous Met. Soc. China, Vol. 24, pp.1387–1392, **2014**.

[124] T. Gurney, "Some recent work relating to the influence of residual stresses on fatigue strength", Welding Inst. Conf. on Residual Stresses in Welded Constructions and Their Effects, TWI, **1978**.

[125] P. Withers, H. Bhadeshia, “Residual stress. Part1 – Measurement techniques, Materials Science and Technology”, pp. 355–365, **2001**.

[126] P. Prevéy, “X-ray diffraction residual stress techniques”, Metals Handbook, 10, ASM International, Materials Park, OH, pp. 380–392, **1986**.

[127] F Kandil, J Lord, A Fry and P Grant, “A Review of residual stress measurement methods - A guide to technique selection”, NPL Report MATC(A)O4, **2001**.

[128] ASTM E 837-99, “Standard test method for determining residual stresses by the hole-drilling strain-gage method”.

[129] C. Zheng, X. Wang, S. Li, C. Shang, X. He, “Effects of inclusions on microstructure and properties of heat-affected-zone for low-carbon steels”, Sci China Tech Sci., Vol. 55, pp. 1556–1565, **2012**.

[130] A. Hasui, T. Matsui, “On the effect of faying face condition on weldability in friction welding”, Trans. Jpn. Weld. Soc., 87. Ross PJ. Taguchi techniques for quality engineering, New Yark, **1987**.

[131] W. Callister, “Materials science and engineering: An introduction”, 7th Ed., Wiley, pp. 69, **2007**.

[132] E. Lucon, R. Chaouadi, A. Fabry, J. Puzzolante, E. Walle, “Characterisation of materials properties by use of full size and subsize Charpy tests: an overview of different correlation procedures”, in Pendulum Impact Testing: A Century of Progress, ASTM STP 1380 (Ed: T.A. Siewert), ASTM, Philadelphia, pp. 146–163, **2000**.

[133] I. Noyan, J. Cohen, “Residual stress measurement by diffraction and interpretation”, Berlin, Springer-Verlag, **1987**.

[134] P. Frankel, M. Preuss, A. Steuwer, P. Withers, S. Bray, “Comparison of residual stresses in Ti–6Al–4V and Ti–6Al–2Sn–4Zr–2Mo linear friction welds”, Materials Science and Technology, Vol. 25, pp. 640–650, **2009**.

[135] A., Ambroziak, M. Korzeniowski, P. Kustroń, “Friction. welding of dissimilar metal joints with intermediate. layers”, J. Achiev. Mater. and Manuf. Eng, Vol. 21, pp. 37–40, **2007**.

[136] N. Ozdemir, “Investigation of mechanical properties of friction welded joints between AISI 304 L and AISI 4340 steel as a function of rotational speed”, Mater. Lett., Vol. 59, pp. 2504–2509, **2005**.

[137] I. Kırık, N. Ozdemir, T. Teker, “Weldability of martensitic stainless steel to medium carbon steel by using friction welding”, International Iron & Steel Symposium, Karabuk, Turkey, Vol. 2, pp. 826– 831, **2012**.

[138] A. Ishibashi, S. Ezoe, S. Tanaka, “Studies on. friction welding of carbon and alloy steels”, Bulletin of the JSME, Vol. 26, pp. 1080–1087, **1983**.

[139] I. Kirik1, N. Ozdemir, U. Caligulu, “Examination of microstructure and mechanical properties of friction welded joints of medium carbon steel to austenitic stainless steel”, 14th International Materials Symposium, **2012**.

[140] S. Ji, J. Liu, Y. Yue, Z. LÜ, L. Fu, “3D numerical analysis of material flow behavior and flash formation of 45 steel in continuous drive friction welding”, Trans. Nonferrous. Met. Soc. China, Vol. 22, pp. 528–533, **2012**.

[141] M. Yilmaz, M. Col, M. Acet, “Interface properties of aluminum/steel friction-welded components”, Mater. Charact., Vol. 49, pp. 421–429, **2003**.

[142] I. Bhamji, M. Preuss, P. Threadgill, A. Addison, “Solid state joining of metals by linear friction welding: a literature review”, Mater. Sci. Technol., Vol. 27, pp. 2–12, **2011**.

[143] R. Winiczenko, M. Kaczorowski, “Friction welding of ductile iron with stainless steel”, Journal of Materials Processing Technology, Vol. 213, pp. 453–462, **2013**.

[144] I. Bhamji, M. Preuss, P. Threadgill, R. Moat, A. Addison, M. Peel, “Linear friction welding of AISI 316L stainless steel”, Mater. Sci. Eng., Vol. 90, pp. 528–680, **2010**.

[145] H. Ma, G. Qin, P. Geng, F. Li, B. Fu, X. Meng, “Microstructure characterization and properties of carbon steel to stainless steel dissimilar metals joint made by friction welding”, Mater., Vol. 86, pp. 587–597, **2015**.

[146] Z. Zhang, H. Zheng, J. Dong, X.Yan, Y. Sun, H. Xu, “Surface enhanced fluorescence by porous alumina with nanohole arrays”, Sci China-Phys Mech Astron, Vol. 55 pp. 767–771, **2012**.

[147] H. Ma, G. Qin, P. Geng, F. Li, B. Fu, X. Meng, “Effect of post-weld heat treatment on friction welded joint of carbon steel to stainless steel”, Journal of Materials Processing Technology, Vol. 227, pp. 24–33, **2016**.

[148] K. Lee, H. Cho, D. Choi, “Effect of isothermal treatment of SAF 2205 duplex stainless steel on migration of δ/γ interface boundary and growth of austenite”, J. Alloy Compd, Vol. 285, pp. 156–161, **1999**.

[149] I. Lo, W. Tsai, “Effect of heat treatment on the precipitation and pitting corrosion behavior of 347 SS weld overlay”, Mater Sci Eng A, Vol. 355, pp.137–143, **2003**.

[150] B. Mateša, I. Samardžić, M. Dunđer, “The influence of the heat treatment on delta ferrite transformation in austenitic stainless steel welds”, Metalurgija, Vol 51, pp. 229–32, **2012**.

[151] L. Zhou, W. Zhou, Y. Huang, J. Feng, “Interface behavior and mechanical properties of filling friction stir welded joints”, Int J Adv Manuf Tech., Vol. 81, pp. 1–7, **2015**.

[152] N. Arivazhagan, S. Singh, S. Prakash, G. Reddy, “Investigation on AISI 304 austenitic stainless steel to AISI 4140 low alloy steel dissimilar joints by gas tungsten arc, electron beam and friction welding”, Mater Des., Vol. 32, pp. 3036–3050, **2011**.

[153] N. Lah, A. Ali, “Fatigue strength improvement of MIG-welded joint by shot peening”, Materials Science and Engineering, Vol. 17, pp. 1–6, **2011**.

[154] A. Abdullah, M. Malaki, A. Eskandari, “Strength enhancement of the welded structures by ultrasonic peening”, Materials and Design, Vol. 38, pp. 7–18, **2012**.

[155] X. Liu, G. Frankel, “Effects of compressive stress on localized corrosion in AA2024-T3”, Corros. Sci., Vol. 48, pp. 3309–3329, **2006**.

[156] I. Altenberger, R. Nalla, Y. Sano, L. Wagner, R. Ritchie, “On the effect of deep-rolling and laser-peening on the stress-controlled low- and high-cycle fatigue behavior of Ti–6Al–4V at elevated temperatures up to 550 °C”, Int. J. Fatigue, Vol. 44, pp. 292–302, **2012**.

[157] M. Abdulstaar, M. Mhaede, M. Wollmann, L. Wagner, “Investigating the effects of bulk and surface severe plastic deformation on the fatigue, corrosion behaviour and corrosion fatigue of AA5083”, Surface & Coatings” Technology, Vol. 254, pp. 244–251, **2014**.

[158] S. Topolska, J. abanowsk, “Impact-toughness investigations of duplex stainless steels”, Materials and Technology, Vol. 49, pp. 481–486, **2015**.

[159] P. Marushchak, R. Bishchak, T. Vuherer, V. Hlad’o, “Impact toughness of specimens cut out from the rollers of machines for continuous casting of blanks with fused layers”, Materials Science, Vol .48, pp. 704–713 **2013**.

[160] M. Attallah, M. Preuss, S. Bray, “Microstructural development during Linear Friction Welding of titanium alloys”, 8th International Conference on Trends in Welding Research, pp. 486–491, **2009**.

[161] J. Romero, M. Attallah, M. Preuss, M. Karadge, S. Bray, “Effect of the forging pressure on the microstructure and residual stress development in Ti–6Al–4V linear friction welds”, Acta Materialia, Vol. 57, pp. 5582–5592, **2009**.

[162] H.Emre, R. Kaçar, “Effect of post-weld heat treatment process on microstructure and mechanical properties of friction welded dissimilar drill pipe” , Mat. Res, São Carlos, Vol. 18, **2015**.

[163] Measurements Group, Technical Note TN 503, “Measurement of residual stresses by the hole drilling strain gage method”, www.vishay.com/brands/measurements_group/guide/tn/tn503/, accessed 10 Okt. **2017**.

[164] P. Barsanescu, P. Carlescu, “Residual stress measurement by the hole-drilling strain-gage method: Influence of hole eccentricity”, Technical University, Iasi, Romania, **2007**.

[165] O. Hatamleh, R. Mishra, O. Oliveras, “Peening effects on mechanical properties in friction stir welded AA 2195 at elevated and cryogenic temperatures”, Materials and Design, Vol. 30, pp.3165–3173, **2009**.

[166] L. Wagner, “Mechanical surface treatments on titanium, aluminum, magnesium alloys”, Materials Science Engineering, Vol. 263, pp. 210–216, **1999**.

[167] E. Maawad, “Residual stress analysis and fatigue behavior of mechanically surface treated titanium alloys”, PhD thesis, TU-Clausthal, Clausthal-Zellerfeld, Germany, **2011**.

[168] G. Lütjering, “Commercially pure titanium and alpha alloys”, **2007**.

[169] N. Paton, B. Hickman, J. Chesnutt, W. Thompson, AGARD Conf. Proc. 185, National Technical Information Service, Springfield, VA, pp. 4-1 to 4-14, **1976**.

[170] C. Liu, Y. Liu, L. Ma, J. Yi, “Effects of solution treatment on microstructure and high-cycle fatigue properties of 7075 aluminum alloy”, Metals, Vol. 7, pp. 193, **2017**.

[171] A. Vairis, M. Frost, “On the extrusion stage of linear friction welding of Ti6Al4V”, Mater. Sci. Eng. A, Vol. 271, pp. 477–484, **1999**.

[172] O. Roder, D. Helm, G. Lutjering, “Microstructure and mechanical properties of inertia and electron beam welded Ti-6246”, Tenth World Conference on Titanium. Hamburg, Germany: WILEY VCH, **1999**.

[173] R. Mishra, Z. Ma, “Friction Stir Welding and Processing”, Materials Science and Engineering R, Vol. 50, pp. 1–78, **2005**.

[174] Y. Ji, Z. Chai, D. Zhao, S. Wu, “Linear friction welding of Ti–5Al–2Sn–2Zr–4Mo–4Cr alloy with dissimilar microstructure”, Journal of Materials Processing Technology, Vol. 214, pp. 979–987, **2014**.

[175] W. Li, T. Ma, Y. Zhang, Q. Xu, J. Li, S. Yang, H. Liao, “Microstructure characterization and mechanical properties of linear friction welded Ti-6Al-4V alloy”. Advanced Engineering Materials, Vol. 10, pp. 89–92, **2008**.

[176] N. Kumar, A. Sachdeva, L. Singh, H. Tripathi, “Experimental investigation of effect of roller burnishing process parameters on surface roughness and surface hardness of C40E steel”, Int. J. Machining and Machinability of Materials, Vol. 18, Nos. 1/2, pp. 185–199, **2016**.

[177] N. Rao, A. Reddy, V Rao, “The effect of roller burnishing on surface hardness and surface roughness on mild steel specimens”, International Journal of Applied Engineering Research, Dindigul Vol.1, pp. 777–785, **2011**.

[178] U. Shirsat, B. Ahuja, “Parametric analysis of combined turning and ball burnishing process”, International journal of engineering and material science,Vol. 11, pp. 391–396, **2004**.

[179] P. Withers, “Residual stress and its role in failure”, Rep. Prog. Phys., Vol. 70, pp. 2211–2264, **2007**.

[180] J. Romero, M. Attallah, M. Preuss, M. Karadge, S. Bray, “Effect of the forging pressure on the microstructure and residual stress development in Ti–6Al–4V linear friction welds”. Acta Materialia, Vol. 57, pp. 5582–5592, **2009**.

[181] P. Frankel, M. Preuss, A. Steuwer, P. Withers, S. Bray, “Comparison of residual stresses in Ti–6Al–4V and Ti–6Al–2Sn–4Zr–2Mo linear friction welds”. Materials Science and Technology, Vol. 25, pp. 640–650, **2009**.

[182] A. Steuwer, J. Santisteban, M. Turski, P. Withers, T. Buslaps, “High-resolution strain mapping in bulk samples using full-profile analysis of energy-dispersive synchrotron X-ray diffraction data”, J. Appl. Crystallogr., Vol. 37, pp.883–889, **2004**.

[183] L. Wagner, G. Luetjering, “Titanium stream turbine blading”, in: R. I. Jaffe (ed.), Pergamon Press, pp. 233, **1989**.

List of Figures and Tables

List of Figures

List of Tables

Curriculum vitae

Name: Mahmoud Basha

Date of birth: 10.07.1984

Place of birth: Cairo, Egypt

Education

04/2014 - present: Clausthal University of Technology (TU Clausthal), Institute of Materials Science and Engineering (IWW)
Target degree: Doctor of Engineering (Dr.-Ing.)

05/2009 - 01/2012: Ain Shams University, Faculty of Engineering, Egypt
Degree: Master’s degree (M.Sc.) in mechanical engineering

09/2001 - 07/2006: Ain Shams University, Faculty of Engineering, Egypt
Degree: Bachelor’s degree (B.Sc.) in mechanical engineering

Professional Experience

Since 04.2014: Doctoral candidate and research assistant, IWW, TU Clausthal

Since 04.2007: Teaching and research assistant, Ain Shams University, Faculty of Engineering, Egypt

10.2009 – 09.2013 Inspection Engineer, Materials Engineering & Metallurgy Consultancy Unit, Ain Shams University, Egypt.

05.2009 – 10.2009 Research Assistant, School of engineering, University of British Columbia Okanagan (UBCO), Canada

10.2006 – 03.2009 Mechanical Engineer for Product Development, MSM for metal fabrication Co., Egypt

Scholarships/Awards

- GERLS scholarship (Call 2013) for a full PhD study at IWW, TU Clausthal
- Scholarship from University of British Columbia Okanagan (UBCO), Canada for a semester abroad, 2009
- University honours from Ain Shams University for superior academic performance, 2007
- University honours from Ain Shams University for superior academic performance, 2006
- IAESTE scholarship (07–08.2005) at PUK, TU Clausthal

Further Qualifications

- Languages: Arabic (native language), German and English
- Computer skills: MS office, Autodesk INVENTOR, AutoCAD – Mechanical and ANSYS Workbench 17

This page intentionally left blank

Publications

M. Basha, U. Raab, A. Ahmed, M. Mhaede, M. Wollmann, L. Wagner, “Effect of Shot Peening and Roller-Burnishing on the Fatigue Performance of CP-Ti Friction-Welded Joints” 13th World Conference on Titanium, August 16-20, **2015** * Manchester Grand Hyatt * San Diego, California

A. Ahmed, M. Mhaede, M. Basha, M. Wollmann, L. Wagner, “The effect of shot peening parameters and hydroxyapatite coating on surface properties and corrosion behavior of medical grade AISI 316L stainless steel”, Surface & Coatings Technology Vol. 280, pp 347–358, **2015**.

O. Mohamed, M. Basha, L. Wagner, “Optimizing the Process Parameters and Investigating the Influence of Shot Peening and Roller Burnishing on Surface Layer Properties and Fatigue Performance of Al 6061 T4”, Sohag J. Sci. 1, No. 1, pp 65-72, **2016**.

J.Fuhr, M. Basha, M. Wollmann, L. Wagner, “Effects of shot peening on the HCF performance of Ti-6Al-4V by variation of coverage and impact angle” 2nd International Conference on Light Materials LightMAT 2017, 08. - 10. November **2017**, Bremen (Germany).

J.Fuhr, M. Basha, M. Wollmann, L. Wagner, “Coverage and Peening Angle Effects in Shot Peening on HCF Performance of TI-6AL-4V”, Procedia Engineering, Vol. 213, pp 682-690, **2018**.